Babcock & Wilcox
a McDermott company

TMI-1 REACTOR COOLANT PUMP
SHAFT FAILURE ANALYSIS

RESEARCH AND DEVELOPMENT DIVISION
LYNCHBURG RESEARCH CENTER

SPONSORED BY
GENERAL PUBLIC UTILITIES

AUGUST 1984

TMI-1 REACTOR COOLANT PUMP SHAFT
FAILURE ANALYSIS

Lynchburg Research Center Report
RDD:84:5183-06:01

by

D. L. Baty
S. C. Inman

August 1984

CONTENTS

CONTENTS (Cont'd)

List of Tables

List of Figures

List of Figures (Cont'd)

List of Figures (Cont'd)

List of Figures (Cont'd)

ABSTRACT

The failure analysis of the reactor coolant pump 1B shaft from Three Mile Is-
land Unit-1 is contained in this report. Visual examinations, macrophotogra-
phy, metallography, scanning electron microscopy and a variety of chemical
analyses were performed on a short section of the shaft containing the defect.
These examinations show that the shaft failed by high cycle fatigue. Crack
initiation occurred at one of the two anti-rotation pin holes in the shaft.
These pin holes prevent slippage of the thermal sleeve in the event it lost
its shrink fit to the shaft. Surface wear, fretting, residual stress and sur-
face finish may have been factors leading to reduced resistance to crack ini-
tiation. Crack growth continued at low to near threshold crack growth rates.
The results suggest that the bulk of crack propagation occurred during the ex-
tended reactor shutdown for the Three Mile Island Unit-2 incident when the
failed pump was operated alone in its highest combined cyclic stress state for
well over 1,000 hours. Although sulphur was found on the fracture surface,
the fractographic and metallographic results from this investigation, along
with the reported effects of sulphur on stainless steel, do not support the
possibility that sulphur accelerated the shaft failure.

SUMMARY

This report contains the Babcock & Wilcox (B&W) failure analysis of the pump shaft from reactor coolant pump 1B out of Three Mile Island Unit 1. This work was contracted to B&W through General Public Utilities Corporation.

A short length section of the shaft containing the crack and the shaft thermal sleeve were supplied to B&W early in April 1984. The work scope on the examination included:

o   Visual inspection
o   Macrophotography
o   Sectioning
o   Ultrasonic inspection
o   Light microscope metallography
o   Scanning electron microscopy for fractographic features
o   Energy dispersive x-ray spectroscopy
o   Electron microprobe analyses
o   Auger electron spectroscopy
o   X-ray diffraction of deposits
o   Emission spectroscopy of deposits
o   Total sulphur analysis of deposits

The results from these analyses show that the shaft contained a crack extending 227° around its circumference and penetrating to the shaft axis. The crack was initiated and propagated by high cycle fatigue at relatively low to near threshold crack growth rates. The initiation site was at one of the two anti-rotation pin holes used to position the thermal sleeve. The crack was driven by the rotational bending of the shaft which produced asymmetric crack growth, with fastest growth occurring in the direction against shaft rotation.

Fractography and metallography revealed the fracture to be nearly all transgranular with only minor, short length secondary cracks extending off the primary crack. These secondary cracks were only 1 to 2 grains in length and were predominantly transgranular.

A well preserved beachmark pattern around the initiation site indicated that the majority of beachmarks were present within about 1 inch of the fracture surface. A large red-brown corrosion deposit outlined by a heavily pitted beachmark suggests that the crack had initiated and grown to a depth of about 1 inch prior to the 1979 shutdown of Unit 1 for refueling. Rapid growth of the crack from that location to its final position is attributed to the higher rotational bending stresses from the use of this pump in single pump operation with a cold system during the layup mode of Unit 1 in 1983 and early 1984. Although sulphur was found on the fracture surface, there was no evidence to suggest that its presence had initiated the cracks and/or accelerated crack growth. No other deleterious species, such as chlorine, were found, and the shaft material chemistry was within specification.

Detailed stress and fracture mechanics analysis for crack initiation and growth, and correlation of pump operational history with the fatigue fracture information were not part of this work scope but should be performed.

ACKNOWLEDGEMENTS

Many individuals assisted in this investigation and in the preparation of this report. The authors extend their gratitude for the professional help of the following individuals:

G. M. Bain	Color Macrophotography
N. W. White	Scanning Electron Microscopy, Energy Dispersive X-ray Analysis, Specimen Cleaning
B. J. Parham	Light Metallography, Macrophotography
W. A. Shield	Light Metallography, Specimen Cleaning, Figure Preparation, Macrophotography, Dye Penetrant Testing
W. T. Hamilton	Photographic Records, Figure Preparation
B. C. Dudley	Sectioning, Dimensional Documentation
J. C. Dillard	Sectioning, Machining Consultation
J. E. Seagle	Sectioning, Fixturing

C. E. Stinnett	Fixturing
	Engineering Drawings
C. W. Dalton	Fixturing
D. R. Harris	Health Physics
W. S. Pennington	Health Physics
J. B. Younger	Health Physics
J. C. Bullard	Emission Spectroscopy
	X-ray Diffraction
	Sulfur Analyses
T. R. McCue	Auger Spectroscopy
M. E. Scott	Electron Microprobe
M. E. Hensley	Photo Printing
T. Marsh	Report Preparation
S. W. Knox	Manuscript Typing
W. M. Latham	Ultrasonic Inspection
P. J. Latimer	Ultrasonic Inspection
W. A. Pavinich	Fracture Mechanics Consultation
J. M. Bloom	Fracture Mechanics Consultation

L. W. Sarver	Failure Analysis Consultation
G. O. Hayner	Failure Analylsis Consultation
T. A. McNary	Corrosion Consultation
G. T. Theus	Corrosion Consultation

1. INTRODUCTION

1.1 Discovery Of The Failure

The Three Mile Island Unit-1 (TMI-1) nuclear power plant was in cold shutdown in January, 1984 with primary system pressure at 315 psig and one reactor coolant pump, 1b, (rcp-1b) running to provide reactor coolant mixing during layup conditions. On January 27, 1984, vibration on the pump increased from the typical 9-12 mils to 12-15 mils peak to peak. Another step increase to 19 mils in vibration occurred on January 30, 1984. This step increase was followed by a continuous increase in vibration to the 24 to 28 mil range on January 31, 1984. The RCP-1B was shut down on January 31, 1984 for detailed evaluation. Attempts to reduce the vibration by adding balance weights were somewhat successful at the pump operating speed but increased the vibration at 2 times the operating speed. Operation of the motor alone did not show any abnormal vibration at operating or 2 times the operating speed. Ultrasonic examination of the pump shaft by General Public Utility (GPU) staff suggested the presence of a discontinuity above the impeller taper fit. Based upon the vibration analyses, the UT results, and a prior history of pump failures on this pump design at other utilities, GPU concluded that the pump shaft was cracked, most likely in the vicinity of the thermal sleeve. Disassembly of the pump at TMI-1 revealed the presence of an extensive circumferential crack under the thermal sleeve. In addition, evidence of rubbing between the rotating impeller and the diffuser adapter lower stationary labyrinth was found. This wear indicated unusual shaft flexibility. The above information was obtained from GPU in reference 1.

A section of the shaft containing the crack, the removed thermal sleeve and deposit scrapings were sent to the Lynchburg Research Center (LRC) for failure analysis on April 6, 1984.

1. INTRODUCTION

1.1 Discovery Of The Failure

The Three Mile Island Unit-1 (TMI-1) nuclear power plant was in cold shutdown in January, 1984 with primary system pressure at 315 psig and one reactor coolant pump, 1b, (rcp-1b) running to provide reactor coolant mixing during layup conditions. On January 27, 1984, vibration on the pump increased from the typical 9-12 mils to 12-15 mils peak to peak. Another step increase to 19 mils in vibration occurred on January 30, 1984. This step increase was followed by a continuous increase in vibration to the 24 to 28 mil range on January 31, 1984. The RCP-1B was shut down on January 31, 1984 for detailed evaluation. Attempts to reduce the vibration by adding balance weights were somewhat successful at the pump operating speed but increased the vibration at 2 times the operating speed. Operation of the motor alone did not show any abnormal vibration at operating or 2 times the operating speed. Ultrasonic examination of the pump shaft by General Public Utility (GPU) staff suggested the presence of a discontinuity above the impeller taper fit. Based upon the vibration analyses, the UT results, and a prior history of pump failures on this pump design at other utilities, GPU concluded that the pump shaft was cracked, most likely in the vicinity of the thermal sleeve. Disassembly of the pump at TMI-1 revealed the presence of an extensive circumferential crack under the thermal sleeve. In addition, evidence of rubbing between the rotating impeller and the diffuser adapter lower stationary labyrinth was found. This wear indicated unusual shaft flexibility. The above information was obtained from GPU in reference 1.

A section of the shaft containing the crack, the removed thermal sleeve and deposit scrapings were sent to the Lynchburg Research Center (LRC) for failure analysis on April 6, 1984.

1.2 Reactor Coolant Pump 1-B (RCP-1B) Shaft Description

RCP-1B is a Westinghouse Model 93A pump of which 82 are in use in the United States and in foreign reactors. A cutaway view of this pump is shown in Figure 1.2-1. The area of interest relative to the TMI-1 pump shaft failure is circled in Figure 1.2-1 and enlarged in Figure 1.2-2. In Figure 1.2-2 the location of the TMI-1 pump shaft crack and two other pump shaft failures, Surry-1[2] and Prairie Island Unit-2 (PI-2)[3], are shown. The Surry-1 failure was opposite the upper thermal barrier labyrinth, just below the radial bearing. The Surry-1 shaft had a shrunk-fit thermal sleeve in place near the crack. Both the PI-2 and TMI-1 failures occurred opposite the lower thermal barrier labyrinth. Both PI-2 and TMI-1 shafts had shrunk-fit thermal sleeves over the area of cracking. Figure 1.2-3 provides an overall view of the shaft configuration associated with the Surry-1 failure (type A shaft) and the PI-2 and TMI-1 failure (type B shaft.) The type B shaft reflects design changes in the area of the Surry-1 failure. These changes[4] include elimination of 1) the shrunk-on thermal sleeve just below the radial bearing, 2) a groove in the shaft below the bearing, and 3) anti-rotation pins, lock-welded near the site of the Surry-1 failure.

The geometry of the lower end of type B shaft used in TMI-1 RCP-1B is shown in Figure 1.2-4. The majority of the crack in RCP-1B was found by GPU to exist under the thermal sleeve near the shaft diameter step change from 8.750 inches to 9.10 inches. Near this diameter change are two blind holes 180° apart on the shaft. Each of these holes are 0.3906 inches in diameter and extend to a maximum depth of 0.455 inch. Figure 1.2-5 shows the design detail of these holes, the thermal sleeve, and shaft in this area. The holes position the anti-rotation pins which are welded to the thermal sleeve.

For a primary coolant loop temperature of 557°F, the shaft temperature in the location of the PI-2 and TMI-1 failures would be less than 180°F under steady state conditions.

NO. 3 SEAL
NO. 2 SEAL
WATER LEAKOFF
NO. 2 SEAL
NO. 1 SEAL
WATER LEAKOFF
NO. 1 SEAL
MAIN FLANGE
COOLING WATER OUTLET
DISCHARGE NOZZLE
See Enlarged View

MOTOR
SPOOL PIECE
MOTOR SUPPORT HOUSING
NO. 1 SEAL BYPASS
MAIN FLANGE BOLT
THERMAL BARRIER PRESSURE TAP
COOLING WATER INLET
THERMAL BARRIER PRESSURE TAP
INJECTION WATER
PUMP SHAFT
RADIAL BEARING
THERMAL BARRIER HEAT EXCHANGER
TURNING VANE-DIFFUSER
IMPELLER
DIFFUSER ADAPTER
CASING
SUCTION NOZZLE

Figure 1.2-1.   Schematic of Westinghouse Model
93 A Reactor Coolant Pump
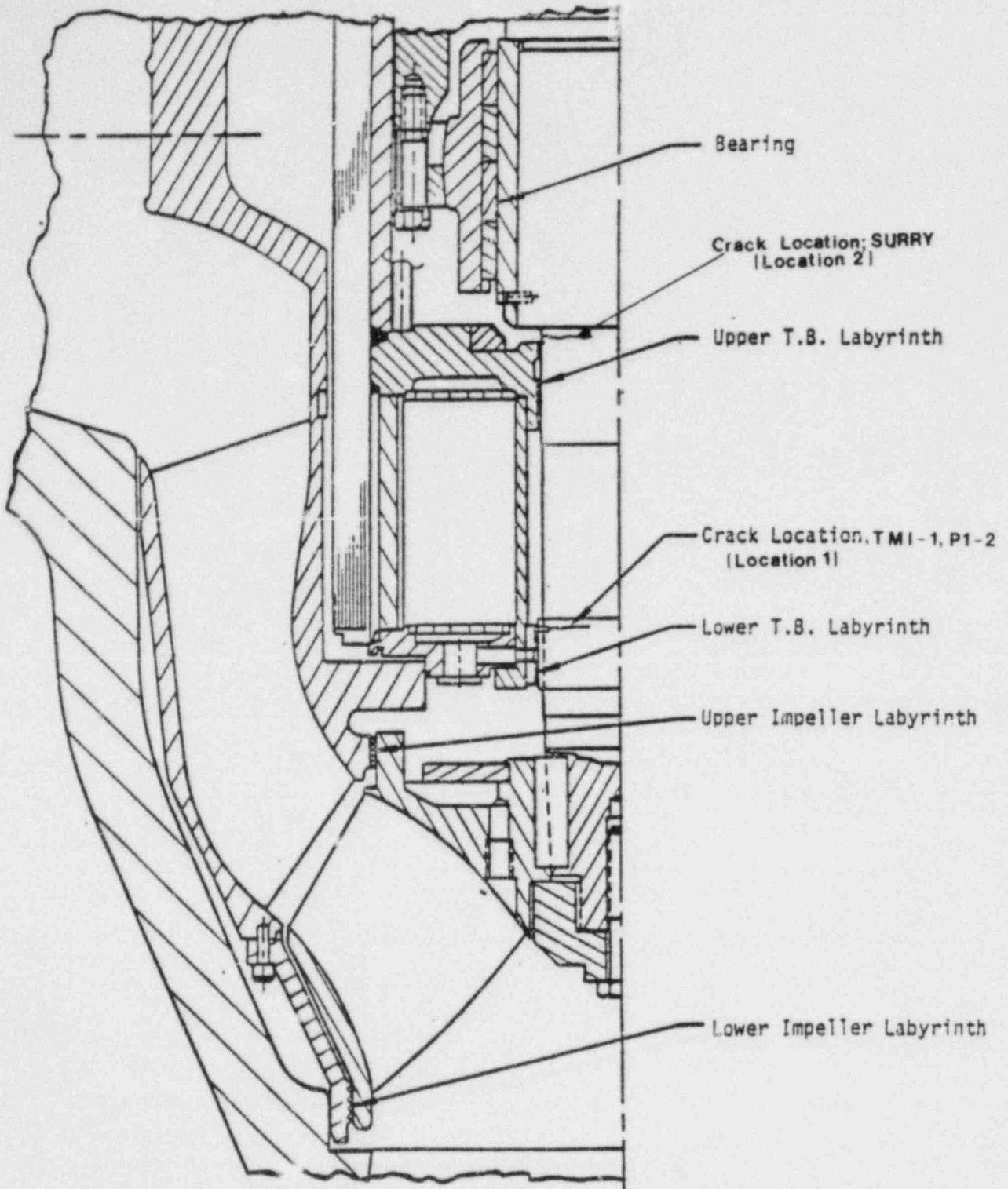
Figure 1.2-2. Enlarged Section View of Pump in Failure Area
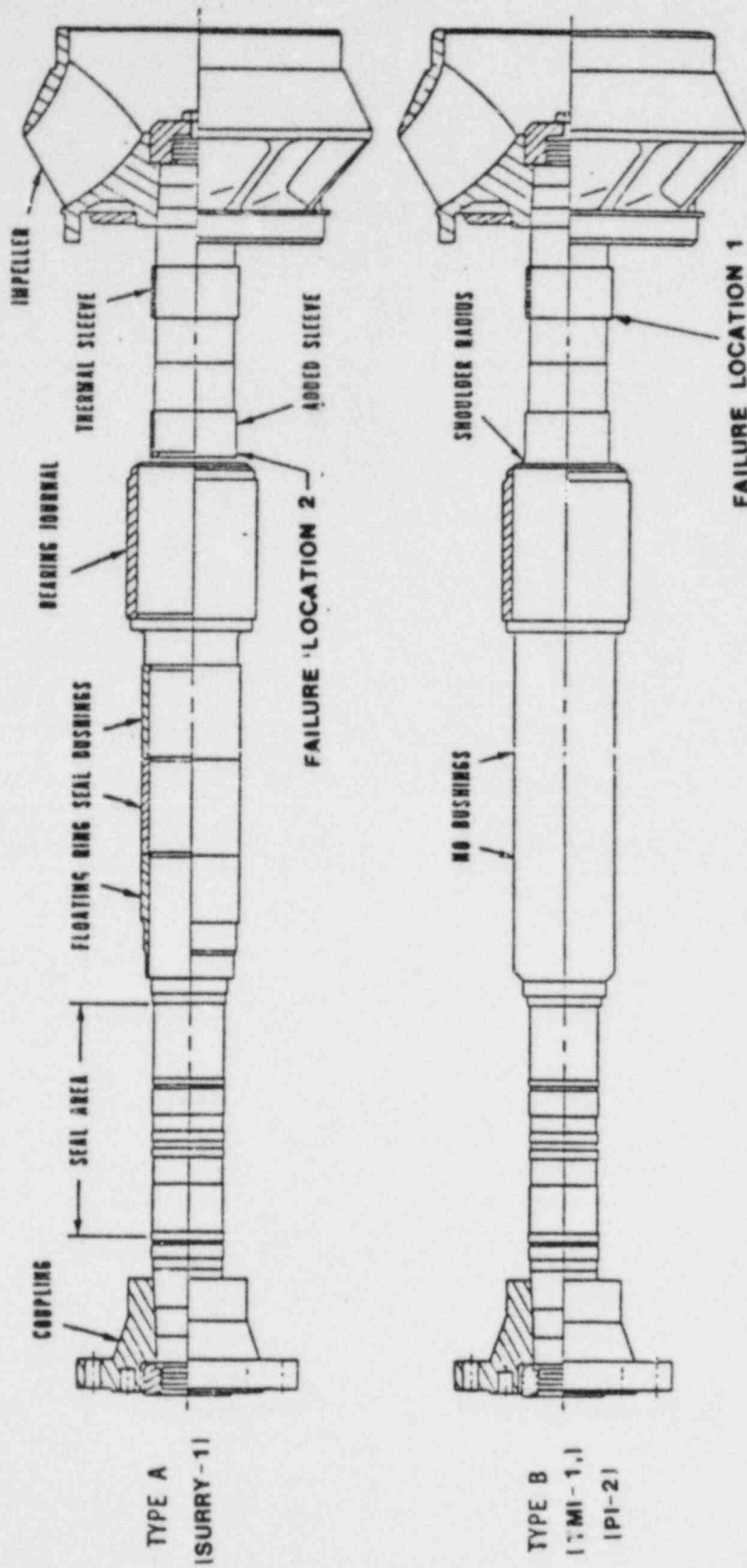
Figure 1.2-3. Comparison of Type A and B Pump Shafts

Journal Sleeve

.06R

Circumferential Crack
Location 1

Thermal Sleeve

Impeller Taper

$\frac{13.983}{13.981}$

$\frac{9.266}{9.262}$

9.10

$\frac{9.266}{9.262}$

$\frac{8.751}{8.750}$

0.3906" ⌀
Anti-Rotation Pin Hole (2)

.015 max.

16.10

34.75
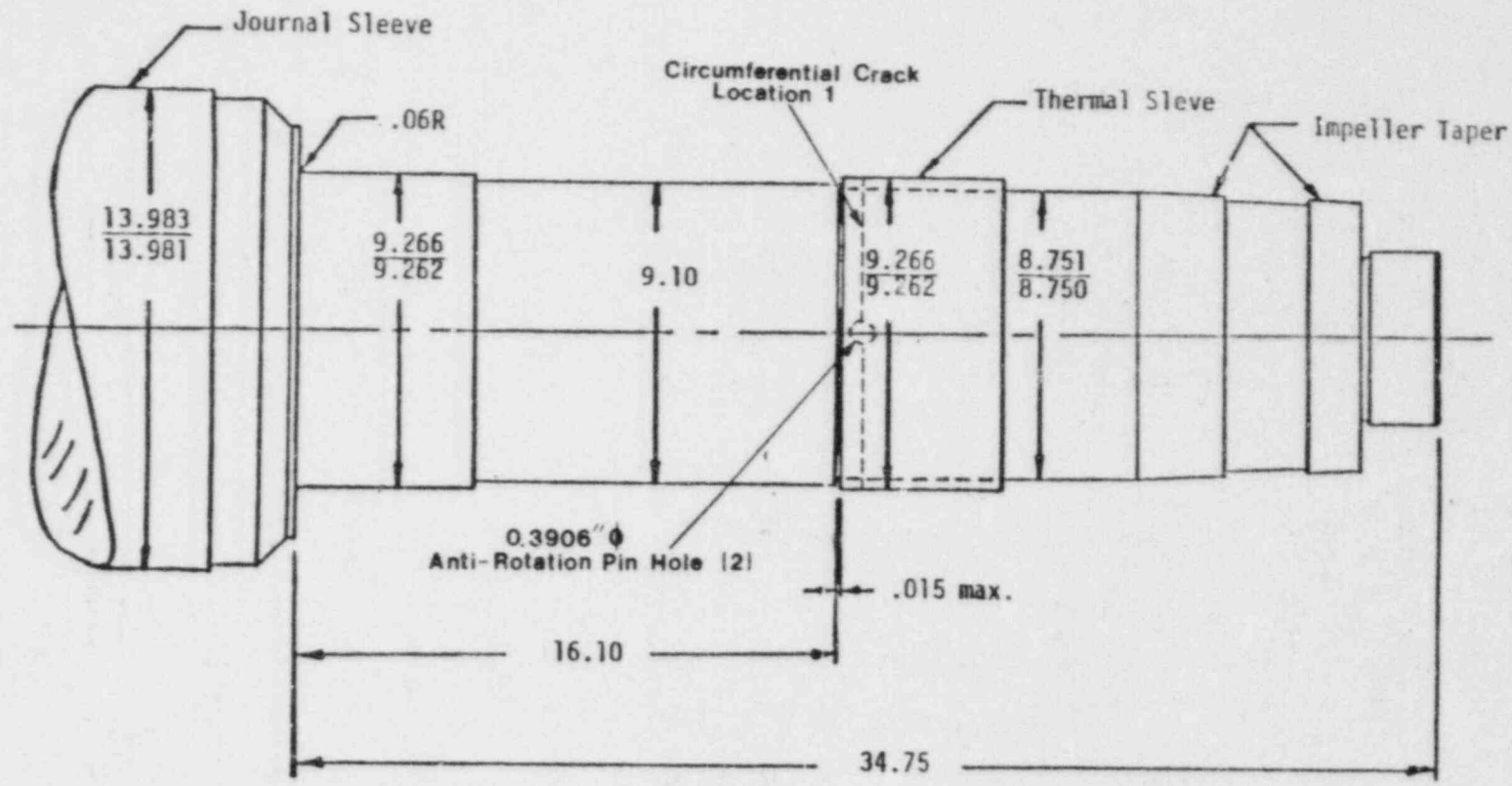
TYPE B SHAFT

Figure 1.2-4. Geometry of Type B Shaft in Failure Area

① MEASURED DIMENSION
② DRAWING DIMENSION
③ CALCULATED
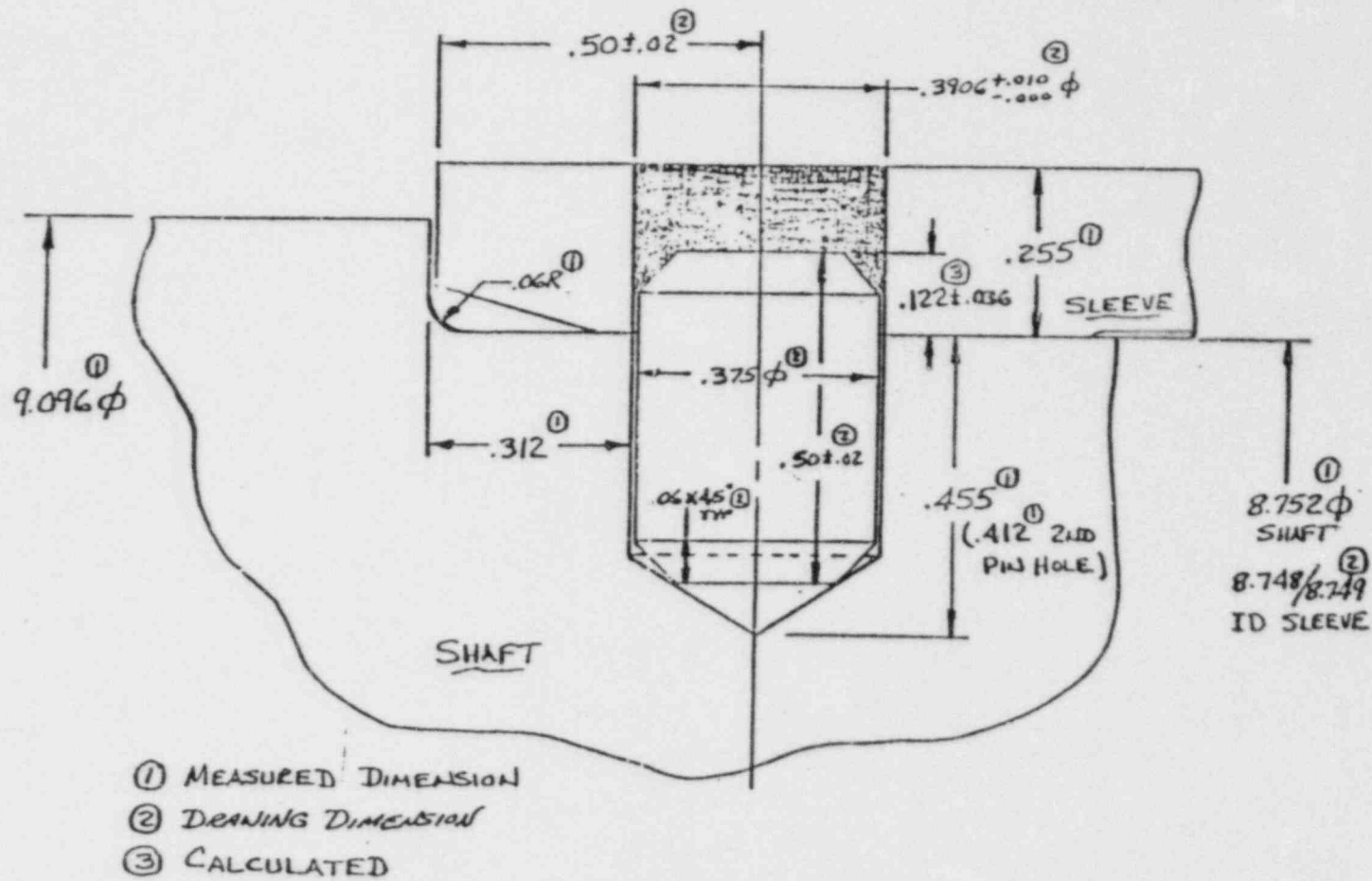
Figure 1.2-5. Pin Hole Geometry i⁻ Type B Shaft

1.3 Pump Shaft Material

The pump shaft is machined from a rough turned forged bar of type 347 stainless steel. The material was procured to ASTM A182-71 Grade F347 with additional requirements imposed by Westinghouse. The heat treatment of the shaft prior to machining consists of a two-step solution treatment and water quench, and a stabilizing treatment as follows:

Solution treatment:

(1) heat to 1800°F over a 7 hour period

(2) hold at 1800°F for 7 hours

(3) heat to 1960°F over a 1 hour period

(4) hold at 1960°F for 2 hours

(5) water quench

Stabilizing treatment:

(1) heat to 1525°F over a 5 hour period

(2) hold at 1525°F for 28 hours

(3) furnace cool

This heat treatment was designed to assure complete stabilization of the carbon in the form of niobium carbides and provide a fully annealed micro-structure. Typical properties of seven samples of material subjected to this heat treatment are 33.5 to 37.0 ksi 0.2% offset yield strength, 77.5 to 83.5 ksi ultimate tensile strength, 53.5 to 58.0% elongation in 2 inches, and 67.0 to 70.5% reduction in area.[5]

The fatigue endurance limit for the shaft material is reported to be 21 to 22 ksi in references 3 and 4. However, in the presence of thermally induced residual stresses and a notch (k_t = 5.3), the material has failed in 5×10^6 cycles with an axial stress of 7-8 ksi and no mean stress.[4]

1.4 Shaft Stresses

A detailed stress analysis of the TMI-1 pump shaft (type B) at the TMI-1 failure (location 1) is not available to B&W. From references 2, 3 and 4, the stress state for type A or B shafts at location 1 or 2 are provided in varying completeness. In reference 2, a general review of the Surry-1 pump shaft failure is provided. This failure occurred on a type A shaft at location 2. In reference 4, a review of the stress state and fatigue margin was provided for the TMI-1 type B pump shaft at location 2. While the stress analysis performed was for the same shaft and primary coolant loop design, the location was different from the current failure. Reference 3 provides the stress analysis for a type B shaft at location 1 but for the Westinghouse PI-2 primary coolant loop. Tables 1 and 2 summarize the stress state information available from references 2-4. Table 1 covers the cold loop, one pump running mode while Table 2 addresses a hot loop with all pumps running. Table 3 addresses stresses in the type B shaft at location 1 with B&W primary loop hydraulic loads. In general, the cold loop, one pump running mode produces the highest stress levels at both steady state and cyclic conditions. This is particularly true for the cyclic loading from rotational bending caused by radial thrust. This radial thrust is responsible for the highest cylic stress regardless of the primary system design or temperature.

The shaft configuration and failure location in PI-2 is identical to that of TMI-1 so that geometric effects on stress are the same, however, differences in motor horsepower and primary system hydraulic loads will cause some differences in stresses. In making stress approximations for the TMI-1 location 1 failure, the location 2 data for TMI-1 can be utilized or modified slightly. For location 1, motor torque, cyclic torque, and rotating radial load should be approximately the same as that shown for TMI-1 location 2. The axial thrust is increased to a stress of 826 psi during cold operation and 943 psi

during hot operation at location 1. This change is the result of a decrease in the deadweight load, which is offset by a decrease in diameter from 9.262 inches at location 2 to 8.75 inches at location 1. Cyclic axial load for location 1 or 2 is unknown but is probably very low based upon the low value for PI-2. The radial thrust from bending is reduced to about 2836 psi during cold operation and 1347 psi during hot operation at a location 1. This bending stress is generated from a cantilevered beam (shaft) analogy where location 2 is at the fixed end, location 1 is approximately halfway along the beam and the concentrated load is applied at the free end of the beam. Appendix A provides the calculations of the modified axial and radial thrust loads. Table 3 summarizes these approximate stress values for TMI-1 location 1. It should be noted that the largest alternating stress from rotational bending (radial thrust) is larger in TMI-1 than in PI-2.

1.5 Shaft Operational History

Prior to the Unit 2 incident in 1979, RCP 1B had received 2.4×10^9 turns.[3] Of these, 4.2×10^5 were in the single pump, cold loop operational mode (6 hrs. operation). After the Unit-2 incident, another 1.04×10^8 revolutions were put on the shaft in the same single pump mode (1472 hours). The pump was only operated in the single pump, cold loop mode after the Unit-2 incident (the single pump operation history provided by J. Janiszewski, GPU).

Table 1. Comparison of Shaft Loads and Stresses* for PI-2, TMI-1 and Surry-1 During One Pump - Cold Operation

	PI-2 (W)[1] Type B Shaft Location 1	TMI-1 (B&W)[2] Type B Shaft Location 2	Surry-1 (W)[1] Type A Shaft Location 2
Motor Torque	2880 (31566)	2904	-
Axial Thrust	1183 (71140)	742 (50000)	-
Radial Thrust	+1425 (5140)	+4484 (10000)	+2850
Cyclic Torque	+16 (180)	+87	-
Cyclic Axial Load	+5 (297)	-	-
Rotating Radial Load	176 (635)	285 (635)	-

*First number is stress in psi, second number in brackets is load in lbs.

[1]Values from reference 3
[2]Values from reference 4

Table 2. Comparison of Shat Loads and Stresses* for
PI-2 and TMI-1, During Hot Operation

	PI-2 (W)[1] Type B Shaft Location 1	TMI-1 (B&W)[2] Type B Shaft Location 2
Motor Torque	2330 (25546)	2691
Axial Thrust	928 (55800)	846 (57000)
Radial Thrust	+999 ($\overline{3}$605)	+2130 ($\overline{(}$4750)
Cyclic Torque	+8 ($\overline{8}$9)	+81
Cyclic Axial Load	+2 (1$\overline{4}$7)	
Rotating Radial Load	133 (480)	215 (480)

*First number is stress in psi, second number in brackets is load in lbs.

[1] Values from reference 3
[2] Values from reference 4

Table 3. Shaft Loads and Stresses* at Location 1
for Type B Shaft at TMI-1

	One Pump-Cold Operation	Hot Operation
Motor Torque	2904	2691
Axial Thrust	826 (49690)	943 (56690)
Radial Thrust	+2836 (10000)	+1347 (4750)
Cyclic Torque	+87	+81
Cyclic Axial Load	N/A	N/A
Rotating Radial Load	285 (635)	215 (480)

*First number is stress in psi, second number in brackets is load in lbs.

2. WORK SCOPE TASK DESCRIPTION

GPU requested a proposal and cost estimate for performing a failure analysis on the TMI-1 pump shaft in GPUN Inquiry No 1142. Reference 6 responded to that request. This original B&W proposal was subsequently modified by references 7 and 8 to arrive at the final work scope reported in this document. A brief outline of the task in this final work scope is provided below.

2.1 Receipt, Documentation And Visual Inspection

- o Radiation survey of shaft and thermal sleeve
- o Orientation documentation
- o Fixturing for inspection
- o Visual inspection of shaft and thermal sleeve (unaided eye and stereo light microscopy)
- o Macrophotography of shaft and thermal sleeve in color (35 mm, Polaroid) and black & white
- o Stereo light microscopy
- o Ultrasonic inspection
- o Dimensional characterization of crack path and thermal sleeve contact area over the crack
- o Dye penetrant test of uncracked pin hole in shaft
- o Review of inspection and microscopy results with GPU

2.2 Specimen Removal

- o Develop sectioning plan
- o Protect shaft outer surface near crack and fracture surface from chemical alteration prior to examination
- o Review sectioning plan with GPU for concurrence

o   Specimen sectioning and identification

o   Ultrasonic inspection

2.3 Fractography And Metallography

o   Implement surface cleaning technique for fractography

o   Light and scanning electron microscopy (SEM) of fracture features
     from initiation to final crack tip position

o   Energy dispersive X-ray spectroscopy (EDS) of selected locations
     along fracture path for qualitative chemical analyses.

o   Light metallography for fracture path detail and microstructural
     features at:

     -    a continuous crack path from OD to crack tip
     -    initiation site
     -    unique fracture surface features

2.4 Microchemical And Bulk Chemical Analyses

o   Quantitative Auger electron spectroscopy (AES) of fracture surface
     films

o   Electron microprobe of

     -    unopened fracture cross section
     -    fracture surface after controlled fracture separation
     -    inclusion population in a polished longitudinal section of the
          shaft

o   Bulk chemical analysis of shaft material near initiation site

2.5 Deposit Analyses

o   Emission spectroscopy, x-ray diffraction, and wet chemical analysis
     for composition, structure, and sulphur content on GPU scrapings
     from

- thermal sleeve
- flange

3. TASK RESULTS

In the following subsections, the task results, discussion, and where appropriate, task experimental procedure is provided.

3.1 Receipt, Documentation And Visual Inspection

3.1.1 General Information

The radiation survey of the pump shaft section shown in Figure 3.1-1 indicated a combined $\beta + \gamma$ field of < 1 mR/hr at 1 ft with a smearable surface contamination of approximately 2000 dpm. Later, exposure of the fracture surface revealed a much higher smearable contamination of 30,000 dpm. The radiation field of the thermal sleeve was also < 1 mR/hr ($\beta + \gamma$) at 1 ft. Smearable contamination was high, however, at 50,000 dpm.

During this receipt inspection stage, either white cotton gloves or powder-free latex gloves were employed while handling the specimens. When not under examination, the shaft and thermal sleeve were covered with a polyethene bag or sheet.

3.1.2 Pump Shaft Examination

The shaft section received was approximately 6.75 inches long. A nominal diameter of 9.10 inches extended for about 2.95 inches of length with a reduced diameter of 8.75 inches extending over the remaining 3.80 inches.

Initial inspection revealed that GPU personnel had already provided orientation markings on the impeller side of the shaft as seen in Figure 3.1-1. These marks divided the circular cross section into octants, numbered consecutively in a clockwise direction starting at a pin hole which was intersected by the crack.

This orientation scheme was retained throughout the examination. GPU personnel had also indicated, on the impeller side cross section, the extent of the crack (as best they could determine) around the circumference. This indication is given by a heavier ink marking dividing the shaft into two sectors: one marked "crack" covering about 2/3 of the circumference and one marked "no crack". Thus, in a clockwise direction from the cracked pinhole, the crack extended into the #2 octant and counterclockwise into the #5 octant.

Visual examination of the pump shaft with the unaided eye provided several general observations. Figure 3.1-2 provides a series of reduced power macrophotographs showing more detail of the shaft surface. The shaft, in general, had a bright metallic appearance with some occasional reddish-brown deposits scattered over the cylindrical surface. These reddish-brown deposits were most prevalent within about a 1 inch band extending from the step change in diameter toward the impeller end. These can be readily seen in Figure 3.1-2. The most dominant of these deposits were two narrow, linear, and purely circumferential streaks approximately 3/4 inch apart. Later in examination of the thermal sleeve, it will be seen that these streaks correspond to the interface between the shaft and a nominal 3/4 inch wide contact surface of the thermal sleeve.

The width of these streaks vary but those closer to the step seem to be broader and have a much darker brown to black appearance. In octants 7 and 8 (Figure 3.1-2d) several other shorter streaks appeared within the 3/4 inch wide band.

Both pin holes had worn or polished areas around their circumference which disrupted the local pattern of deposits as shown in Figure 3.1-3. The crack can be clearly seen to intersect the pin hole at the border of the #1 and #8

octants (Figure 3.1-3a-c). The crack shown in Figure 3.1-3 can only be discerned near the #1-#8 pin hole (views a and c) where the crack was bordered on one side by a bright metallic worn area and a linear streak of deposits on the other.

Examination of th shaft surface along the crack was performed using a Nikon Stereo-Zoom came ₄ equipped for 35mm color photography. A continuous series of color photographs of the cracked area was taken at 8X over the entire circumferential extent of the crack. This examination revealed several facts about the fracture at the shaft surface.

The crack path at the surface is not truly circumferential but inclined at about 2-4° on the average from the circumferential direction as seen in Figure 3.1-4. The path traveled axially toward the impeller end as the crack is followed in a clockwise path viewed from the impeller side.

When followed to its extremity in the #5 octant, the crack went up and over the step change in diameter from the nominal 8.75 inch to the 9.10 inch diameter. This change is shown in Figure 3.1-5. In contrast to the sharply defined cracks in other parts of the path, the crack at this extremity was poorly defined, showing signs of surface deformation. At its other extremity in octant #2, the crack was about 3/4 inch axially displaced, toward the impeller, from its other end in octant #5. Its appearance is shown in Figure 3.1-6. The gouge shown in Figure 3.1-6 was created during the removal of the thermal sleeve by GPU personnel. A deposit appears to have built up or exuded from the crack in this location. At both extremities, (Figure 3.1-5 and -6), the angle of the crack changes rather dramatically from the 2-4° average to approximately 15° from the circumferential direction. The length of paths at

this greater inclination was rather short, about 1/4 inch in octant #2 and 5/8 inch in octant #5.

A striking difference in the coarseness of the surface finish on the 8.75 inch diameter compared to the 9.10 inch diameter can be seen in Figure 3.1-5. The 8.75 inch diameter section which contained the bulk of the crack has machine marks which are about 12 mils apart. On the 9.10 inch diameter surface, the marks are not well defined, and the finish is at least an order of magnitude finer.

Aside from the changes in crack path angle at the extremities, other sharp changes in path angle were noted along its length. In Figure 3.1-7, two prominent changes in angle are shown. In view A, at about 1-1/2 inches from the nearest edge of the cracked pin hole (in octant #8), the angle increased to about 9° for about 3/8 inch and then resumed the 2-4° angle. In view B, two reversals in path angle occurred in octant #1 at about 1 inch and again at 1-3/8 inches from the nearest edge of the cracked pin hole. At each of these two locations in view B of Figure 3.1-7, the path angle went from +2 to 4° to about -10°. In later results in Section 3.2, these angle changes are related to changes on the fracture surface.

Other rather sharp changes in the fracture path angle occurred at the pin hole. In Figure 3.1-8, a gradual increase in path angle is seen on the #8 octant side but a rather sharp increase and decrease is seen on the #1 octant side. In this figure, a higher magnification view of the wear around the pin hole shown previously in Figure 3.1-3 can be seen. This wear has created a polished plane at an oblique angle to the coarse machining marks, enhancing their apparent depth and root sharpness. Also shown is the circumferential wear band which followed the motor side of the crack near its intersection with the pin hole.

Examples of other wear patterns and deposits previously pointed out in Figures
3.1-2 and -3 are shown in more detail in Figure 3.1-9. Following the crack
from its extremity in octant #5 back toward the cracked pin hole, the crack
went down from the 9.10 inch diameter section onto the 8.75 inch diameter
where it passes through a rather bright metallic surface which appears unworn
in Figure 3.1-9a. Some dark brown filming may have been present right at the
crack opening. Continuing further toward the pin hole, the crack eventually
crossed one of the nearly continuous dark brown bands shown in all of the
views in Figure 3.1-2. A higher magnification view of this area is shown in
Figure 3.1-9b. Some irregularities in the film pattern can be seen in this
view and appear to be spalling. As indicated earlier, this deposit band
corresponds to the edge of the thermal sleeve seating surface closest to the
motor end of the shaft. After crossing the nearly continuous deposit, the
crack proceeded toward the pin hole; however, a band of worn surface devoid of
the dark brown deposits developed between the crack and the nearly continuous
deposit band as shown in Figure 3.1-9c. Additional spalling or cracking of
the adjacent band of deposits can be seen. As the pin hole is approached, the
surface of the worn area became more polished in appearance and none of the
machining marks were present. This was previously shown in Figure 3.1-8.

As the crack emerged from the other side of the pin hole, the brightly worn
area on the motor side of the crack persisted for about 2 inches and contained
some very large gouges which were previously shown in Figure 3.1-7b. The
gouges were elongated in either the circumferential direction, or at about
40-50° from the pure circumferential orientation. Beyond this region,
proceeding toward the extreme of the crack in octant #2, the motor side of the
crack appeared less worn and the color changed from dull gray to a light
red-brown color and became virtually indistinguishable from the other side of
the crack. Examples of these changes are shown in Figure 3.1-9d and Figure
3.1-6 at the crack tip.

Examination into the cracked pin hole clearly revealed the crack, scattered red-brown deposits and machine marks. The machined surface appeared to have grooves or ripples going around the circumference of the hole's inside surface. Other finer marks at 90° to the circumferential grooves were also present. These features are shown in Figure 3.1-10.

Although the crack did not extend to the other pin hole, there was concern that a crack may also have started in that location as well. Visual examination of the hole revealed many of the same features observed for the cracked hole. Figure 3.1-11 shows a similar narrow band of   ar around the circumference of the hole at the shaft OD surface. .ne effects of the wear on the coarse machine marks near the hole is most noticeable in the shaft transverse direction as shown in the higher magnification views taken 90° apart adjacent to the hole. The inside surface of this hole also had the circumferential grooves and other fir   ~ol marks 90° to the grooves. In the bottom of the hole were what appe   ~e the remnant of an initial starter hole which was mislocated and re   igure 3.1-12 shows the internal features of the holes. Dye pene   of the hole did not reveal any crack indications.

The overall position of the crack at the shaft surface is shown in Figure 3.1-13. This figure is based upon the visual and low magnification observations made earlier, and measurements made with a scale, dial caliper micrometer and metal tape measure prior to any sectioning of the shaft specimen. The crack extended a total of 227° around the shaft circumference with 146° covering the #8, #7, #6 and part of #5 octants (i.e., counterclockwise from the cracked pin hole when shaft viewed from impeller end) and 81° covering the #1 and part of the #2 octant. The circumferential component of the crack path was about 17.378 inches. The axial component of the crack was about 0.73 inch. Crack path coordinates are given in Figure 3.1-13. Also,

shown in Figure 3.1-13 are the nominal dimensions of the pin holes. Actual
diameter measurements showed the cracked hole diameter to be 0.390 inch in the
shaft circumferential directions and 0.385 inch in the shaft axial direction.
At the 180° pin hole location, the diameter in the shaft circumferential di-
rection was 0.388 inch and in the axial direction 0.389 inch.

3.1.3 Thermal Sleeve Examination

The thermal sleeve was removed from the pump shaft by GPU personnel. The
sleeve was cut approximately in half. Both pieces "A" and "B" were sent to
the LRC. Figure 3.1-14 shows the inside and outside surface views of both
pieces. The outer diameter surfaces of the sleeve were heavily scored in the
circumferential direction except for two bands of material. One was located
at the motor side and was about 1/2 inch wide. The second was located about
3-1/4 inches from the motor side of the sleeve and was about 1 inch wide. The
general color of the outer surface was a light gray metallic.

The inside of the sleeve halves contained the anti-rotation pin, a motor side
seating surface about 3/4 inch wide, and an impeller side seating surface
about 1/4 inch wide. The bulk of the inside surface was recessed below the
seating surface to permit a layer of coolant to exist between the sleeve and
the shaft. A flow slot had been machined into the impeller side seating
surface directly opposite from the anti-rotation pin. These features can be
seen in Figure 3.1-14.

From visual examination of the wear and corrosion patterns on both the pump
shaft surface and the inside surfaces of the thermal sleeve, piece "A" was
found to contain the pin which had been in the cracked pin hole of the shaft.
The inside surface had an elongated circumferential wear pattern extending
from either side of the pin. This elongated wear band is shown in Figure

3.1-14. In Figure 3.1-15 this wear band is shown at higher magnification, and the mating pump shaft wear patterns are also shown. In general, the wear patterns on the pump shaft and thermal sleeve matched well. The heaviest corrosion deposits on the inside surface of the "A" section were on the chamfer area on the extreme end (motor side) of the sleeve, a band about 1/8 inch wide around the pin at the seating surface, and in a local area around the flow slot. The chamfer deposits were red-brown and heavy enough to obscure machine marks. In this area the film had spalled off revealing bright metal and faint machine marks. The area around the pin was more of a gray-brown color. The machine marks which were clearly visible on the majority of the seating surface were somewhat obscured in this area. Both the chamfer films and the films around the pin can be seen in Figure 3.1-15. The flow slot deposits appeared to be heavy but had not been subjected to wear, and the machine marks could still be observed. A very narrow band of deposits could also be observed at the inner edge adjacent to the recessed area of the 3/4 inch wide seating surface as shown in Figure 3.1-15. This band followed the entire edge of the seating surface.

The examination of the "B" section of the thermal sleeve revealed all of the same results mentioned for the "A" section except the large circumferential wear band in the vicinity of the pin on the "A" section was not present on the "B" section. Figure 3.1-16 shows the "B" sleeve section near the pin. The area to either side of the pin had a corrosion film which appeared undisturbed compared to the same location for the 0° pin in the "A" section (Figure 3.1-15). A small specimen containing the pin of the "B" section thermal sleeve was examined on the SEM. EDS spectra showed sulphur to be present in deposits on the sleeve's ID surface, particularly near the pin. No sulphur was observed in worn or deposit-free areas. The cut edges of this specimen also did not show any sulphur to be present.

Measurements were made on selected locations of both the "A" and "B" sections to determine if any gross dimensional variations were present. Figure 3.1-17 shows the results of that survey. In general, very little wear was found even on the "A" section where only a 1-2 mil smaller thickness in the worn seating area was observed. Neither pin appeared to have suffered any metal removal and had the same diameter of 0.375 inch in the axial and circumferential direction of the shaft.

3.1.4 Visual Examination Summary and Discussion

The results from the visual examination of the shaft and thermal sleeve revealed the following key points:

o   The crack extended approximately 227° around the shaft circumference.

o   The crack path was not purely circumferential but had an axial component or pitch of about 3/4 inch over the 227°.

o   The crack was primarily on the smaller diameter (8.75 inch) portion of the shaft, with a small portion extending up to the 9.10 inch diameter section.

o   The crack path was fairly linear but changed direction sharply near its ends, at the pin hole, and at two locations, one on either side of the pin hole.

o   The crack revealed no surface deformation except at one end where it went up to the 9.10 inch diameter and changed direction sharply. Surface deformation was seen in this area.

o   Coarse machine marks were present on the 8.75 inch diameter
    section compared to the 9.10 inch diameter.

o   No cracking was observed in the 180° pin hole.

o   Bands of red-brown to brown-black corrosion product bordered
    the interface between the thermal sleeve seat and the shaft.
    These bands were seen on the sleeve and the shaft.

o   As the crack passed under the thermal sleeve seat, one side of
    the crack developed a worn or fretted area. This was particu-
    larly true near the 0° pin hole.

o   A band of worn metal was found around the cracked pin hole and
    partially around the uncracked 180° pin hole.

o   Neither the thermal sleeve nor the pins appeared to have any
    major amounts of metal removal despite having obvious surface
    wear marks.

o   The starter hole for the 180° pin hole appeared to have been
    initially mislocated.

o   The wear patterns on the shaft and mating thermal sleeve
    matched very well.

o   Sulphur was found in deposits on the ID surface of the thermal
    sleeve near the 180° pin.

The sharp changes in crack path noted suggest that changes in stress state on fracture mode were occurring in these areas. The sharp change at the extremes of the crack are in the directions expected for entering shear overload. The general orientation of the crack path suggests a predominantly axial stress is driving crack growth. However, the slight pitch of the crack path indicates that a small torsional stress may also be influencing crack growth direction.

The non-symmetric wear along the crack path under the thermal sleeve and on the pin hole suggests that permanent deformation, possibly from torsion has occurred leaving one side of the shaft crack in contact with the sleeve and the other side twisted away. The band of corrosion film outlining the edges of the thermal sleeve seating surface on the shaft suggests that localized corrosion was occurring around the circumference of the shaft at this location.
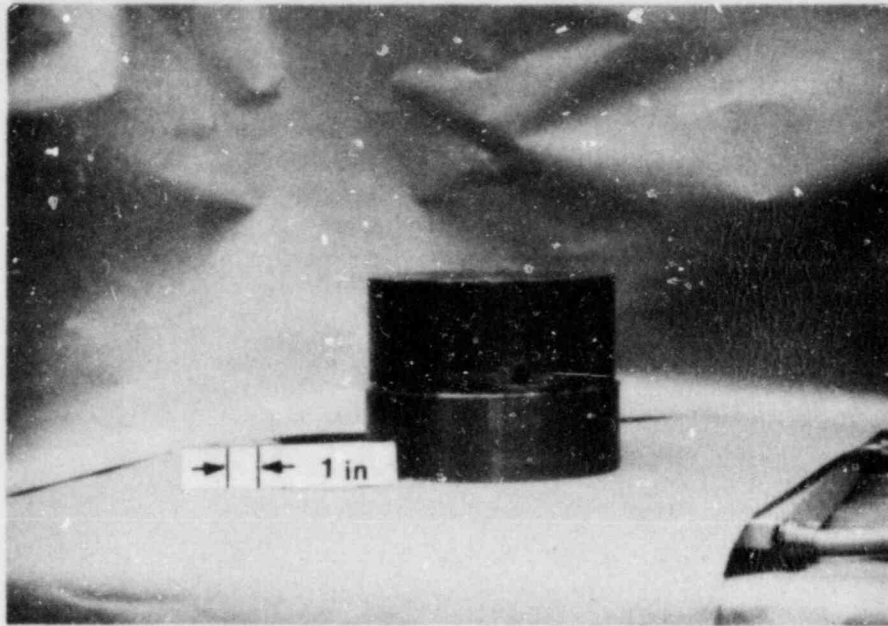
A
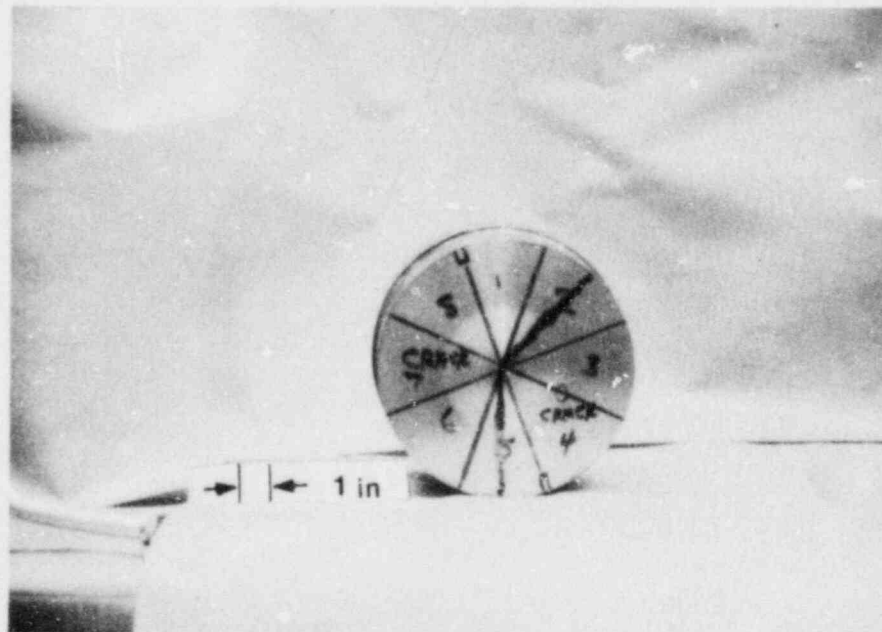
B

Figure 3.1-1.   Reduced Magnification View of Pump Shaft
Section Containing Crack at Pin Hole in A;
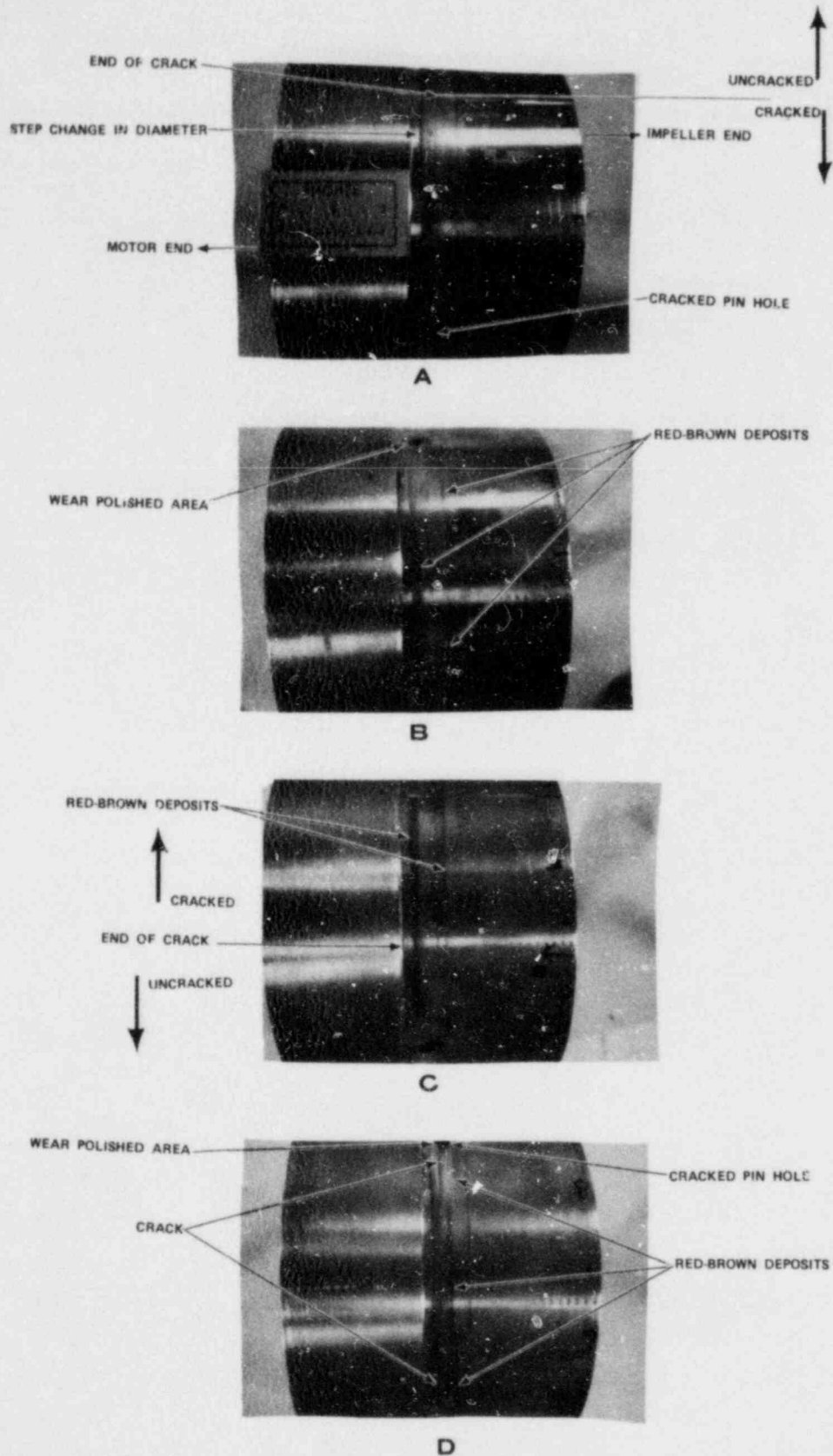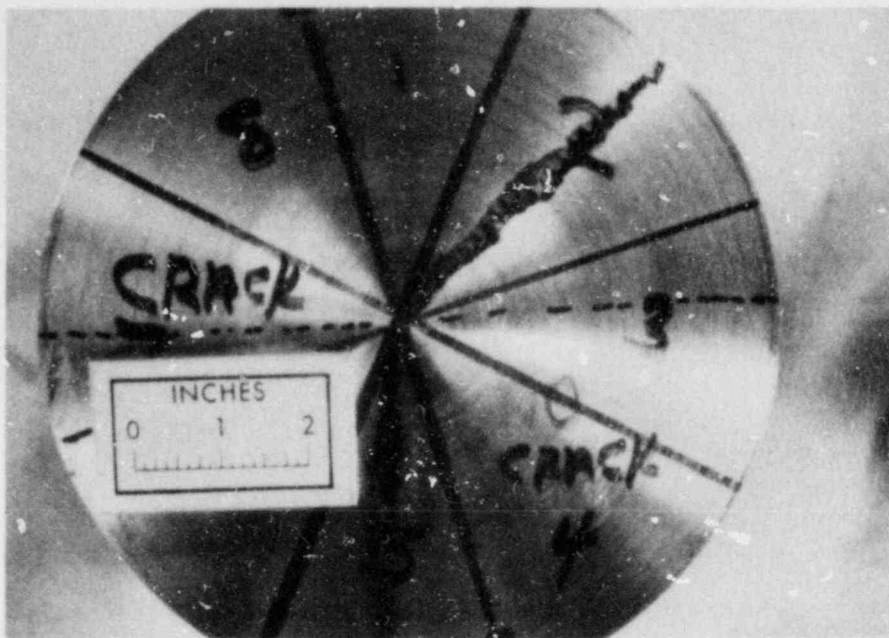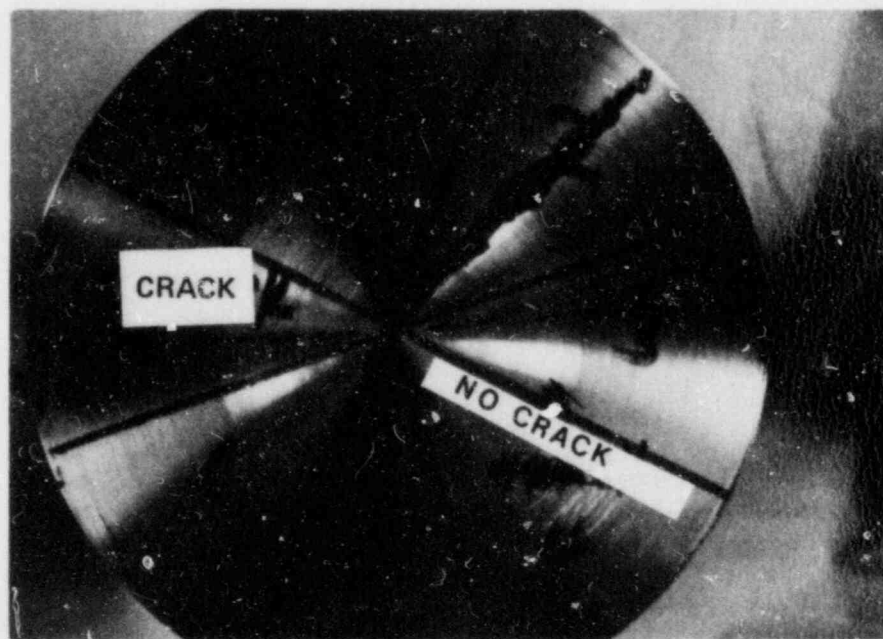B Shows Orientation Markings

Figure 3.1-2.   Reduced Magnification Views of Pump Shaft;
Rolled Down the Page From A to D
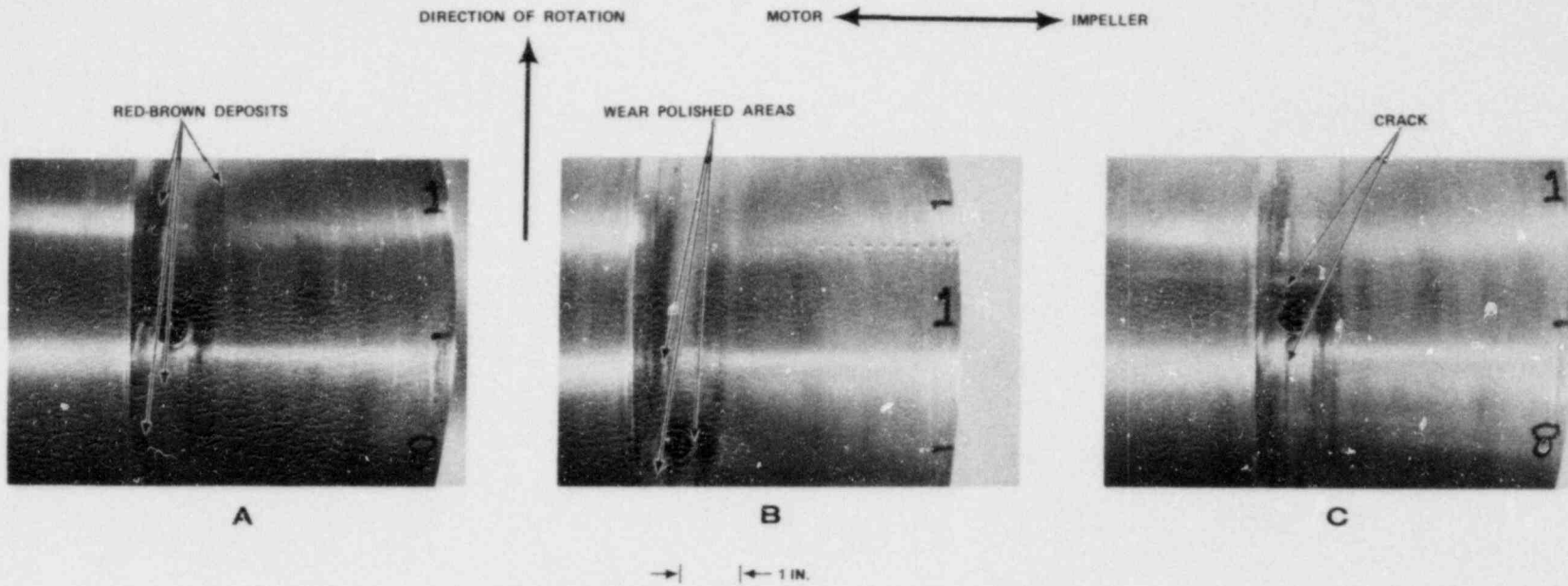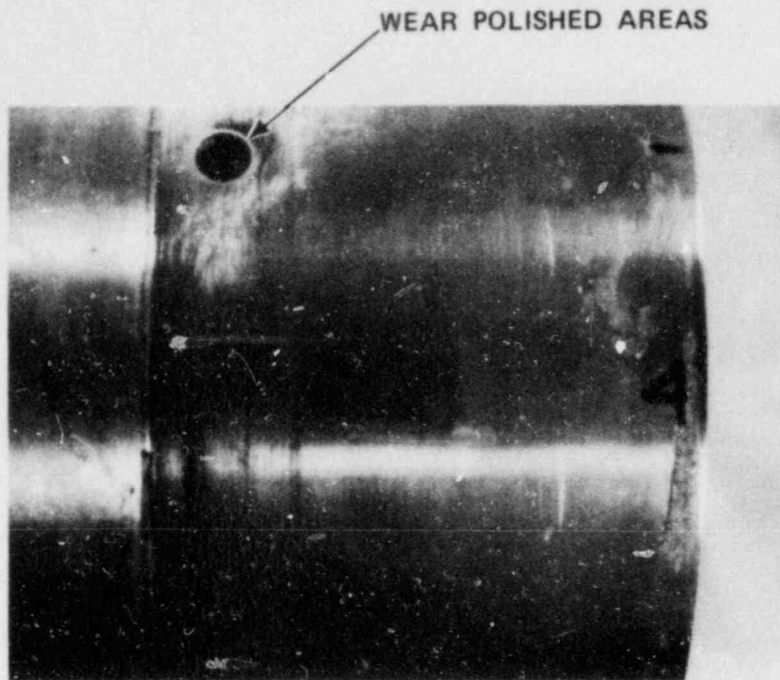
E

F

Figure 3.1-2, continued

Figure 3.1-3. Enlarged Views of Pin Holes. A, B, and C Shot at Different Angles or Different Illumination at Cracked Pin Hole. D and E Shot at Uncracked Pin Hole
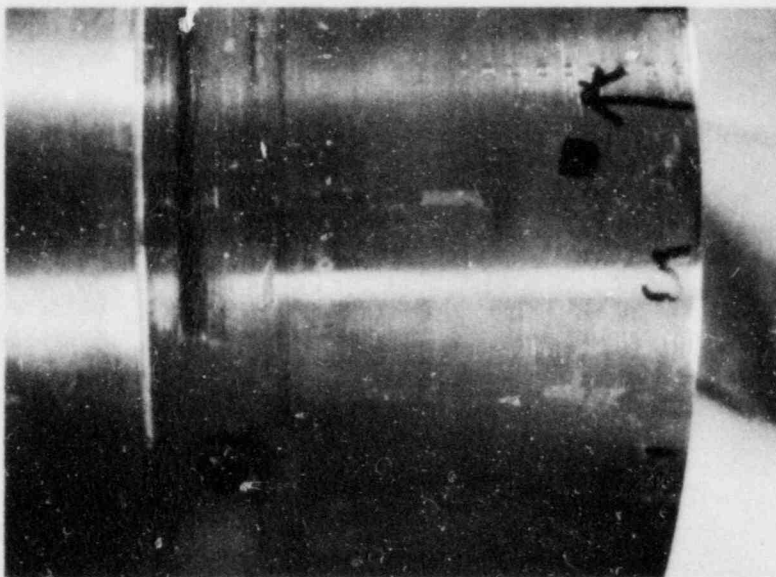
WEAR POLISHED AREAS

D

ROTATION DIRECTION

MOTOR ◄─────────► IMPELLER

E

|← 1 IN.

Figure 3.1-3, continued

ROTATION

IMPELLER

COARSE TOOL MARKS

CRACK

FINE TOOL MARKS

2-4°

STEP IN SHAFT DIAMETER

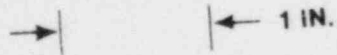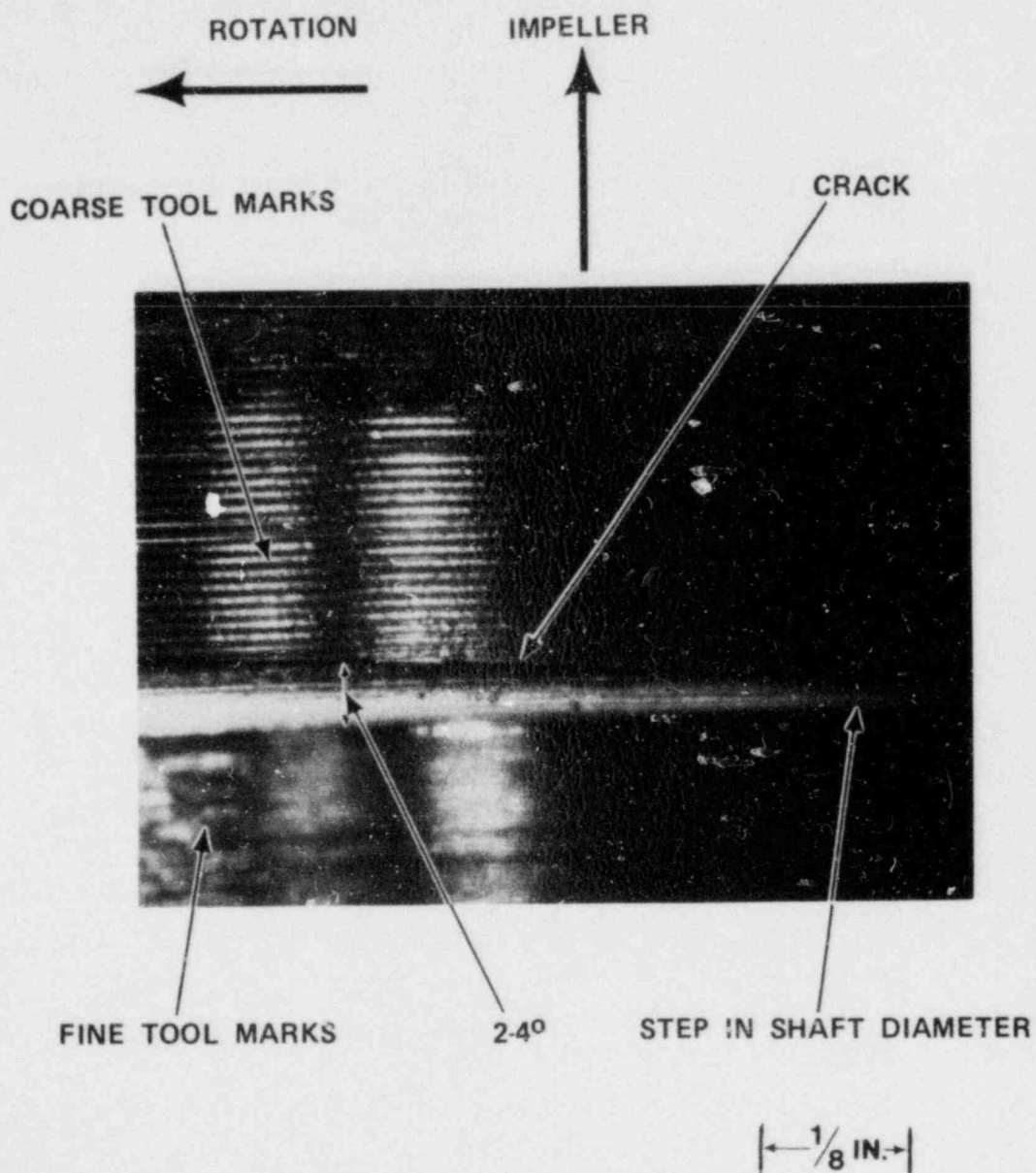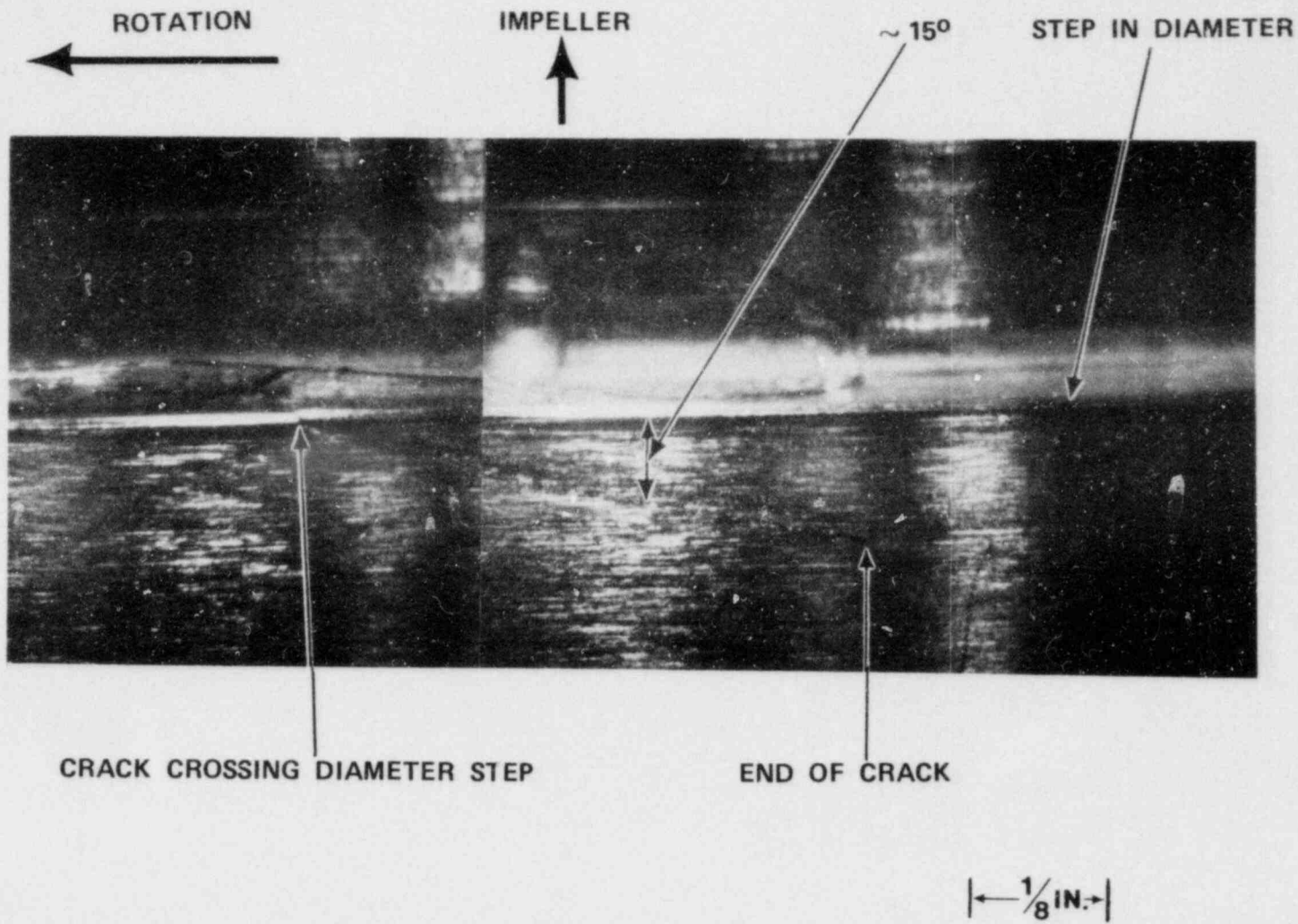|← ⅛ IN. →|

Figure 3.1-4. Angle of Crack to Shaft
Circumferential Direction

Figure 3.1-5. End of Crack at Surface in Octant 5

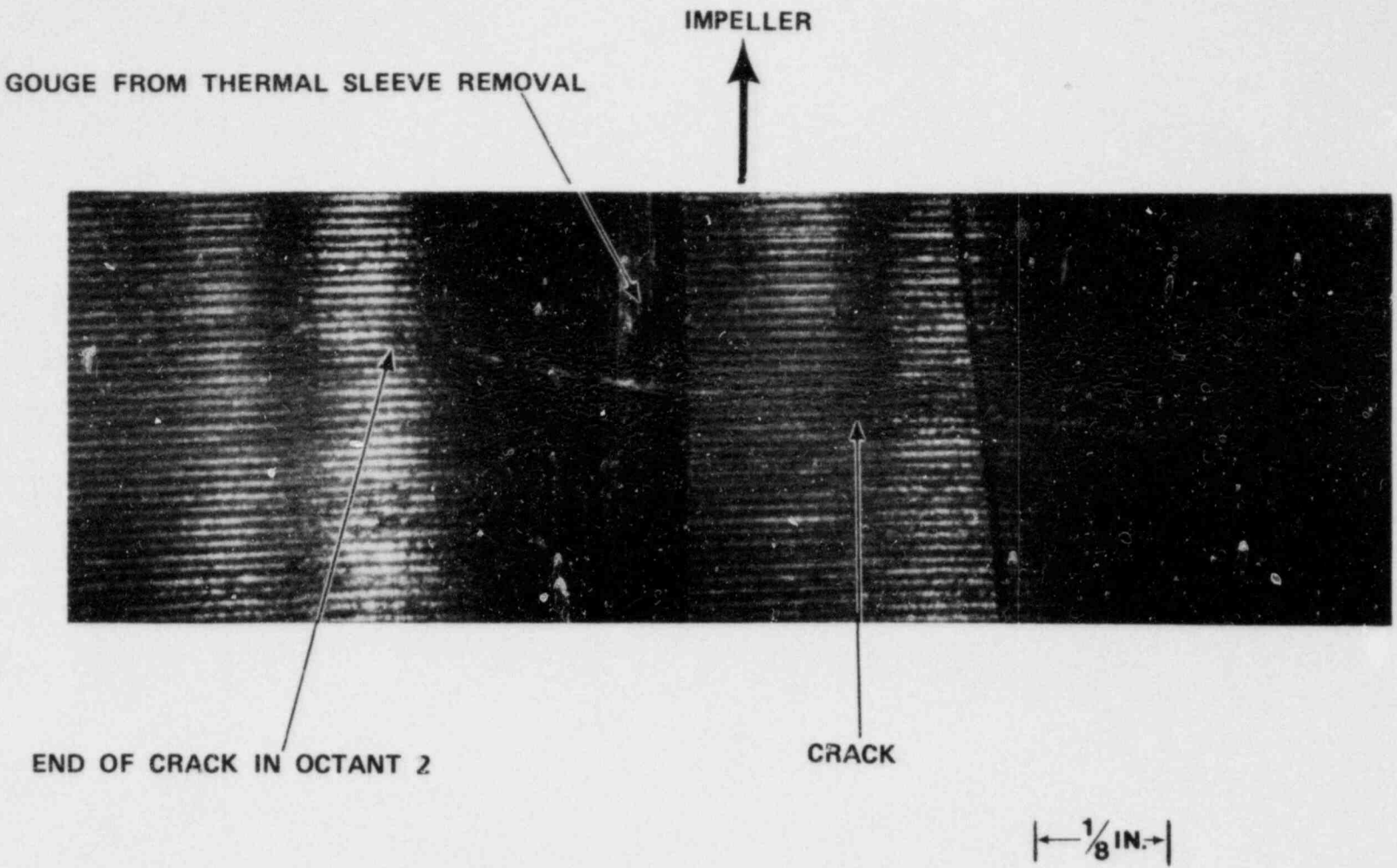GOUGE FROM THERMAL SLEEVE REMOVAL
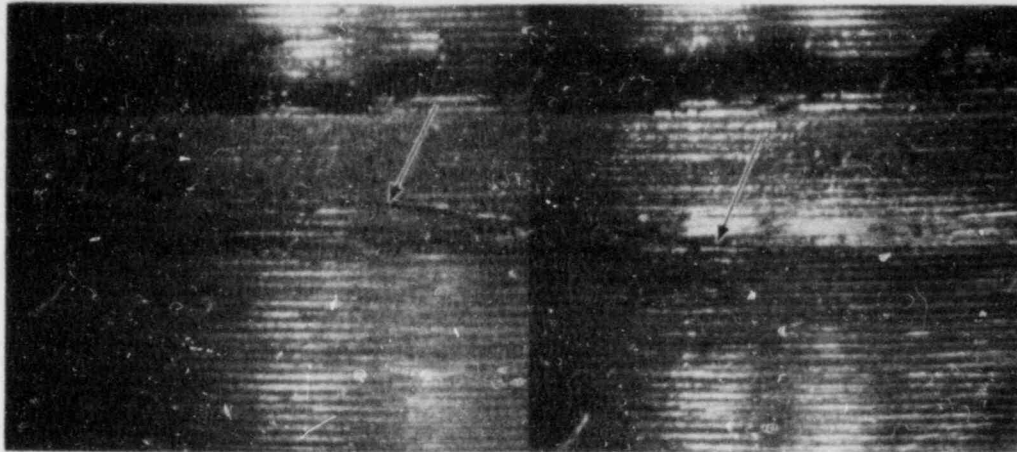
IMPELLER

END OF CRACK IN OCTANT 2

CRACK

|←⅛ IN.→|

Figure 3.1-6. End of Crack at Surface in Octant 2
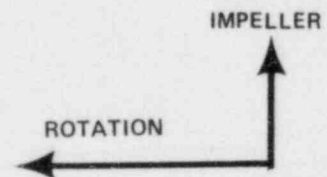
A

IMPELLER ↑

ROTATION ←

|← ⅛ IN. →|
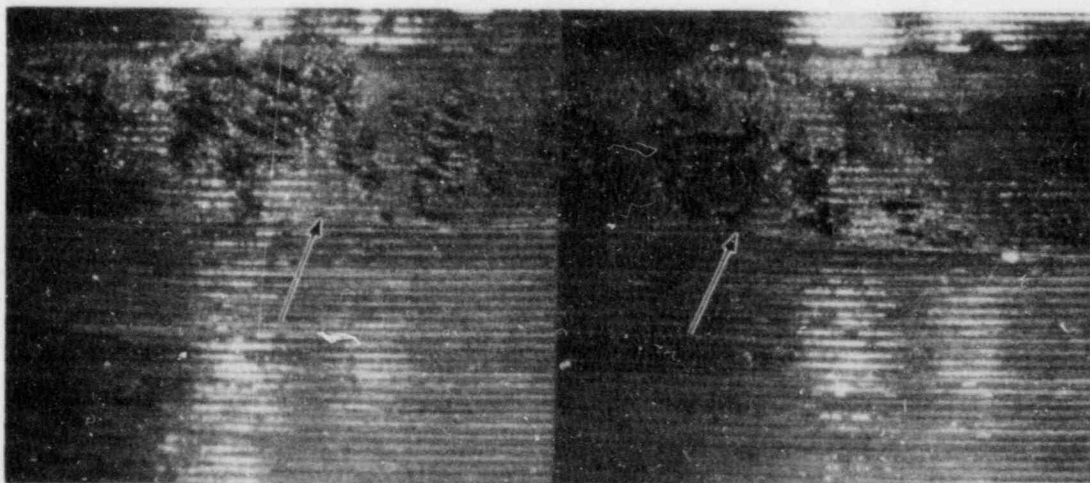
B

Figure 3.1-7. Local Change in Crack Path Direction at
Arrows A in Octant 8, B in Octant 1

WEAR

A

CRACK

IMPELLER

ROTATION

WEAR

B

CRACK

¼ IN.
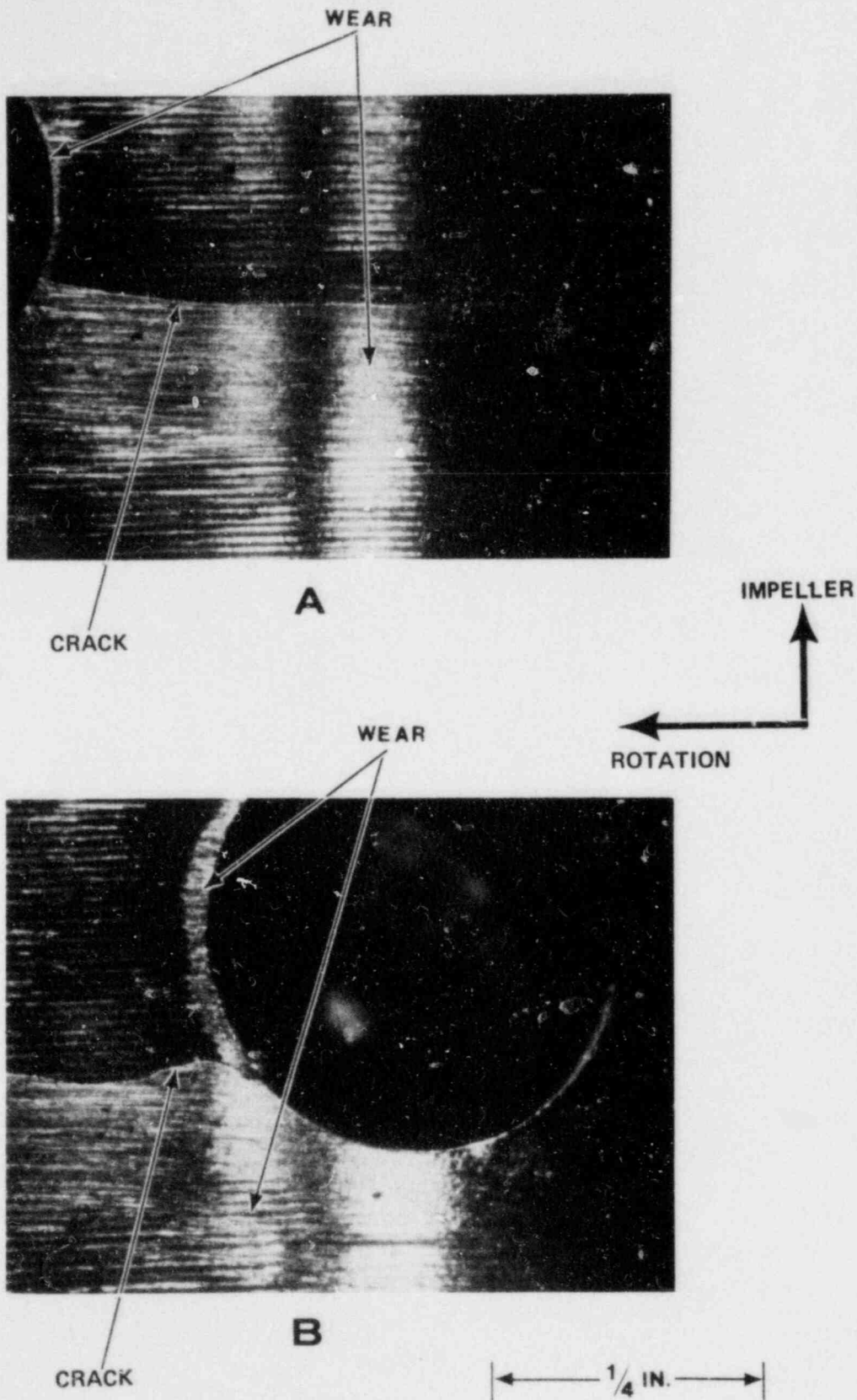
Figure 3.1-8.   Change in Crack Path Near Pin Hole
A.   Octant 8 Side of Pin Hole
B.   Octant 1 Side of Pin Hole

IMPELLER

ROTATION

← CRACK

⊢—⅛ IN.—⊣

A

CRACK

RED-BROWN DEPOSITS

⊢—⅛ IN.—⊣

B
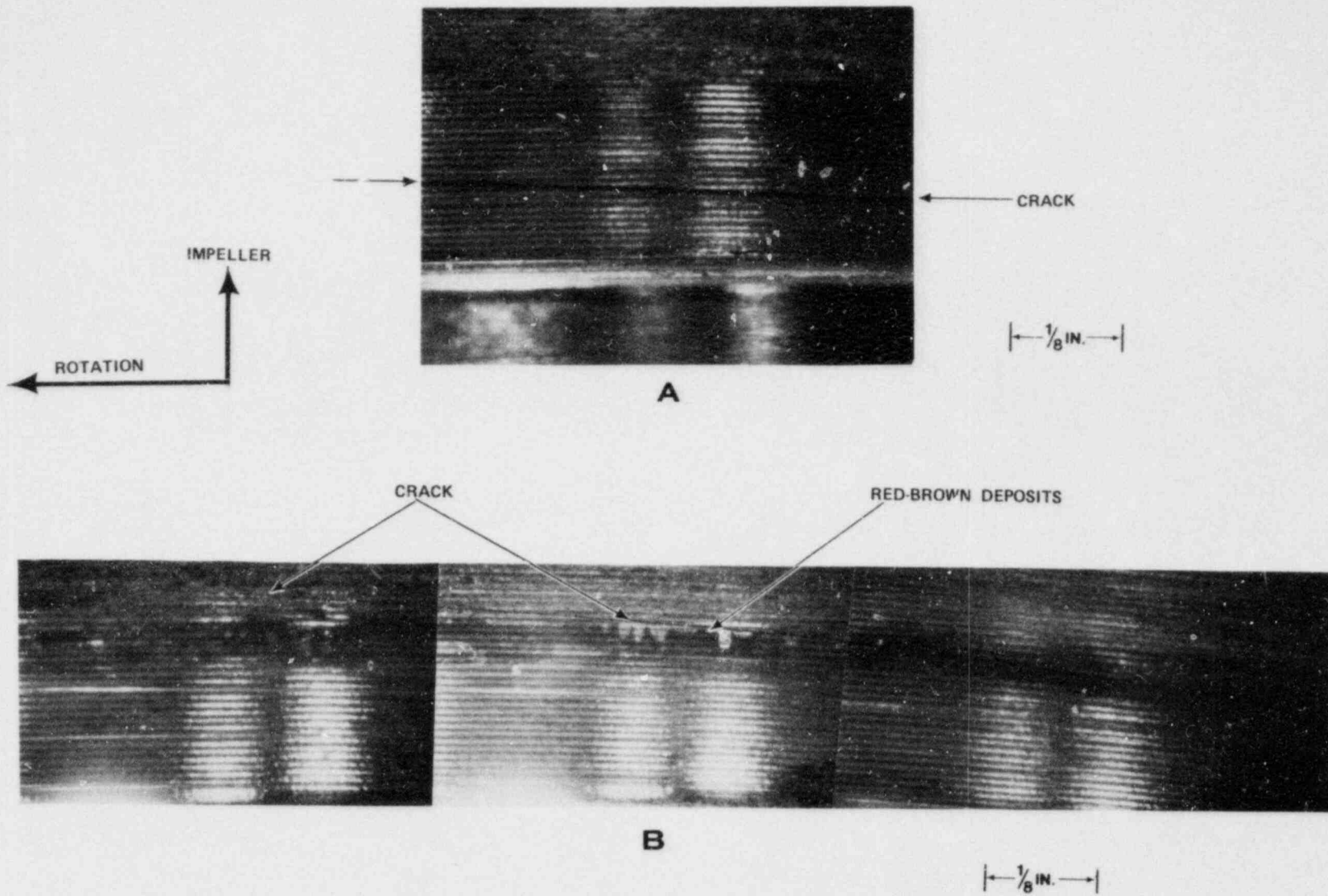
Figure 3.1-9.   Surface Appearance of Shaft Near Crack
   A.   Unworn and Un-corroded Area With Crack
   B.   Crack Passing Through Spalled Deposits

C

D
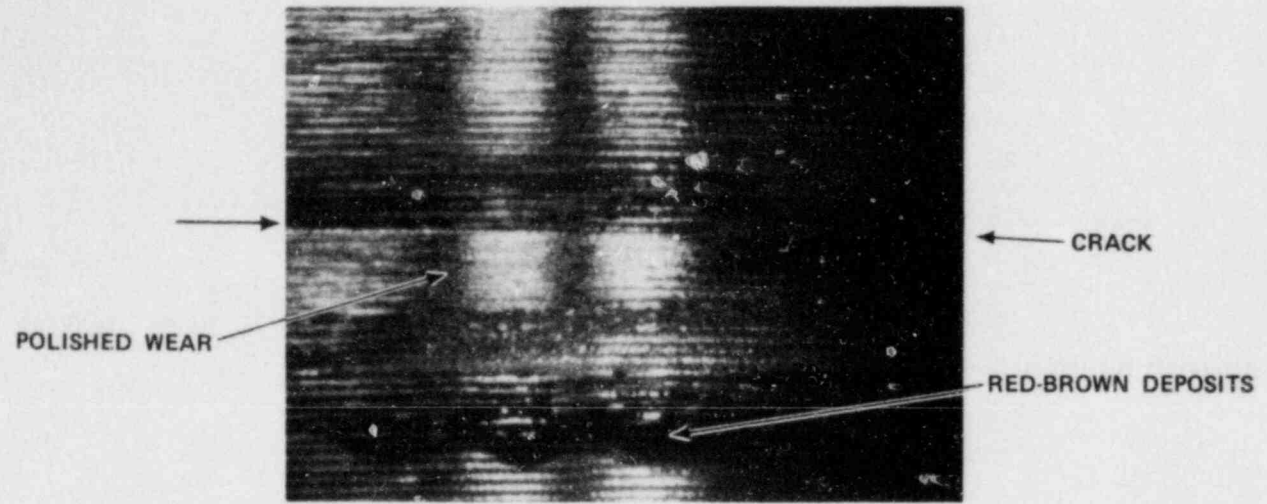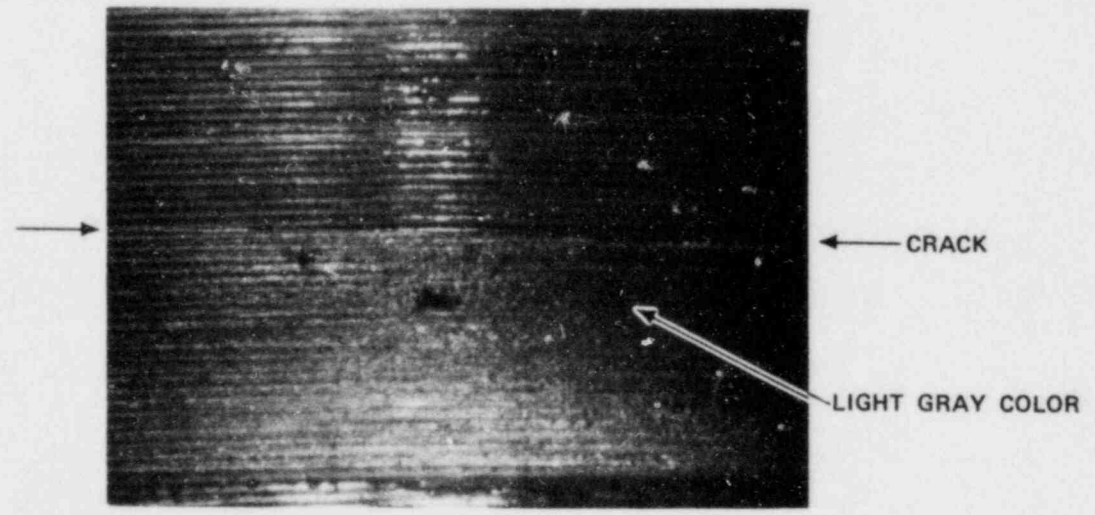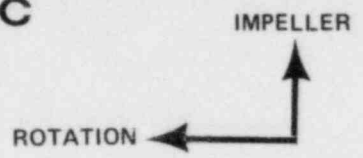
Figure 3.1-9, continued
     C. Polished Wear Area Next to Crack
     D. Gray Deposit Area Adjacent to Crack
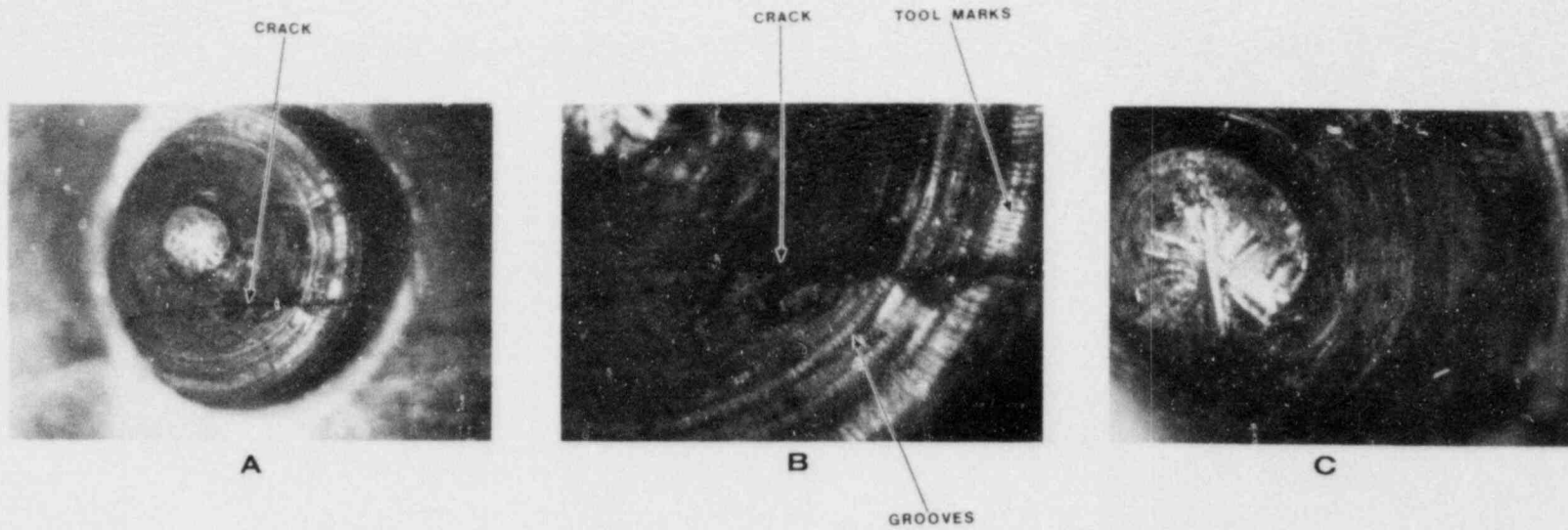
Figure 3.1-10. Internal Surface Condition of Cracked Pin Hole
A. General View Showing Crack
B. Enlarged View of Crack
C. View of Hole Bottom
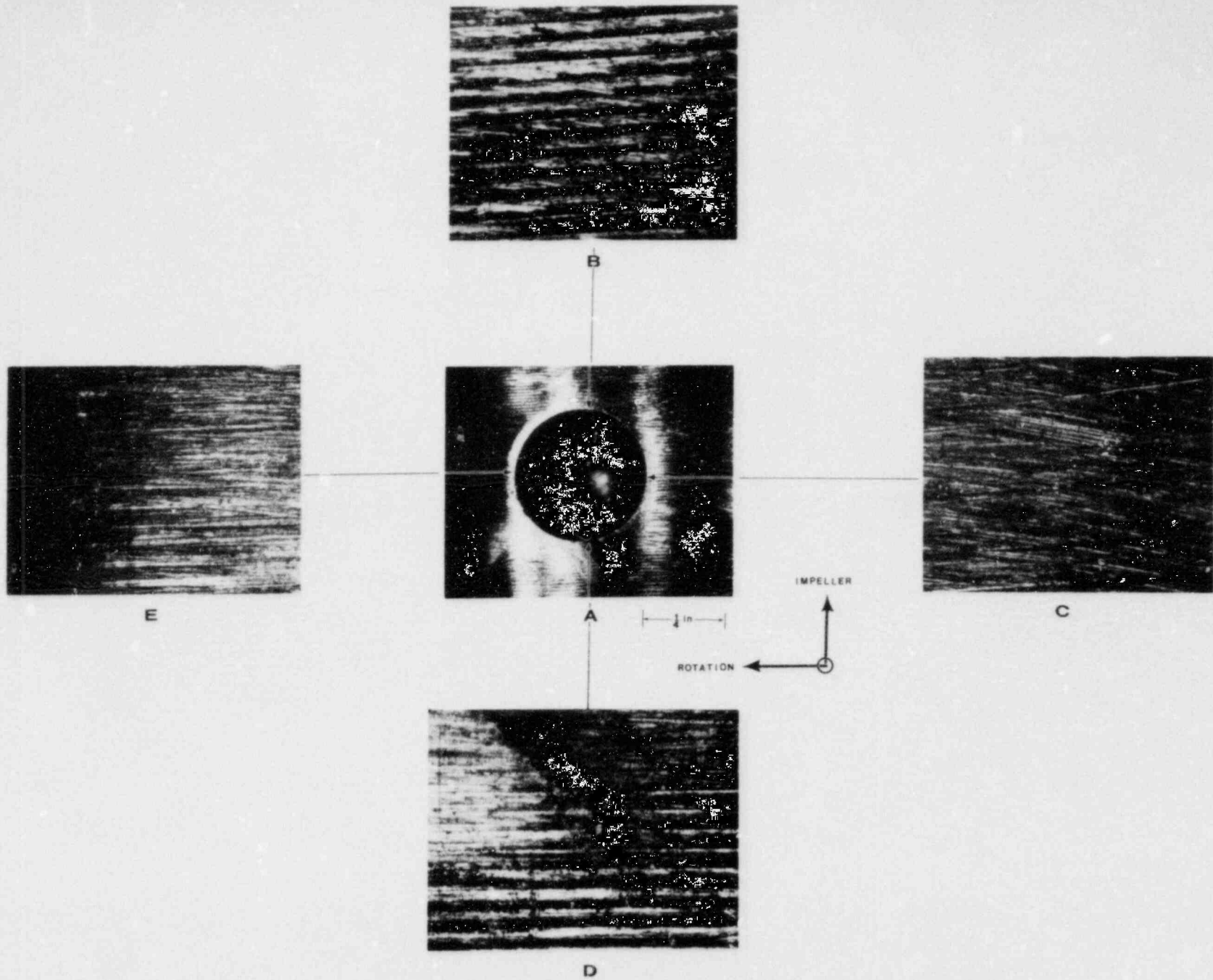
Figure 3.1-11.   Shaft Surface Appearance Near Uncracked
Pin Hole.   View A Shows Pin Hole. Views
B, C, D, and E Show Coarse Tooling Marks.
Views C and E Show Wear Marks
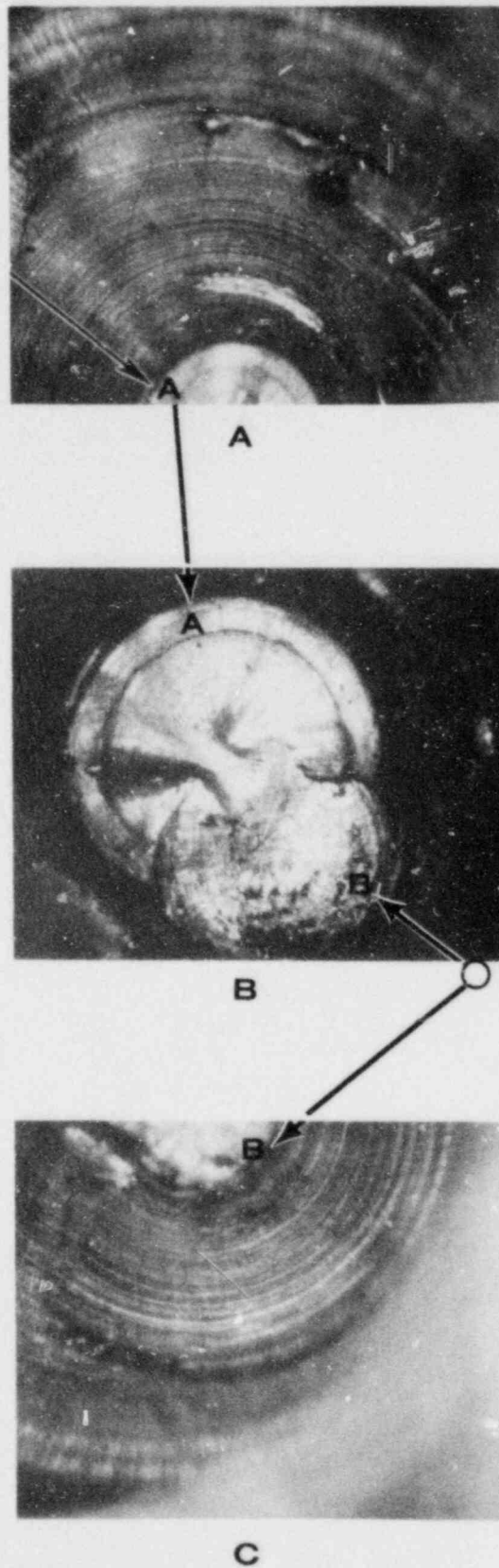
Figure 3.1-12.   Internal Surface Features
of Uncracked Pin Hole

CRACK COORDINATES

INCHES FROM CENTER OF
DRILLED HOLE (0,0)

POINTS	CIRCUMFERENTIAL X	AXIAL Y
1	−11.188	0.602
2	−10.688	0.490
3	−10.000	0.466
4	−8.000	0.376
5	−6.000	0.326
6	−4.000	0.231
7	−2.063	0.163
8	−2.000	0.134
9	−1.813	0.128
10	−0.194	0.082
11	0.194	0.111
12	2.000	0.049
13	4.000	−0.011
14	6.000	−0.124
15	6.188	−0.129

NOTE: DRILLED HOLE IS OVAL DUE TO DIFFERENCE
IN HORIZONTAL AND VERTICAL SCALES
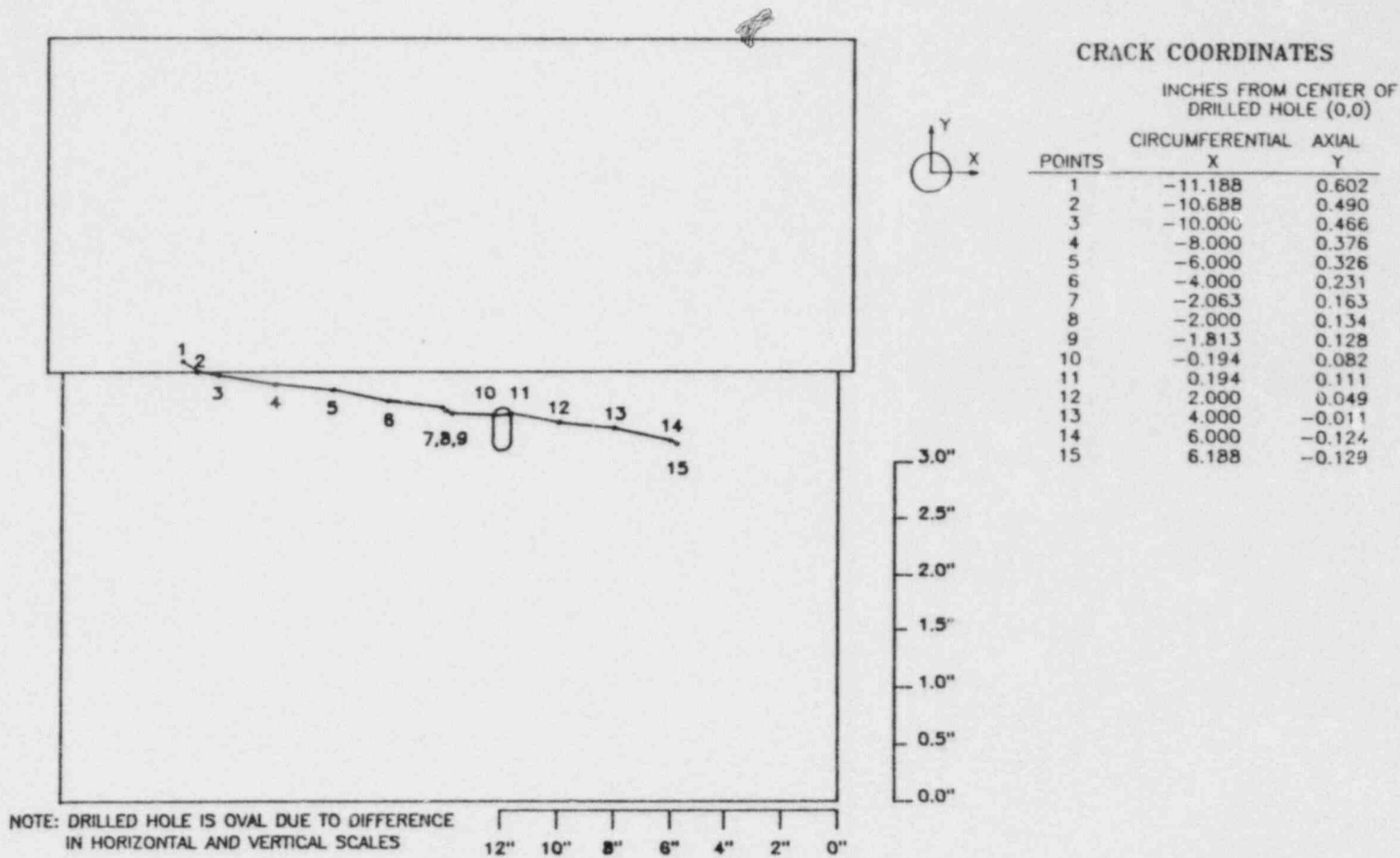
Figure 3.1-13. Pump Shaft Dimensions and Crack Location
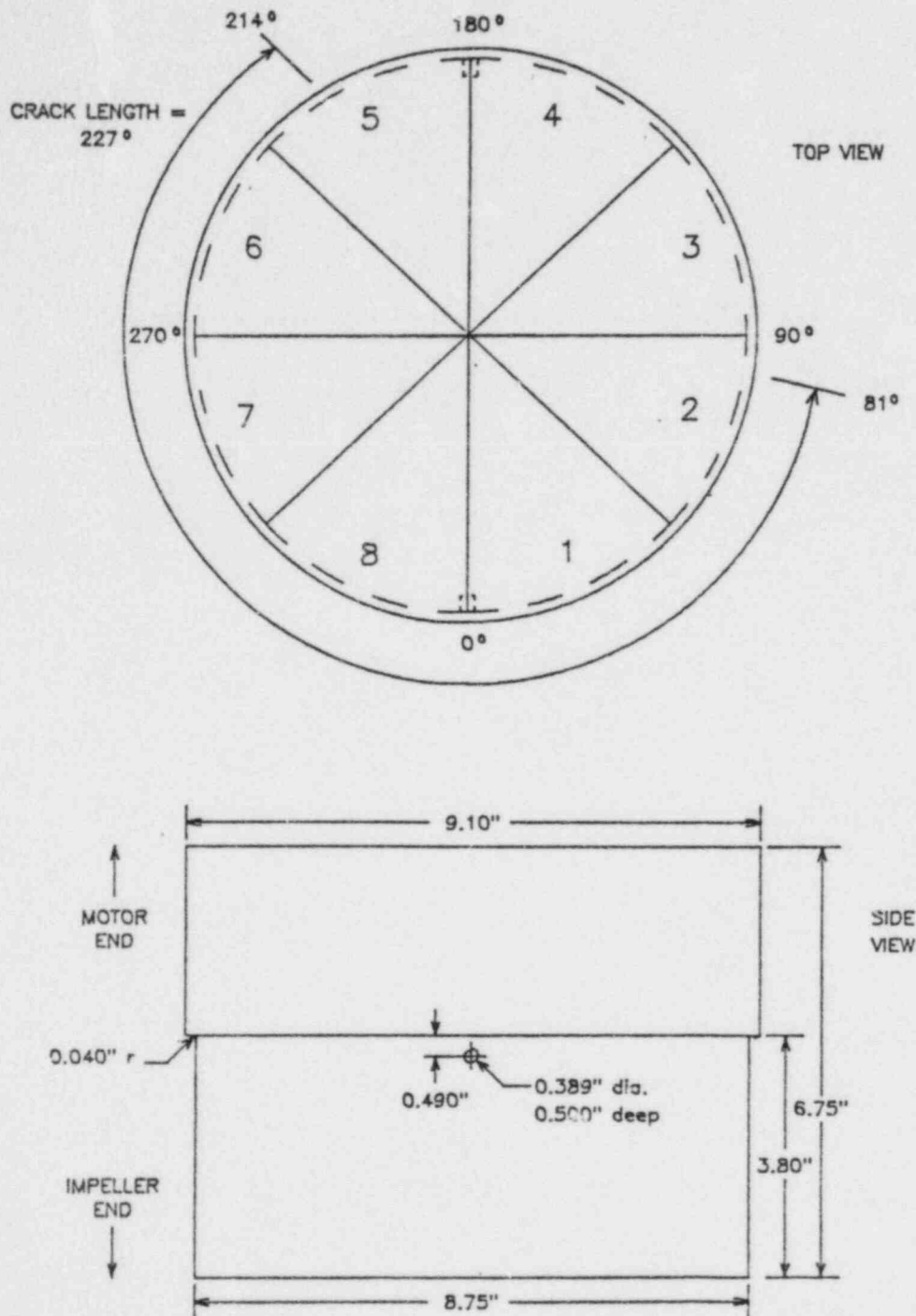
Figure 3.1-13, continued; Pump Shaft Crack
Location and Coordinates

PIN LOCATION

MOTOR

ROTATION

A
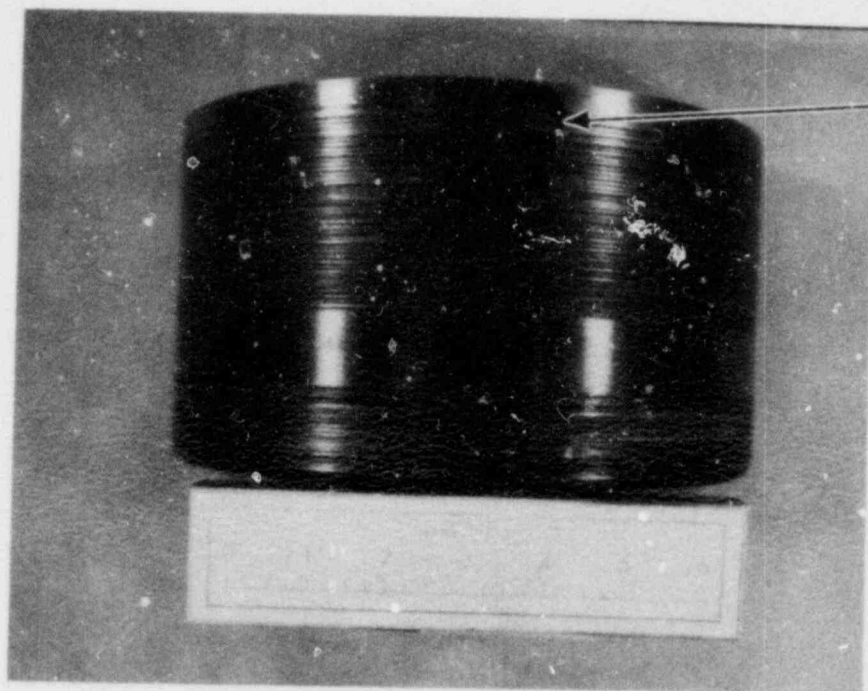
FLOW SLOT

ROTATION

PIN

MOTOR

Figure 3.1-14. "A
A
B
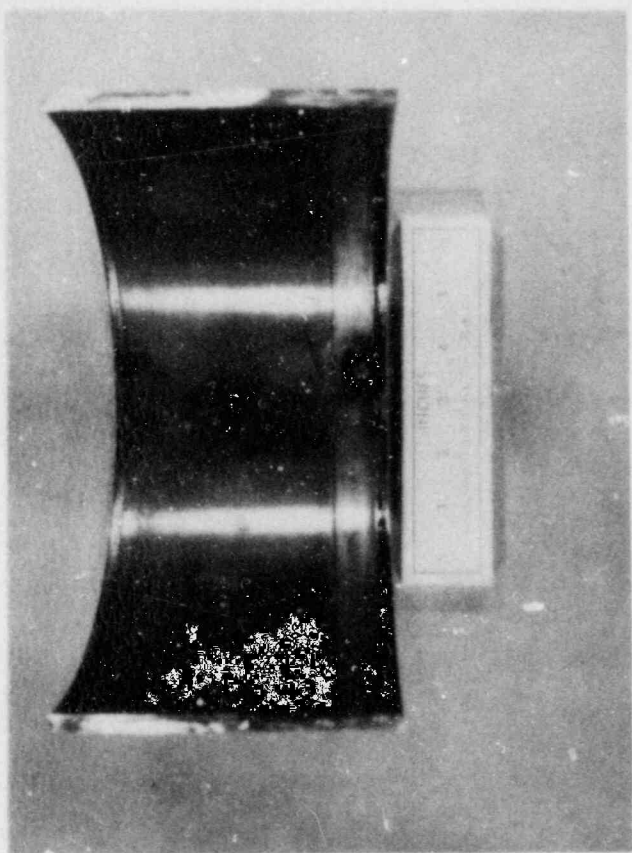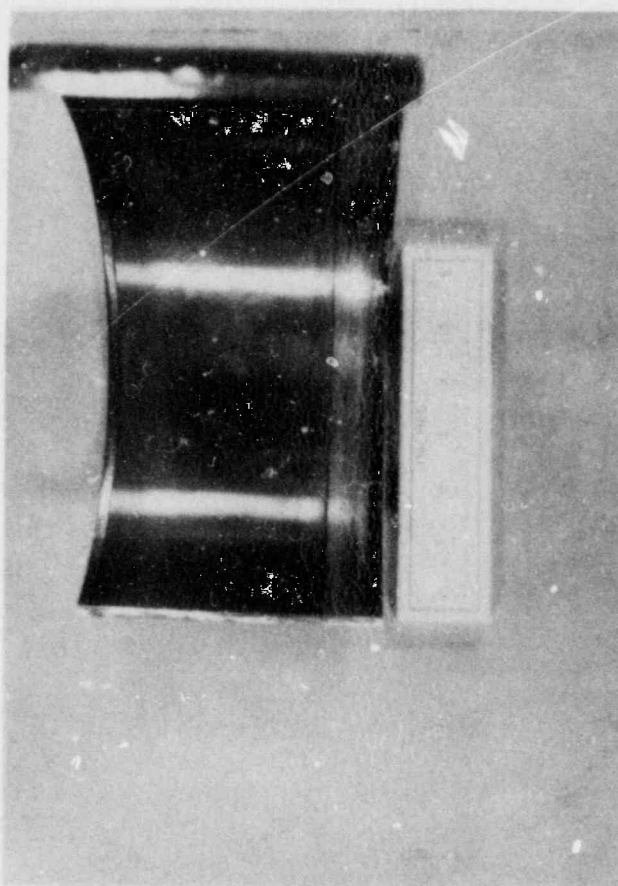
TI
APERTURE
CARD

Also Available On
Aperture Card

Section of Thermal Sleeve
OD View
C, D: ID Views

A SECTION SLEEVE

PIN LOCATION

MOTOR

ROTATION

A
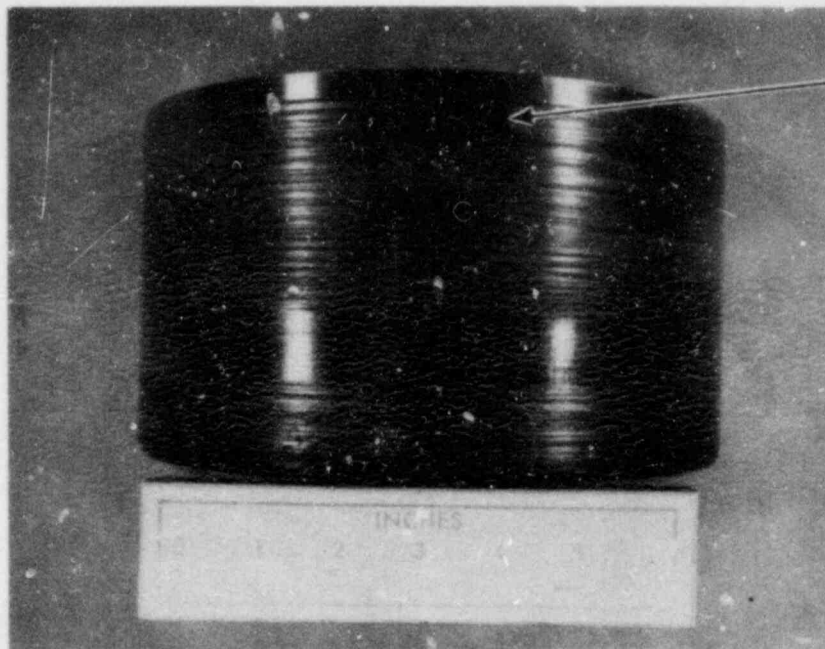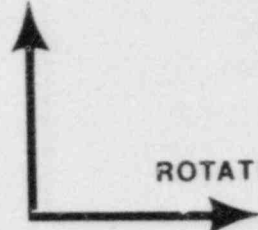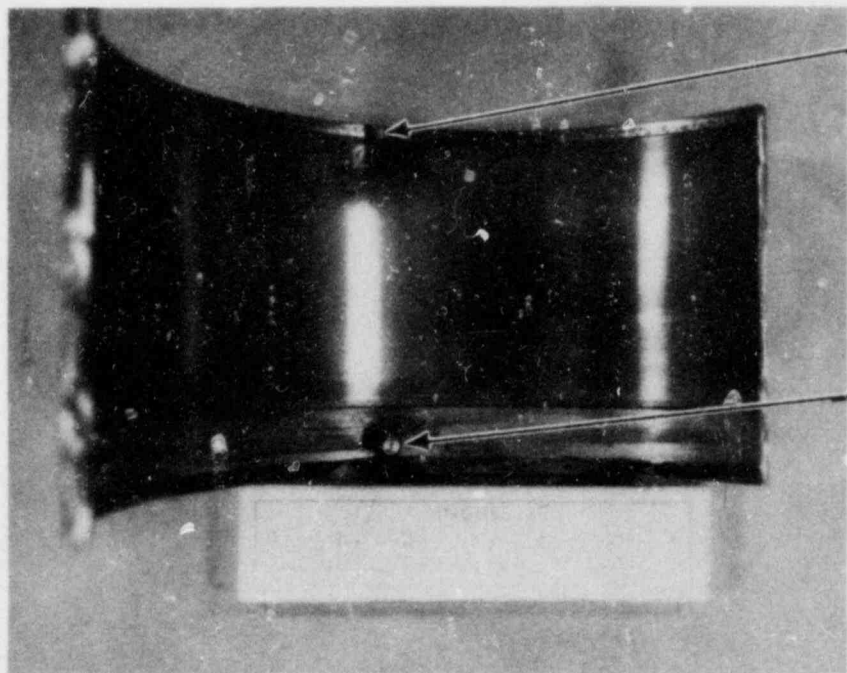
FLOW SLOT

ROTATION

PIN

MOTOR
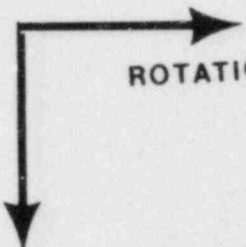
B

Figure 3.1-14, continue
A: OD V
B, C, D:

C

D
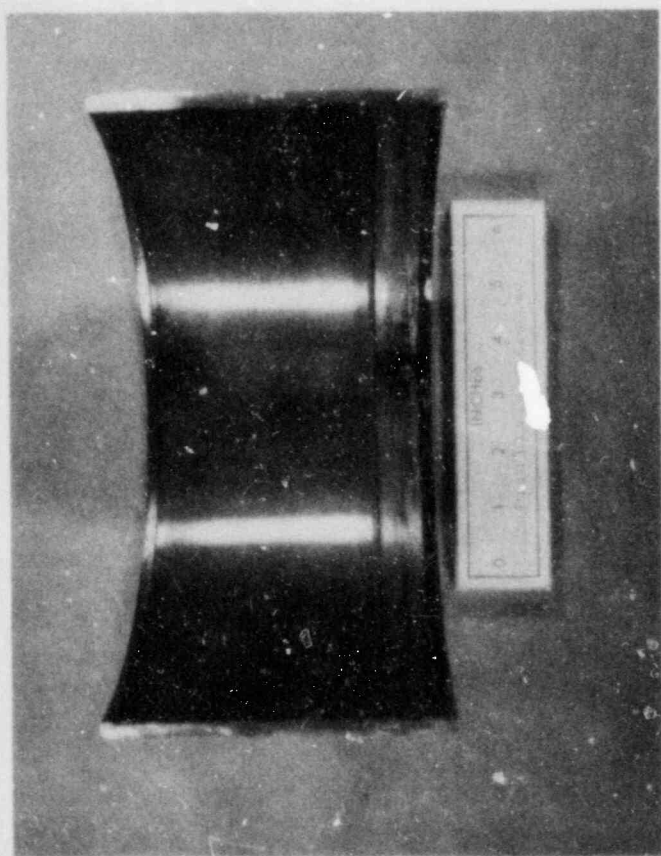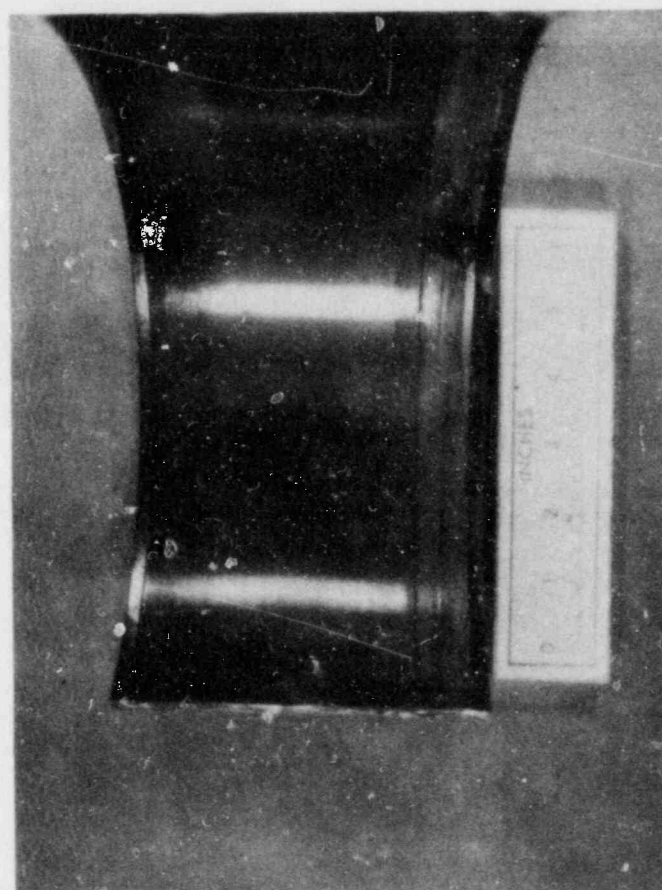
d; "B" Section of Thermal Sleeve
iew
ID Views

TI
APERTURE
CARD

8410170270-02

A. SECTION "A" THERMAL SLEEVE

RECESSED AREA

RED-BROWN DEPOSITS

SEATING SURFACE

PIN

CHAMFER

MATCHING WEAR

PIN HOLE

CRACK

B. PUMP SHAFT SURFACE AT PIN HOLE
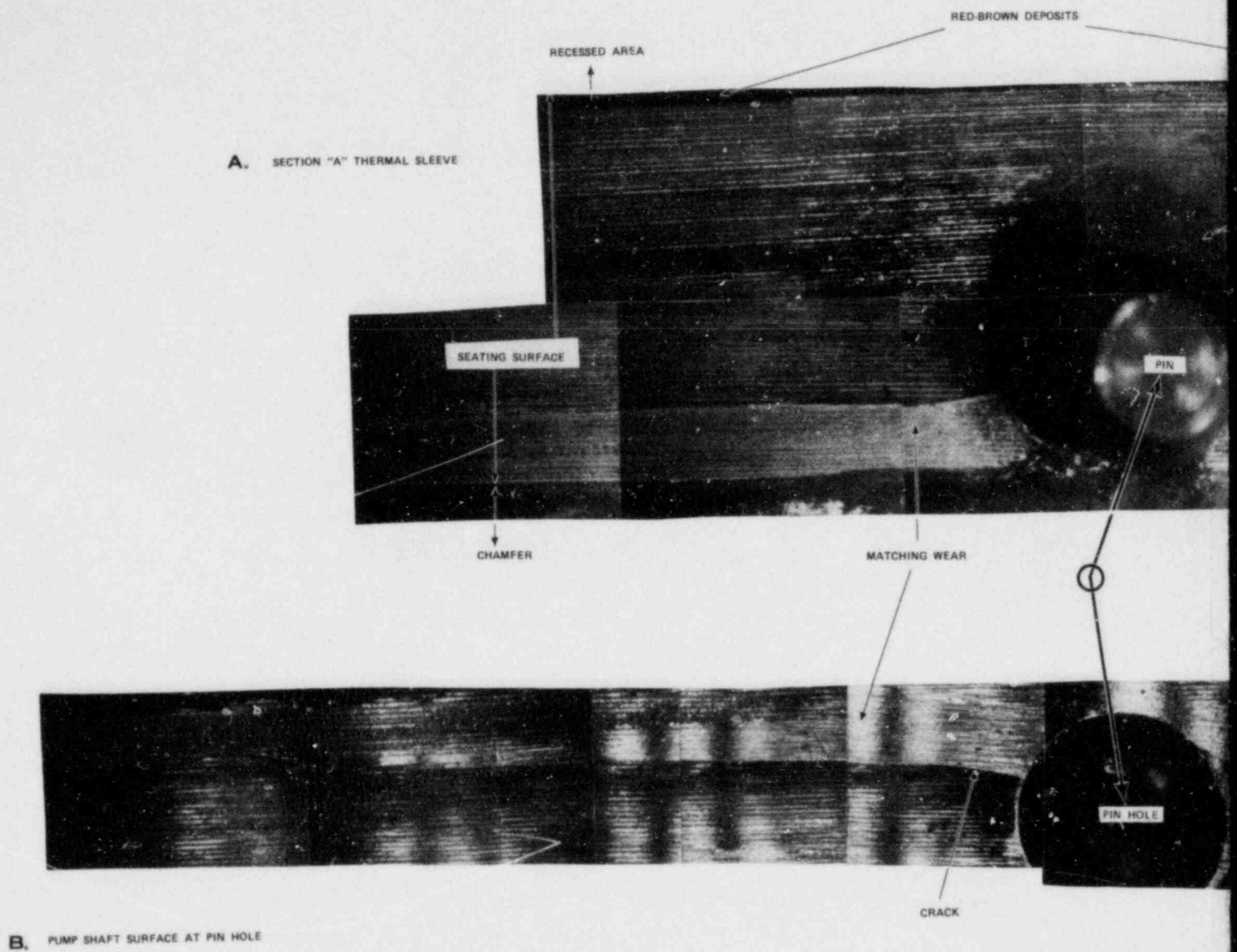
Figure 3.1-15.   Inside Surface
Thermal Sleeve
A. Thermal Sle

GRAY-BROWN DEPOSITS

IMPELLER
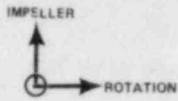
ROTATION

Also Available On
Aperture Card
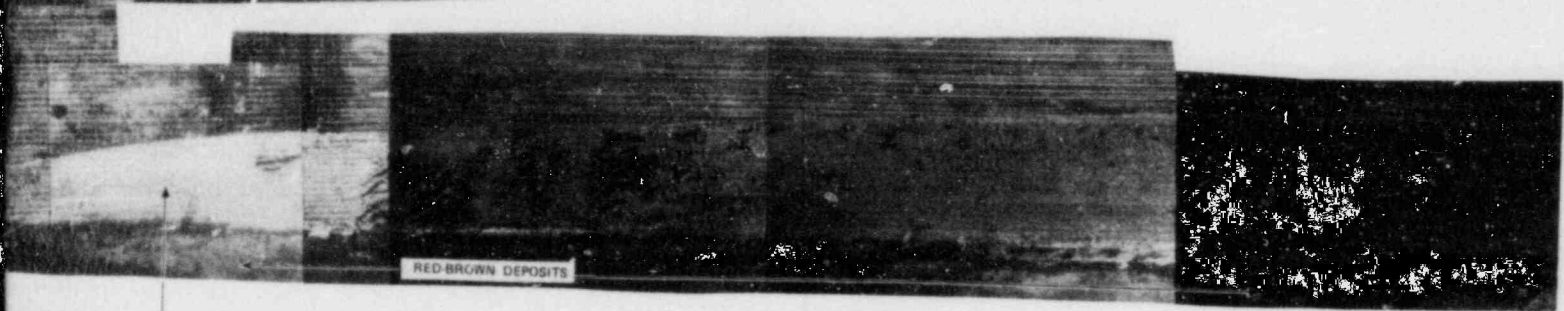
RED-BROWN DEPOSITS

MATCHING WEAR

CRACK

ROTATION

IMPELLER
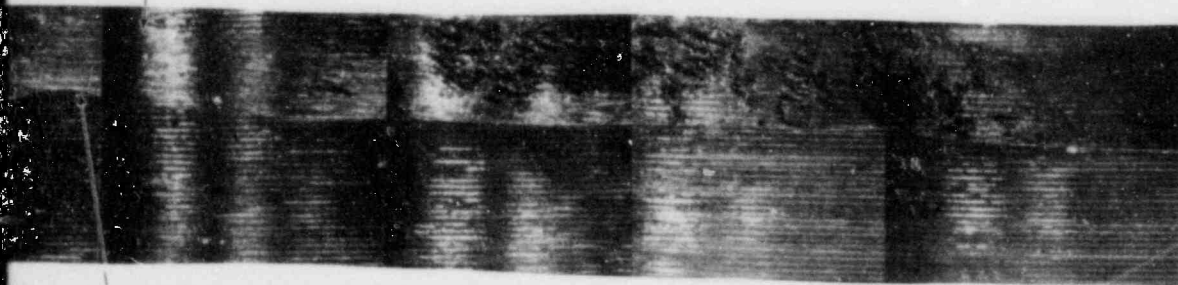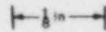
f the "A" Section of the
t the Anti-Rotation Pin
ve, B. Mating Pump Shaft Surface

TI
APERTURE
CARD

SEATING SURFACE   RECESSED AREA

RED-BROWN DEPOSITS   CHAMFER   SEATING SURFACE
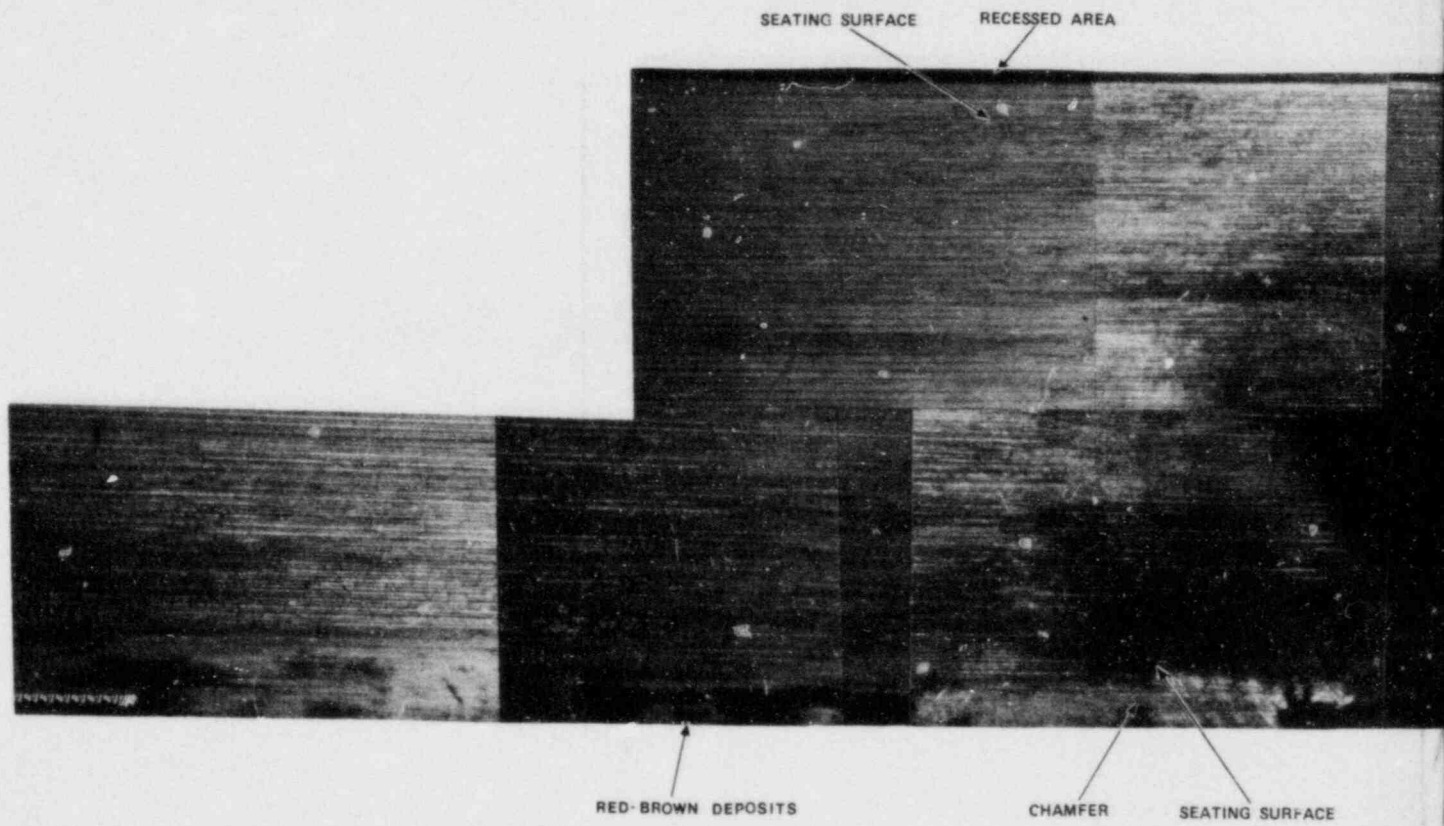
Figure 3.1-16.   Insi
                 Ther

SHAFT AXIS

MOTOR END

RED-BROWN DEPOSITS

GRAY-BROWN DEPOSITS

RED-BROWN DEPOSITS

PIN
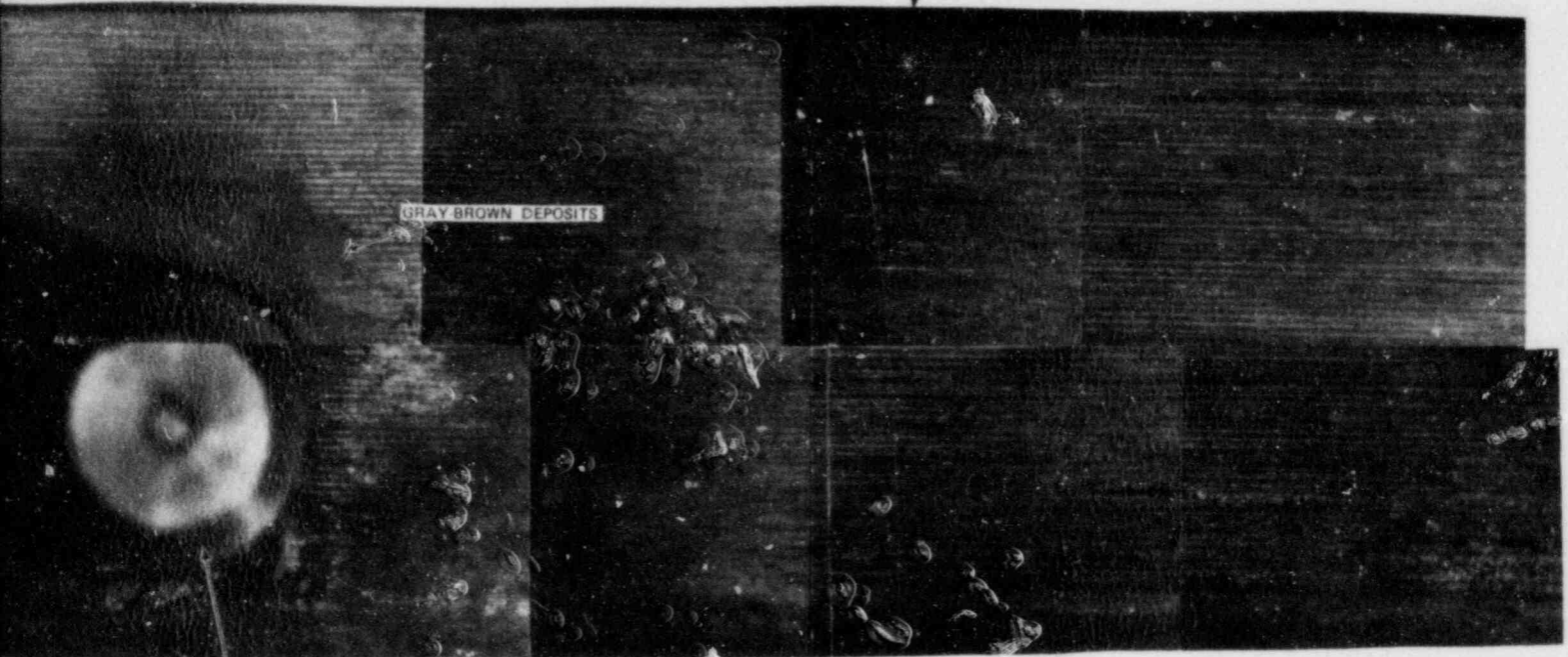
|←— 1/8 IN. —→|

e Surface of the "B" Section of the
al Sleeve at the Anti-Rotation Pin

PIECE "A"
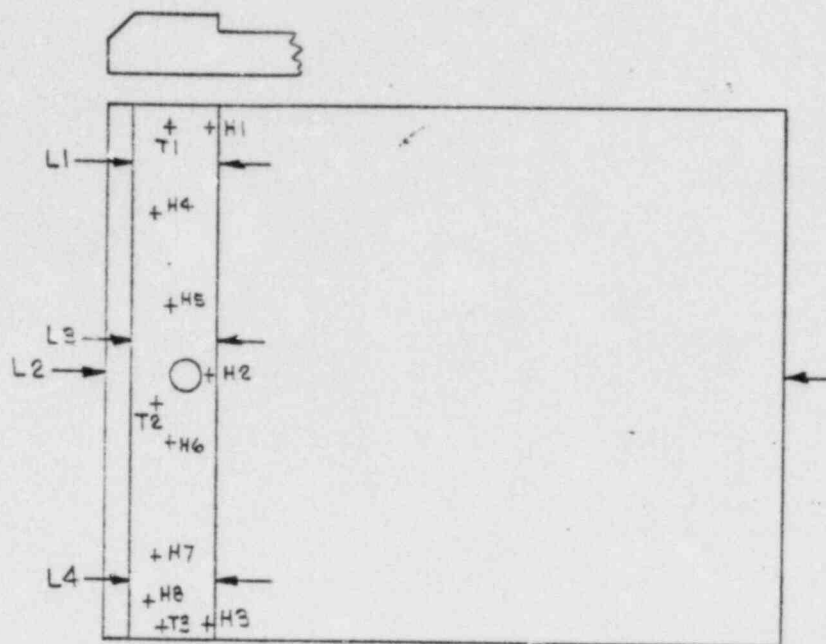
Recess Depth, Inches

H-1 = .014
H-2 = .014
H-3 = .013

Thickness at Seating Surface, Worn (Inches)

H-4 = .256   H-7 = .256
H-5 = .255   H-8 = .256
H-6 = .255

Seating Surface Width, Inches

L-1 = .770
L-3 = .767
L-4 = .769

Thickness at Seating Surface, Unworn (inches)

T-1 = .257
T-2 = .254
T-3 = .257

Overall Length, Inches

L-2 = 5.199

A

Figure 3.1-17. Thermal Sleeve Dimensions
A. "A" Section, B. "B" Section,
C. Pin Diameters

PIECE "B"
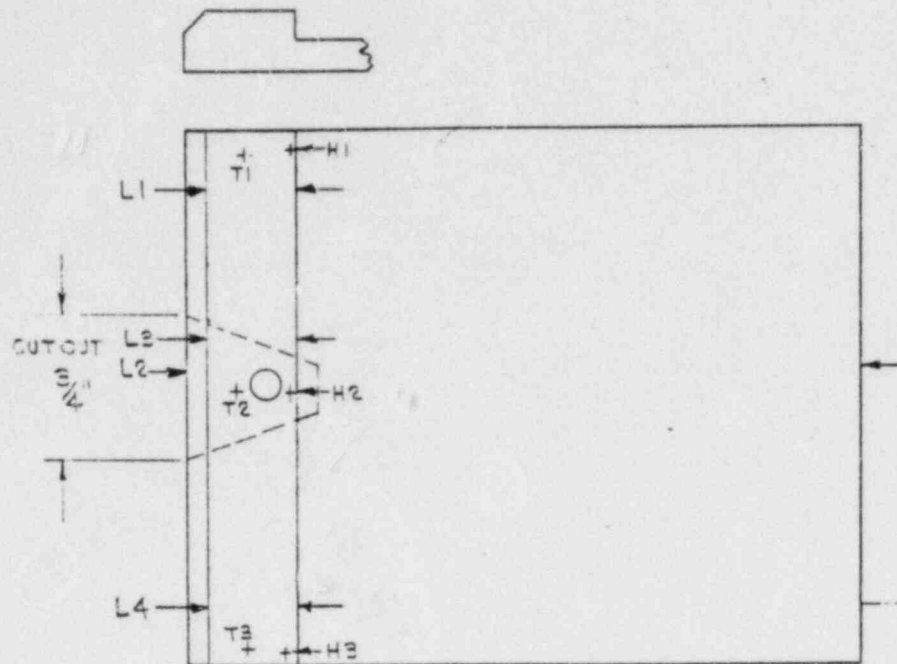
Recess Depth, Inches

H-1 = .015
H-2 = .014
H-? ? .014

Overall Length, Inches

L-2 = 5.198

Seating Surface Width, Inches

L-1 = .770
L-3 = .768
L-4 = .769

Thickness at Seating Surface, Inches

T-1 = .256
T-2 = .255
T-3 = .256

Figure 3.1-17, continued

B

Piece A or B ID
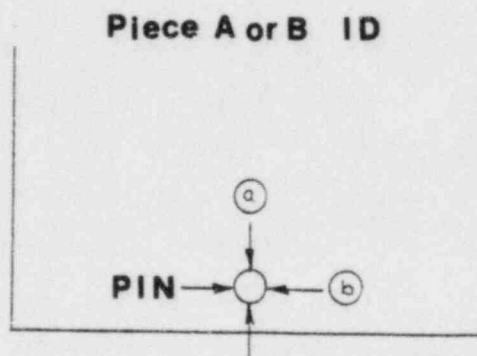
Piece A = (a) .375 inch - shaft axis direction
          (b) .375 inch - circumferential direction

Piece B = (a) .375 inch - shaft axis direction
          (b) .375 inch - circumferential direction

C

Figure 3.1-17, continued

3.2 Sectioning

Using the results of the visual observations and field ultrasonic inspections, a sectioning scheme was agreed upon by representatives of B&W and GPUN. Figures 3.2-1 to -4 show how the shaft section was cut at the LRC to obtain specimens for analysis.

Initially the shaft was longitudinally sectioned in half as shown in Figure 3.2-1 and labeled "Piece A" and "Piece B". Piece B was selected for fracture morphology since it contained the thermal sleeve pin hole through which the crack intersected and the smaller amount of uncracked material. To precisely determine the amount of intact or uncracked material on Piece B, an ultrasonic inspection was performed and is described in Section 3.2.1. To reveal the crack surfaces, hydraulic pressure was used to separate Piece B along the crack as shown in Figure 3.2-2. The two halves of Piece B were labeled Piece B1 and B2, with B1 containing the outer diameter (OD) step reduction. After photography, the entire fracture surface was removed from Piece B1 in sample B1A. Sample B1A was then subdivided into three smaller specimens labeled B1A1, B1A2, and B1A3 according to Figure 3.2-3. Notches, to use as reference points, were placed on one edge of Specimen B1A1 every 1/4-inch beginning at the shaft OD. Scanning electron microscopy and metallographic specimens were sectioned from Specimen B1A1 as shown in the figure, with the identification numbers on the individual specimens corresponding to the 1/4-inch notch locations.

Piece A was sectioned into three specimens according to Figure 3.2-4 and labeled A1, A2, and A3. From Specimen A1 was sectioned three 1/2-inch wide strips, A1A, A1B, and A1C. Since the crack extended nearly the entire length of strip specimen A1A, holes were drilled approximately every 1/4-inch through which bolts were inserted to hold it together. Metallographic specimens A1A-1 through A1A-8 were then sectioned. Specimens for Auger electron spectroscopy

(AES) and electron microprobe analysis (EMA) were obtained from the crack tip region of strip samples A1B and A1C, respectively.

All sectioning described in this section was performed using either a horizontal or vertical band saw with no lubricant to prevent chemical contamination of the crack surface. Additional sectioning of specimen B1A1 was required to further examine regions of interest. A slow speed diamond saw with no lubricant was used for some of these smaller specimens.

3.2.1 Laboratory Ultrasonic Inspection

After the initial longitudinal section providing Pieces A and B of the shaft, the method to separate Piece B was dependent upon the location and amount of intact material present. To precisely determine this, an ultrasonic inspection was performed and the intact material was "mapped out" on the impeller end of the shaft portion. Details of the ultrasonic inspection are described in the memorandum in Appendix B.

To prevent possible damage to the crack surface during separation, it was decided to bend Piece B as described in Section 3.2 rather than pull the halves apart.
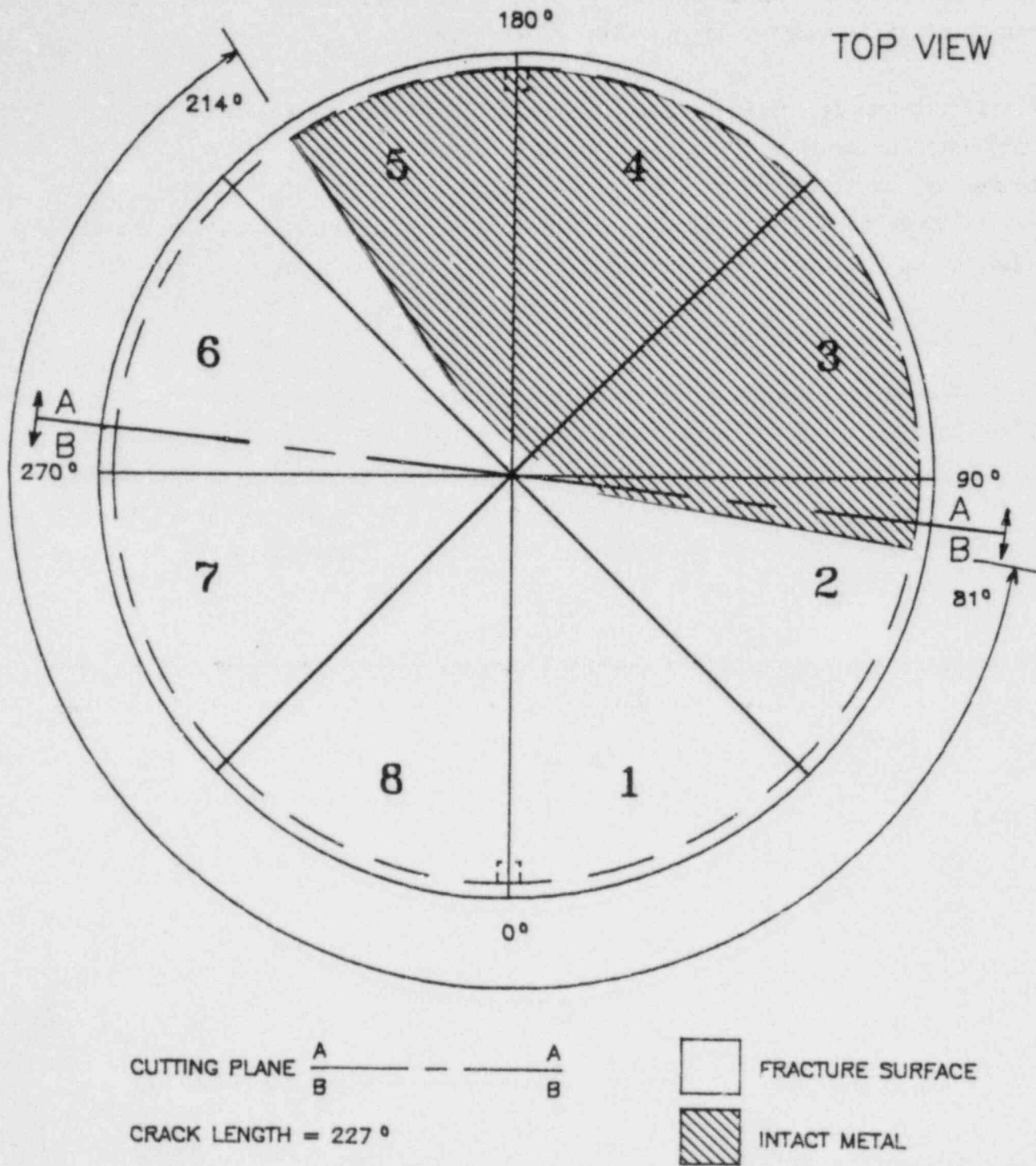
Figure 3.2-1. Initial Section of the Pump Shaft,
Viewed from the Motor End
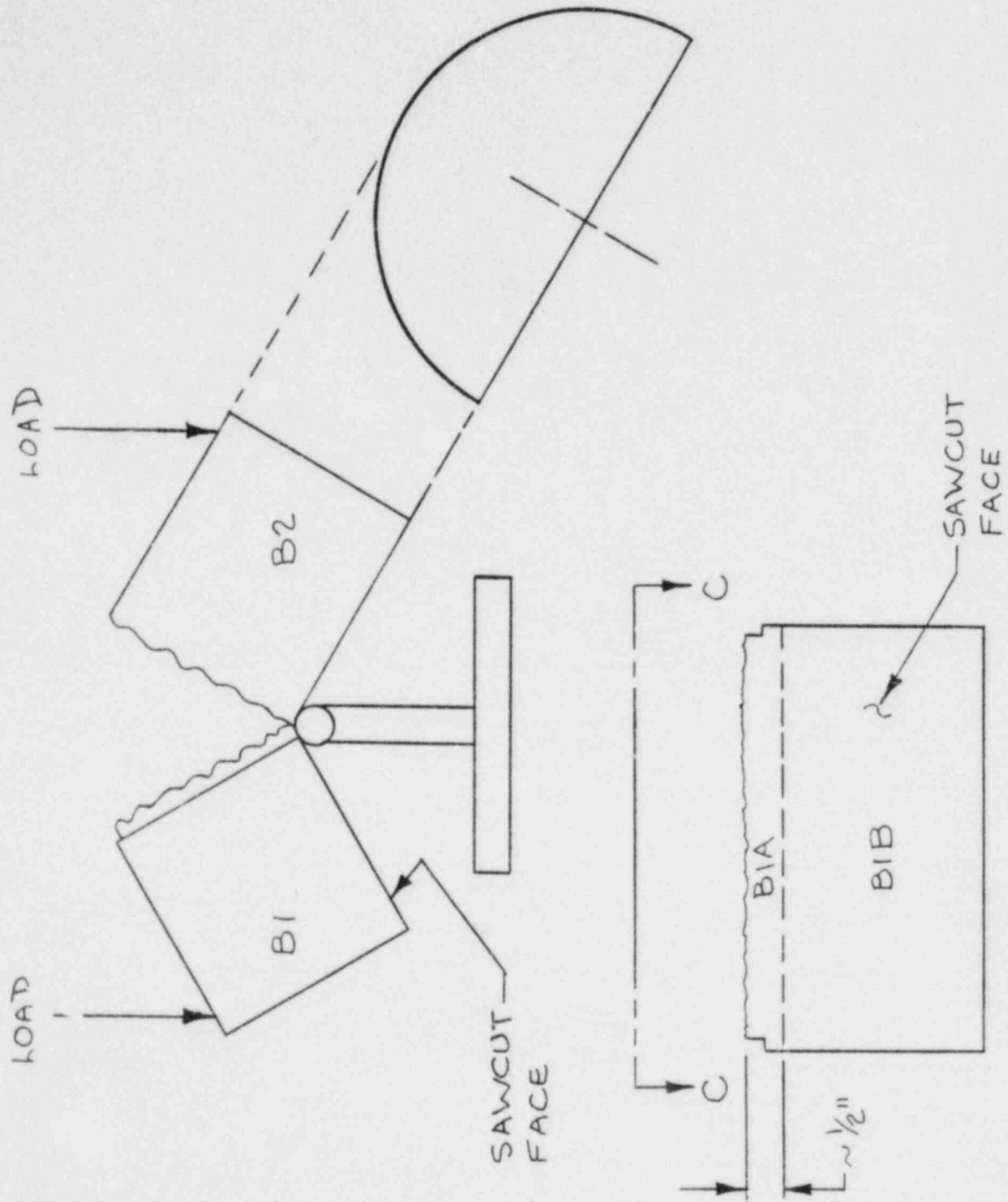
Figure 3.2-2. Separation of the Fracture in Section B
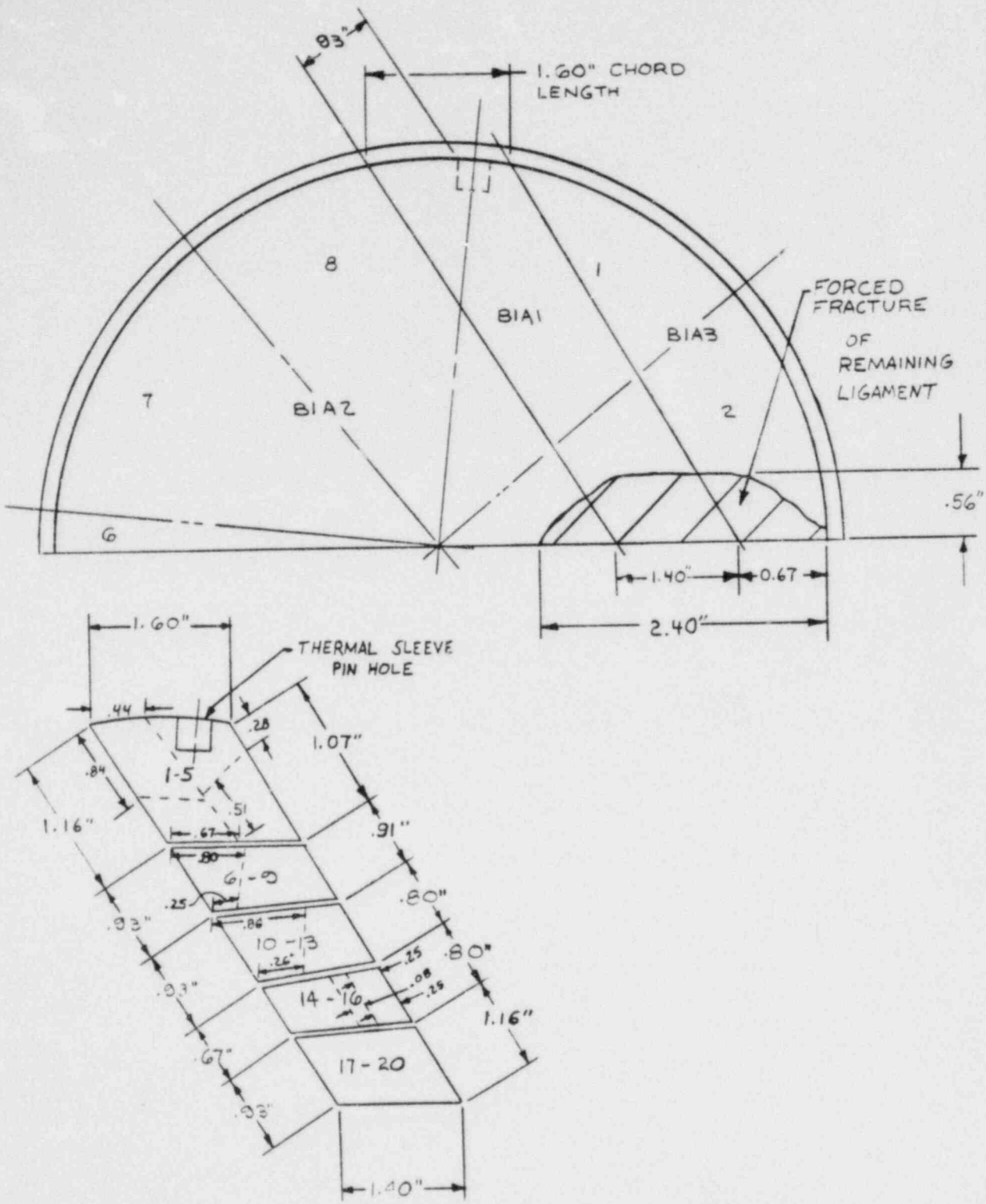
Figure 3.2-3.   Subdivision of Sections B1 and B1A1
Into Specimens for SEM Examination
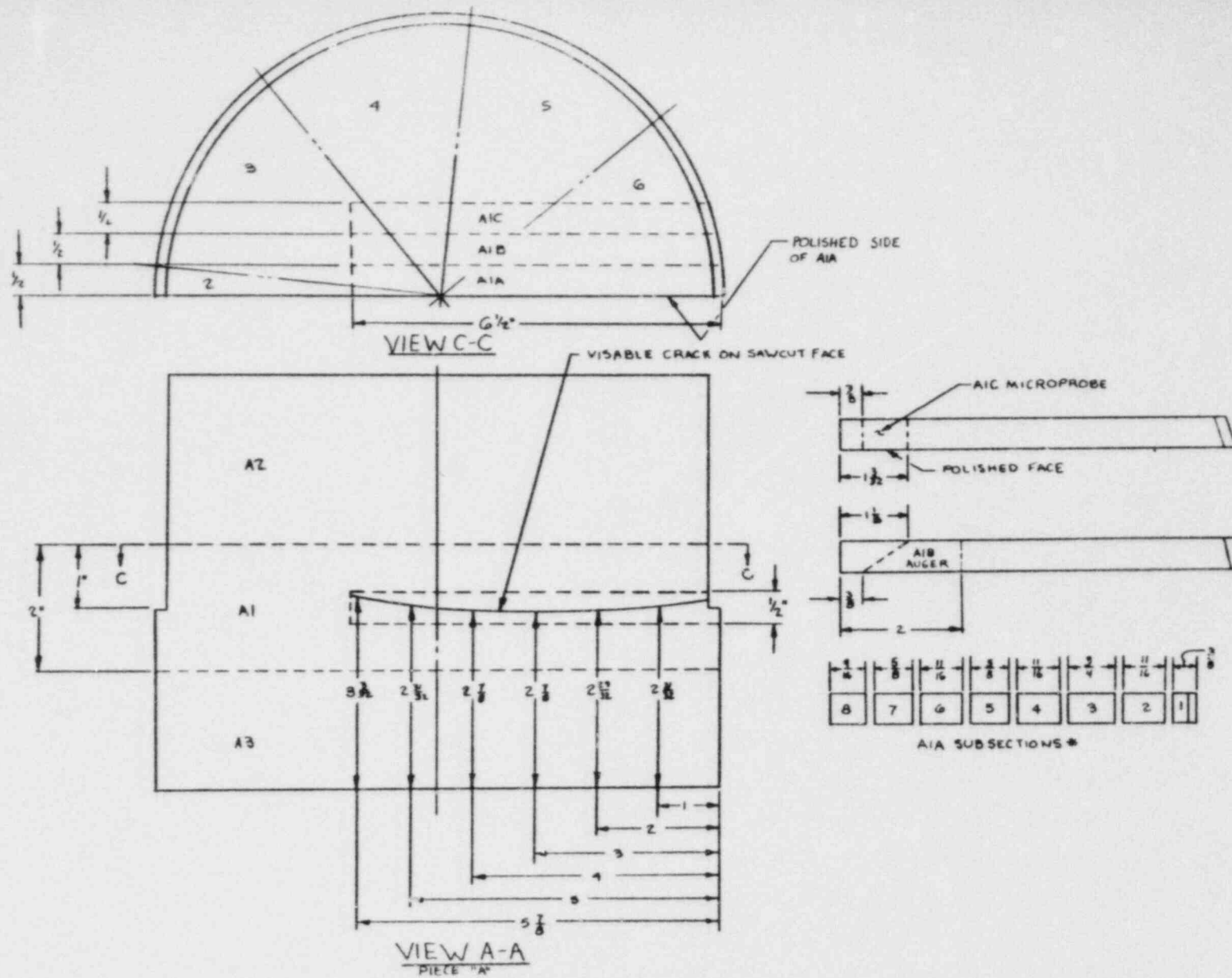
Figure 3.2-4. Subdivision of Section A Into Specimens for Metallo-
graphic, Auger, and Electron Microprobe Examinations

3.3 Fractography And Metallography

As indicated previously in Section 3.2, piece B of Figure 3.2-2 was chosen for initial crack separation in the laboratory and piece A was used extensively for metallography (A1A-1 to A1A-8), electron microprobe analysis (A1C), and Auger electron spectroscopy (A1B). Later as a result of fractographic observations, additional metallographic specimens were taken in section B1A1, specifically specimen 14-16M taken from subsection 14-16B, and specimens 1-5B-1M and 1-5A-M from subsection 1-5. The fractographic examination proceeded in parallel with the metallography on specimens from Piece A. Metallography on specimens from Piece B was performed in parallel with, but near the conclusion of the fractographic examination.

The fractographic examination was performed in three stages and will be reported in that manner, namely: 1) visual and light microscopy of the fracture surface in the as-received condition, 2) scanning electron microscopy* (SEM) and energy dispersive X-ray spectroscopy (EDS using Kevex on SEM) of the fracture surface in the as-received condition and, 3) SEM of the cleaned fracture surface. The cleaning was required to remove corrosion deposits which masked fine fractographic detail. Cleaning was initially attempted by stripping with acetate tape, but was only partially effective. Final cleaning was achieved using an electrolytic ENDOX solution. The details of the various stages of fractography and metallography are provided in the following paragraphs.

---

*The ETEC Autoscan microscope used automatically records perinent data on the micrographs.

Example:
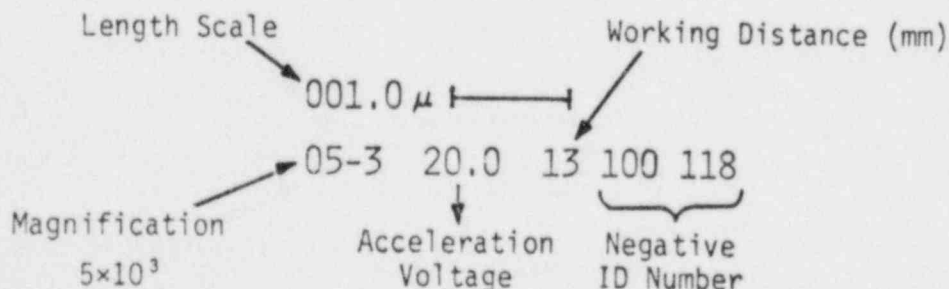
3.3.1 Fractographic Examination

3.3.1.1 Macro-Examination by Light Microscopy

The two mating sections of Piece B, B1 and B2, are shown in Figure 3.3-1. Immediately evident was a well-preserved beachmark and colored corrosion pattern which were identical on the B1 and B2 fracture faces. The fracture was massive in piece B of the shaft leaving only a small intact ligament for laboratory fracture. This ligament was in the lower right side of B1 and its mirror image on the lower left in B2. Based upon the beachmark patterns, it was obvious that the crack initiated at the pin hole, in its upper right side of the shaft surface when viewed on the B1 fracture surface. The crack growth pattern was not symmetric about the pin hole. The growth was more rapid in the counterclockwise direction in the B1 view or against the direction of shaft rotation. Crack growth which started out in the clockwise (B1 view) direction (or direction of rotation) begins to curve away from pure clockwise growth as shown by the crack growth direction arrows in Figure 3.3-1.

To document the beachmark and color variations, color photography at about 8X was used to make photomontages of the initiation site and path along the fracture surface starting at the initiation site and ending at the laboratory fracture. Figures 3.3-2 and -3 show these photomontages. In both figures, the B view contains an overlay showing the beachmark locations as best they could be interpreted. A total of 29 beachmarks were observed, 15 of them occurring within about 1 inch from the shaft surface. Table 4 provides a summary of the beachmark numbers, and their distance from various locations near or at the initiation site. These two figures show several important features. The beachmark evidence clearly shows initiation to have occurred at the upper right corner of the pin hole where it intersects the shaft surface. Further initiation at the pin hole and crack growth rapidly enveloped the entire pin hole so that by beachmarks #5 to #10 a fairly symmetric crack

pattern had developed. By beachmarks #14 and #15, considerable asymmetry in crack growth had occurred, with fastest growth having occurred against the direction of shaft rotation. As shown earlier in the overall view of the B1 fracture surface, this asymmetry in growth continued throughout the B1/B2 section. Based upon the prior visual examination results of crack position at the shaft surface, and now the knowledge of the initiation site, it can be concluded that crack growth was decidedly faster in the direction opposite shaft rotation. The crack tip in octant #2 and the initiation site at the octant #1/#8 boundary were both present in B1. The crack tip against the direction of rotation was in octant #5, which is now in the unopened piece A.

In Figure 3.3-3, the continual change in crack growth direction can be clearly seen from the changing orientation of the beachmarks and the radial fracture lines perpendicular to the beachmark position. This change in direction reflects the bias toward faster growth in the direction opposite shaft rotation.

Figures 3.3-2 and -3 also enhance the perception given in Figure 3.3-1 of color variation over the fracture surface. To beachmark #15, the general color was a red-orange to brown color with occasional small black regions. Bright metallic areas were smeared metal from contact with the mating fracture faces. The beachmarks appeared to be darker, or in some cases lighter, in color than the general corrosion film color. Beyond beachmark #15, however, the corrosion deposits were dull gray with some hint of a straw or bronze coloration. Bright metallic streaks following the radial fracture lines became prevalent. Nowhere else on the fracture was the color of the initiation area out to beachmark #15 duplicated in terms of continuous area coverage. In addition, at beachmark #15 were rather obvious pits which were found nowhere else on the fracture surface. The changes in topography at beachmark #15 were also quite obvious. Prior to beachmark #15, the fracture surface appeared rather flat and featureless except for color variations and beach-

marks. Beyond beachmark #15, the fracture became coarser. The plane of fracture was still flat on a coarse scale, but was composed of ridges and valleys aligned parallel to the direction of crack growth.

As was seen visually using the stereo light microscope and is shown later with the SEM, the bright metallic smeared areas were on the clockwise (Figure 3.3-2) sides of the ridges and on the ridge tops. This would be expected from the torsional loading and clockwise rotation (viewed in Figure 3.3-2) which would preferentially bring those faces into contact with the mating surfaces of B2. Piece B2 was examined with the stereo light microscope and confirmed this torsional smearing orientation. This coarse topography continued to beachmark #25 and then diminished into a finer, flatter structure. More detailed evaluation of the beachmarks, topography, and pitting will be continued in subsequent sections describing the SEM examinations.

Earlier in Section 3.1.2 and in Figure 3.1-7, two sharp changes in angle of crack path on the shaft surface were noted at 1 to 2 inches from either side of the pin hole. With the crack now opened, these changes in crack path direction were located with the stereo light microscope and were correlated with fracture surface features. This examination showed that both of these changes in crack direction started at beachmark #15 and probably ended at either beachmark #18 or #19. Figure 3.3-4 shows this change relative to fracture surface.

3.3.1.2 SEM and EDS Examination of the As-Received Fracture Surface

As indicated earlier, all SEM and EDS work on the fracture surface was performed on the B1A section. This section is shown in Figure 3.3-5 before and after subdividing it into specimens 1-5, 6-9, 10-13, 14-16, and 17-20. The initial examination was performed on each of these specimens in the unaltered condition, that is, just after opening of the fracture and sectioning.

Each specimen was kept in a separate plastic container. All cutting was performed dry after the band saw and blade had been cleaned to remove any residual cutting lubricant.

The examination of the specimens in the as-received condition was limited to EDS and a general evaluation of the macro-fractographic features since the corrosion films were potentially obscuring finer fractographic features. Figure 3.3-6 is an SEM photomontage of specimen 1-5 at low magnification showing the general topography, beachmark structure, and pitting at several locations. The EDS spectra show the presence of a significant amount of sulphur (S) at each location examined. No particular trend with position on the fracture could be observed. While the sulphur $K\alpha$ peak does overlap with Nb L series lines and there is expected to be 0.80% Nb, the effect of Nb in this amount could not alone account for the height of the peak at the sulphur $K\alpha$ energy position. A higher magnification view of a typical film, its sulphur dot map, and EDS spectra are shown in Figure 3.3-7. The dot map shows that although certain areas have more sulphur, there was in general a large sulphur presence over the filmed area. In Figures 3.3-6 and -8, the change to the coarser topography can be seen to occur at beachmark #15 which contains the large pits. The ridge and valley formation is readily seen as is the preferential smearing on the one side and occasionally the top of the ridges. Views of the pit interiors showed a cracked "mud-cake" deposit as well as corrosion nodules as shown in Figure 3.3-9.

Specimen 6-9 was found to primarily contain the ridge and valley topography with a continued general presence of sulphur. Figure 3.3-10 shows typical fractographic features and EDS spectra for this specimen.

Specimen 10-13 was found to contain the ridge and valley formation also. However, further away from the initiation site at notches 12-13 (about 3 to

3-1/4 inches from shaft surface), the fractography gradually flattened and began to develop small islands of a very faceted structure as shown in Figure 3.3-11. Sulphur was still present at this location.

Similar results were found in specimen 14-16 shown in Figure 3.3-12. This specimen also contained some of the coarse ridge and valley formation but it was only in an extreme corner where beachmark #26 passed through the specimen.

Sulphur was still present in specimens 17-20. The fractography before the final forced fracture consisted of a relativly flat but blocky appearing structure as shown in Figure 3.3-13.

3.3.1.3 Cleaning of Fractographic Specimens

Because the complicated and fine fractographic features were possibly being obscured by the corrosion films, only a very quick and limited examination was performed in this "as-received" condition. Each specimen (i.e., 1-5, 6-9, etc.) was further subdivided into an A and B section. The A sections (B section for 1-5) were cleaned in an electrolytic ENDOX solution using the procedure recommended in reference 9. Prior to cleaning, verification that this treatment would not alter the fractographic features was made on as-fractured and air-oxidized tensile specimens of type 304 stainless steel. The ENDOX treatment showed no effect on fractographic features at 10,000X for exposures up to 34 min. This was the longest cleaning interval to be used on the shaft specimens. In contrast, another common cleaning treatment using 6N

HCl solution inhibited with 2g/l of hexamethylene tetramine did show fine pitting at 10,000X after less than 10 minutes exposure.

The ENDOX cleaning treatment was very effective in removing the corrosion films after 17 to 34 minutes exposure. Only specimen 1-5 and 6-9 retained

some corrosion products. Specimens 1-5 contained the heavy red-brown corrosion film shown in Figure 3.3-2.

3.3.1.4 SEM Examination of the Cleaned Fractography Specimens

Figure 3.3-14 shows the B1A section reconstructed after cutting into the A and B subsections. The two large gaps show where the additional fracture path metallography specimens were taken. The path of the detailed SEM fractographic examination is shown in this figure. Initially, the examination included a detailed examination at the pin hole initiation site on specimen 1-5. The examination then proceeded from the shaft outer surface in a path parallel to the side wall of the pin hole until the end of the 1-5B-1 specimen. The path continued on the left side of the 1-5B-2 specimen, parallel to the cut edge. The examination path there crossed over to the A sections of the 6-9, 10-13, 14-16 and 17-20 specimens. This examination path traversed the entire fracture path from initiation to final fracture.

This entire path was examined on the SEM at about 500 to 1000X with frequent increases in magnification to the 5000X to 15000X range. Location of each key examination area was maintained by the use of low magnification "locator photos" showing the area of interest relative to the nearest location notch on the specimen edge. As noted earlier, these notches were placed at approximately 1/4" intervals along the edge of B1A prior to further sectioning. In areas where relating position to a notch was not practical, position was measured from another readily locatable landmark (such as distance to the OD surface along the examination path line) using the SEM stage micrometer. Because of the vast amount of surface to be examined, documentation was performed by making a series of discontinuous photomontages at regions typifying the general structure or where significant fractographic changes occurred.

In the following sections, the results are reviewed starting with the examination of the initiation area and then proceeding along the examination path starting at the shaft OD surface and continuing to the laboratory forced fracture area. Table 5 is a summary of all key fractographic features observed along the fracture path.

3.3.1.4.1 Initiation Region

Figure 3.3-15 shows a series of low magnification SEM photomicrographs of the shaft OD surface at the crack initiation area. Some pitting was observed near the pin hole, but none directly intersected the fracture plane. Examination of the pits revealed an etched structure inside the pits with stepped grain and twin boundaries and etching along slip planes. Figure 3.3-16 contains an example of one of the pits. In Figure 3.3-15, it can be seen that these coarse pits are all located within the wear area adjacent to the pin hole. The coarse unworn machine marks are obvious outboard of the worn area. Close examination of these coarser machine marks in Figure 3.3-17 shows that deposits have accumulated in the machine mark root. The sharp change in crack path direction near the initiation site can be seen in Figure 3.3-15. This sharp change in path direction at the pin hole had been previously observed prior to fracture separation and is shown in Figure 3.1-8.

Figure 3.3-18 shows a series of different oblique views of the fracture surface at the initiation site. From these views, the plane of fracture can be seen to change sharply over the first several hundred microns. Secondary cracks, or intersecting primary cracks from another initiation site, along the hole edge and along the OD surface were also observed. These can better be seen in Figure 3.3-19. In this view, it appears that the radial fracture lines extend back to the inside surface of the hole as opposed to the corner junction of the hole and OD surface. These indications seem to show that

initiation was occurring at several locations: at the corner, at the shaft OD surface near the corner and at the hole inside surface near the corner.

In both Figures 3.3-18 and 3.3-19, extensive amounts of smeared metal can be observed in the initiation region and along the hole edge. Where fractographic features can be seen, they appear transgranular and crystallographic. Locations A, B, and C in Figure 3.3-18 are examples of this structure and are shown in Figure 3.3-20.

3.3.1.4.2 Specimen 1-5B-1

The detailed scan for fractographic features started at the shaft OD surface and traversed in a straight path parallel to the edge formed by the crack/hole intersection. This path is marked M-M and is shown with arrows in the upper part of Figure 3.3-19. Figure 3.3-21 contains the 100X photomontages across the M-M path in this specimen. In each of these montages, the general crack growth direction is labelled, and the numbered small arrows indicate where beachmarks or features similar to those of known beachmarks were found. In each montage are one or two vertical arrows which indicate the distance at that location from a known reference point. In Figure 3.3-21, the distance along M-M is referred to the shaft OD surface at reference point "a". Letters are used to designate the location of photomicrographs showing important fractographic features. While not all higher magnification views are shown, Table 5 summarizes the key observations at each of these locations. The following observations were made on this fractographic specimen:

a.   A flat, transgranular, and rather cleavage-like mode of
     fracture was present over most of the fracture surface.
     Figure 3.3-22 shows several examples of this fracture mode,
     and changes in fractography which occur at beachmarks. At
     beachmarks, the crack appeared to re-initiate at many loca-

tions along the crack arrest line. When the crack front moved
again, the many small crack planes appear to merge after a
short distance to produce a broader, less detailed fracture
structure. In a few locations, fine parallel lines can be
seen on the fracture which are parallel to the crack front and
are spaced at about .1 to .5 .

b. Beachmarks which could be seen by light microscopy were also
    observed using the SEM. The features at these known beach-
    marks are typical of those shown in Figure 3.3-22 at locations
    4 and 5. As the examination continued, many areas contained
    beachmark arrest features indicating possibly more and finer
    beachmarks than could be observed by light microscopy alone.
    This is seen in Table 5 where beachmarks 4 and 5 from the SEM
    exam are the singular beachmark #2 in Figures 3.3-2 and -3 and
    Table 4.

3.3.1.4.3 Specimen 1-5B-2

Figure 3.3-23 shows a low magnification view of this specimen. The
fractographic examination path is again labeled M-M and key beachmarks are
numbered in this view. The small arrowheads show the general crack growth
direction which curves downward in this view from left to right. Pitting was
seen between beachmarks #55 and #56. This is the same pitting identified in
Figure 3.3-2 at beachmarks #14 and #15 as determined by light microscopy. As
in the previous specimen, continuous montages at 500X were made along path M-M
and are shown in Figure 3.3-24. Each numbered arrow refers to a beachmark and
each lettered location contains a group of beachmarks or other important
fractographic information. This information is summarized in Table 5.
Observations from specimen 1-5B-2 include:

a. The flat, transgranular, cleavage-like fractography found in the prior specimen 1-5B-1 existed on this sample to beachmark #55 which is 1.2 to 1.3 inches from the shaft outer surface. Figure 3.3-25 shows this fractography at location P just in front of beachmark #55.

b. Between beachmarks #55 and #57 were the large pits found to parallel the large beachmark structure in this area. Figure 3.3-24 includes a higher magnification montage of pitting in this area. The structure inside these pits, which were cleaned, revealed a faceted or grainy surface with intergranular penetrations. In certain locations of the pits, a heavily etched structure was also present. In general, this etched structure appeared to be nearer to the fracture surface than the smooth faceted structure found deeper in the pits. Higher magnification examples of the pits in the montage in Figure 3.3-24 are shown in Figure 3.3-26. Centered at the bottom of many of these pits appeared to be inclusions or the hole left by an inclusion. These are shown by arrows in locations B, C, E, and G in Figure 3.3-26.

c. The fracture surface beyond the pits had a different topography. From the low magnification views in Figure 3.3-24, it can be seen that smeared ridges and valleys are present which are not found on the fracture surface before reaching the pits. This structure continued into specimen 6-9 where it was examined in more detail.

d. From specimens 1-5B-1 and -2, a total of 61 actual or potential beachmarks were observed. Of these, 55 occurred between

the initiating location and the linear array of coarse pits
bracketed by beachmarks #55 and #56. This occured over a
linear distance of about 1 inch from the initiating corner.
For the entire fracture surface only 71 beachmarks were ob-
served during both light and electron microscopy. Thus, the
vast majority of pump operational history is beachmark docu-
mented in these first fractographic specimens, 1-5B-1 and
1-5B-2.

3.3.1.4.4 Specimen 6-9

Figure 3.3-14 shows the 6-9 specimen location and the fracture examination
path discussed in this report section. Figure 3.3-27 contains four dis-
continuous fracture surface montages at 500X of specimen 6-9. The entire
fracture path on specimen 6-9 was composed of the coarse ridge and valley
topography which began at the large pits at beachmark #56. The smearing of
the raised areas is very dominant in this section, indicating a coarser
topography. The smeared ridges lie parallel to the crack growth direction.

At high magnification (10,000X), the undisturbed "valley" regions revealed an
intricate transgranular structure which contained fine striations, typically
with about 0.2μ spacing and lying parallel to the general direction of crack
growth. Figure 3.3-28 shows several examples of this transgranular, striated
fracture surface. The striated structure in these views shows that on a fine
scale, crack growth was proceeding on many planes and generally in the
direction of overall crack growth.

3.3.1.4.5 Specimen 10-13

The 500X montages documenting the typical fractographic features are shown in
Figure 3.3-29. The coarse ridge and valley topography existed over parts of

its examination path down to about 2.5 to 3.0 inches from the shaft outer surface. The ridge and valley formation appeared to be less prevalent, indicating less surface relief. The structure in the valley portion was still similar to that found in 6-9 and shown in Figure 3.3-28. Figure 3.3-30 shows this same type of intricate transgranular fracture with striations in specimen 10-13. In these views, the striations or line spacing were approximately 0.1 to 0.2 . Over the fracture surface from about 2.5 to 3.0 inches, a gradual change occured in topography. The smeared ridges began to disappear and the general surface relief became flatter. The fine transgranular structure with faint striations still remained similar, but less distinct, to that seen in the valley structure of specimens 1-5, 6-9, and the first part of 10-13. Most notably, however, was the gradual increase in frequency of islands of a blocky or faceted structure. This faceted structure was very evident in the last two montages of Figure 3.3-29. Higher magnification views of this structure is shown in Figure 3.3-31. Several observations were made about this fractographic feature:

a. The faceted areas were isolated colonies approximately 5 to 10 grains. These islands are surrounded by the fine transgranular structure seen on prior specimens.

b. The faceting appeared to be predominantly intergranular although instances of very flat, planar structures were observed occasionally. Grain boundary separations and triple points were seen in many locations (views E, F, G in Figure 3.3-31). At some locations, it appeard that intergranular as well as flat cleavage planes may have been present within the same faceted island.

c.   The switch in fractography from the coarse faceted to the fine
transgranular was generally very abrupt. Locations E, F, and
G in Figure 3.3-31 each show regions where one side of a flat
facet was intersected by the fine transgranular structure.
The line of intersection showed a cross section of the fine
transgranular structure.

d.   Several of the facets showed curved linear patterns on their
surface. This is shown in the 1500X view of location G in
Figure 3.3-31. These curved arrays appeared to be composed of
very fine pits and/or precipitates or inclusions. These
patterns were bowed toward the direction of crack growth.

3.3.1.4.6 Specimen 14-16

The 500X montages of typical locations in specimen 14-16 are shown in Figure
3.3-32. In general, the fracture features on specimen 10-13 from about 2.5 to
3.0 inches and deeper persisted in specimen 14-16. Islands of faceted
structure surrounded by the feathery transgranular fracture were the main
features. Smeared metal was present but represented a very infrequent oc-
currence. It appeared that the frequency of the faceted islands had increased
and covered a larger area fraction. Figure 3.3-33 shows some higher magnifi-
cation views of this faceted structure. Observations made for this type of
structure on specimen 10-13 apply for specimen 14-16 as well. In Figure
3.3-33, evidence of intergranular separation, flat cleavage-like facets and
curved patterns on the flat facets seeming to indicate temporary crack arrest
locations, can all be found. At location A, parallel steps on the flat facet
were seen.

While not documented at high magnification, faint striation-like markings were
occasionally found in the feathery or fine transgranular "sea" surrounding the

faceted islands. Their appearance and spacing was similar to those previously
shown on specimens 6-9 and 10-13.

3.3.1.4.7 Specimen 17-20

Figure 3.3-34 shows the 500X fractography montages for this specimen. The
examination path ended with the laboratory forced fracture in this specimen.
The fine transgranular structure was still present, but a noticeable increase
in the frequency of the faceted islands had occurred. The cusp and void
formation at the far end of the last montage indicates the start of the forced
fracture.

At higher magnification in Figure 3.3-35 were some of the striation-like
features observed at various locations within the fine transgranular region.
These patterns have a spacing of about 0.3μ .

3.3.2 Metallography

The shaft fracture was oriented in the circumferential direction (a plane
normal to the shaft axis). Therefore, longitudinal views (parallel to the
axis) were used to metallographically examine regions of interest. A 10%
oxalic acid solution was used to electrolytically etch the specimens and
reveal the microstructure. Optical metallographs were used to inspect and
photograph all specimens. Regions examined are discussed separately in this
section.

3.3.2.1 Crack Path Morphology

The entire crack path was documented by photographing specimens A1A-1 through
A1A-8 in the as-polished condition at 50X. Specimens A1A-1, -4 and -8 were
etched and photographed at higher magnifications.

Shown in Figure 3.3-36 are photomicrographs of specimen A1A-1, which contain the first 0.260-inch of the crack beginning at the outer surface of the pump shaft. A 0.006-inch offset between the two halves of the specimen was observed at the shaft outer surface. Several other observations were made along the crack path which strongly indicate deformation of the pump shaft at the crack location during operation. The crack width (axial dimension) was wider in specimens near the shaft outer surface and became tighter near the center indicating either sliding wear of the crack surfaces or plastic deformation in the shaft axial direction. A lack of alignment between inclusions and grains which were intersected by the crack was observed nearer the shaft outer surface. Figures 3.3-37, -38 and -39 show micrographs of specimen A1A-4 from approximately midway along the crack and Specimen A1A-8 from the crack tip region, which depict these observations.

Propagation of the main crack was entirely transgranular, with an occasional intergranular penetration observed. A minor amount of secondary cracks, or branching, was observed in specimens near the shaft center, while none was observed near the outer surface. The secondary cracks were also transgranular and sometimes were observed to follow twin boundaries as shown in Figure 3.3-39.

Except for the relatively large population of inclusions, the microstructure looked typical of an annealed stainless steel. Grain size was ASTM 4 to 5 and uniform throughout the shaft. Inclusion density, on the other hand, varied from ASTM Type C Thin near the shaft outer surface to Type C Heavy at the center. Figures 3.3-36, -37, -38 and -39 show this variation in inclusion density.

3.3.2.2 Crack Initiation Region

The crack initiation region in specimen 1-5B-1 adjacent to the thermal sleeve anti-rotation pin hole was examined using longitudinal views parallel to the

right side of the hole. Micrographs of this region are shown in Figure 3.3-40.

The major portion of crack surface was present at nearly a constant angle of 12° from a plane normal to the shaft axis until approximately 0.060-inch from the shaft outer surface. At this point, the crack angle reversed directions and tapered off. In the tapered region, the crack surface was relatively irregular and some undercutting, or branching, occurred. The undercutting was most likely either "folds" of deformed metal or intersection of another primary crack observed in this region of the fracture surface using the scanning electron microscope as stated in Section 3.3.1.4.1.

At the shaft outer surface, a small piece of protruding material of undetermined origin was observed. A "lip" of deformed metal was observed in this region using the SEM. The "lip" may have been caused by sliding of the crack surfaces during pump operation. Although not observed using SEM, a burr from the pin hole drilling may also have caused this piece of metal to protrude into the plane of polish shown in Figure 3.3-40.

Surface damage in the form of machining grooves was observed on the outer surface of the shaft during the previous visual inspection (Sections 3.1.2 and 3.3.1.4.1). These grooves were also observed metallographically as shown in Figure 3.3-41. A cold-worked layer approximately 0.003-inch deep was observed along the shaft outer surface in which slip planes were readily visible on the grains. This layer was apparently caused by the machining operation and was not observed elsewhere in the shaft material.

Inclusion density in specimen 1-5B-1 was the same as that in Specimen A1A-8, ASTM Type C Thin, while no detectable grain size difference was observed.

3.3.2.3 Pit Region

The band of pits observed on the crack surface of specimen 1-5 using the SEM was sectioned so that the pits could be metallographically examined with longitudinal views. Figure 3.3-42 shows photomicrographs of the pits in specimen 1-5A. The pits were irregularly shaped and penetrated to various depths of which 0.011-inch was the maximum observed. Some of the pits overlapped each other. Crystallographic features observed using the SEM were visible within several of the pits and on the crack surface at the pit mouths. Many of the individual pits appear to have been located at inclusion sites, with the remaining inclusion ligament stemming from the pit base. This observation may just be an artifact, but it was observed in more cases than not. Since the pits were located at beachmark #15 on the crack surface, this may indicate that inclusions intersected by the crack front provided sites more susceptible for initiation of pitting corrosion.

3.3.3 Fractography and Metallography
Summary And Discussion

3.3.3.1 Summary of Key Results

A substantial amount of information was obtained from the fractographic and metallographic examination. A distillation of the key points is provided below:

a. The fracture initiated at one side of the pin hole and rapidly enveloped the entire pin hole.

b. A well preserved beachmark pattern was readily observable with the majority of the beachmarks located within about 1 inch of the fracture surface.

c.   The area containing the vast majority of beachmarks was also
the area of highest corrosion deposit, exhibiting a distinct
red-brown coloration.

d.   Crack growth eventually became asymmetric with the most rapid
crack growth <u>against</u> the direction of shaft rotation.

e.   The fracture surface showed a higher than normal concentration
of sulphur as measured by EDS.

f.   The #15 beachmark (by light metallography) boundary between
the heavy red-brown corrosion deposit and the remaining
fracture contained an array of large pits which followed the
beachmark. This was the only location in the fracture which
had any pitting.

g.   The pits were in general not deep (about 0.011 inch max) but
exhibited an etched and faceted appearance on the walls. No
integranular penetrations were observed extending from the pit
walls. Both SEM and light metallography suggest that the pit-
ting preferentially occurs at locations of inclusion string-
ers.

h.   The fractography over the initial 1 inch of depth is a low
ductility, transgranular crystallographic fracture mode.

i.   From about 1 inch, starting at the pitted beachmark #15, to
about 2.5 to 3.0 inches in depth, the fracture is a fine
transgranular structure with crack propagation occurring on
many planes or plateaus. Striations were found, but not

consistently observed. When observed, they are about 0.2μ in
spacing. The many fine planes or plateaus of crack growth are
generally elongated in the direction of crack growth.

On a macroscopic scale, the fracture surface is not as flat as
from 0 to 1 inch but is now composed of ridges and valleys
aligned in the direction of crack growth. The ridges are
smeared consistently on one side or on their tops from frac-
ture surface contact during continued pump operation.

j.   From about 2.5 inches to the final crack position (4.75
     inches on the fracture path examined) a mixed mode fracture
     occurred with the fine transgranular fatigue still present,
     but islands of intergranular and/or cleavage facets exist.
     The frequency of these islands increases with crack depth up
     to a point and then decreases to a nearly negligible feature.
     Near the final fracture, striations when seen, have a spacing
     of about 0.3 .

k.   Although secondary cracking and patches of intergranular frac-
     ture were observed on the fracture surface, metallography re-
     vealed that the secondary cracking was rather shallow, extend-
     ing only about 1 or 2 grains deep. These secondary cracks
     were infrequent and were predominantly transgranular.

l.   Grain structure appeared to be uniform on all metallographic
     sections examined with a grain size of about ASTM 4 or 5
     (about 80 to 55 micron intercept lengths respectively).

m.   The inclusion population appeared to increase from the outer
     portion of the shaft toward the center.

n. A deformed layer of 3 mils existed on the outer surface of the
    shaft. This was presumably from the machining operations on
    the shaft.

3.3.3.2 Failure Mode

The observations summarized above strongly suggest a high cycle-low stress
amplitude fatigue failure of the pump shaft. The presence of a set of well
preserved beachmarks about a large material discontinuity (the shaft pin hole)
are very incriminating. The asymmetric fatigue crack growth against the
direction of shaft rotation is a well documented phenomenon when rotational
bending occurs.[10] Rotational bending creates the dominant alternating load on
the pump shaft. The sharp change in crack direction after a short distance
from the initiation site is typical of a change from Stage I to Stage II
fatigue crack growth.[10] The transgranular crystallographic fracture in the
initiation area is typical of Stage I fatigue or crack growth at low stress
intensity ranges (ΔK) in austenitic alloys.[11,12] The fine transgranular frac-
ture with faint striations occasionally present is also a well-documented
crack growth mode of austenitic alloys.[11,12] When this mode is observed, it
is generally in the early stages of crack growth but just after the transgran-
ular fracture in Stage I propagation. The mixed mode of fracture observed in
later stages is also associated with crack growth at near threshold (low ΔK)
conditions. This mixed mode behavior has been observed in type 316 stainless
steel,[13,14] alloy steel [15,16] and in Ti-6A1-4V[17] at low crack growth rates.
References 14 and 18 provide good summaries of alloys where this mixed mode
has been observed and factors influencing its occurrence. Grain size, R ratio
(K_{min}/K_{max}), environment, K and K_{max} have all been shown to be important fac-
tors in mixed mode crack growth. In summary, the investigative results from
fractography and metallography of the failed shaft strongly indicate a fatigue
failure.

Review of the available data on the PI-2 failure show it to also be attributed to high cycle fatigue with crack initiation assisted by residual stresses. No contribution from chemical contamination was alluded to. The TMI-1 failure occurred in the same location as PI-2 and, as shown in Table 3, had higher rotational bending stresses than PI-2.

The possibilities of stress corrosion cracking (SCC) and corrosion fatigue were also considered but have been given a lower probability than pure fatigue. The type 347 stainless steel used in the pump shaft is a stabilized grade designed to prevent sensitization. Sensitized stainless steels are well-known for their susceptibility to intergranular attack and intergranular SCC in various environments. In the absence of sensitization, many grades susceptible to these forms of attack become immune. Type 347 is inherently more resistant to intergranular attack and SCC than unstabilized grades. Reference 19 showed that in oxygenated, high temperature water, type 347 stainless steel was the most resistant to intergranular SCC of the commonly used austenitic stainless steels. The effect of the presence of sulphur in the form of the thiosulfate anion has been recently reviewed[20] and has been shown to cause intergranular SCC in sensitized type 304 stainless steel. Even for this very susceptible condition, a stress intensity, K, of 33 MPa$\sqrt{m}$ or lower did not cause crack growth. The steady K value for the pump shaft is estimated to be less than 11 MPa$\sqrt{m}$ for the entire crack path examined. Furthermore, no intergranular cracking except for small isolated patches was observed in the fractography or metallography. Thus, even though a form of sulphur was present on the fracture surface, neither the metallography, fractography, shaft material condition or stress level support a case for SCC.

It has also been shown in reference 21, that the fatigue behavior of types 304 and 316 stainless steels is essentially identical in air and in PWR coolant chemistries covering a range of pH from 4.2 to 10.5. The strongest effect

came from the stress intensity ratio, R. No information was found regarding the effect of sulphur on the fatigue behavior of stainless steels, however, there is general belief that for unsensitized material such as type 347 there would be little or no effect.

The results do not indicate any gross metallurgical defects which would clearly have initiated a fatigue crack. However, the presence of the sharp cornered pin hole and the associated stress concentration factor are obvious considerations in the initiation mechanism. The coarse machine marks and the deformed surface layer may also have been factors particularly if tensile residual stresses were created at the surface. The rather coarse tooling marks observed inside the pin hole may also have been a factor through surface finish or residual stress effects. Residual stress from the welding operation of the anti-rotation pins into the thermal sleeve was previously[2,3] assigned chief responsibility for raising surface stresses into the range where fatigue failure could be predicted based upon fatigue limit data derived from S-N curves from actual shaft material.

Wear areas on the shaft and thermal sleeve at the pin and hole and at the thermal sleeve/shaft interfaces delineated by corrosion deposits also suggests that fretting may have been a factor in crack initiation. The wear patterns need to be considered, but it should be kept in mind that a substantial amount of the wear probably occurred after the crack had grown to a certain size and shaft deflection at the crack opening was responsible for most of the wear. A limited review of the fatigue analysis approach in references 3 and 4 using the stresses in Table 3 still shows a factor of safety greater than 2 or 3 for this shaft. However, all of the above degrading factors need to be considered in the detailed stress analysis for fatigue initiation.

3.3.3.3 Implications of Beachmark Distribution,
         Red-Brown Corrosion Deposit and Pitting

The heavy red-brown corrosion film present on the fracture from the initation
site to beachmark #15 (by light microscopy) indicates that the fracture up to
that point had been exposed to an oxidizing medium for a longer period of time
than the balance of the fracture. Crevice corrosion under stagnant conditions
may have selectively oxidized the Fe. Crevice corrosion of stainless steels
is a well documented phemonenon. Wear in certain areas of this fracture sur-
face over a longer period of time may also have produced fine particulate mat-
ter which oxidized and coated the fracture. Only tight crevices or areas near
tight crevices and near known or likely wear or fretting sites contained the
red-brown deposits. These were probably composed of mainly $Fe_2O_3 \cdot H_2O$. The
outer surface of the shaft, for example, still had a relatively shiny metallic
coloration. The presence of the majority of the beachmarks in this region and
their close spacing suggests that the crack was slowly growing in this region
for a relatively long time, i.e., covering many operational transients.

Variations between the number of beachmarks observed using light microscopy
and scanning electron microscopy can be attributed to two factors. Using
light microscopy, only 29 were observed; using SEM and light microscopy
combined, 71 were observed. The higher magnification and resolution of the
SEM made it possible to locate fine crack arrest features not visible using
light microscopy. Howevei, some of the fractographic features associated with
beachmarks visible by light microscopy were often observed on the SEM in
smaller and less continuous lines. While some of these were legitimate beach-
marks, some may also have been crack fronts moving through tilt or twist boun-
daries associated with grain, subgrain or twin boundaries. In this case, the
crack may have halted for several cycles at a localized region while the crack
continued to move forward in other areas. Thus, some of the beachmarks
counted in the SEM examination were arrest points and they did not necessarily
represent arrests associated with pump shutdown. Therefore, a minimum of 29

and a <u>maximum</u> of 71 beachmarks were observed which were associated with pump starts and stops. In reality, the correct number should be somewhere between minimum and maximum. This pump's startup and shutdown history is available to GPU and can be correlated with the number and location of beachmarks identified in Tables 4 and 5.

The occurrance of pitting only along beachmark #15 (by light microscopy) and nowhere else on the fracture suggests that the crack front remained at that location for a considerable length of time. The corrosion deposits found on the pits suggest that the pits were not longer actively growing. This pitting probably occurred under acidic conditions at the crack tip and nucleated at locations where the inclusion arrays intersected the fracture surface. The results from light metallography and SEM of the pit interior surface strongly suggest that stringered inclusions were the sites for pit nucleation. Nucleation of pitting in stainless steel has been observed to occur at MnS and FeS inclusions surrounding Al and Cr oxide inclusions.[22]

3.3.3.4 Implications of Fractographic Features on Crack Growth Rates

Although a complete stress and fracture mechanics analysis of the shaft as a function of crack length is beyond the scope of this investigation, the fractographic data and relevant literature provides some insight into these stress intensity values and crack growth rates. This will be attempted in the next few paragraphs. What will be done using the fractography is but one approach or one part of a closed solution to the problem; the other must come from the calculated values. If both approaches are on target (and mother nature is kind), the results or predictions from both methods should agree.

Estimates of the stress intensity range (ΔK) and resulting crack growth rates at various locations on the fracture can be approximated from the fractographic features observed. From the initiation region to about 1 inch in depth,

the transgranular crystallographic fracture mode dominated. This mode of
fracture in type 305 stainless has been associated with crack growth rates of
10^{-6} mm/cycle and lower for ΔK values ≤ 10 MPa$\sqrt{m}$.[22] From 1 inch to about 2.5
inches, the 0.2μ striation spacing suggests a ΔK of about 25 MPa$\sqrt{m}$ and a
crack growth rate of $\sim 10^{-4}$ mm/cycle from the reference 23 data. The occur-
rence of the patches of intergranular and cleavage facets from 2.5-3.0 inches
to final crack position can be related[18] to the ΔK level through the correla-
tion with the reverse plastic zone size P_r where

$$P_r = \frac{1}{3\pi} \left(\frac{\Delta K}{2\sigma_y}\right)^2 , \quad \sigma_y = \text{yield strength}$$

It has been shown[18] that the mixed mode faceted structure occurs when the
reverse plastic zone size is approximately the grain size of the material.
From the metallography performed, the grain size lies somewhere between 50 to
200μ. The yield strength of the shaft material is approximately 31 ksi (214
MPa). Using the two grain size bounds, the ΔK can be calculated to be between
19 MPa$\sqrt{m}$ and 9 MPa$\sqrt{m}$. These values of ΔK can be taken to be the values at
which the greatest amount of faceting occurs. At ΔK values higher or lower
than the 9-19 MPa$\sqrt{m}$ range, decreasing amounts of faceting will occur. From
reference 13, virtually no faceting would be predicted for $\Delta K = 25$ to 30 MPa
$\sqrt{m}$. As ΔK decreases from this range, the percentage of faceted fracture would
increase to 5-10% of the fracture surface at about 12 to 20 MPa$\sqrt{m}$. From
there to $\Delta K \simeq 5$ MPa$\sqrt{m}$ the amount of faceting would decrease to zero. This
gradual increase and then decrease in the amount of faceting was observed
on specimens 10-13 through 17-20, although the area fraction of faceting ap-

pears to be larger than 10% in some locations. Thus, the faceted fractography from the 2.5 inch depth to final crack position appears to suggest either an increasing or decreasing ΔK over a range from 5 MPa $\sqrt{m}$ to 25 MPa $\sqrt{m}$.

However, the changes in R ratio in the shaft with crack growth may also be influencing the amount of faceting even if ΔK was unchanging. Reference 18 shows that for many alloys as R increases, the crack growth rate increases for the same ΔK and the apparent threshold stress intensity range, ΔK_{th}, decreases. However, the amount of faceting observed is less as R increases. In order to evaluate the potential affect of R on the crack growth and fractography of the pump shaft, a simplified model of the shaft loading was evaluated.

Using a simplified fracture mechanics model of three point bending of an axially loaded bar with an edge crack, estimates of ΔK and R could be made as a function of crack length. Steady axial tensile stress from the axial thrust on the shaft and an alternating bending stress from shaft rotational bending were accounted for in these calculations. Two geometry cases were considered; one where shaft deflection was not limited and ΔK increases with increasing crack length, and a second case where ΔK was assumed to stay relatively constant because shaft deflections become limited by impeller rubbing on the pump housing. For the unrestricted deflection case, ΔK increases with increasing crack length and R is negative but tends to become less negative as the crack increases in length. A negative R implies complete fracture closure during cycling, but with increasing crack length the tendency for complete closure becomes less. Where shaft deflections were restricted and a constant ΔK was assumed, the R value goes from larger to smaller negative values to about 2-3 inches of crack depth. At 3 inches and beyond, the R value was positive and increasing.

The latter case's credibility is supported by the heavily smeared fracture features (negative R) over part of the fracture surfaces, decreased levels of smearing at the far extremes of the crack (R becoming less negative and going positive) and the GPU observations of impeller rubbing. If the latter case (constant ΔK) is applicable, then the increasing positive R ratio could also explain the decrease in faceting observed in specimen 17-20. The case for a constant ΔK over the region from about 1 to 4.5 inches is also supported by the relatively constant striation spacing observed in several areas along this region. If a ΔK of 9-19 MPa$\sqrt{m}$ is assumed, a microscopic growth rate of 10^{-5} to 10^{-6} mm/cycle would be predicted from reference 23 data. The macroscopic growth rate may be considerably less because of difficulties in keeping the crack moving through grain, subgrain, and twin boundaries when ΔK is low.[14] A factor of 3 difference has been observed between micro- and macroscopic growth rates in 316 stainless steel at a ΔK = 28 MPa$\sqrt{m}$. This difference is expected to increase at lower ΔK.

In summary, the fractographic data suggests that from about 1 to 2.5 inches, the crack growth rate was $<10^{-4}$ mm/cycle; and from 2.5 to 4.5 inches, the growth rate was $<10^{-5}$ to $<10^{-6}$ mm/cycle. From these growth rates a straight crack path of 3.5 inches could be traversed in about 148 hours at 1180 RPM shaft speed (10^{-4} mm/cycle from 1 to 2.5 inches, 5×10^{-6} mm/cycle from 2.5 to 4.5 inches), assuming each cycle produces incremental crack growth and no additional cycles are needed to cross microstructural boundaries. As an upper bound on growth rate, if 10^{-4} mm/cycle is assumed for the entire crack path, only 12.6 hours would be needed to propagate the crack to its final position. As a lower bound on rate, if 5×10^{-7} mm/cycle is assumed for the entire path, 2511 hours would be required. Considering that the actual curved fracture path would add a fractional increase in total path length and that the macroscopic rate may be less than that observed on the fractography, the time required to move the crack from beachmark #15 to its final position would take

less than a few thousand hours. The time in one pump, cold operation of about 1400 hours falls well into this range.
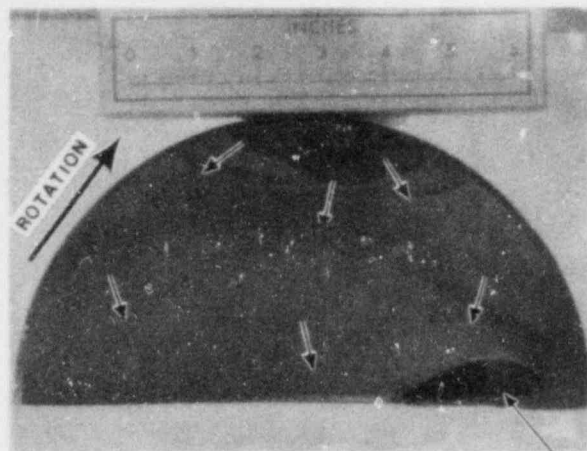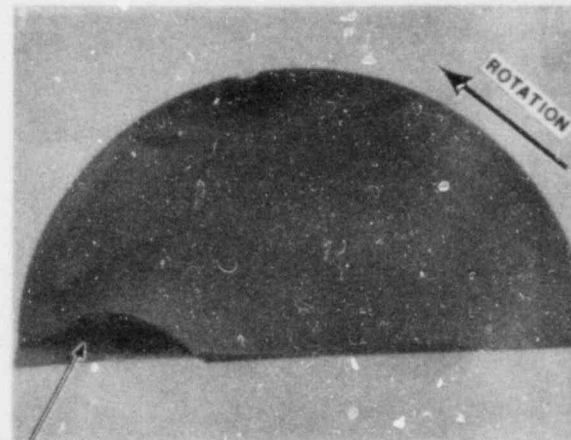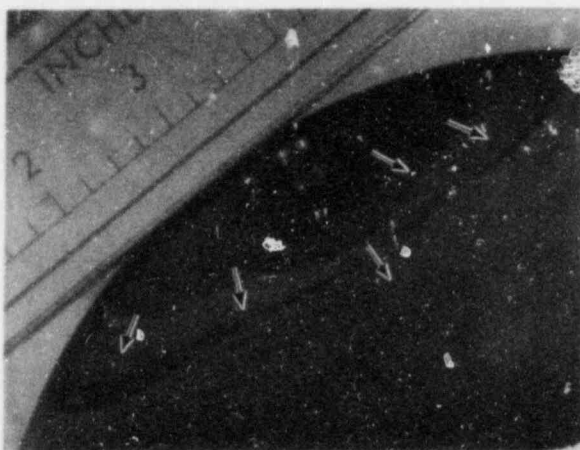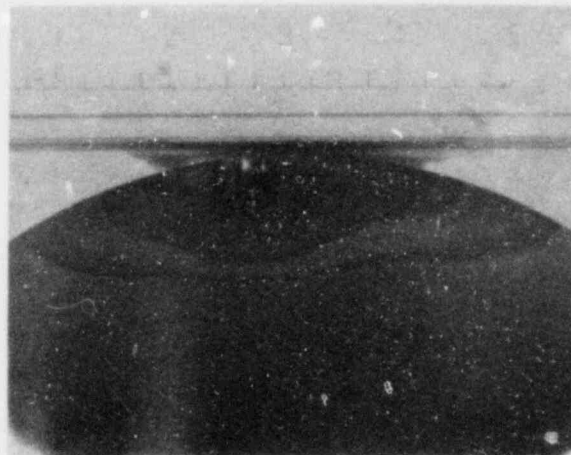
Figure 3.3-1.   Shaft Fracture Surface on Piece "B" Sections
                A, B: Overall View and Initiation Area on B1
                C, D: Overall View and Initiation Area on B2

Table 4. Beachmark Locations From Color Montage[1]

LIGHT MICROSCOPY BEACHMARK NO.	LINE NUMBER ON INITIATION MONTAGE (FIGURE 29)	LINE NUMBER ON PATH MONTAGE (FIGURE 30)	LEFT CIRCUMFERENTIAL INTERCEPT[2]	LEFT VECTOR INTERCEPT[3]	℄ INTERCEPT[3]	RIGHT VECTOR INTERCEPT[3]	RIGHT LIGHT CIRCUMFERENTIAL INTERCEPT[4]
1	1	1	-----	-----	-----	0.068	0.286, 3.75°
2	2	2	-----	-----	-----	0.300	0.509, 6.67°
3	3	3	-----	-----	-----	0.426	0.633, 8.55°
4	4	4	-----	-----	0.611	-----	-----
5	5	-	0.572, 7.49°	0.561	-----	-----	-----
6	6	-	0.675, 8.84°	0.636	-----	-----	-----
7	7	-	0.771, 10.10°	0.691	-----	-----	-----
8	8	-	0.827, 10.83°	0.737	-----	-----	-----
9	9	5	0.937, 12.27°	0.801	0.721	0.651	0.954, 12.49°
10	10	6	0.970, 12.70°	0.836	.742	0.674	0.970, 12.70°
11	11	-	1.462, 19.15°	-----	---	-----	-----
12	12	-	1.543, 20.21°	-----	-----	-----	-----
13	13	-	1.653, 21.65°	1.251	-----	-----	-----
14	14	7	1.685, 22.07°	1.302	0.884	0.869	1.288, 16.87°
15	15	8	1.749, 22.96°	1.372	0.907	0.894	1.370, 17.29°
16	16	9	-----	1.476	0.936	0.956	1.375, 18.01°
17	17	-	-----	1.543	-----	-----	1.415, 18.53°
18	18	10	-----	1.768	-----	1.024	-----
19	19	11	-----	-----	-----	1.084	-----
20	--	12	-----	-----	-----	1.272	-----
21	--	13	-----	-----	-----	1.812	-----
22	--	14	-----	-----	-----	2.162	-----
23	--	15	-----	-----	-----	2.797	-----
24	--	16	-----	-----	-----	3.258	-----
25	--	17	-----	-----	-----	4.784	-----
26	--	18	-----	-----	-----	-----	-----
27	--	19	-----	-----	-----	-----	-----
28	--	20	-----	-----	-----	-----	-----
29	--	21	-----	-----	-----	-----	-----

NOTES:

[1] All measurements made from montages using a planemeter. Distances were divided by photo magnification to obtain true dimensions. Arc angle computed from arc length by

$$\theta = \frac{180S}{\pi r} \quad \text{where } S = \text{arc length (in),}$$

r = shaft radius = 4.375 in and θ = subtended angle in degrees. Beachmark 1-19 measured on Figure 3.3-2 montage; 20-25 on Figure 3.3-3 montage

[2] First number is arc length (in) from centerline of pin hole to beachmark intercept at surface; second number is angle subtended by the measured arc length.

[3] Distance from LV, ℄, or RV vector origin to beachmark intercept. Units are inches.

[4] Same as 2 except arc length measured from crack initiation at right side of hole in montage.

Table 5. Summary of Fractographic Results From SEM Exam

Distance From Surface Reference Points, Inches	Specimen	Fracture Surface Feature			Striation Spacing, μ	Comments
		Type	Label[a]	Photo		
0.037	1-5B-1	Possible striation	A	18-168 18-186	0.18	Striations very faint, very questionable in appearance
0.079	1-5B-1	Beachmark	#1	18-169	--	Note 1
0.130	1-5B-1	Beachmark	#2	18-171	--	Note 1
0.172	1-5B-1	Beachmark	#3	18-183	--	Note 1
0.189	1-5B-1	Beachmark and Possible Striation	#4	18-173, 18-187 18-188, 18-190	-- <0.2	These beachmarks (#4 and #5) are visible as one beachmark, #2, on the light microscopy color montage (initiation). Striations are very faint and highly questionable. Cleavage and river patterns dominate.
0.193	1-5B-1	Beachmark	#5	18-173, 18-187 18-188	-- --	
0.200	1-5B-1	Beachmark	#6	18-174	--	
0.211	1-5B-1	Possible Striation	B	18-174 18-191	<0.2	Striations very faint, highly questionable in appearance.
0.225	1-5B-1	Beachmark	#7	18-175	--	Note 1
0.229	1-5B-1	Beachmark	#8	18-174	--	Note 1
0.234	1-5B-1	Beachmark	#9	18-175	--	Note 1. Beachmark #9 composed of smaller beachmarks. Cleavage and river patterns dominate.
0.234	1-5B-1	Fracture Detail	C	18-192	--	
0.241	1-5B-1	Beachmark	#10	18-175	--	Note 1
0.249	1-5B-1	Fracture Detail And Striation	D	18-175, -176, -208, -210, -211	<0.2	Cleavage and river patterns with very faint striations
0.286	1-5B-1	Beachmark	#11	18-177	--	Note 1. Cleavage and river patterns; Beachmark #11 is characterized by a change to finer river patterns over a short distance.
0.286	1-5B-1	Fracture Detail	E	18-177 18-193	--	

Distance From Surface Reference Points, Inches	Specimen	Fracture Surface Feature			Striation Spacing, μ	Comments
		Type	Label	Photo		
0.292	1-58-1	Beachmark	#12	18-177	--	Note 1
				18-194	--	Note 2
0.297	1-58-1	Beachmark	#13	18-177	--	Note 1
				18-195	--	Note 2
0.306	1-58-1	Beachmark	#14	18-178	--	Note 2
0.316	1-58-1	Beachmark	#15	18-178	--	Note 1
0.324	1-58-1	Beachmark	#16	18-178	--	Note 1
				18-196	--	Note 2
0.324	1-58-1	Fracture Detail	F	18-178	--	Beachmark #16 characterized by change to a finer cleav
				18-196	--	age and river pattern structure over a short distance.
0.345	1-58-1	Beachmark	#17	18-179	--	Note 1
0.346	1-58-1	Beachmark	#18	18-179	--	Note 1
0.348	1-58-1	Beachmark	#19	18-179	--	Note 1
0.348	1-58-1	Fracture Detail	G	18-179,-205,	--	Cleavage and river patterns changing near beachmark
				-206,-207	--	#19.
0.354	1-58-1	Beachmark	#20	18-179	--	Beachmarks 20 and 21 are the start of the very visible
0.354	1-58-1	Beachmark	#21	18-179	--	beachmark #3 on the light microscopy color montage
		Fracture Detail	#21	18-197,-198	--	(initiation) Note 2.
0.370	1-58-1	Beachmark	#22	18-180	--	Beachmark #22 is in center of #3 beachmark on the light microscopy color montage (initiation).
0.380	1-58-1	Beachmark	#23	18-180	--	Beachmark #23 is at the end of beachmark #3 in the light microscopy color montage (initiation).

Distance From Surface Reference Points, Inches	Specimen	Fracture Surface Feature			Striation Spacing, µ	Comments
		Type	Label[4]	Photo		
0.394	1-5B-1	Beachmark	#24	18-181	--	Note 1
0.403	1-5B-1	Beachmark	#25	18-181	--	Note 1
0.408	1-5B-1	Beachmark	#26	18-181	--	Note 1
0.419	1-5B-1	Beachmark	#27	18-182	--	Note 1
0.431	1-5B-1	Fracture Detail	H	18-182,-202, -203,-204	--	Change in detail of cleavage and river pattern at a boundary.
0.435	1-5B-1	Beachmark	#28	18-182	--	
0.443	1-5B-1	Fracture Detail	I	18-182,-183, -199	-- --	Typical cleavage and river pattern topography.
0.945	1-5B-1	Beachmark Fracture Detail	#29 J	18-269,18-247 18-277,18-278	--	May be Beachmark #4 on light microscopy color montage (initiation) Note 2.
0.976	1-5B-1	Fracture Detail Beachmark	K #30	18-247, -248 18-279	--	Note 1,2. All 3 beachmarks (30, 31, and 32) are within ~0.004 inch.
0.979	1-5B-1	Beachmark	#31			
0.980	1-5B-1	Beachmark	#32			
0.986	1-5B-1	Fracture Detail Beachmark	L #33	18-248, -280	--	Note 1,2.
0.987	1-5B-1	Beachmark	#34			Note 1,2.
0.991-0.994	1-5B-1	Beachmark	#35-41			Note 1,2.
0.995	1-5B-1	Fracture Detail Beachmark	M #42	18-248, -281	--	Note 1,2. Beachmark #46 is the start of beachmark #9 in light microscopy color montage. This beachmark, 9 to 10, has residual corrosion, i.e., more adherent, coarser topography, and smeared metal.
0.998-1.002	1-5B-1	Beachmarks	#42-46			

Table 5, continued

Distance From Surface Reference Points, Inches	Specimen	Fracture Surface Feature Type	Label[a]	Photo	Striation Spacing, µ	Comments
		Fracture Detail	N			Note 1; Beachmark #47 is the other end of the broad
1.015	1-5B-1	Beachmark	#47	18-249,-282	--	beachmark #9-#10 in the light microscopy color montage (initiation). The change appears to consist of going to finer fracture details.
	1-5B-1	Fracture Detail	O	18-251		
1.071	1-5B-1	Beachmark	#48	18-283	--	Note 1. Beachmarks very faint on SEM.
1.074	1-5B-1	Beachmark	#49	18-283		
	1-5B-1	Fracture Detail	P	18-254,-255, -285,-286	--	Beachmarks very faint; barely visible as a group just on the initiation side of beachmark #14 in the
1.241	1-5B-1	Beachmark	#50		--	light micorscopy color montage (initiation) Note 2.
1.247-1.248	1-5B-1	Beachmarks	#50-53		--	Possible striations in 18-286 but so faint and unusual
1.249	1-5B-1	Beachmark	#54		--	looking they are not counted.
1.260	1-5B-1	Beachmark	#55	18-255	--	Start of beachmark #14 in light microscopy color montage (initiation).
		Fracture Detail	Q	18-255,18-287	--	Beachmarks #56 & #57 combined form beachmark #15 on
1.279	1-5B-1	Beachmark	#56		--	light microscopy color montage.
1.280	1-5B-1	Beachmark	#57		--	
		Fracture Detail	R	18-257,18-288	--	Probably corresponds to beachmark #16 on light micro-
1.319	1-5B-1	Beachmark	#58		--	scopy color montage. Change in fractography is going to a finer fracture structure.
1.331	1-5B-1	Beachmark	#59	18-257	--	Probably corresponds to beachmark #17 on light micro- scopy color montage. Change in fractographic from fine to coarser structure.
1.411	1-5B-1	Beachmark	#60	18-260	--	Corresponds to starts of beachmark #18 on light micro- scopy color montage (initiation). Start at coarse frac- ture with adherent corrosion deposit.

Distance From Surface Reference Points, Inches	Specimen	Fracture Surface Feature			Striation Spacing, μ	Comments
		Type	Label	Photo		
1.514	1-58-1	Beachmark	#61	18-263,-264	--	Corresponds to beachmark #19 on light microscopy color montage (Initiation). Fracture becomes somewhat finer, smearing and much less corrosion product adherence.
1.586	6-9-4	Fracture Detail A		18-084 to-088 Montage 18-080,-084 Detail	0.10-0.15	Coarse macrotopography. Large smears. Fine feathery type fracture at high magnification.
1.814	6-9-3	Fracture Detail B		18-075 to -079 Montage 17-0985 to -089 Detail	0.17	Same as above but lateral spread of smearing seems less than Detail A.
1.916	6-9-2	Fracture Detail C		18-070 to -074 Montage 17-093 to -096 Detail	0.15	Same as Detail B above.
2.283	6-9-1	Fracture Detail D		18-063 to -067 Montage 17-097 to 18-002 Detail	0.15-0.20	Same as Detail B above.
2.553	10-13-1	Fracture Detail A		18-020 to -025 Montage 17-916 to -919 Detail	0.12-0.15	Generally same topography as in 6-9, but less smearing and possibly less relief. Same fine feathery fractography at high magnification.
2.672	10-13-2	Fracture Detail B		18-026 to -030 Montage 17-920 to -925 Detail	0.12-0.16	Same as A above in 10-13-1. Also beginning to see signs of large cleavage facets or gain faces in with feathery fracture.
2.868	10-13-3	Fracture Detail C		18-031 to -035 Montage 17-931 to -934 Detail	0.16	Same as 10-13 B above.
2.926	10-13	Fracture Detail D		17-935 to -939 Detail No Montage	0.12-0.16	Planar fracture areas at low magnification have slip band striations at high magnification.
2.947	10-13	Fracture Detail E		17-940 to -943 No Montage	--	Intergranular fracture of 5 grains surrounded by trans-granular feather structure.
3.228	10-13-4	Fracture Detail F		18-036 to -041 Montage 17-948 to -051 Detail	--	Generally flatter topography than in prior montage. Less smearing and more islands of IG and coarse cleavage in finer feather fracture background.

Table 5, continued

Distance From Surface Reference Points, Inches	Specimen	Fracture Surface Feature			Striation Spacing, μ	Comments
		Type	Label[4]	Photo		
3.250	10-13-5	Fracture Detail G		18-046 to -50 Montage 18-042 to -045 Detail	--	Same as for Detail F. High magnification clearly shows continuity between feather and IG fractography. IG face appear to have arrest marks in some locations.
3.448	14-16	Fracture Detail A		17-898 to -900 No Montage	--	Island of IG fracture involving 9 grains. Some secondary IG cracking. Surrounded by feathery structure. Some smearing at elevated grain boundary corners. One face has coarse linear markings with a spacing of 0.6μ. Generally more IG showing up than on 10-13.
3.528	14-16-1	Fracture Detail B		18-098 to 102 Montage 17-092 to -097	--	Same as above for 14-16 Detail A.
4.00	14-16-2	Fracture Detail C		18-107 to 18-111 Montage 18-103 to 106 Detail	--	Same as above for 14-16 Detail A.
4.25	17-20	Fracture Detail A		17-901 to -903	.13	
4.368	17-20-1	Fracture Detail B		18-015 to -019 Montage 17-905 to -908	.28	Basically same fractography as seen in 14-16 but less amount of IG or coarse cleavage. Small amounts of smearing.
4.655	17-20-2	Fracture Detail C		18-003 to -014 Montage 17-909 to -912 Detail	.27 to .35	Same as above for Detail B.
4.751	--	Fracture Detail D		Just below Montage in C 17-913 to 915 Detail	--	Laboratory forced fracture.

Note 1   Beachmark not visible on light microscopy color montages.

2   Beachmark characterized by a change to much finer cleavage and river pattern network over a short distance.

3   Reference points shown in Figure 3.3-14. Reference point "A" used for specimen 1-5B-1; reference point "B" used for specimen 1-5B-2; reference point "C" used for 6-9, 10-13, 14-16, and 17-20.

4   Label on SEM fractography montages.
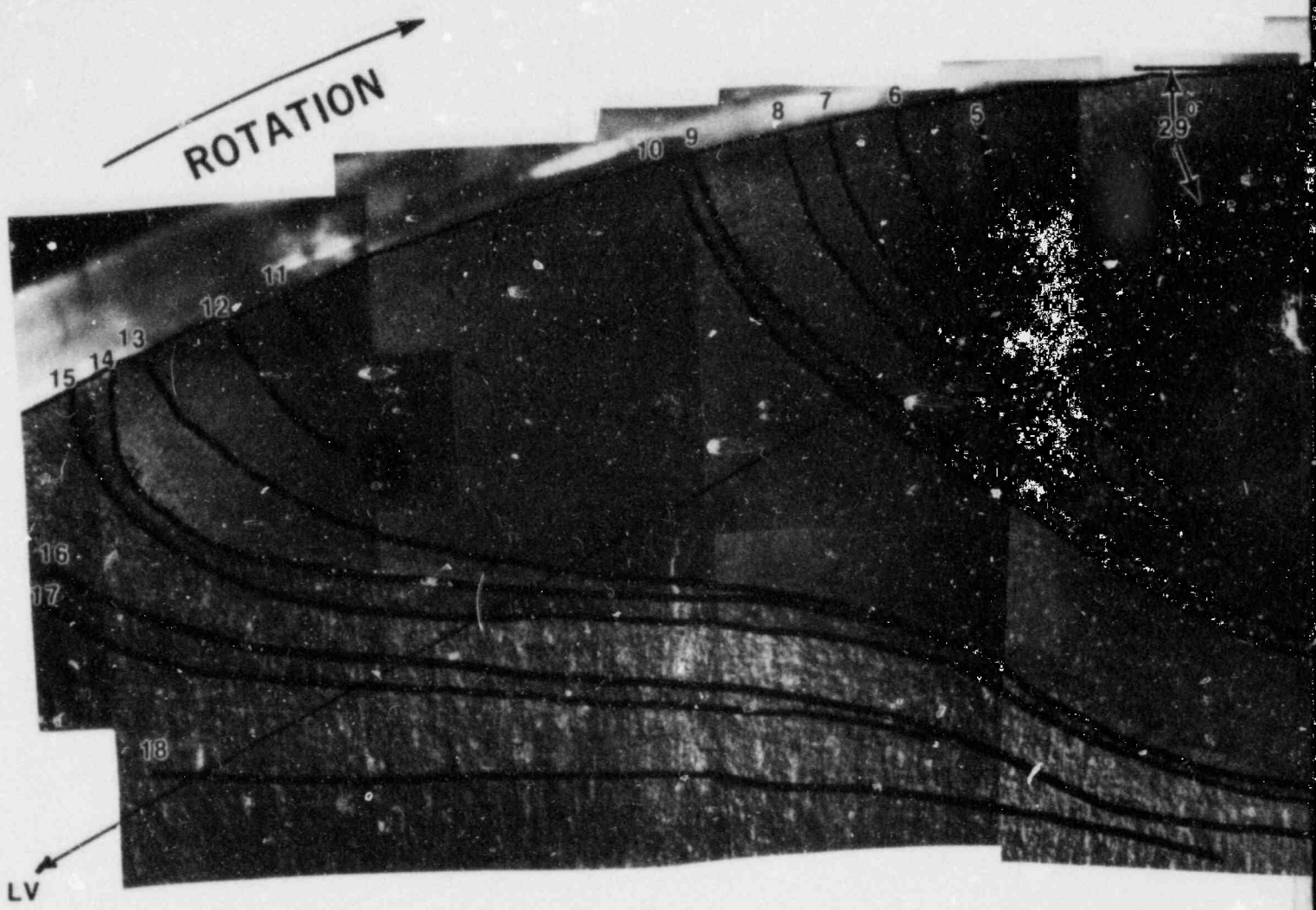
Figure 3.3-2. Initiation
A. As-
B. Overla

TI
APERTURE
CARD
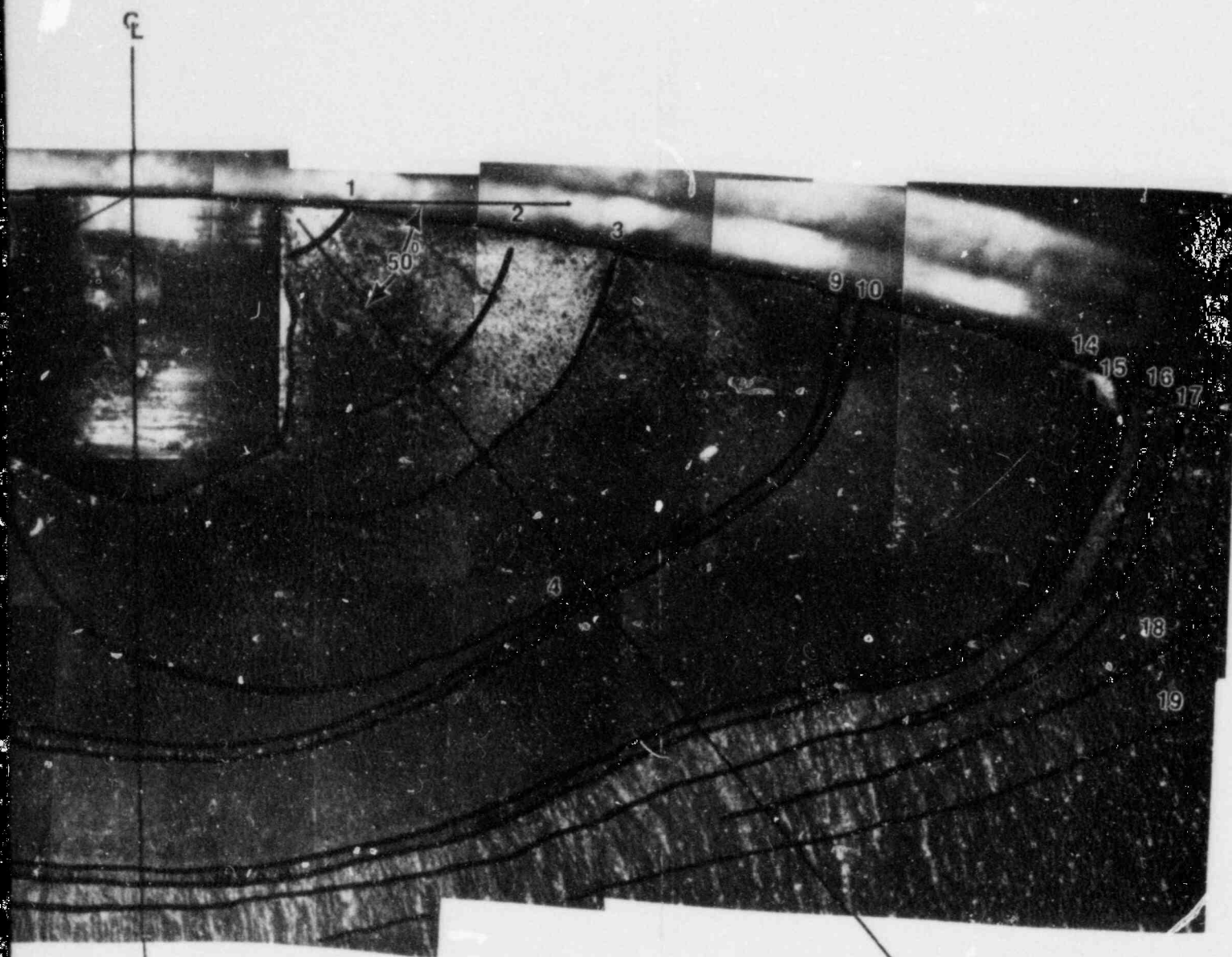
1/4 INCH

Region on Shaft Fracture Surface
ctured
With Beachmarks Emphasized

8410170270 -05
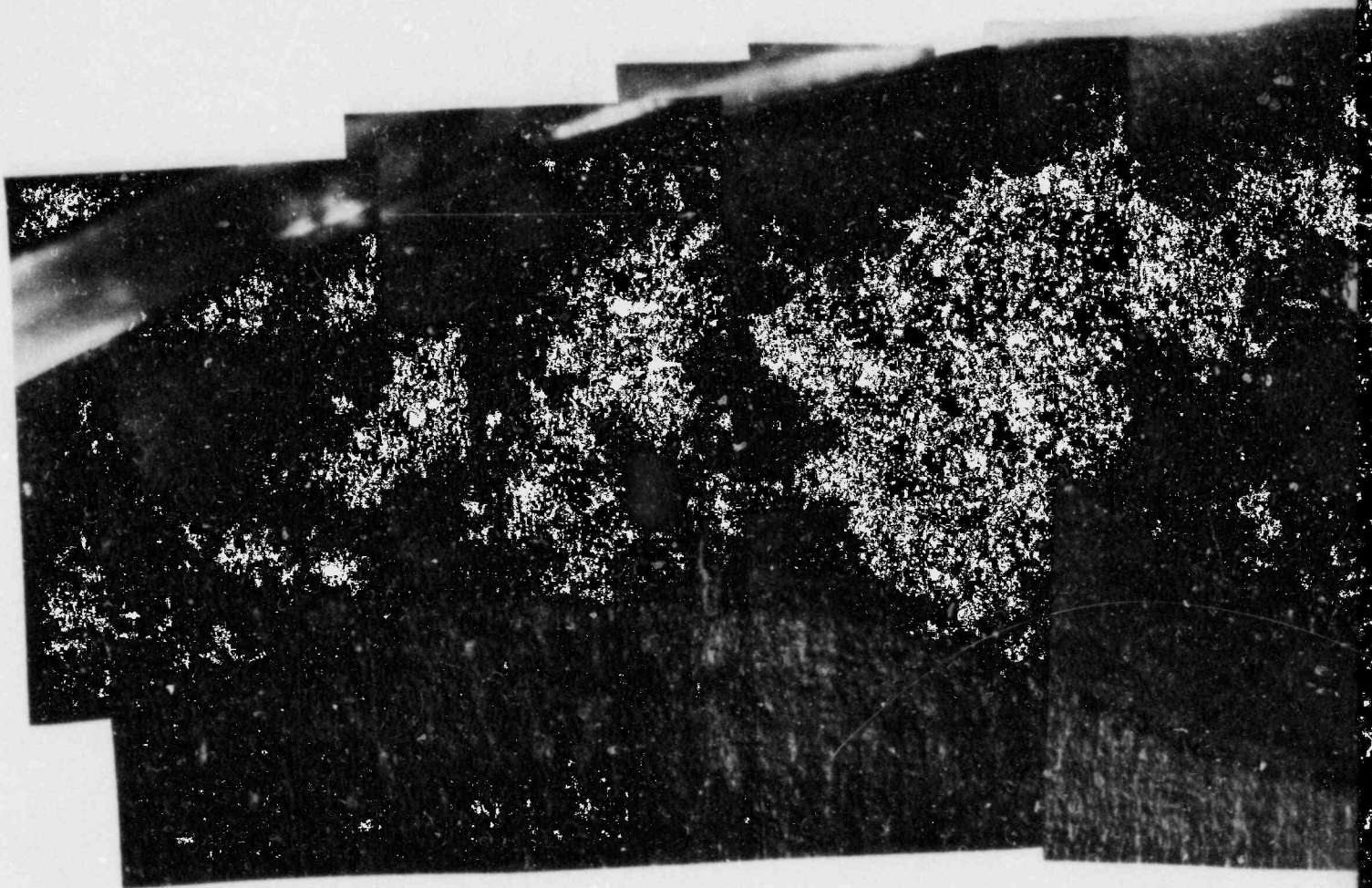
Figure

Also Available On
Aperture Card
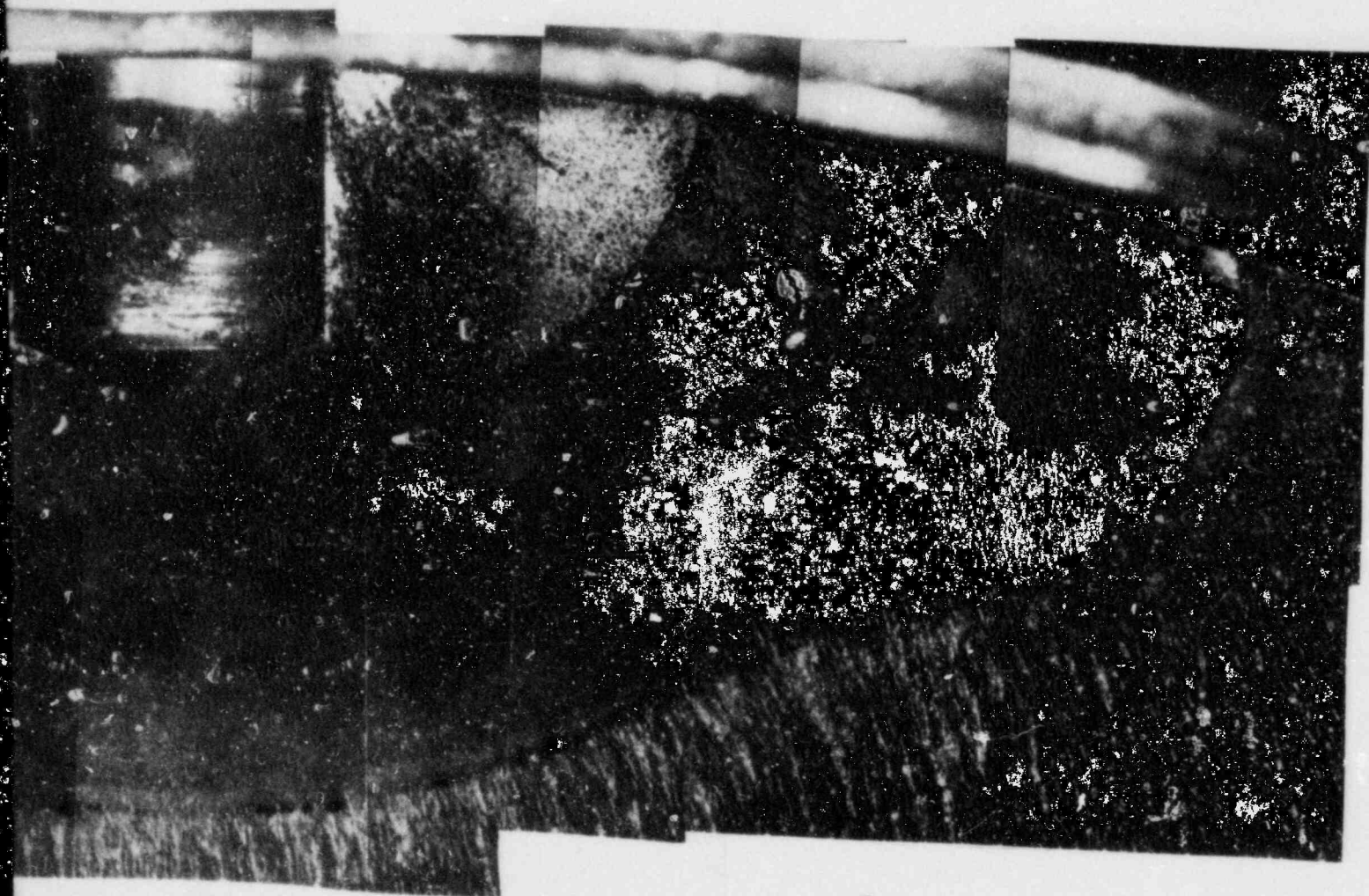
3.3-2, continued

TI
APERTURE
CARD

Figure 3.3-3. Fractur
A. As-
B. Ove

Also Available On
Aperture Card
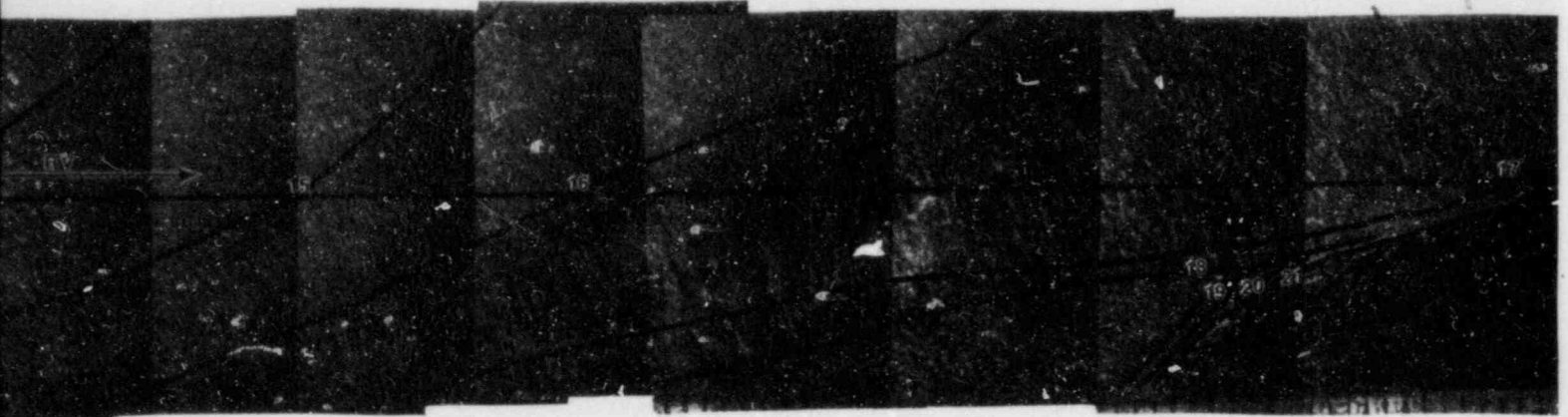
1/4 INCH

e Examination Path
Fractured
rlay With Beachmarks Emphasized

TI
APERTURE
CARD
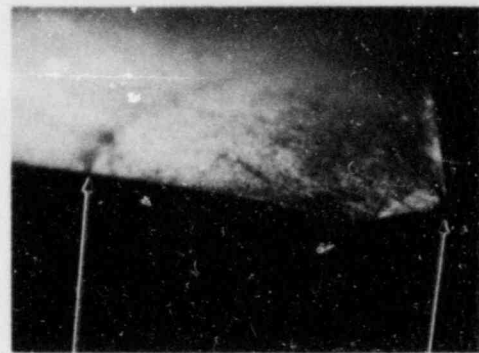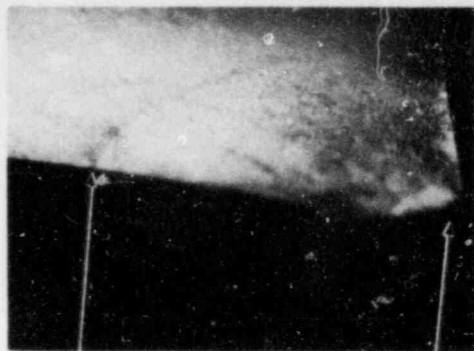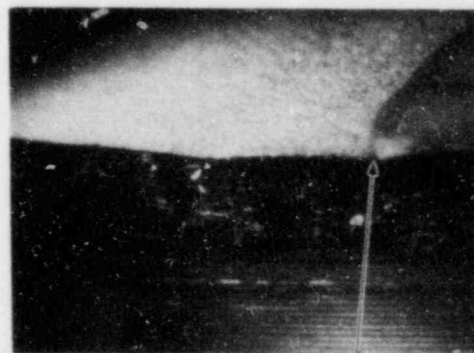
Figure 3.3-4. Views of Crack Path Changes Relative
to Fracture Surface Beachmarks

D

PIN HOLE OCTANT 8
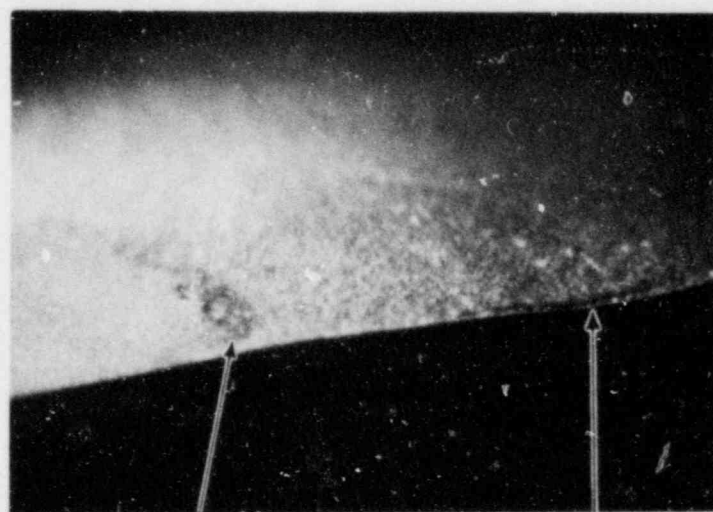
E

BEACHMARK 15 OCTANT 8   BEACHMARK 18 19

Figure 3.3-4, continued
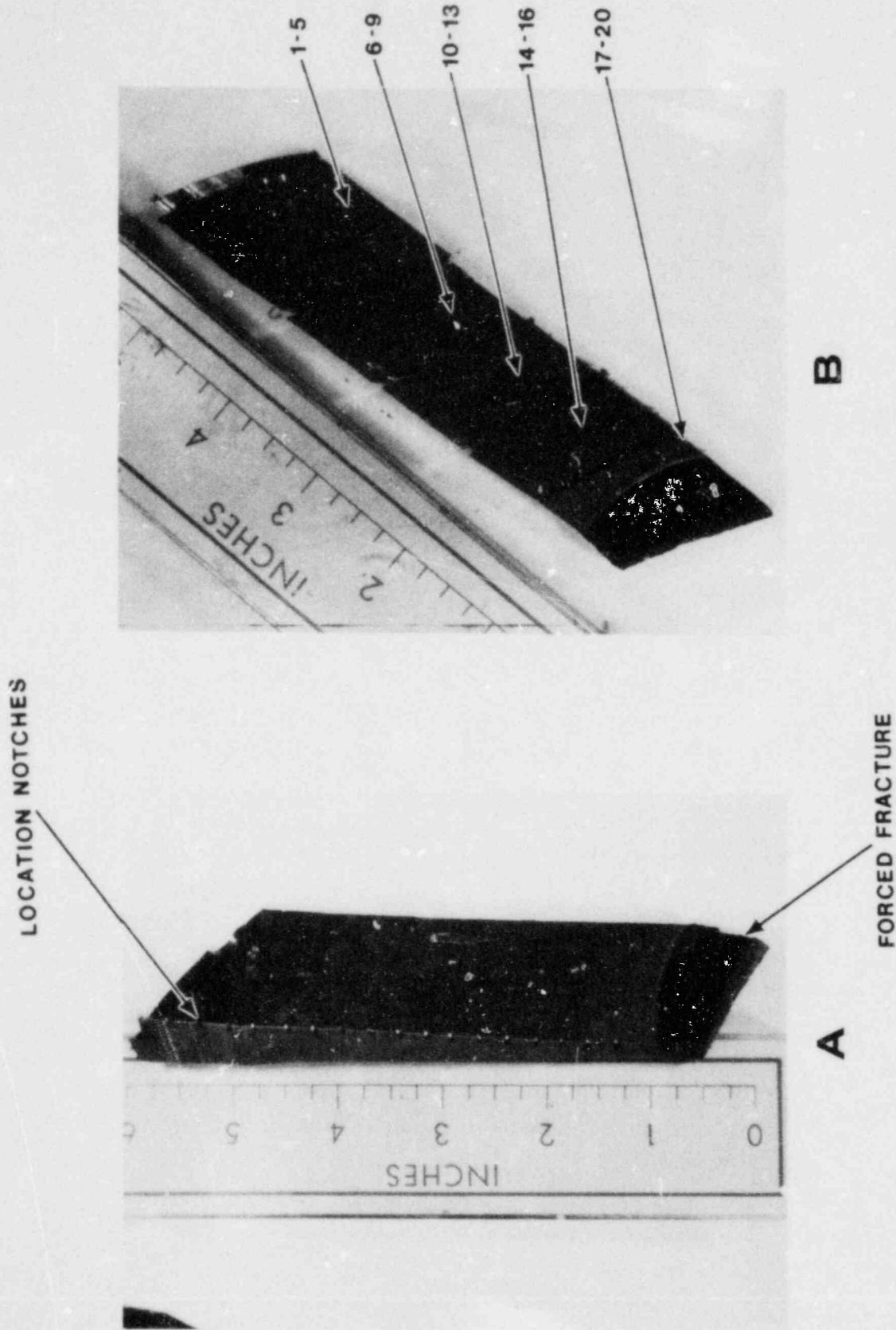
Figure 3.3-5. Specimen B1A1 Preparation for Examination
A. Notches Placed Every 1/4" at Edge
B. Subdivision Into Fractography Specimens
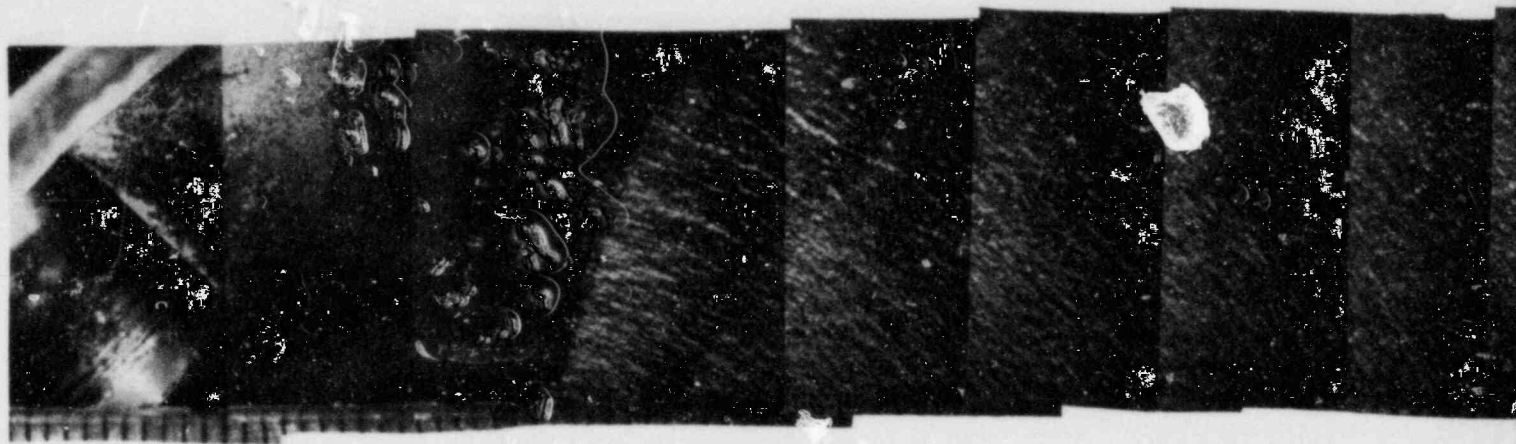
Figure

Also Available On
Aperture Card
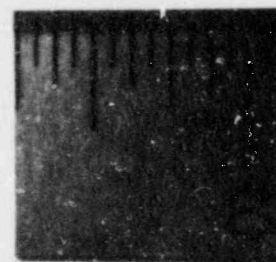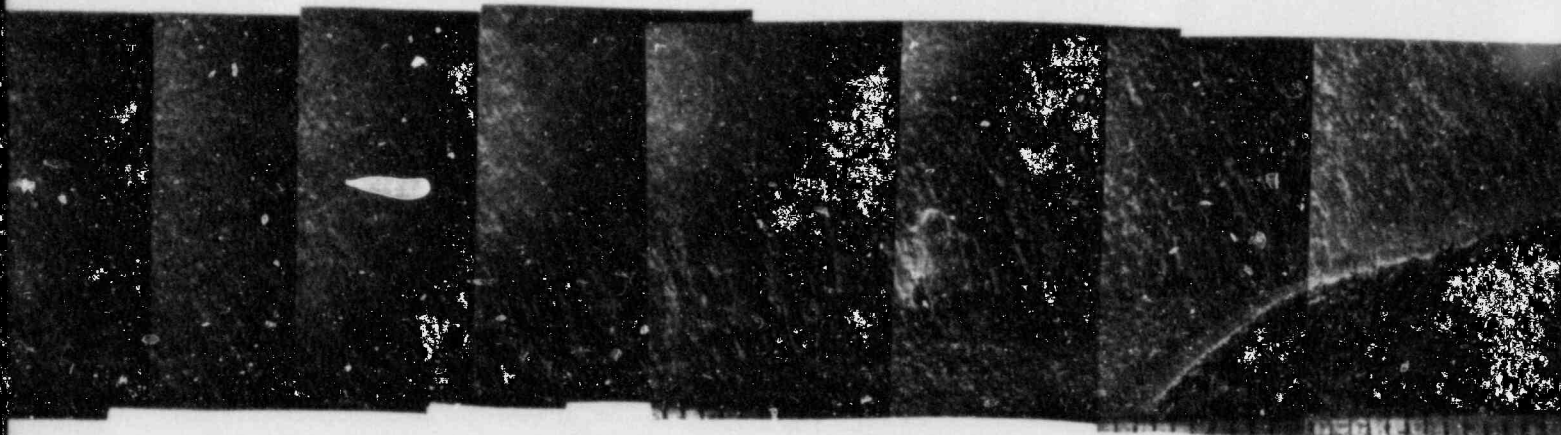
3.3-3, continued

TI
APERTURE
CARD

SMEARED RIDGES

START OF
COARSE
TOPOGRAPHY

END OF SPECIMEN 1-5

BEACHMARK 15
PITTING
ARRAY
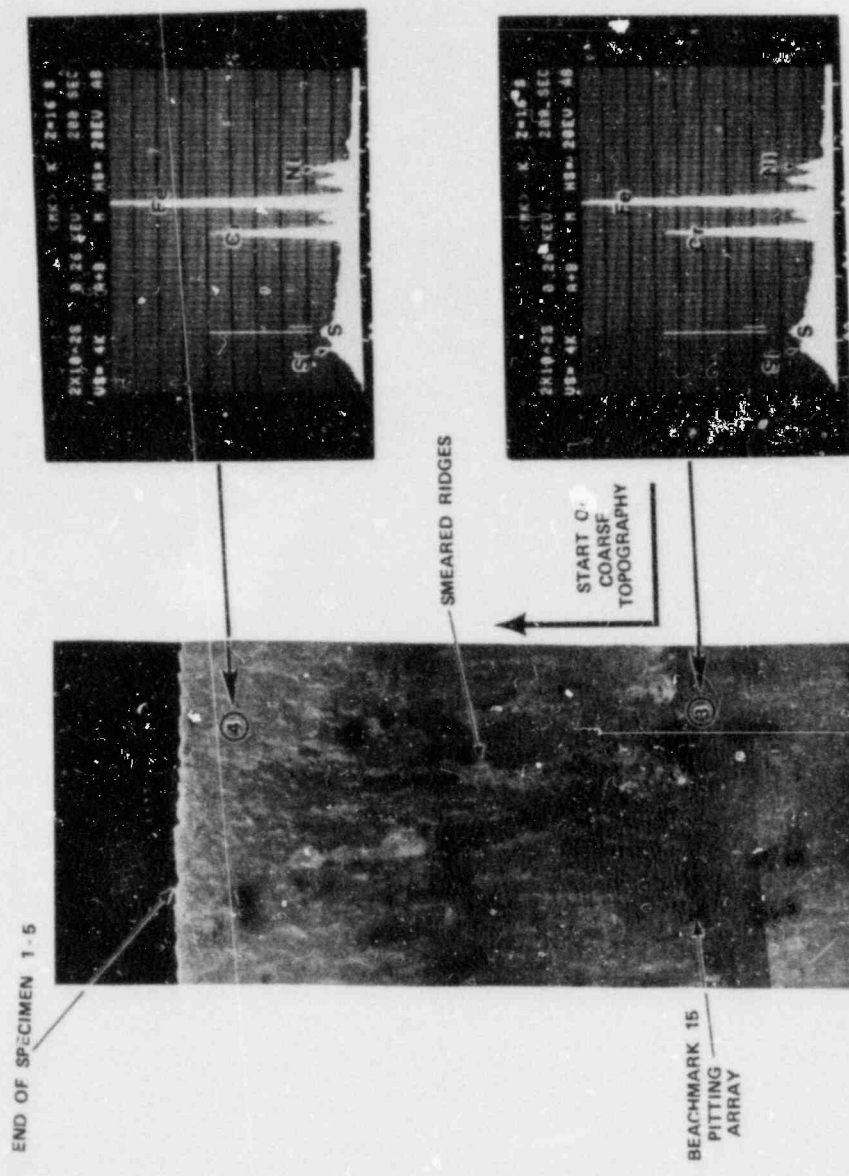
Figure 3.3-6. Low Magni
to Cleani
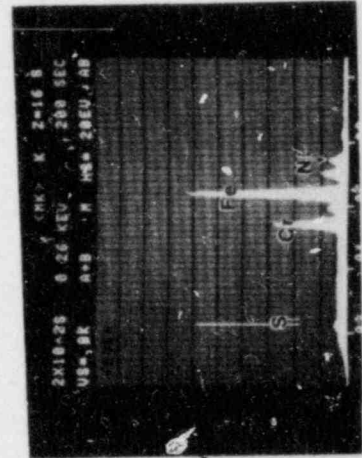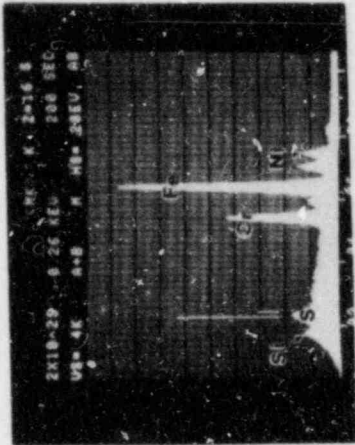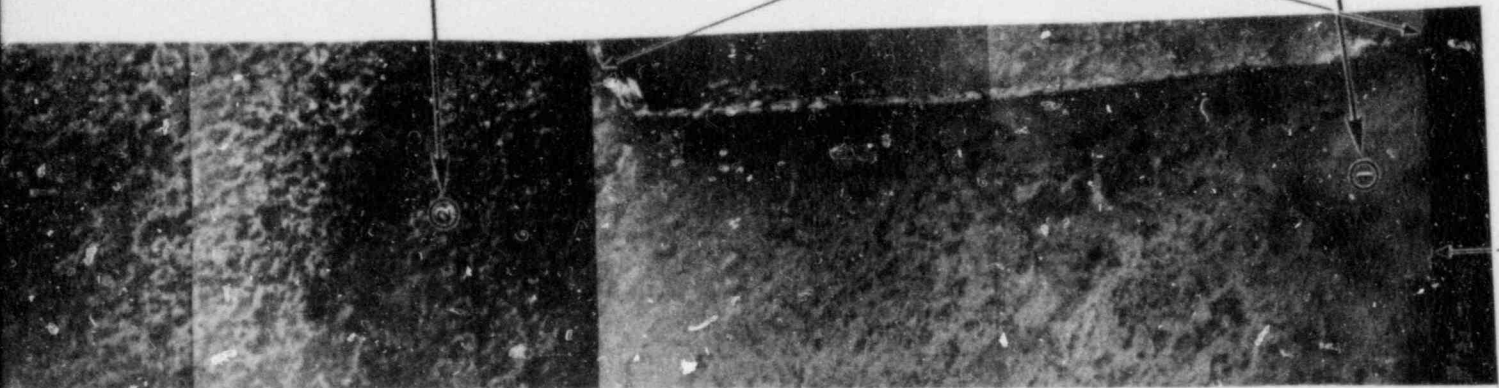
fication SEM Montage of Specimen 1-5 Prior
ng EDS Spectra Taken at Several Locations

TI
APERTURE
CARD

8410170270 -09
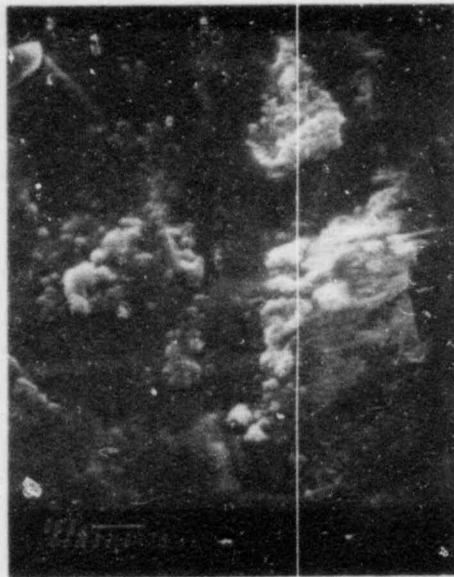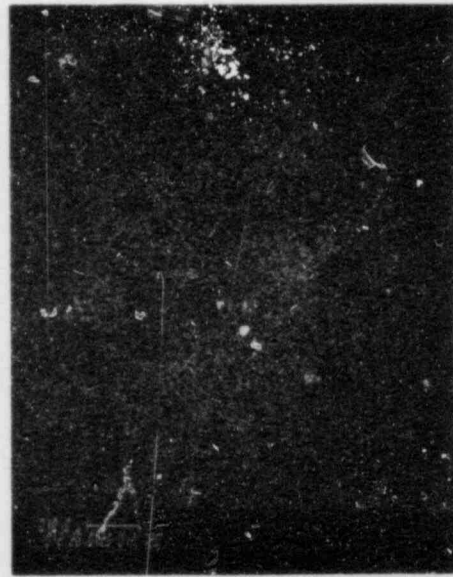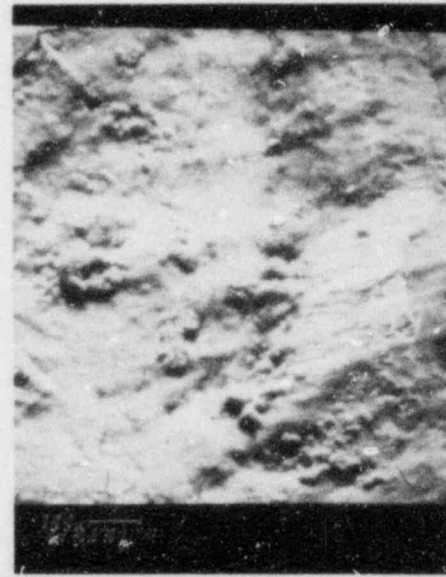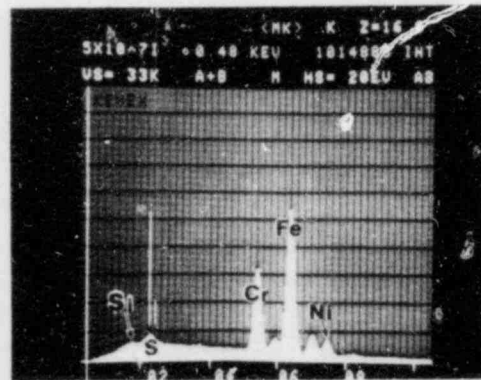
Figure 3.3-7. Typical Surface Film Structure in Specimen 1-5
A. Secondary Electron Image, B. Sulphur Dot Map
C. Backscatter Electron Image, D. EDS Spectrum of Film

SHAFT ROTATION DIRECTION

A

RIDGE VALLEY

SMEARED RIDGES

PITTING
ARRAY AT
BEACHMARK #15

A

A

A

TO SHAFT OUTER SURFACE
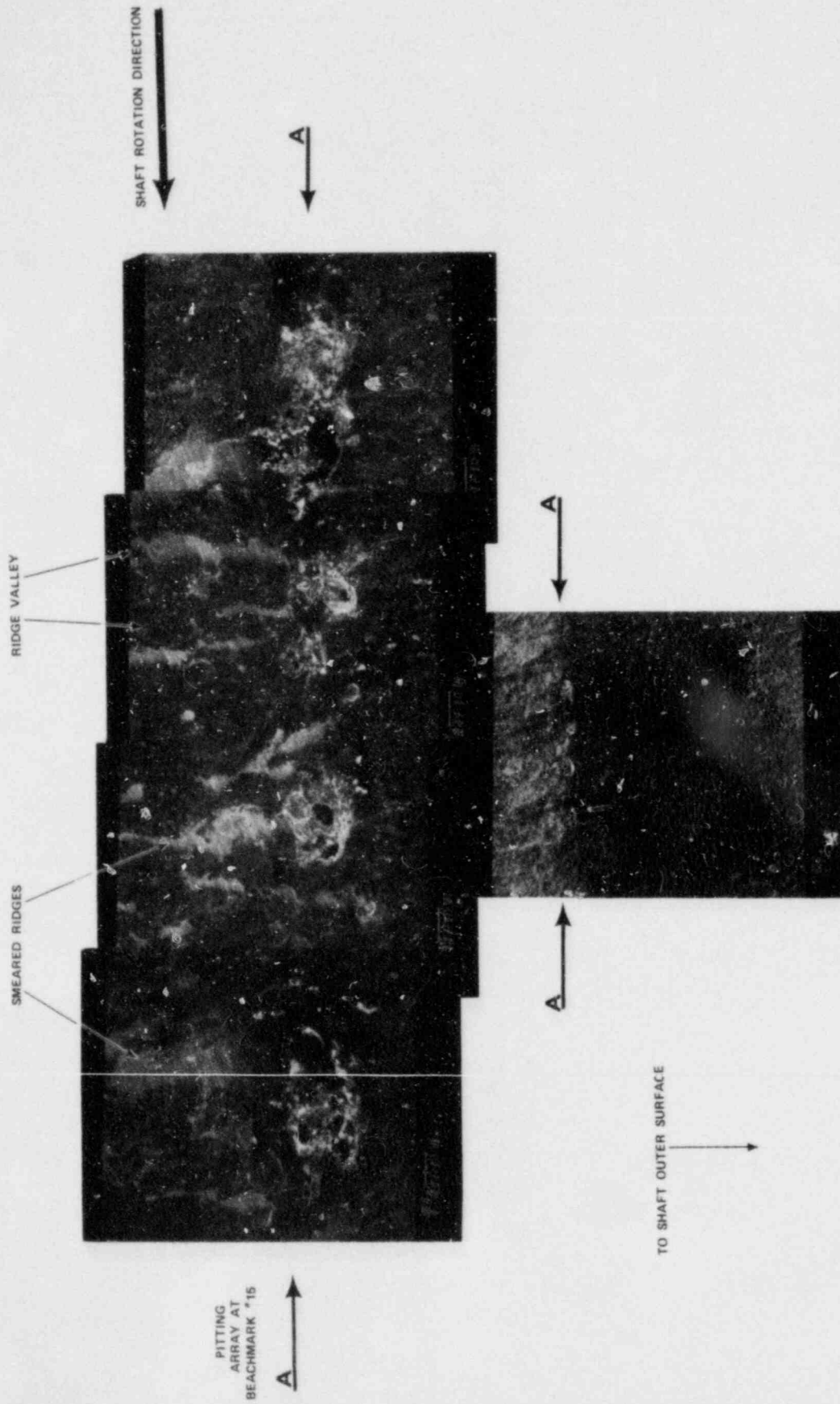
Figure 3.3-8. Transition From Flat Fracture Surface to Ridge
and Valley Structure at Pitted Beachmark #15
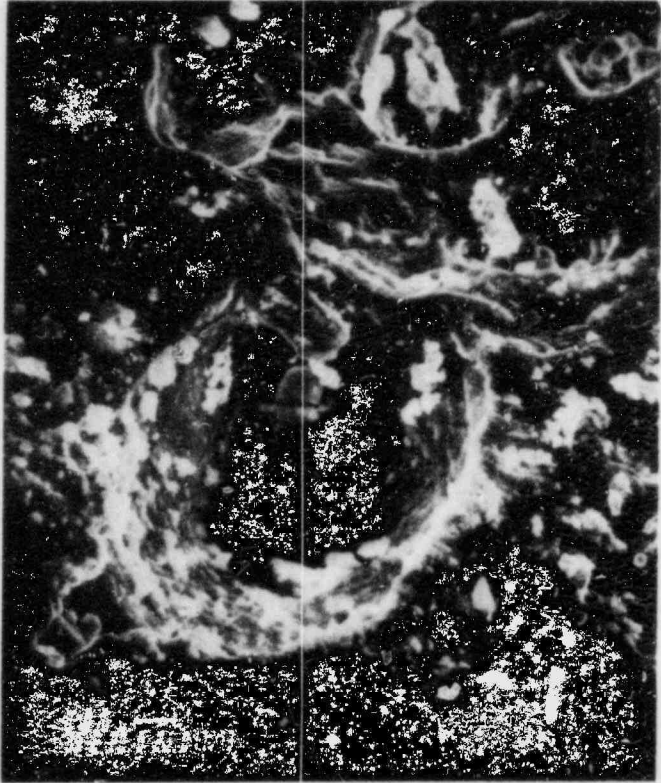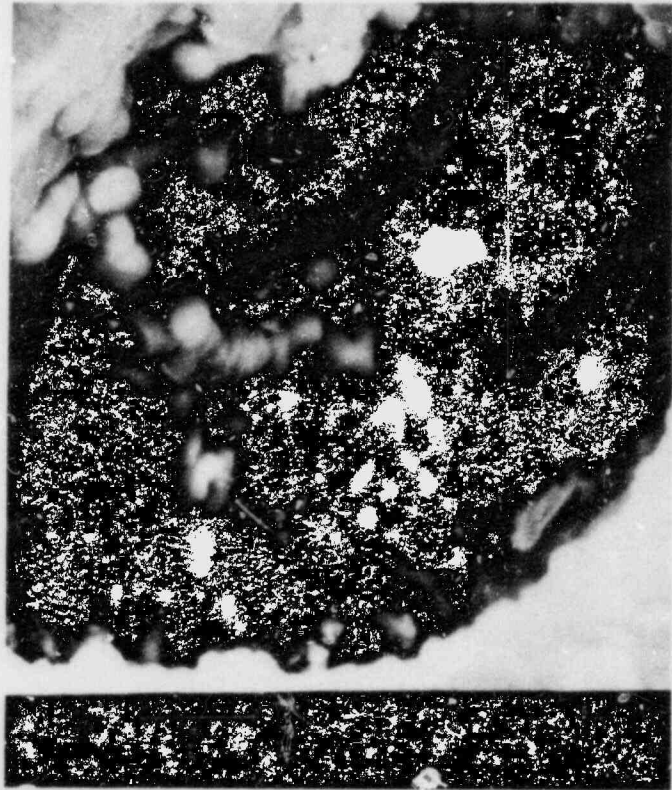
Figure 3.3-9. Appearance of Pits at Beachmark #15 Prior to Cleaning
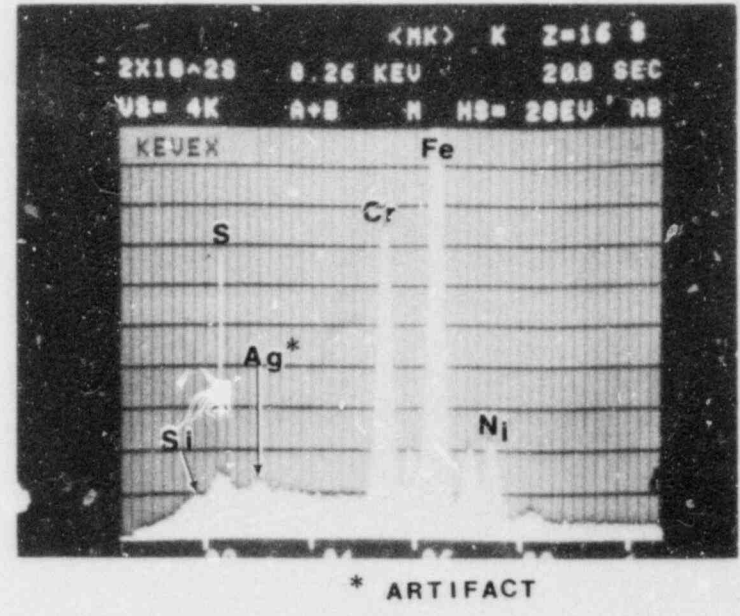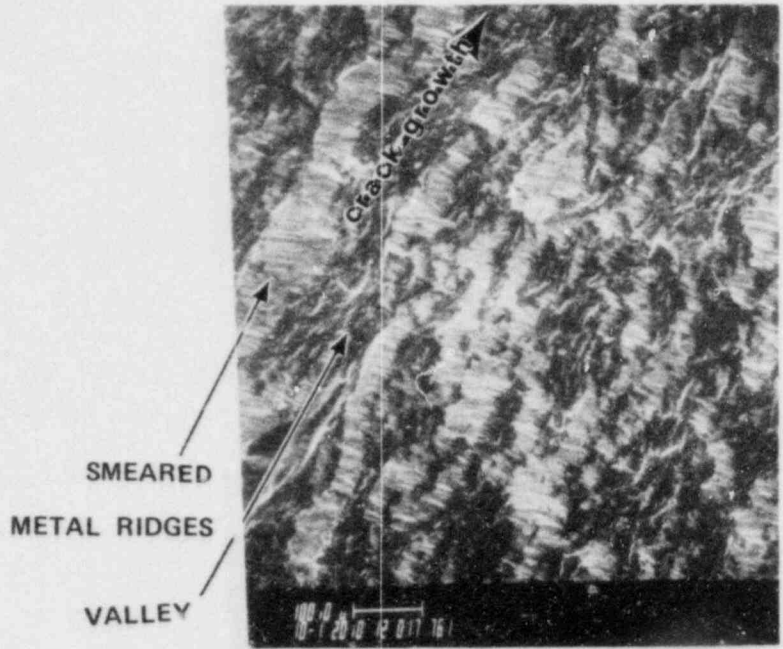
Figure 3.3-10. Ridge and Valley Structure on Specimen 6-9.
Examination Prior to Cleaning, Overall EDS
Spectrum Showing Sulphur
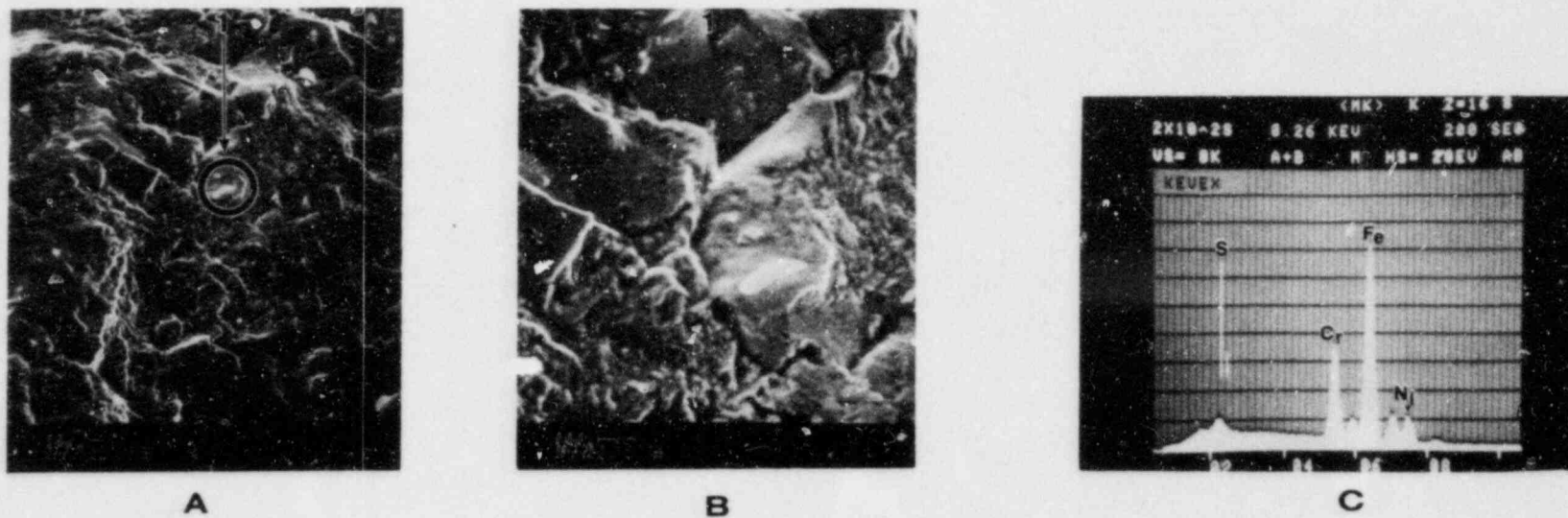
Figure 3.3-11.   Faceted Structure in Fractographic Features of Specimen 10-13
A.   General View of Facet Islands, B.   Enlarged View at 1
C.   EDS at Spectrum Location 1

A
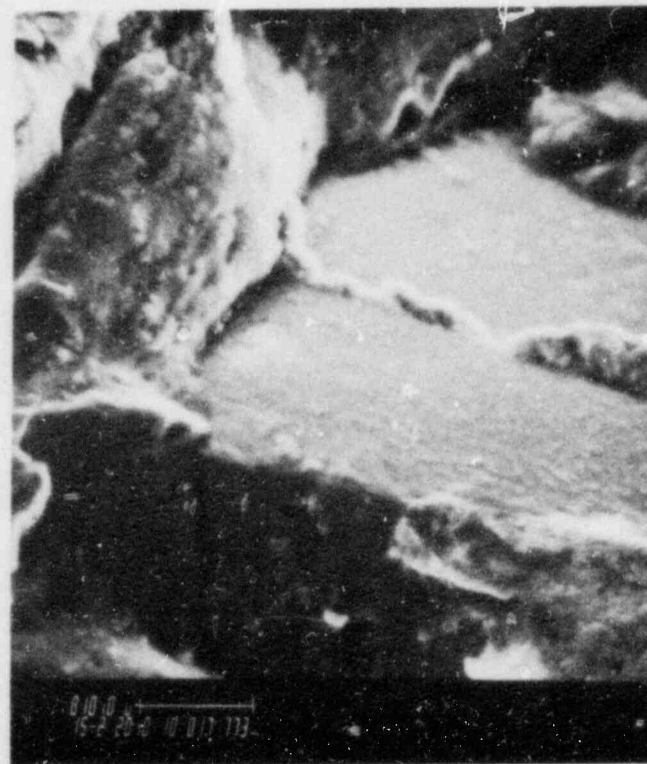
B

Figure 3.3-12.   Typical Faceted Structure on Specimen 14-16
Prior to Cleaning. A and B are General
Views. C and D are EDS Spectra of B
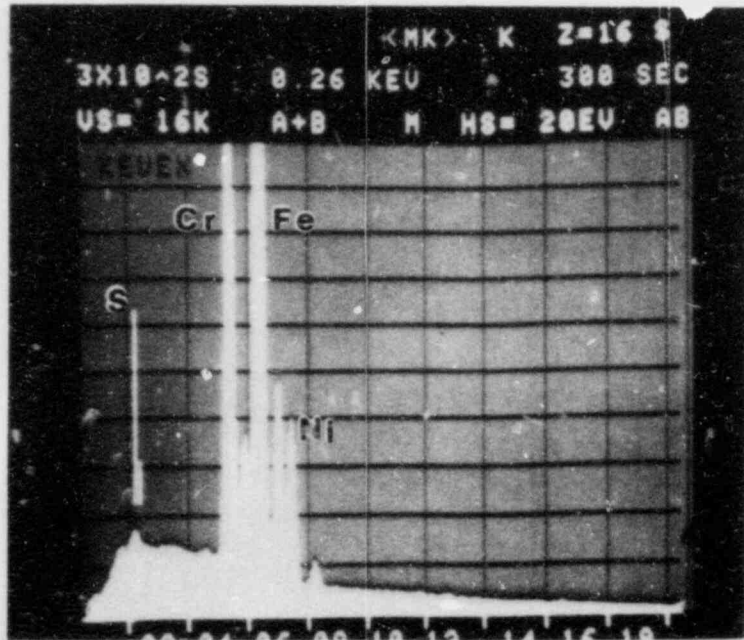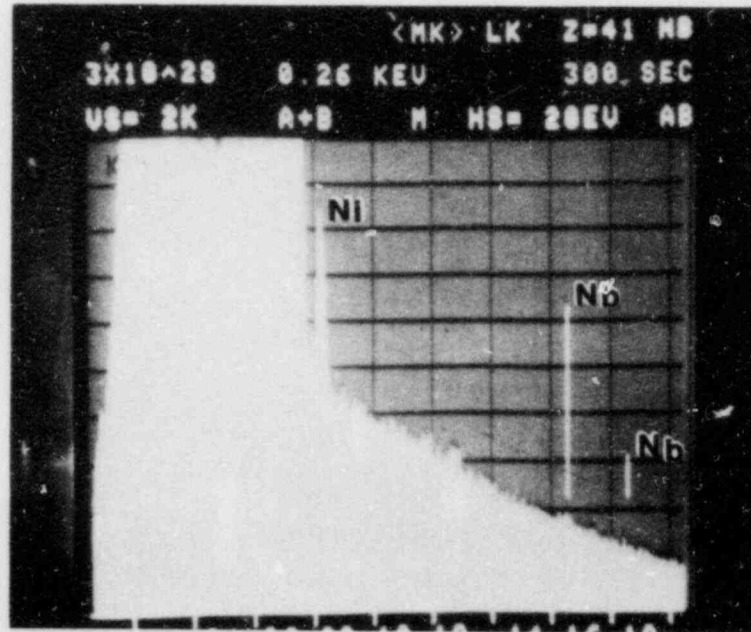
Figure 3.3-12, continued

FORCED
FRACTURE

SERVICE
FRACTURE
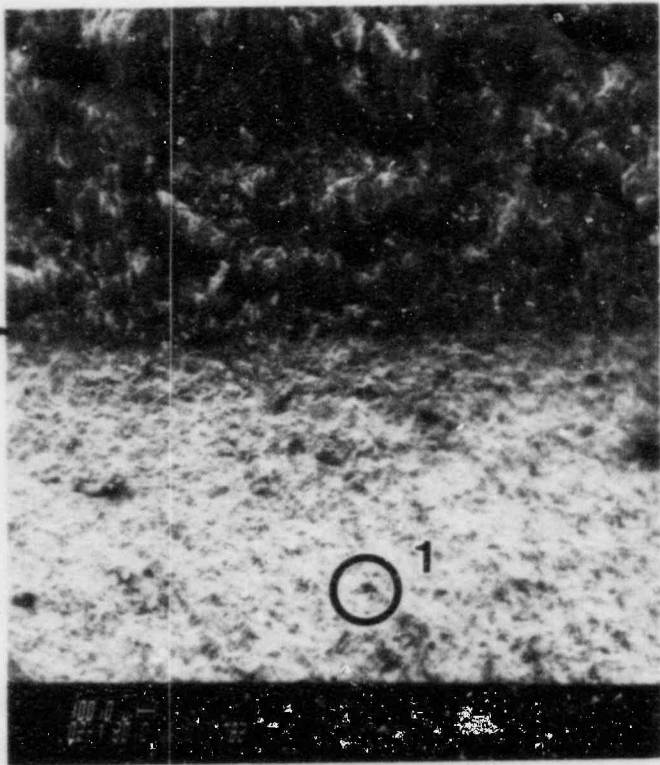
A

B

Figure 3.3-13.   Typical Fracture Structure on Specimen 17-20.
B Shows Enlarged View of Location 1 in A

REFERENCE POINT c

REFERENCE POINT b

1 - 5B - 1 M

EXAMINATION PATH START
REFERENCE POINT a

1 - 5B - 1

1 - 5A - M

1 - 5 - 2

6 - 9 A

6 - 9 B

10 - 13 A

10 - 13 B

14 - 16 A

14 - 16 M

14 - 16 B

17 - 20 A

17 - 20 B

EXAMINATION PATH STOP

$\vdash\!\!\leftarrow \frac{1}{2} \text{IN} \rightarrow\!\!\dashv$
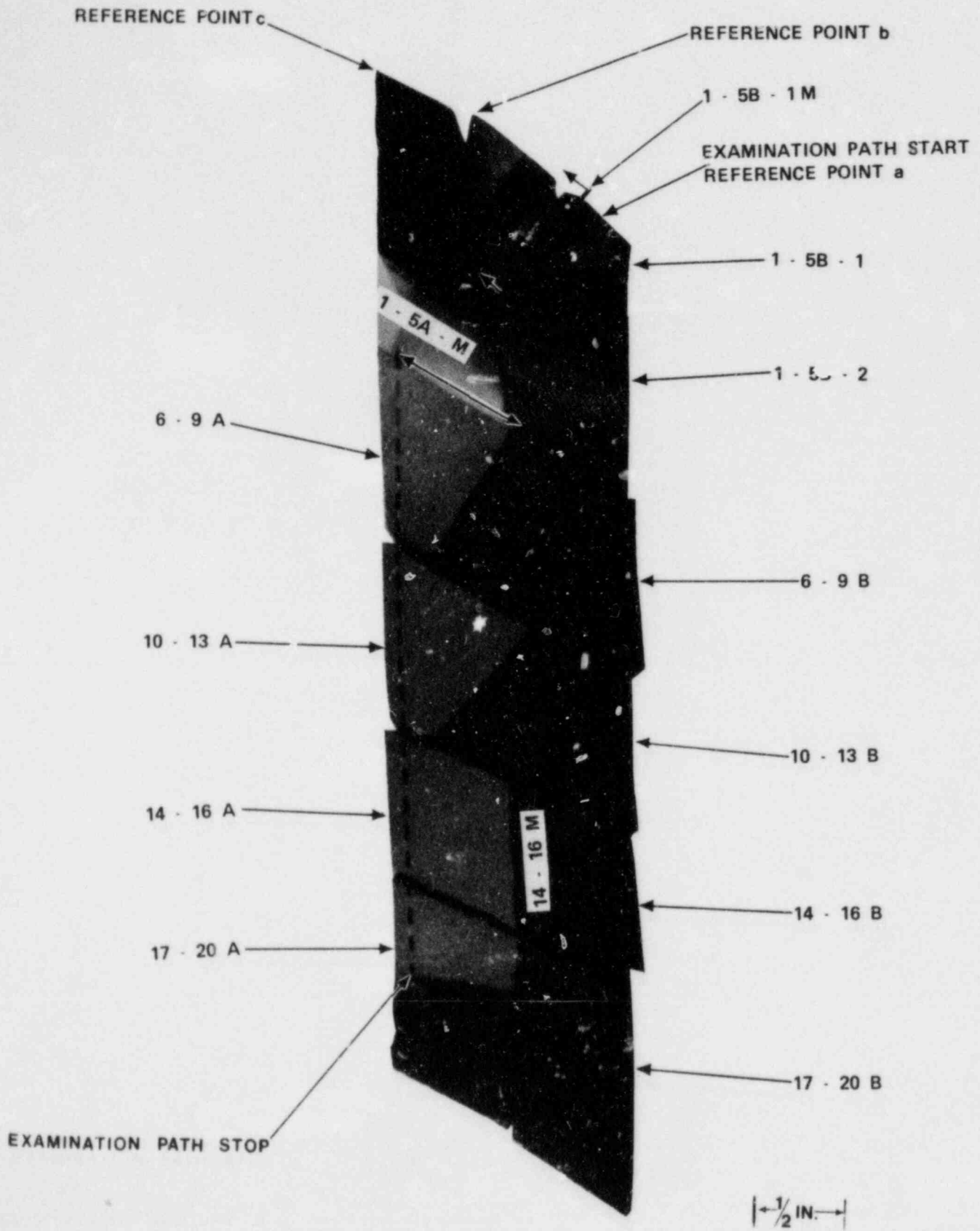
Figure 3.3-14.   Section B1A1 Reconstructed
From Individual Specimens
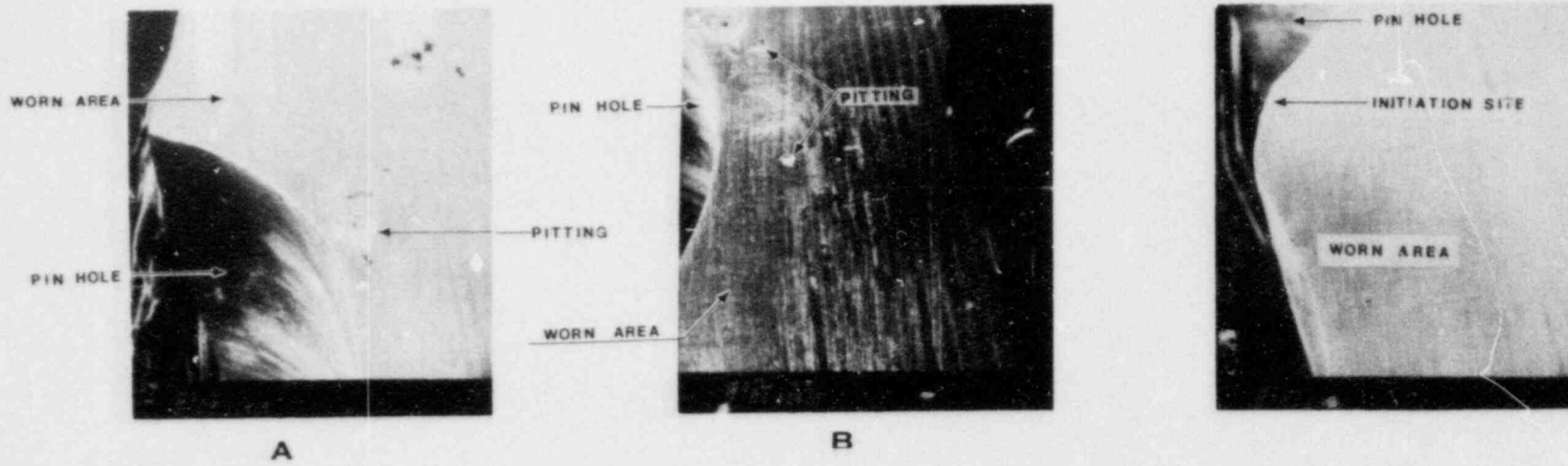
Figure 3.3-15. Shaft Surface Condition Near Cracked Pin Hole. View
A on Octant 8 Side; B in Octant 81, Boundary; C on
Octant 1 Side
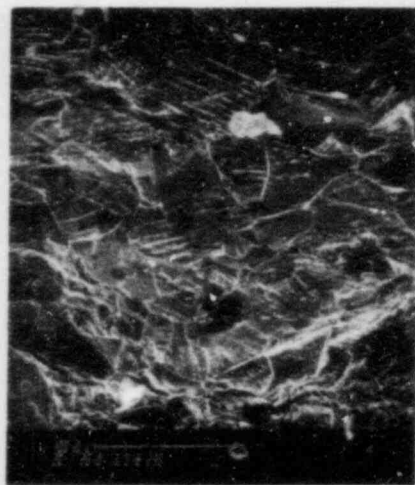
A   B   C

Figure 3.3-16. Typical Pit Structure Seen Near Cracked Pin
Hole on Shaft Outer Surface. Views A, B, C
Show Structure at Increasing Magnification

A
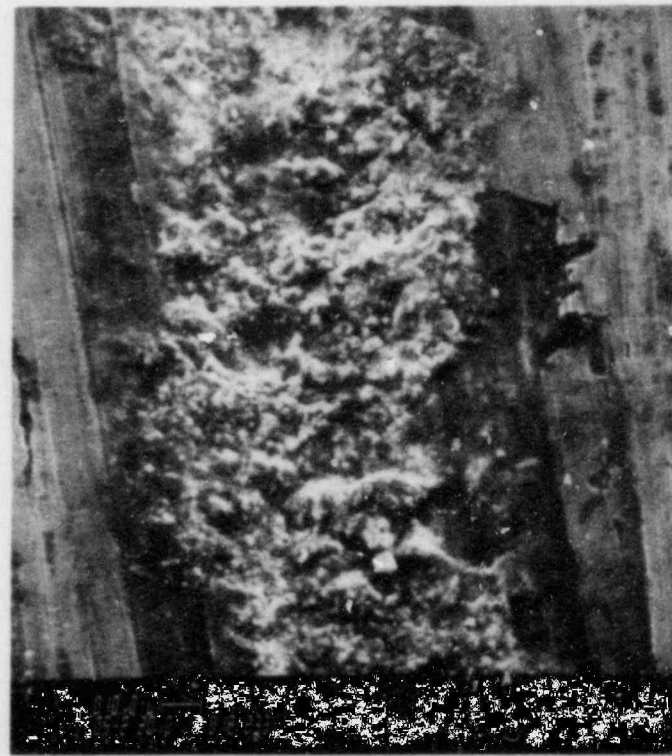
B

Figure 3.3-17. Debris or Corrosion Product Accumulation in Coarse Machine Marks
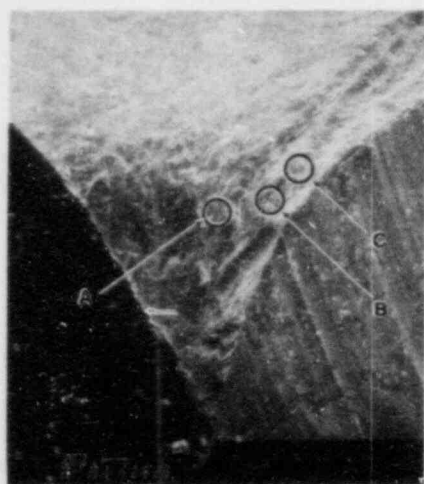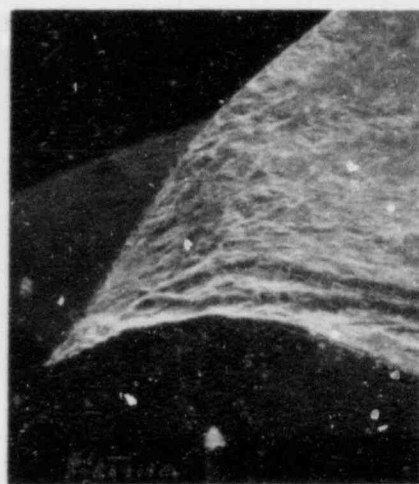
Figure 3.3-18.   SEM Photomicrographs of Initiation
Site from Different Angles
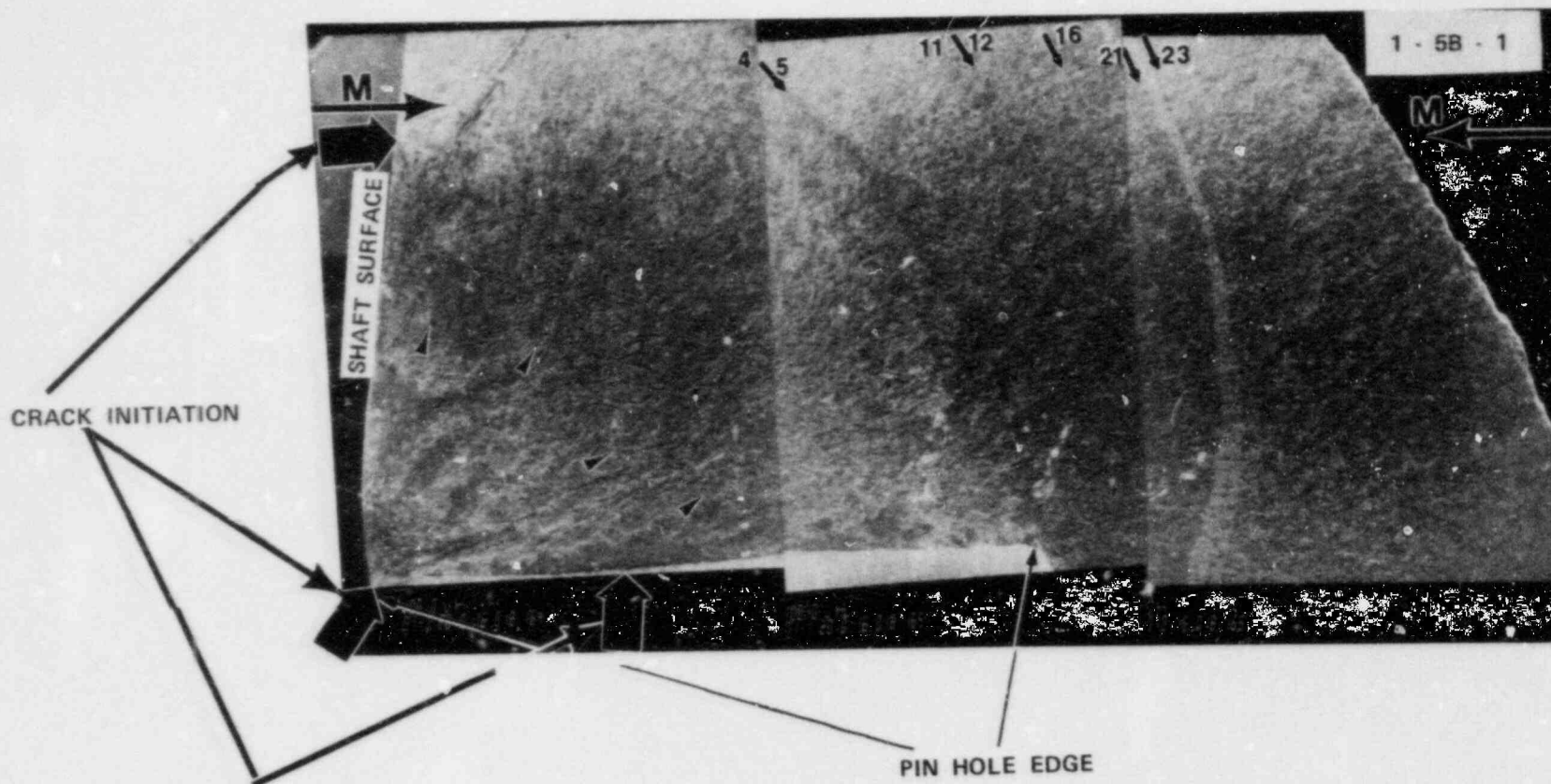
Figure 3.3-19. SEM Photomontage of Crack Initiation Area and
Examination Path Along Line M-M. Prominent
Crack Arrest Marks Seen by SEM Are Numbered
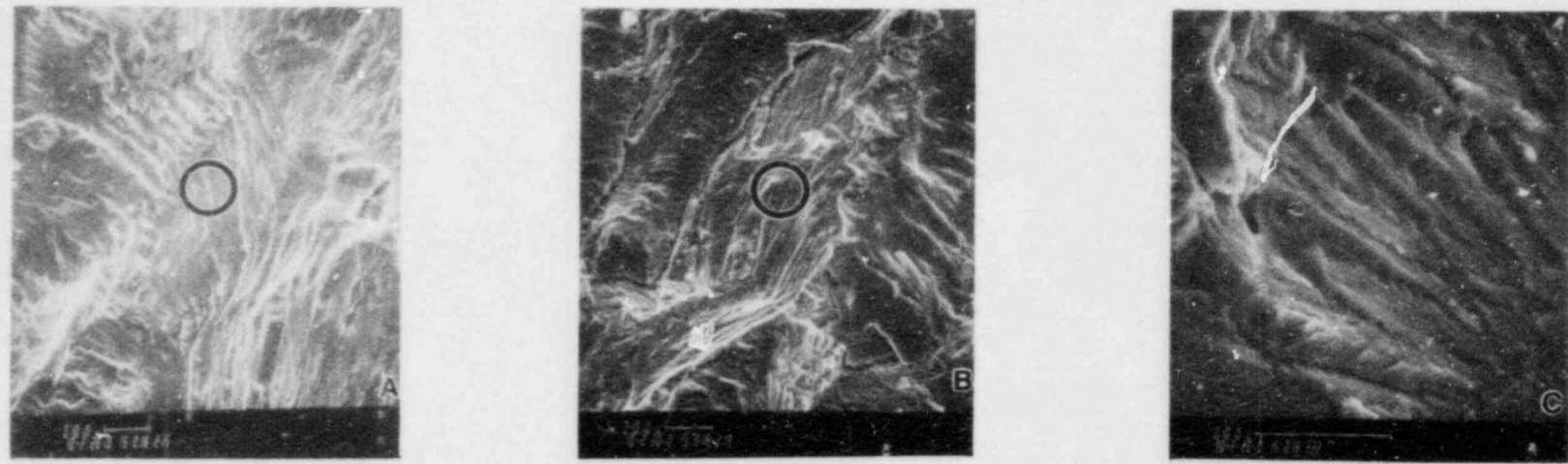
Figure 3.3-20. Typical Fractography in Crack Initiation Area. Locations A, B, and C Show in SEM Views of Initiation Area

Figure 3.3-21. SEM Photomontage of Specimen 1-5B-1
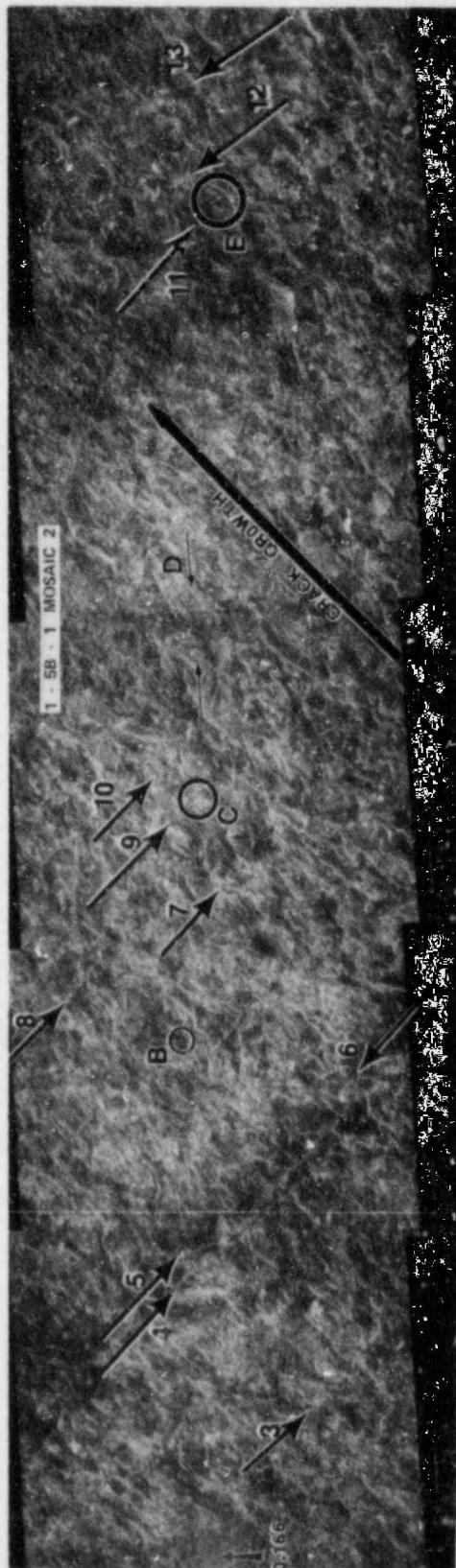
B

Figure 3.3-21, continued
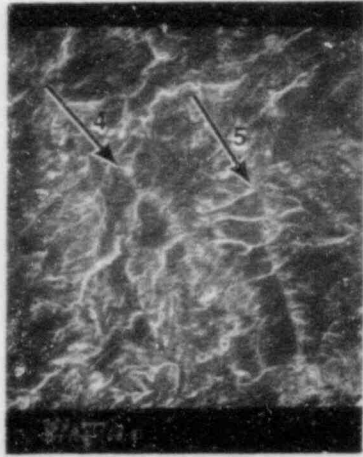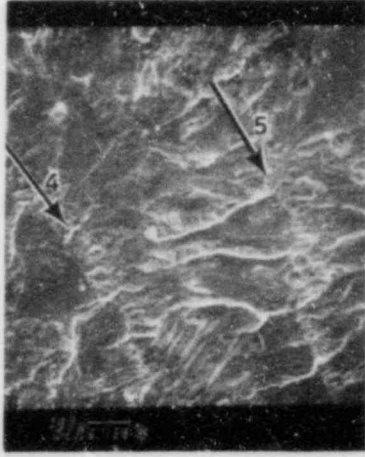
Figure 3.3-21, continued

Figure 3.3-22. Typical Fractography Features on Specimen
1-5B-1. Letters and Numbers on Photomicro-
graphs Refer to Previous SEM Montage
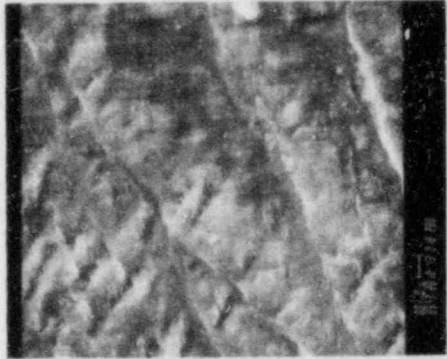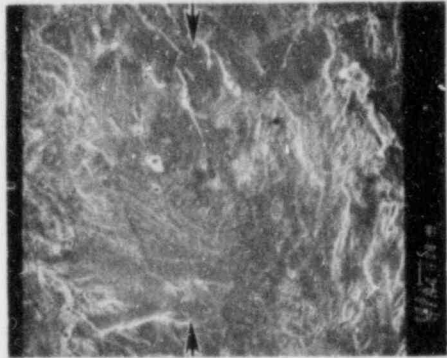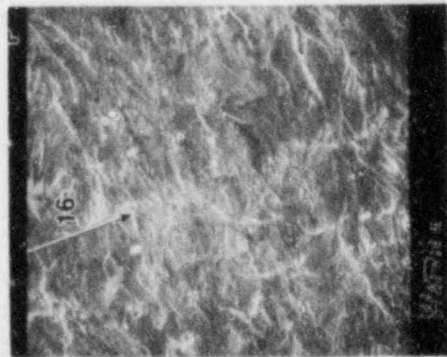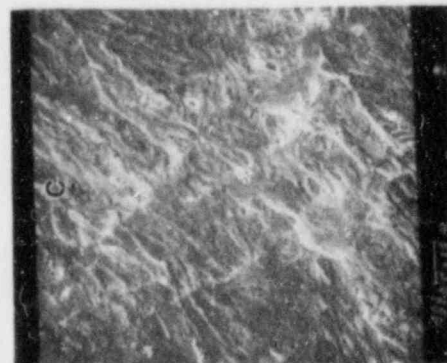
Figure 3.3-22, continued
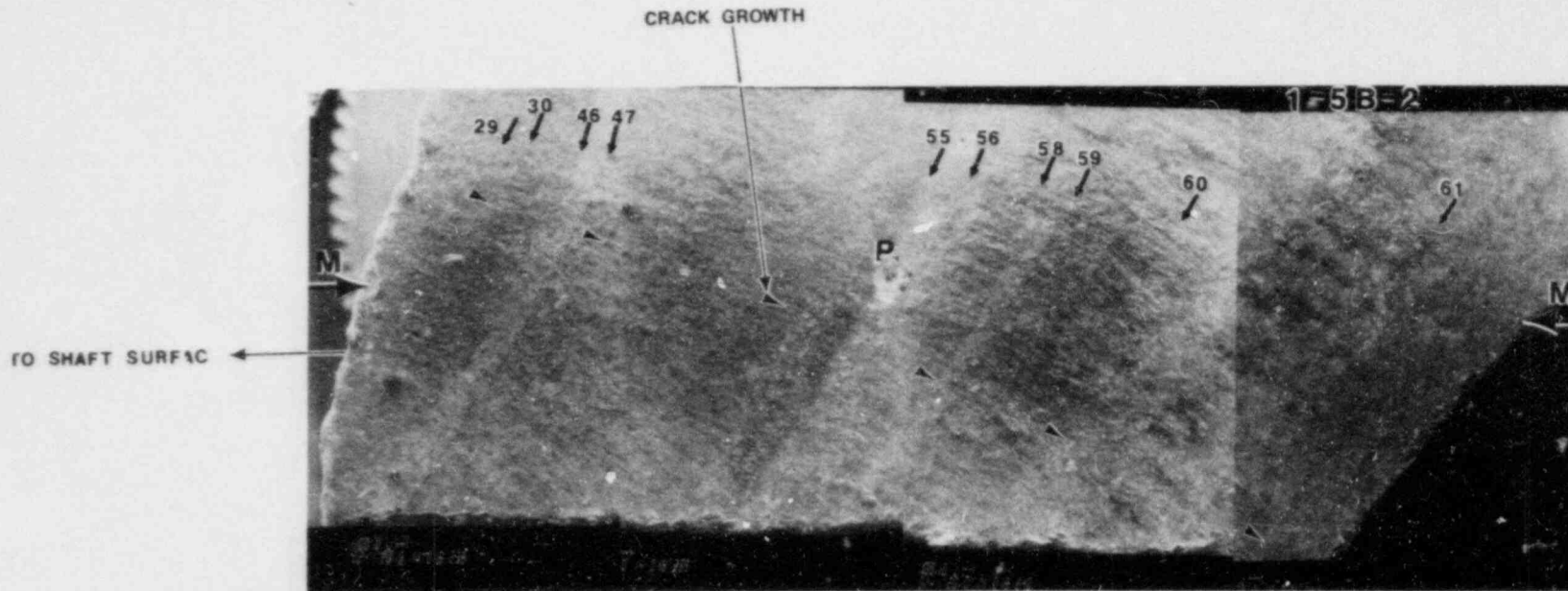
Figure 3.3-23.   SEM Photomontage of Specimen 1-5B-2.   Frac-
ture Examination Along Line M-M.   Prominent
Crack Arrest Marks Are Numbered
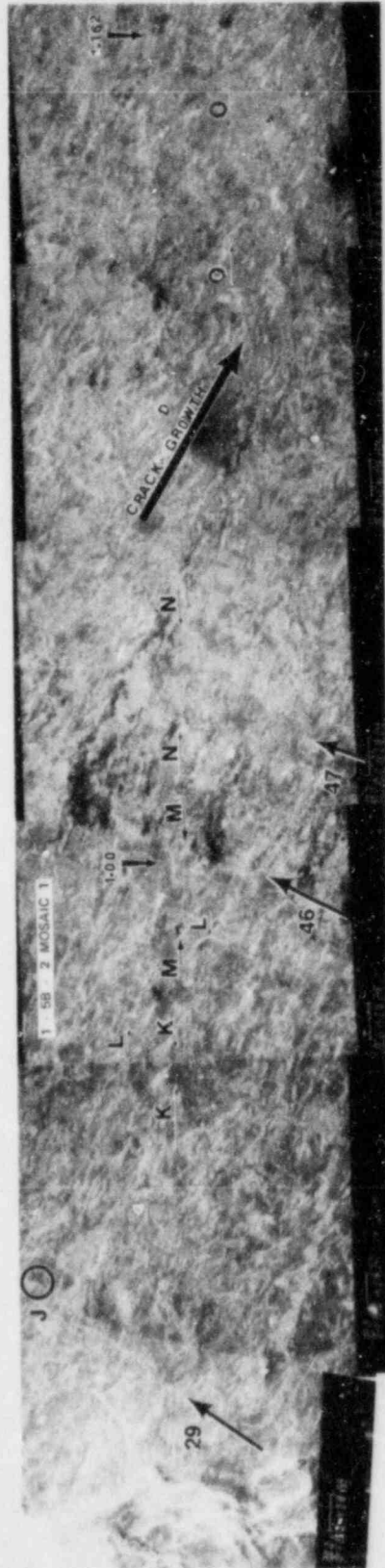
Figure 3.3-24. SEM Photomontages of Fracture Along Line M-M on
Specimen 1-5B-2
A. Montage 1, B. Montage 2, C. Montage 3, Pitting
Near P on Montage 2, D. Montage 4, E. Montage 5
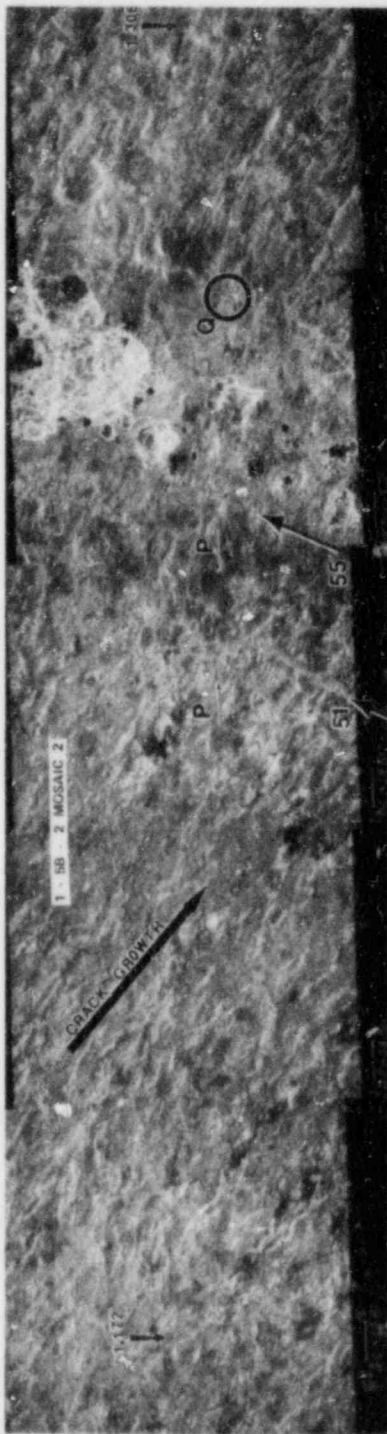
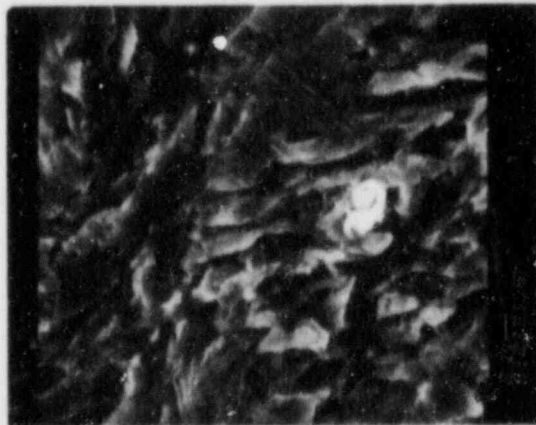Figure 3.3-24, continued

Figure 3.3-24, continued

D
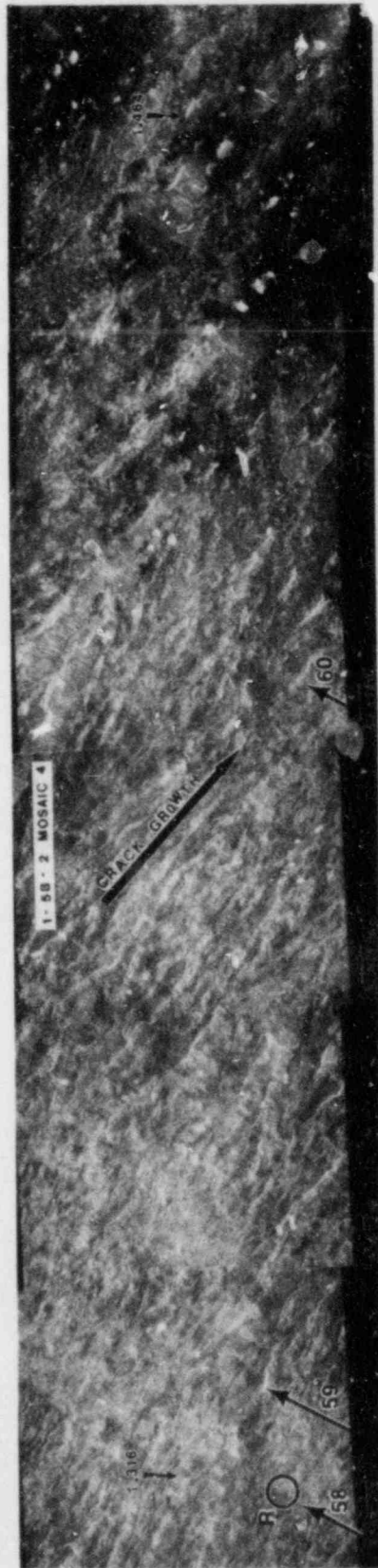
Figure 3.3-24, continued
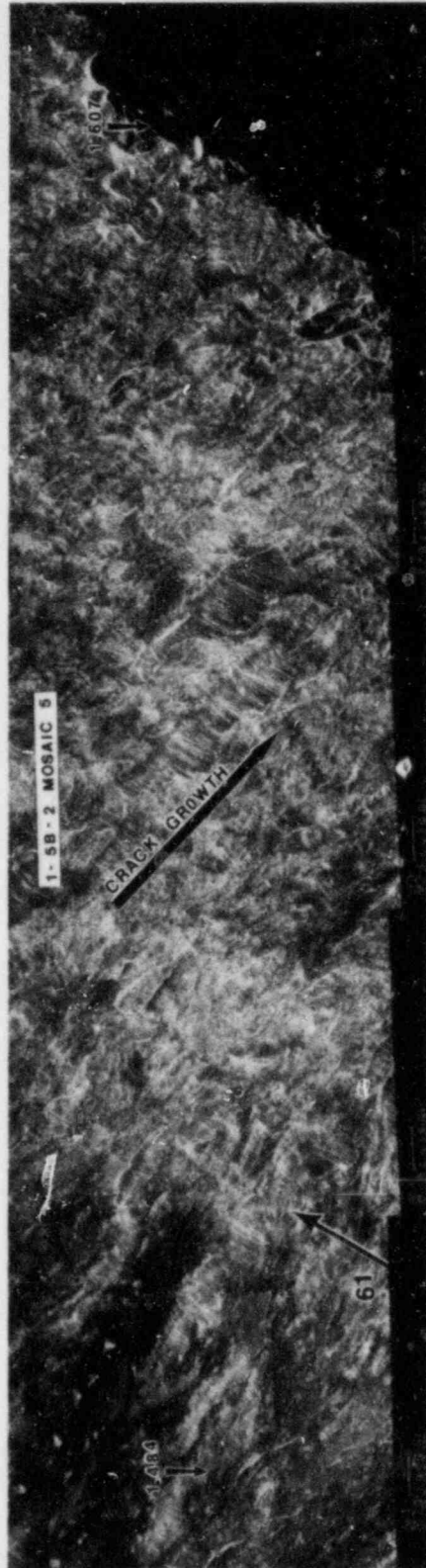
Figure 3.3-24, continued
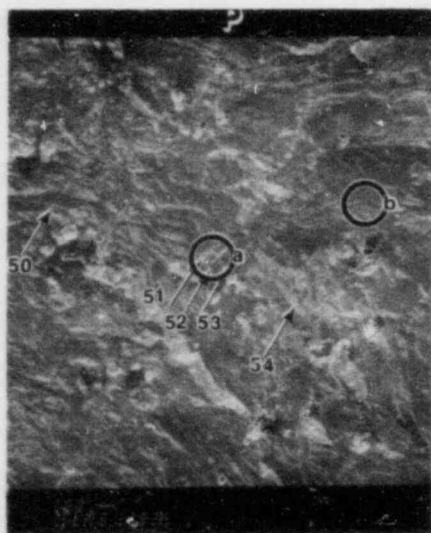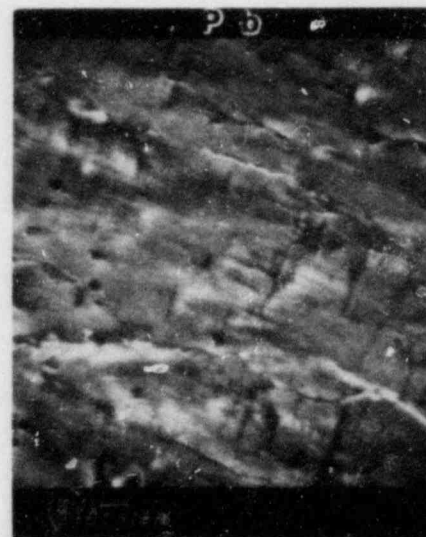
A   B   C

Figure 3.3-25.   Typical Fracture Features
in 1-5B-2 at Location P
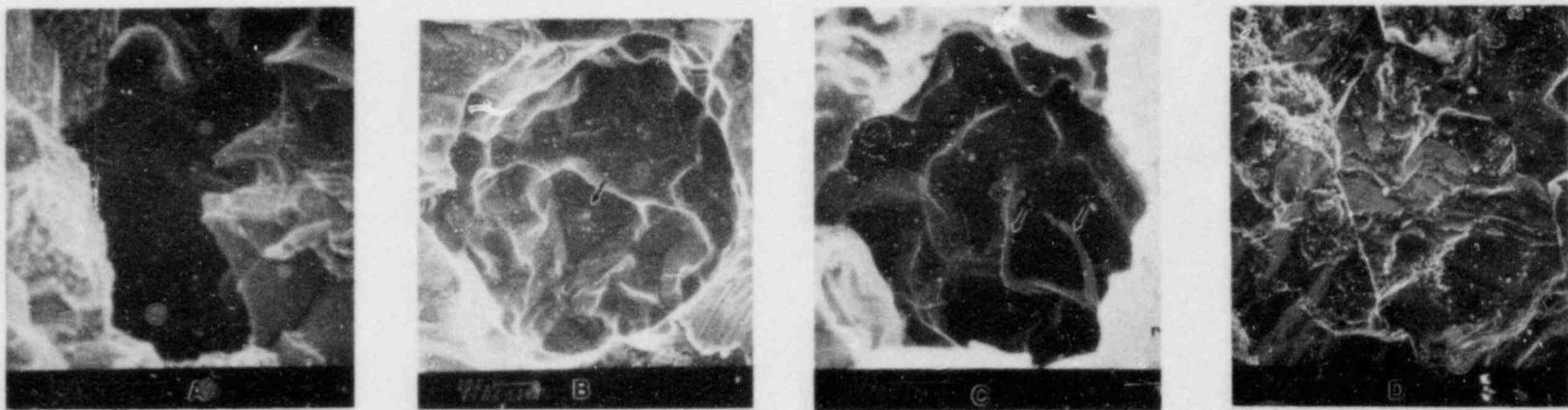
Figure 3.3-26.   Typical Structure Inside Pits in Specimen 1-5B-2.
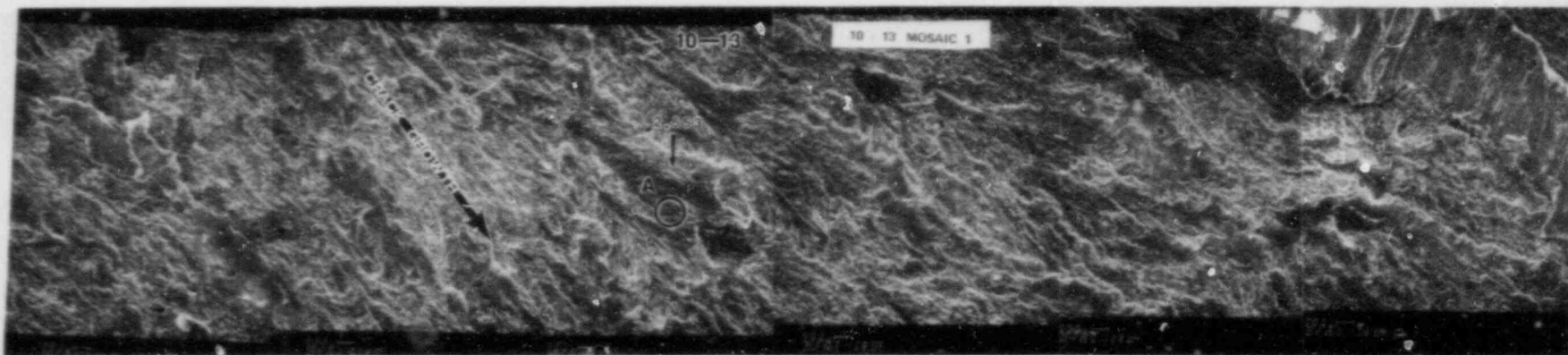Arrows Show Inclusions or Inclusion Sites
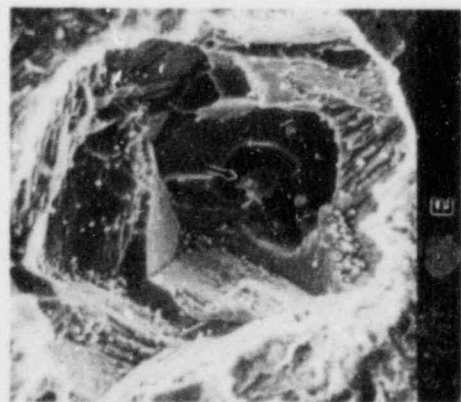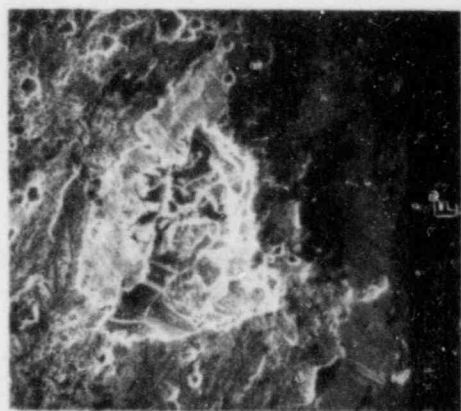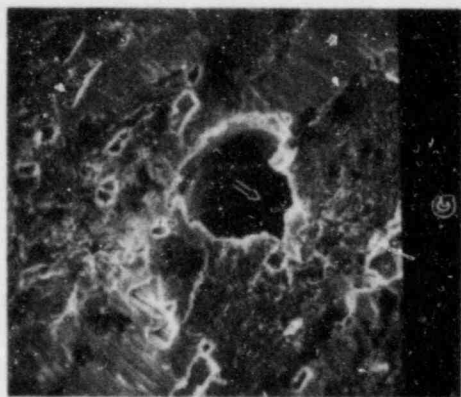
Figure 3.3-26, continued
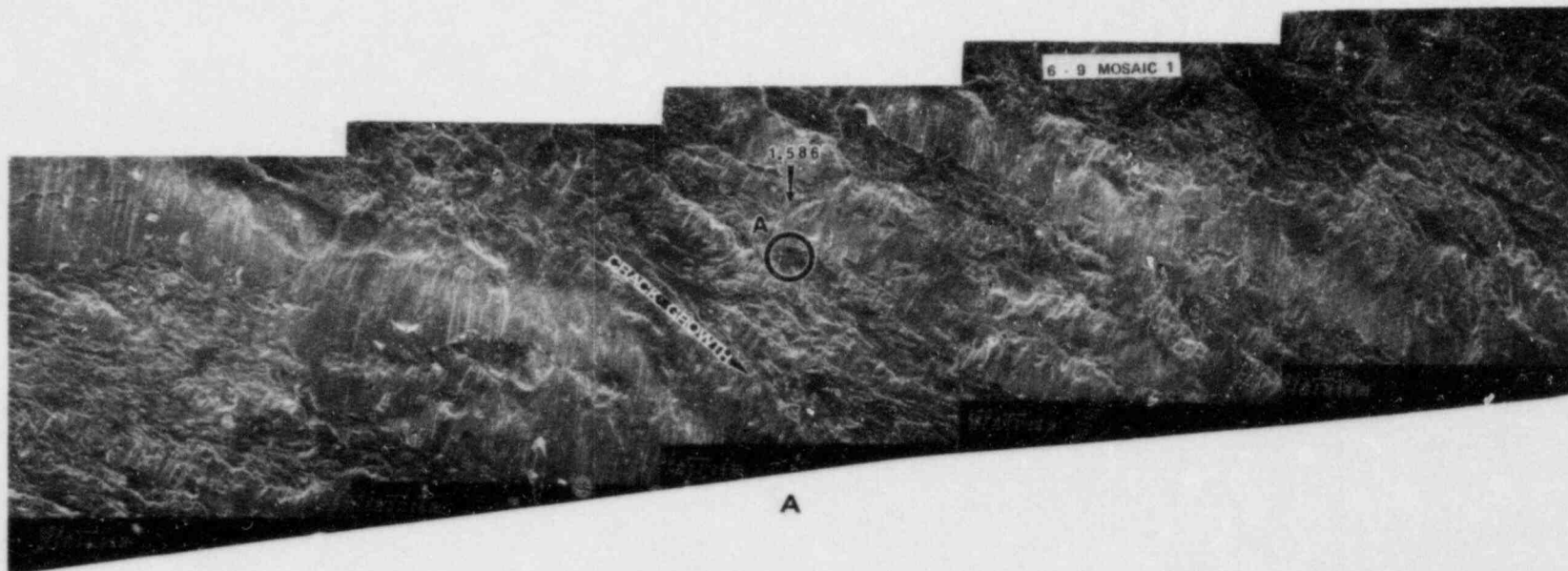
Figure 3.3-27. SEM Photomontages of Typical Fracture
Structures Observed on Specimen 6-9
A. Montage 1, B. Montage 2
C. Montage 3, D. Montage 4
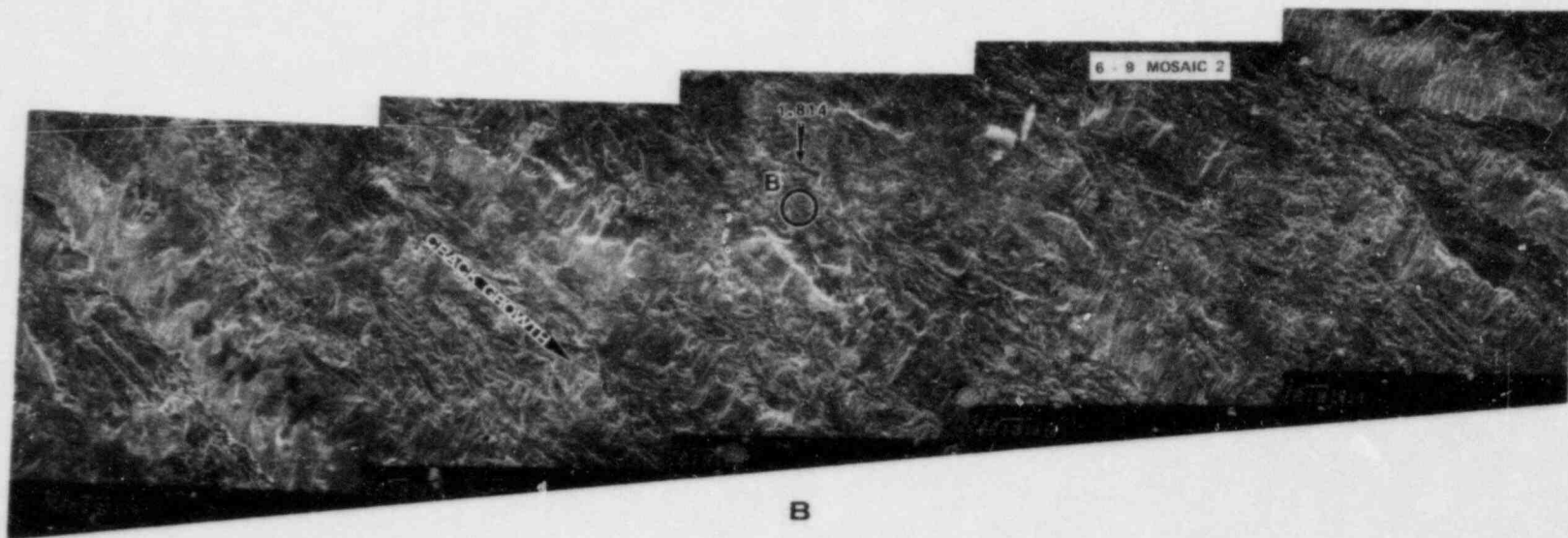
Figure 3.3-27, continued
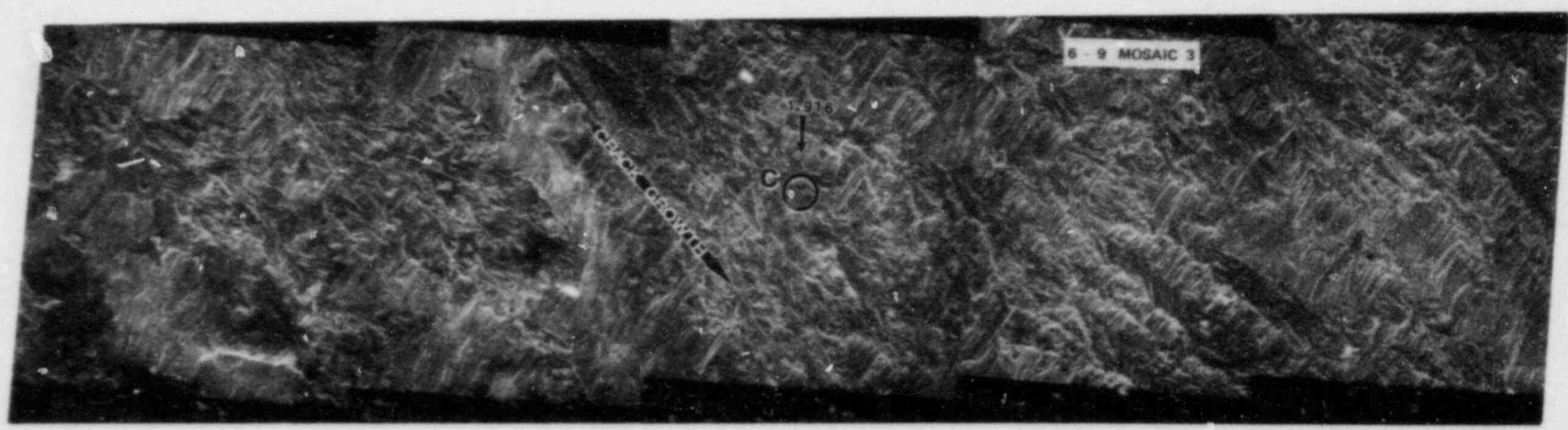
C
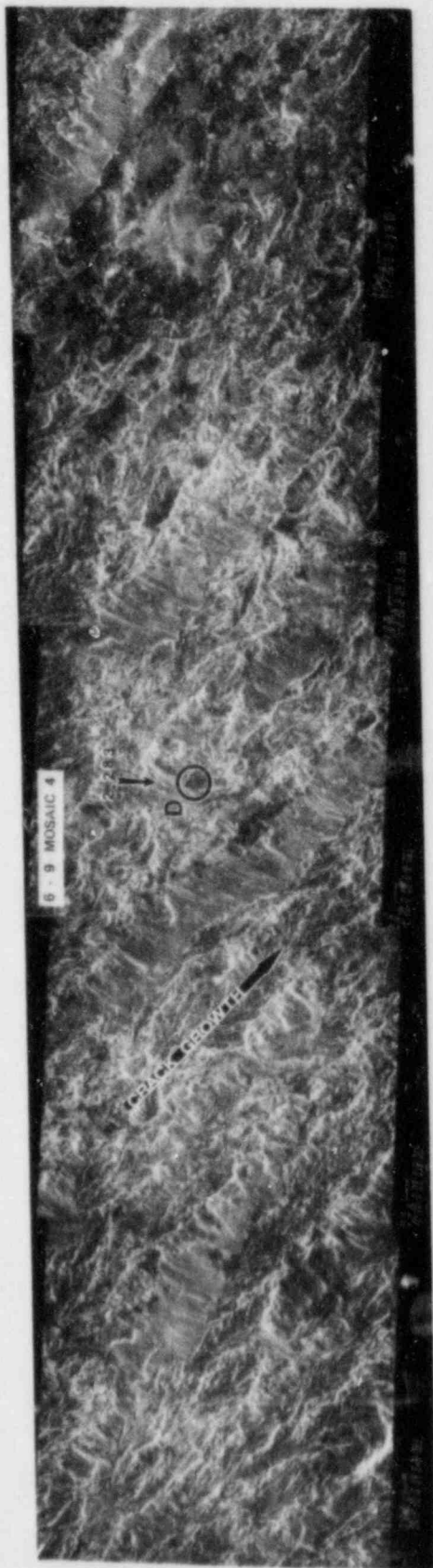
Figure 3.3-27, continued

Figure 3.3-27, continued

A   B   C   D
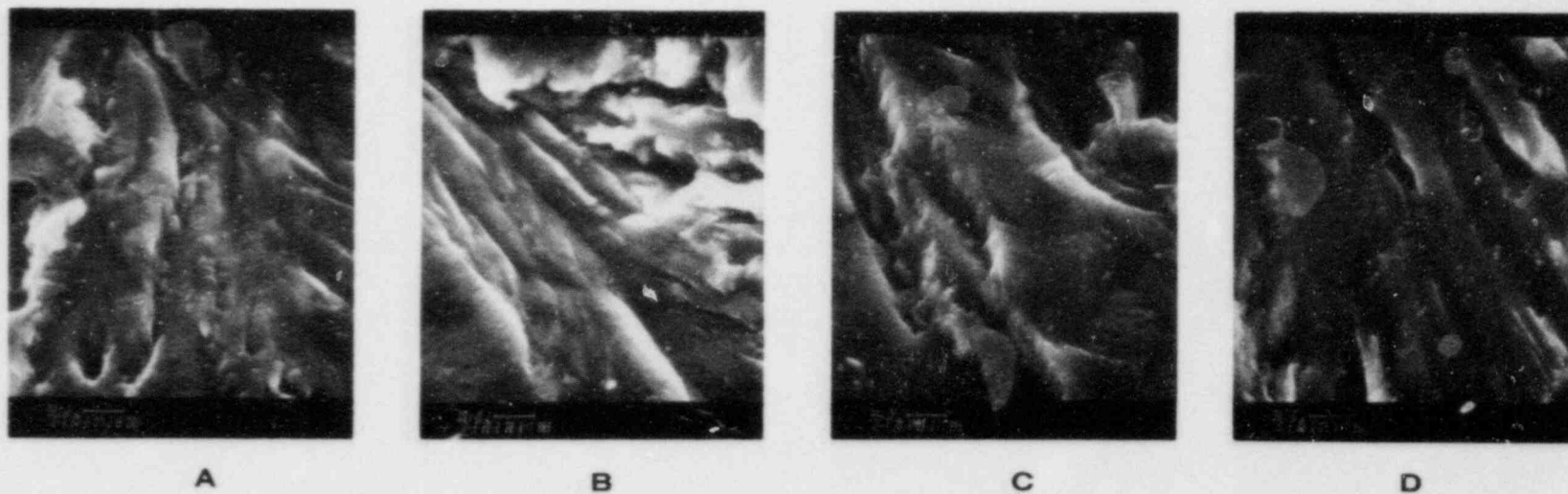
Figure 3.3-28.   Typical Fractographic Features of Specimen 6-9 Viewed at High Magnification.   Views A Through D Are Located on Previous Lower Magnification Montage of Specimen 6-9
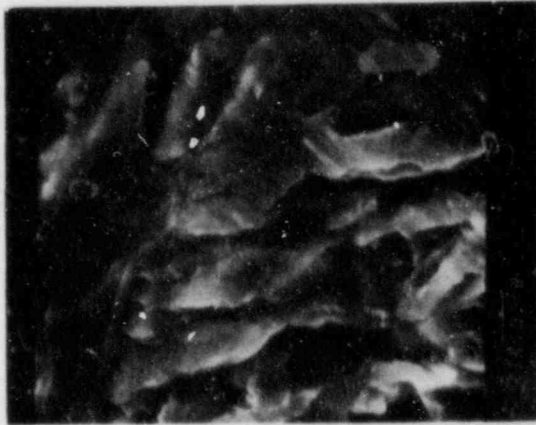
G
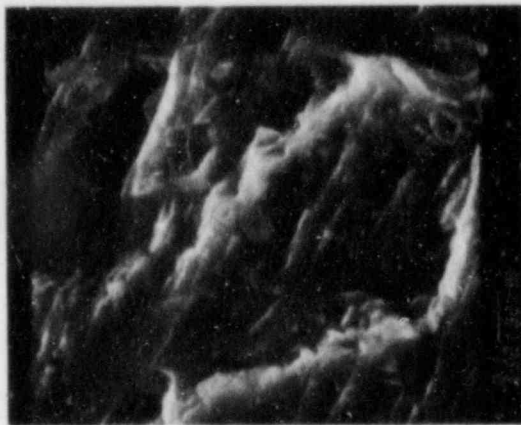
F

E

Figure 3.3-28, continued

A

Figure 3.3-29.   SEM Photomontages of Typical Fracture
Structure Observed on Specimen 10-13
A. Montage 1, B. Montage 2
C. Montage 3, D. Montage 4
E. Montage 5

Figure 3.3-23, continued
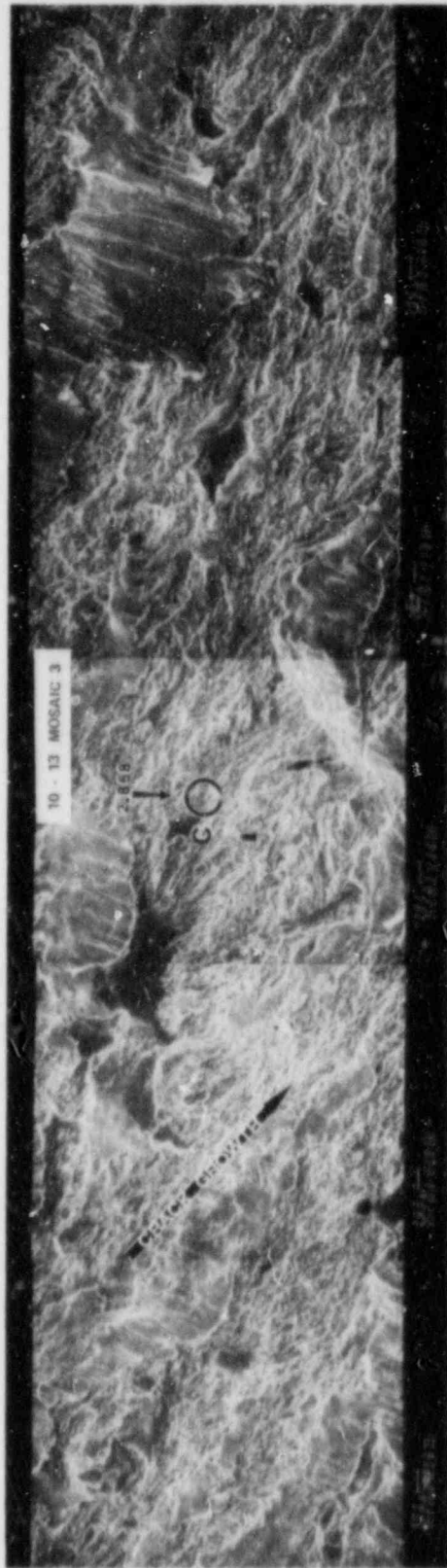
C

Figure 3.3-29, continued
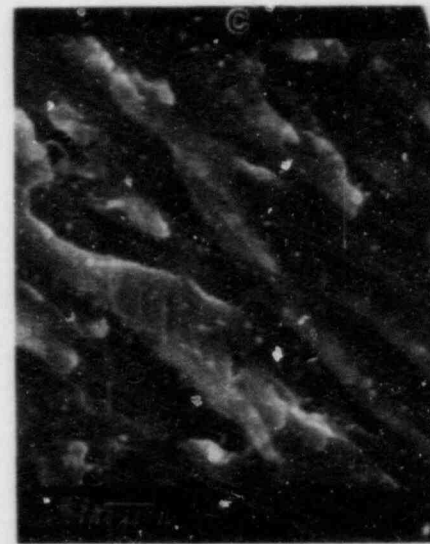
D
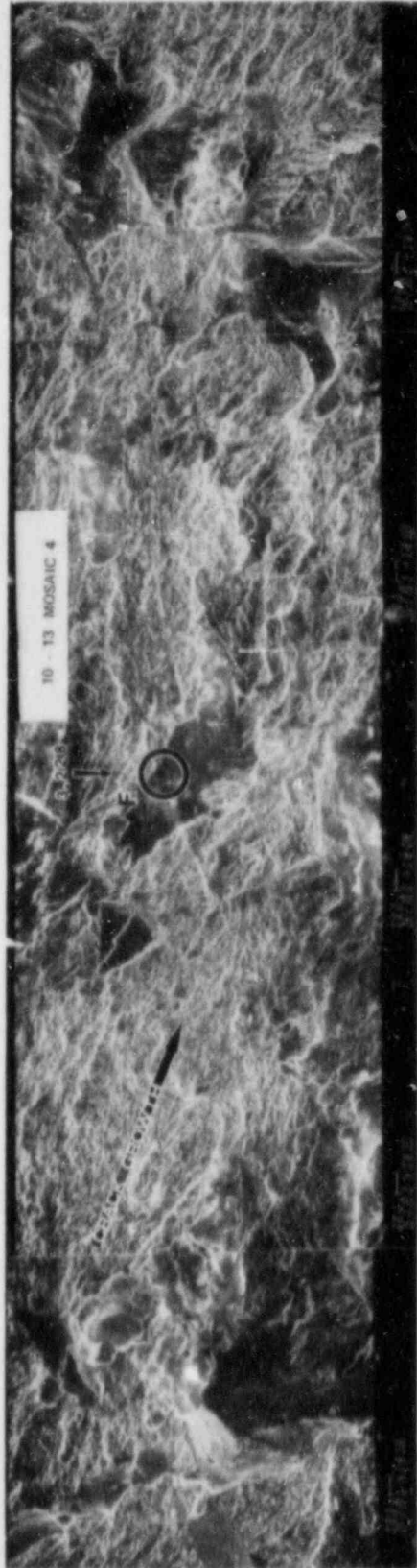
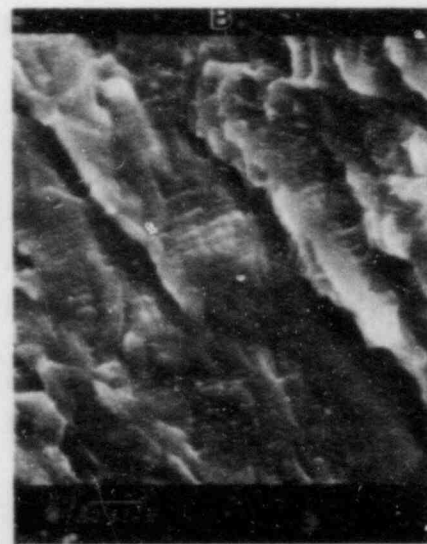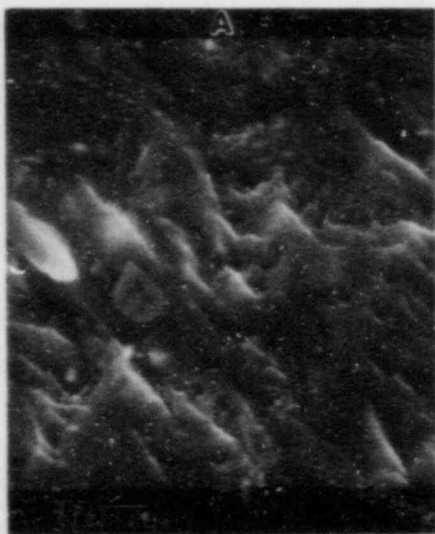Figure 3.3-29, continued
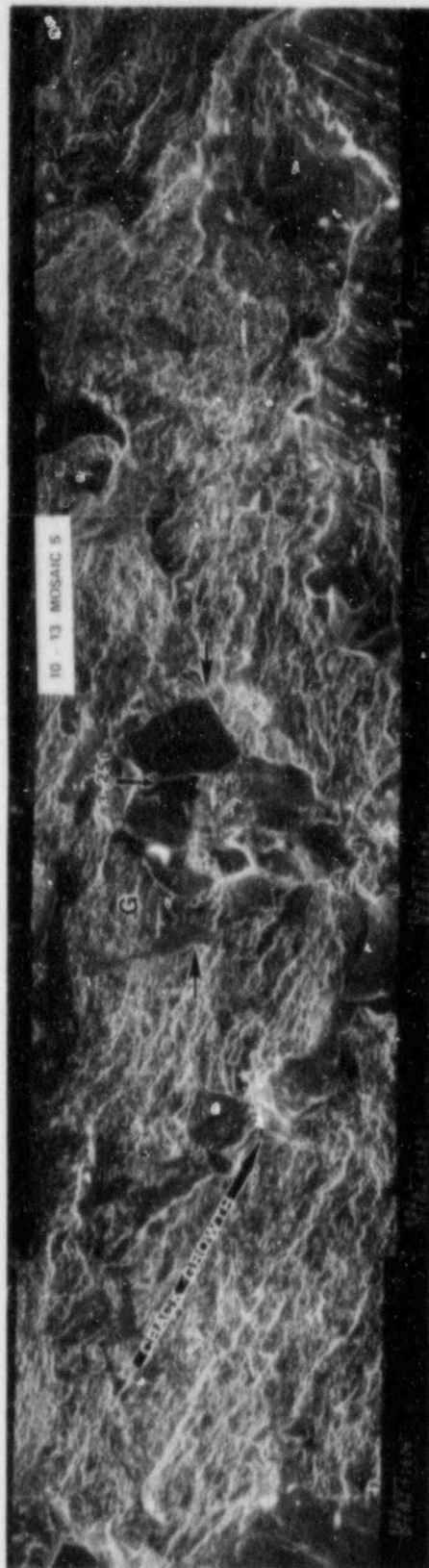
Figure 3.3-29, continued

Figure 3.3-30. High Magnification SEM Photomicrographs of Fine Trans-
granular Fracture With Faint Striations in Specimen 10-13.
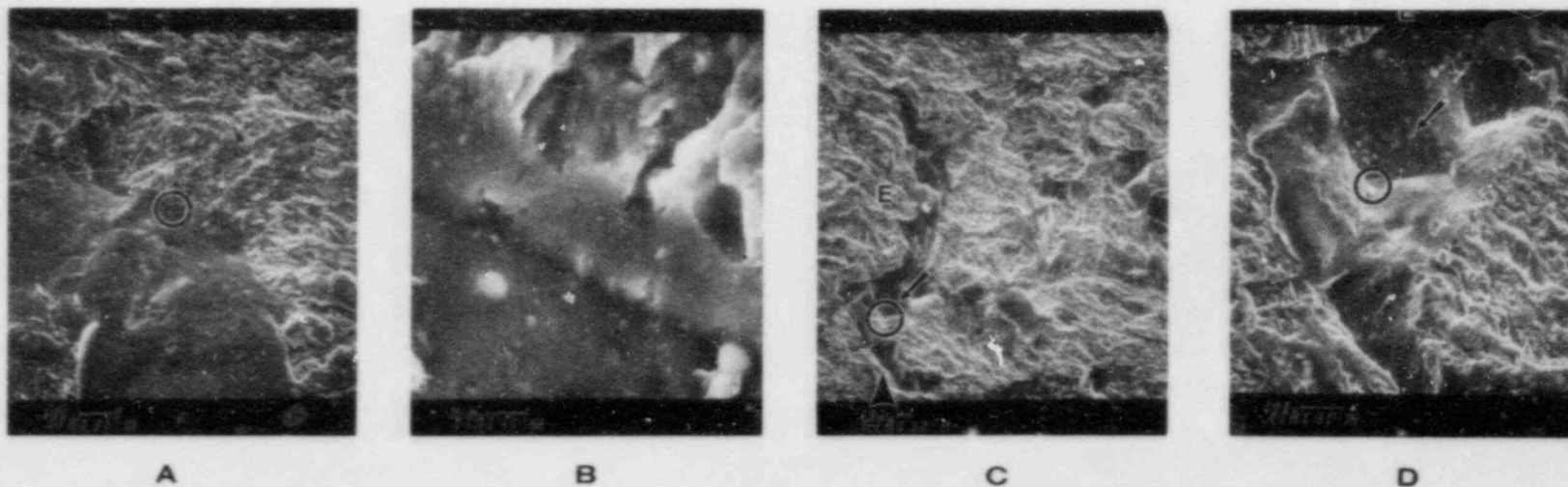Views Are at Locations A, B, and C of Previous Mosaic

Figure 3.3-31. Typical Mixed Mode Fractography Seen on Specimen 10-13. Letter at Top of Photo Refer to Location on Previous Montage). Cleavage and Intergranular Separation Facets Occur in Colonies Surrounde by a Fine Transgranular Structure. A. Intergranular Separation, Enlarged in B, C. Intergranular Separation, Enlarged in D
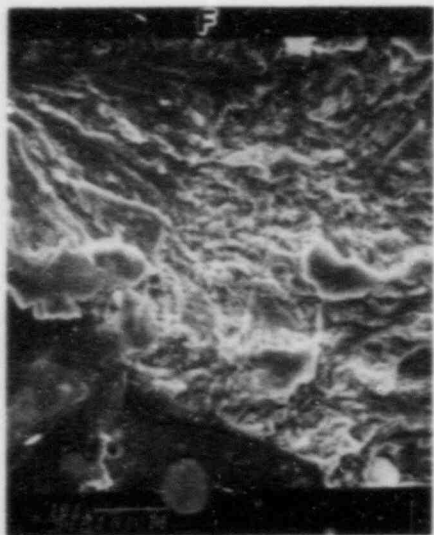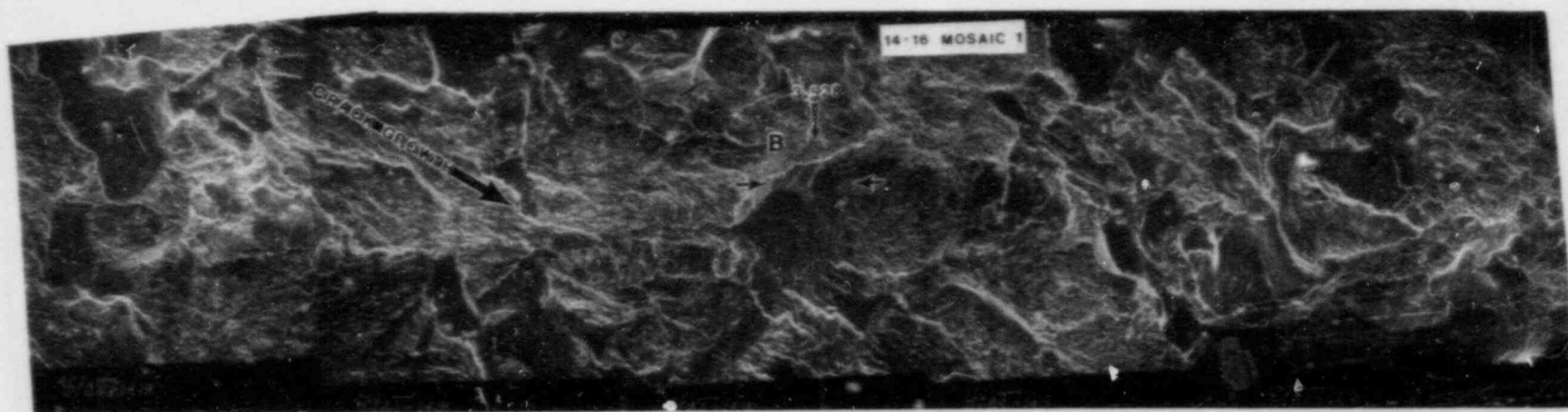
E

F
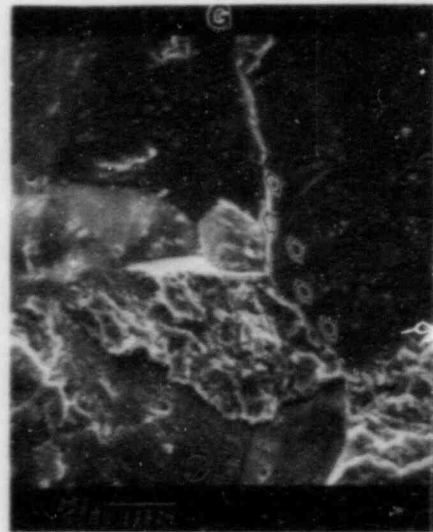
G

Figure 3.3-31, continued
E,F.   Intergranular, Plus Some Cleavage
G.   Enlarged View of F Showing Possible
       Crack Arrest Points on Facet Surface
       (Arrows)

Figure 3.3-32.   SEM Photomontage From Specimen 14-16
A. Montage 1, B. Montage 2

14-16 MOSAIC 2

CRACK GROWTH
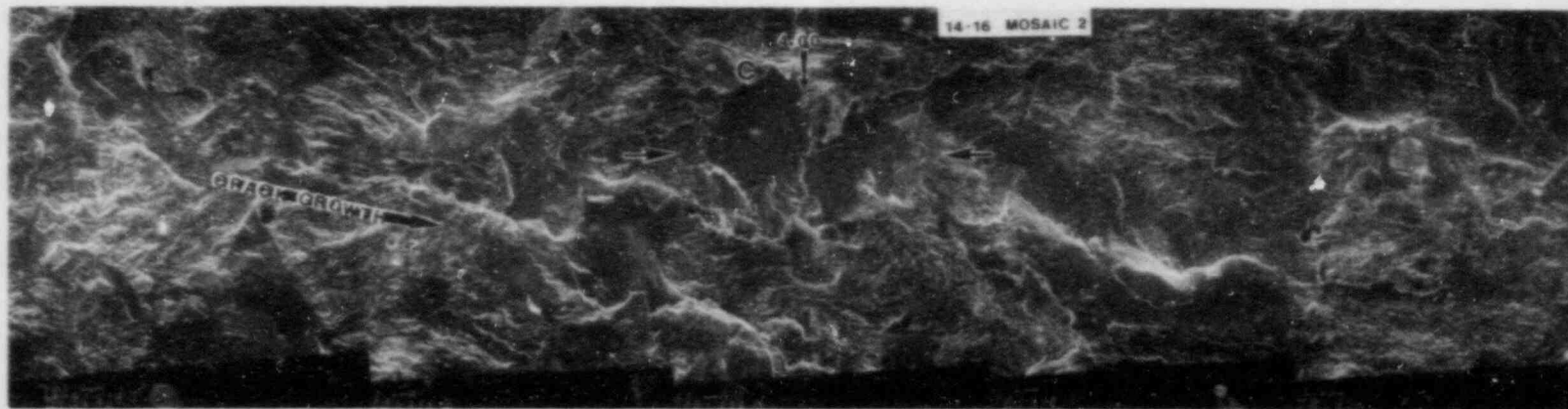
B
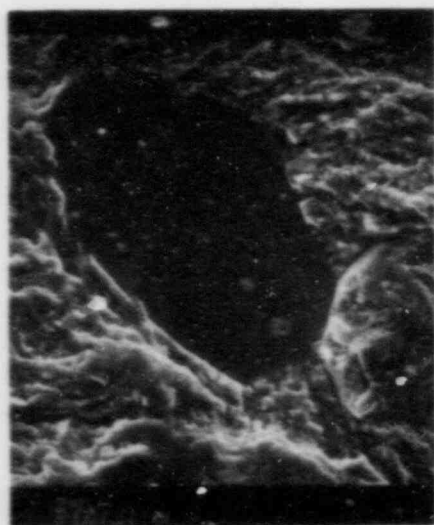
Figure 3.3-32, continued
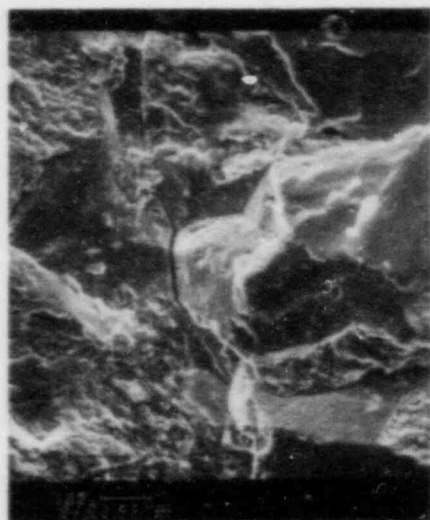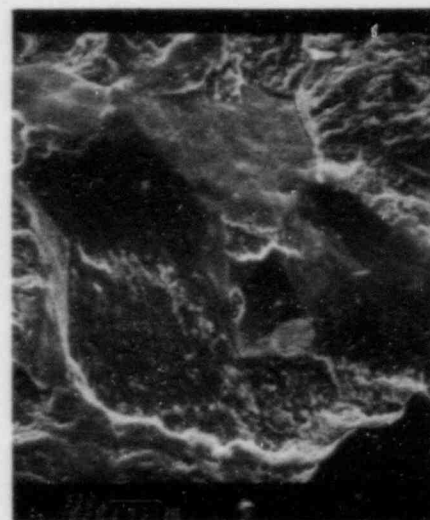
Figure 3.3-33.   Typical Examples of Faceted
Structure in Specimen 14-16.
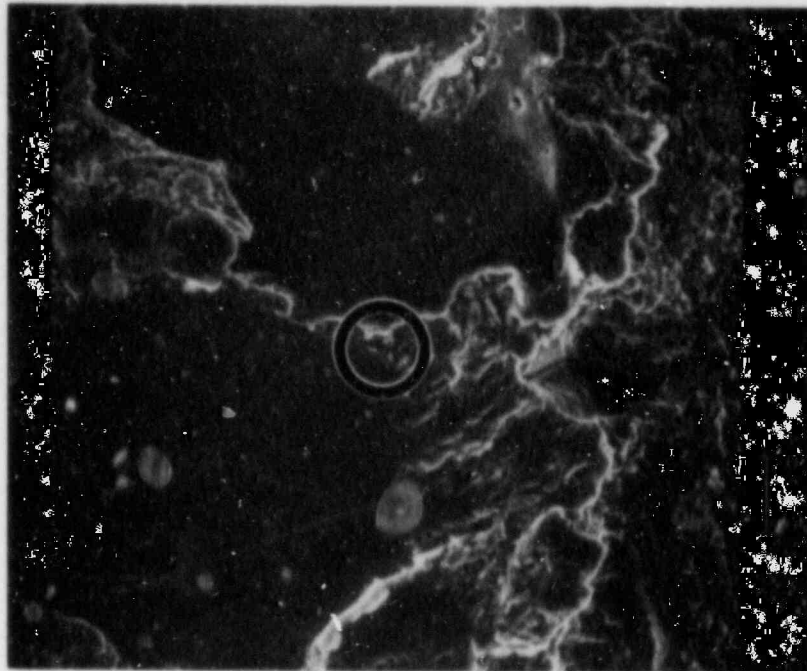
E
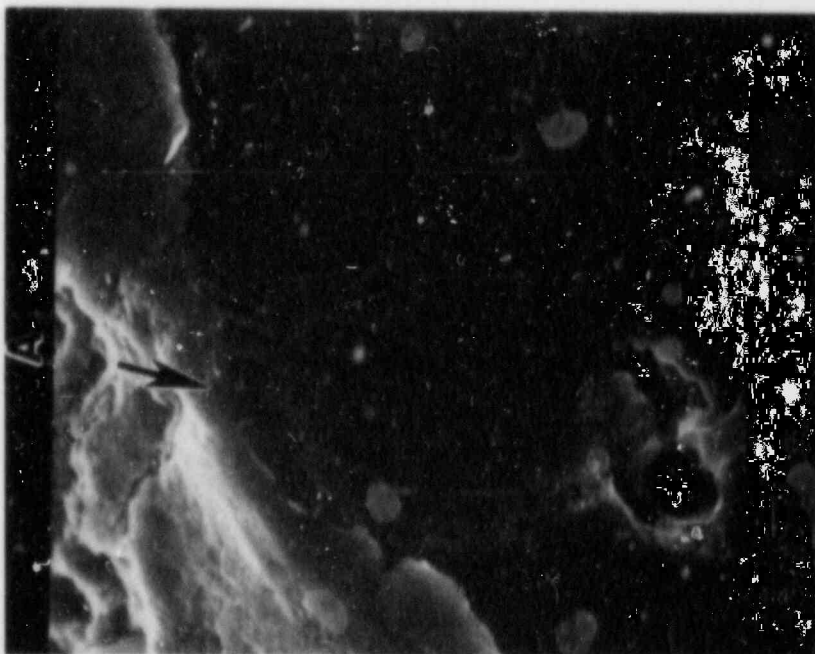
D

Figure 3.3-33, continued
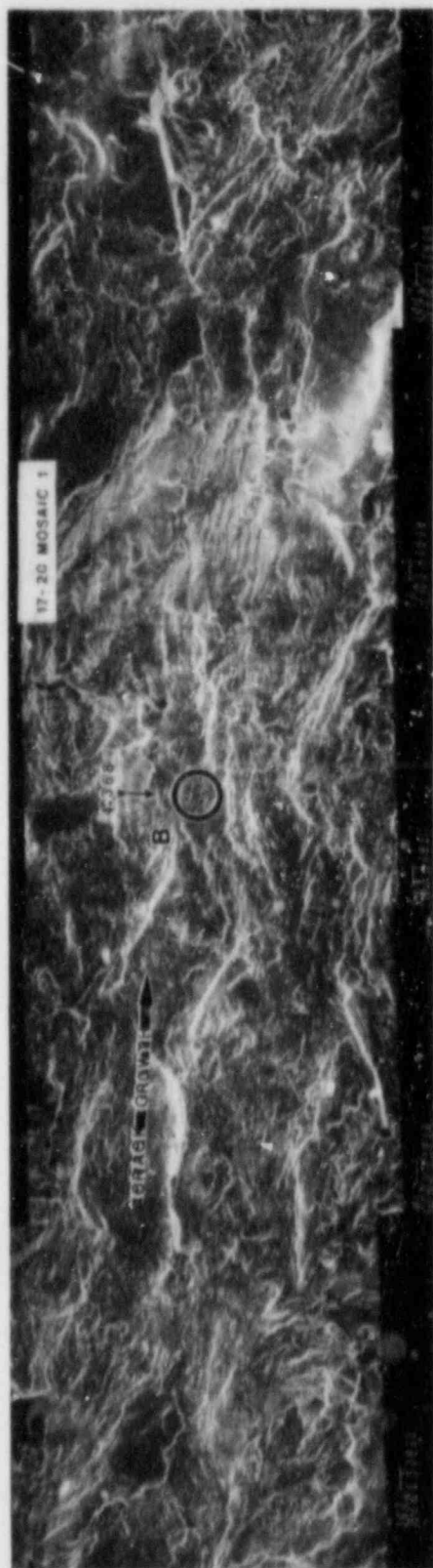
A

Figure 3.3-34. SEM Photomontage from Specimen 17-20
A. Montage 1, B. Montage 2, C. Montage 3
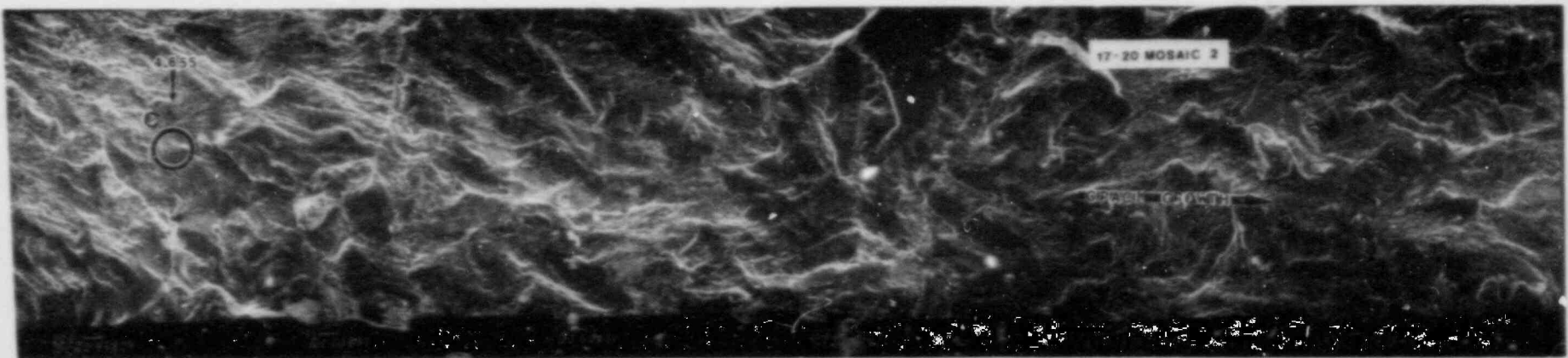
B

Figure 3.3-34, continued
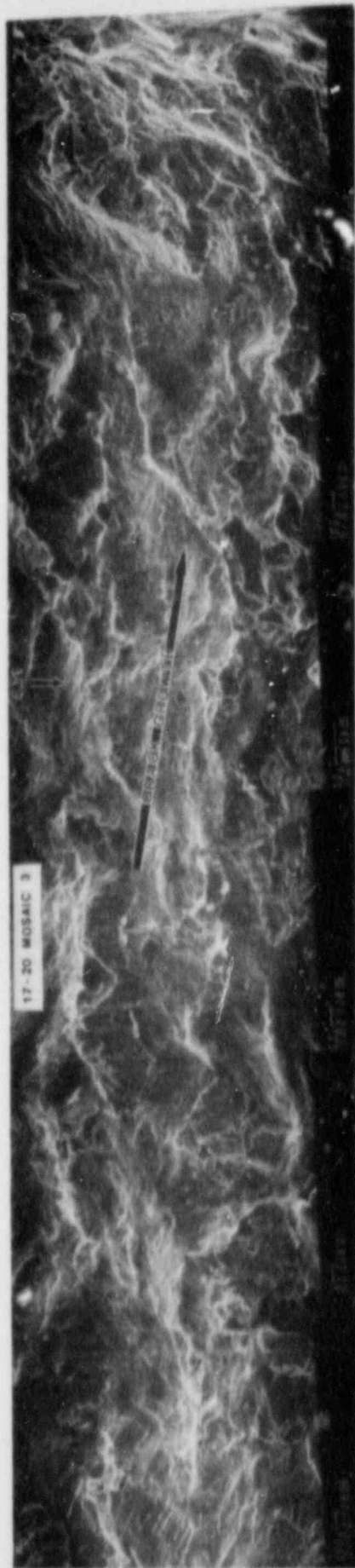
C

Figure 3.3-34, continued
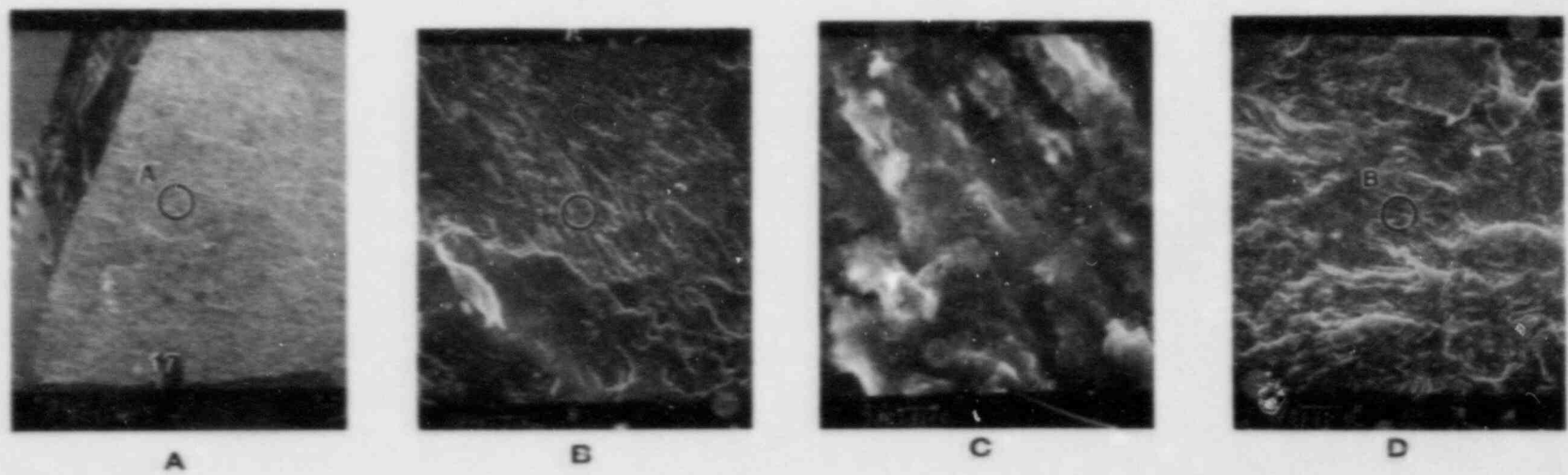
Figure 3.3-35. Higher Magnification Views of Fracture Surface Structure on Specimen
Views B and C Taken at Location A.   Views D and E Taken at Location
B Shown on Previous Montage.   Views F and G Taken at Location C.
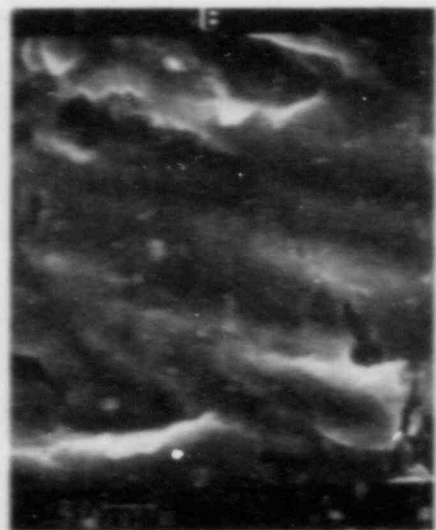
E
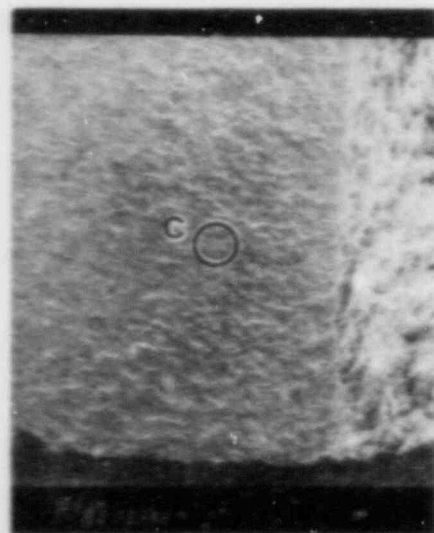
F
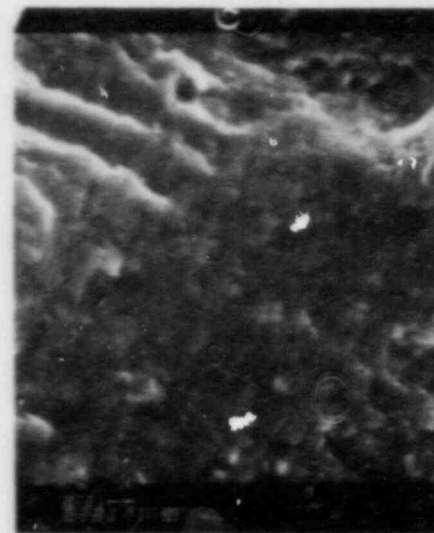
G

Figure 3.3-35, continued

SHAFT OUTER SURFACE

TRANSGRANULAR FRACTURE

500 um
0.020-inch

GRAIN SIZE-ASTM 4-5
INCLUSION DENSITY-ASTM TYPE C THIN

SHAFT AXIS

100 um
0.004-inch

Figure 3.3-36. Longitudinal View of Specimen A1A-1

Figure 3.3-37. Longitudinal View of Specimen A1A-4
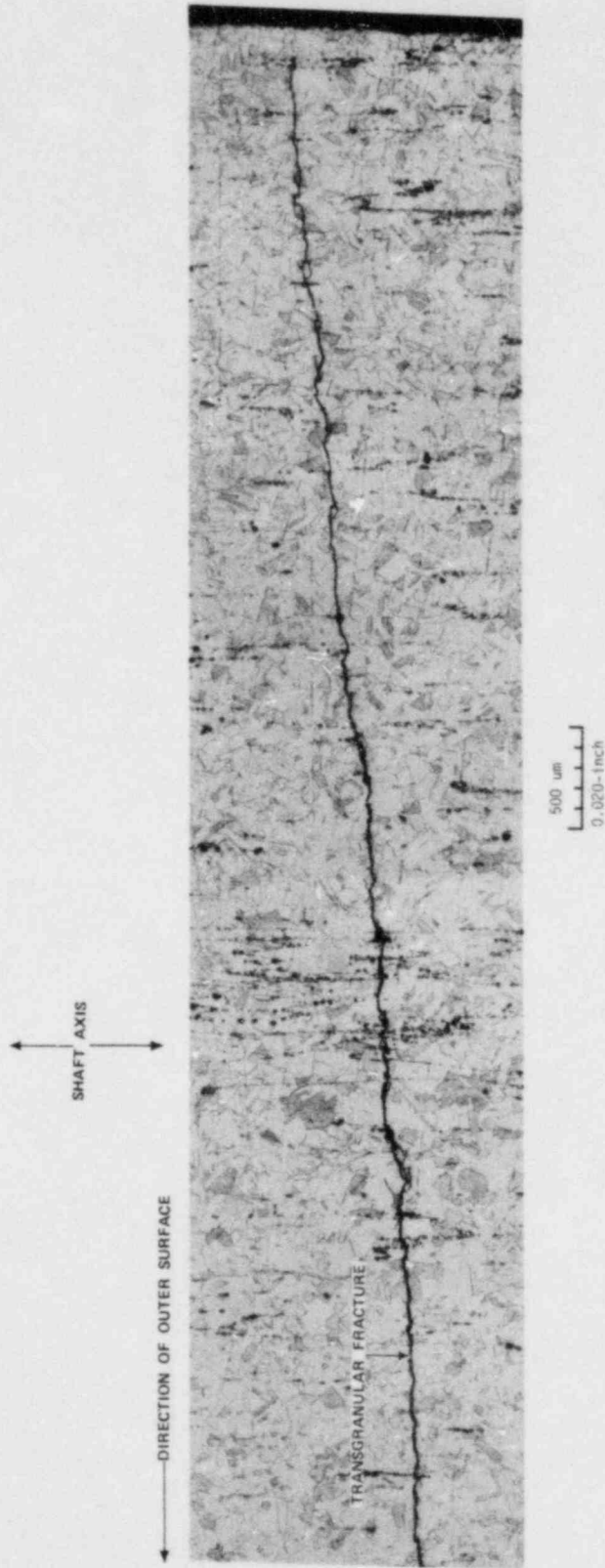
Figure 3.3-38. Longitudinal View of Specimen A1A-8
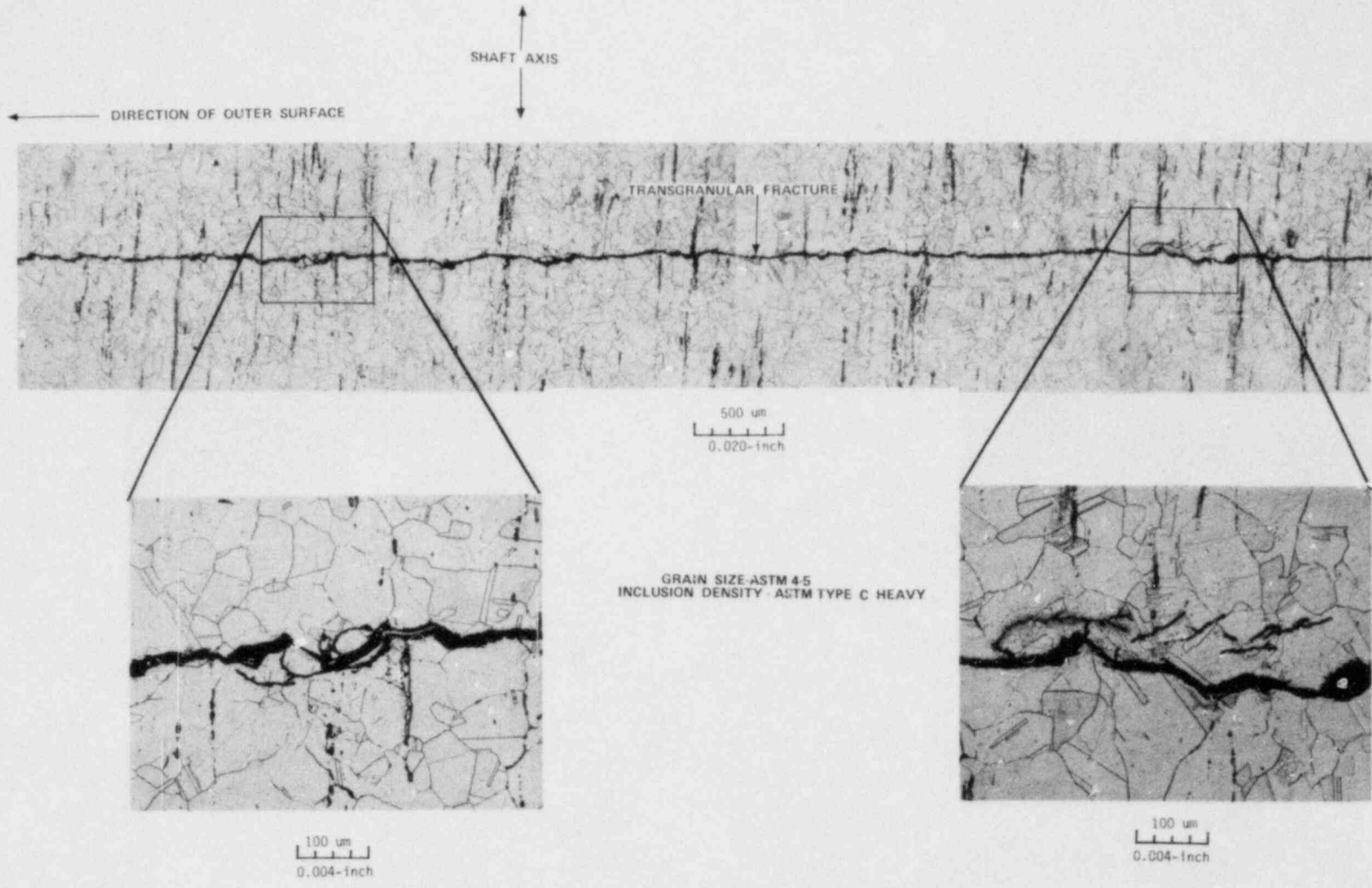
Figure 3.3-39.   Longitudinal View of Specimen A1A-8 Near Shaft Center
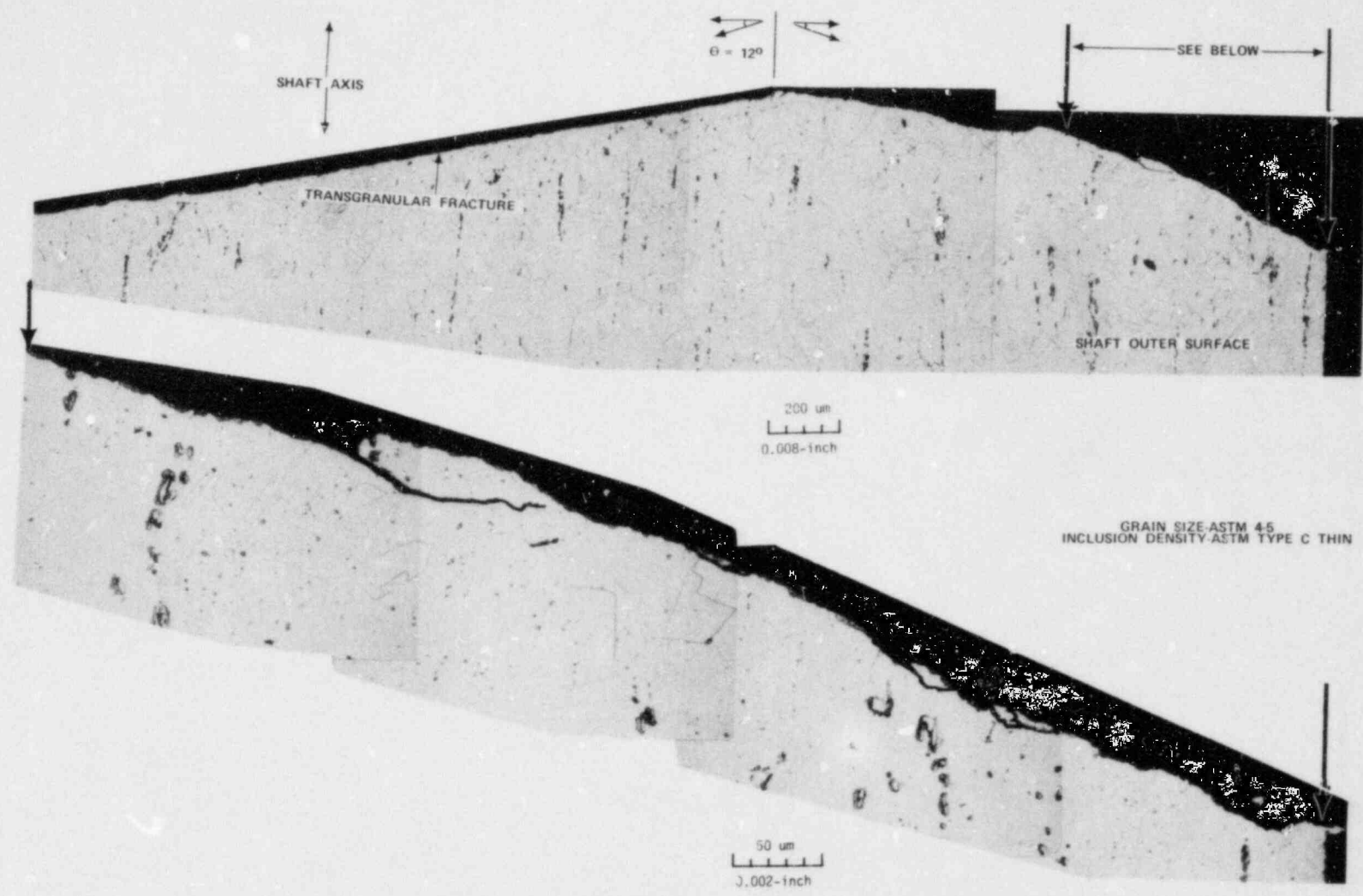
Figure 3.3-40. Longitudinal View of Specimen B1A1-1-5 at Crack Origin
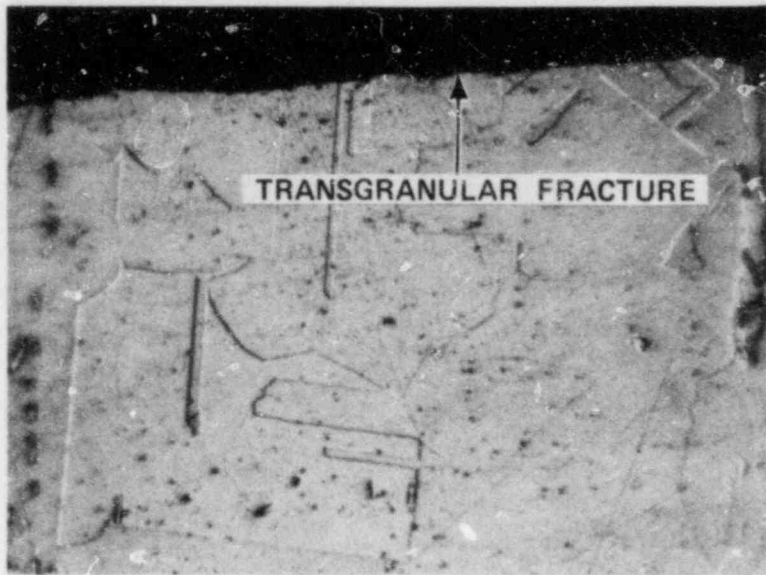
50 um
0.002-inch

SHAFT AXIS

GRAIN SIZE-ASTM 4-5
INCLUSION DENSITY-ASTM TYPE C THIN
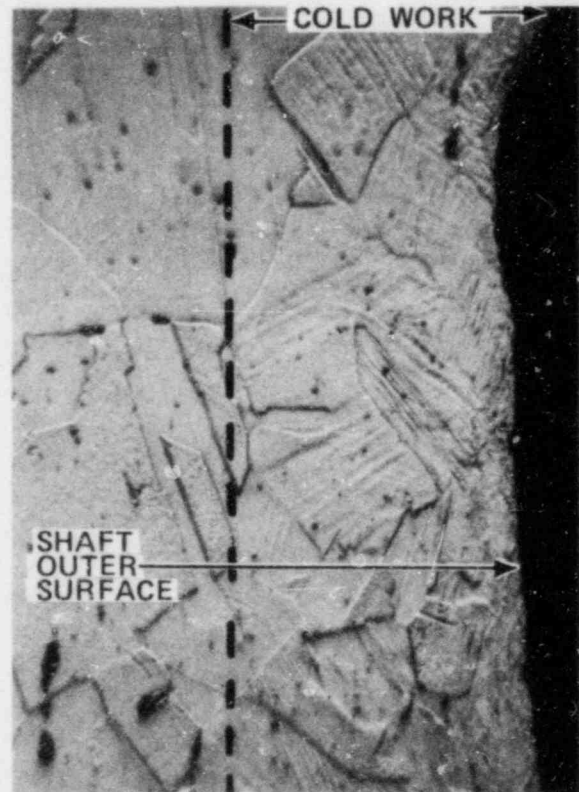
Figure 3.3-41. Longitudinal Views of Specimens B1A1 1-5B-1

GRAIN SIZE-ASTM 4-5
INCLUSION DENSITY-ASTM TYPE C THIN

Figure 3.3-42.   Longitudinal Views of Specimen
B1A1, 1-5A-M Pit Region

3.4 Chemical Analyses

A variety of analytical methods were used in assessing the surface composition on the fracture, the composition of the corrosion film and the bulk chemistry of the material. Auger electron spectroscopy was used for the surface composition of the fracture near the crack tip. Electron microprobe analyses were performed on the fracture surface, on a cross section of the unopened crack, and on a polished cross section to examine the composition of the inclusion population. Bulk chemical analysis was performed on a section of the shaft in sound metal adjacent to the crack initiation site. Scrapings of corrosion film from several locations near the failure were analyzed for bulk composition and for sulphur contents. These analyses were used to determine if chemical alteration at the fracture or of the bulk material played a role in the failure process.

3.4.1 Auger Electron Spectroscopy Results

Because the EDS analyses performed on the thermal sleeve ID and on the fracture surface during the fractography examination indicated the presence of sulphur, it was desired to confirm this with a surface analysis technique and t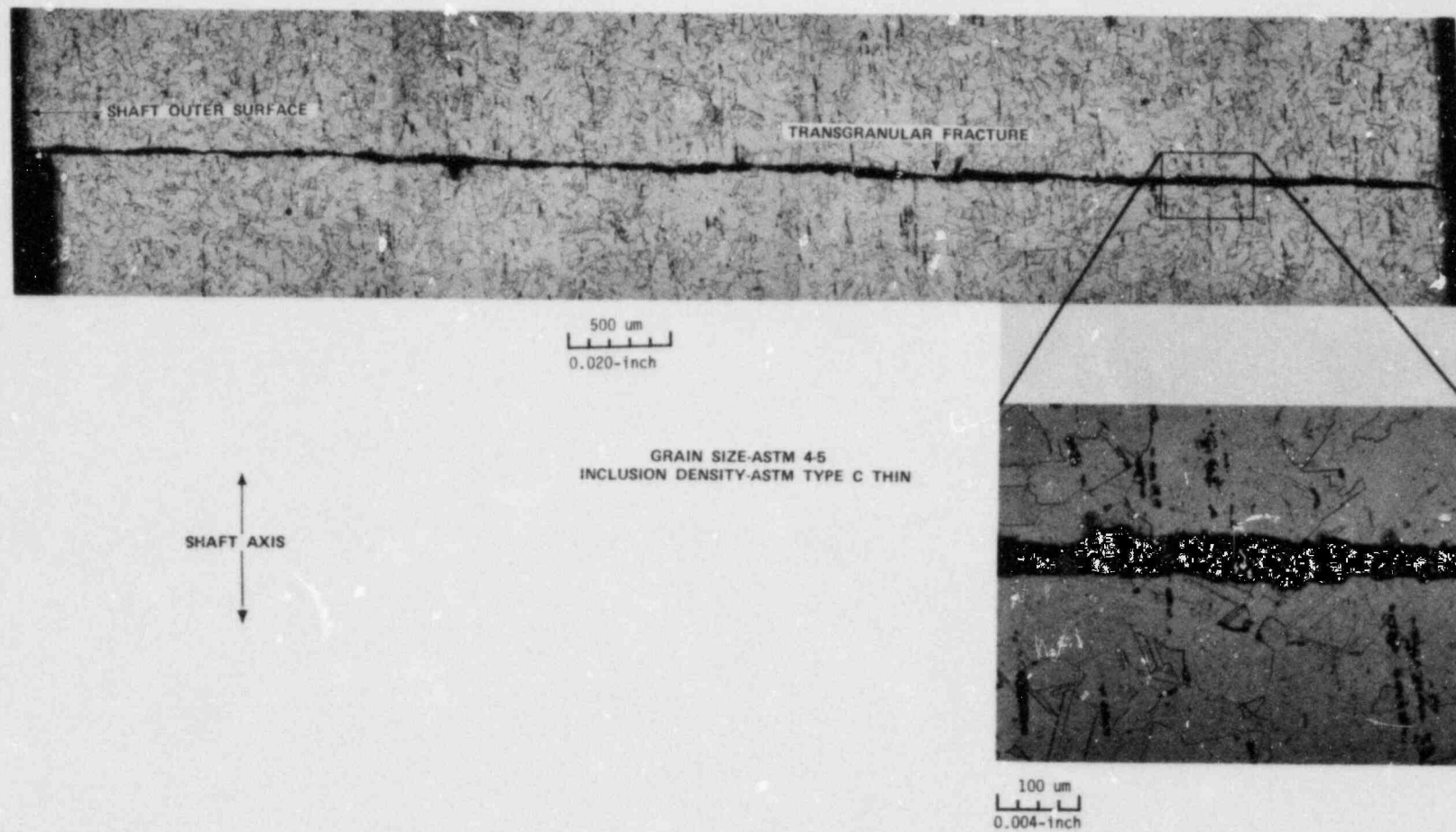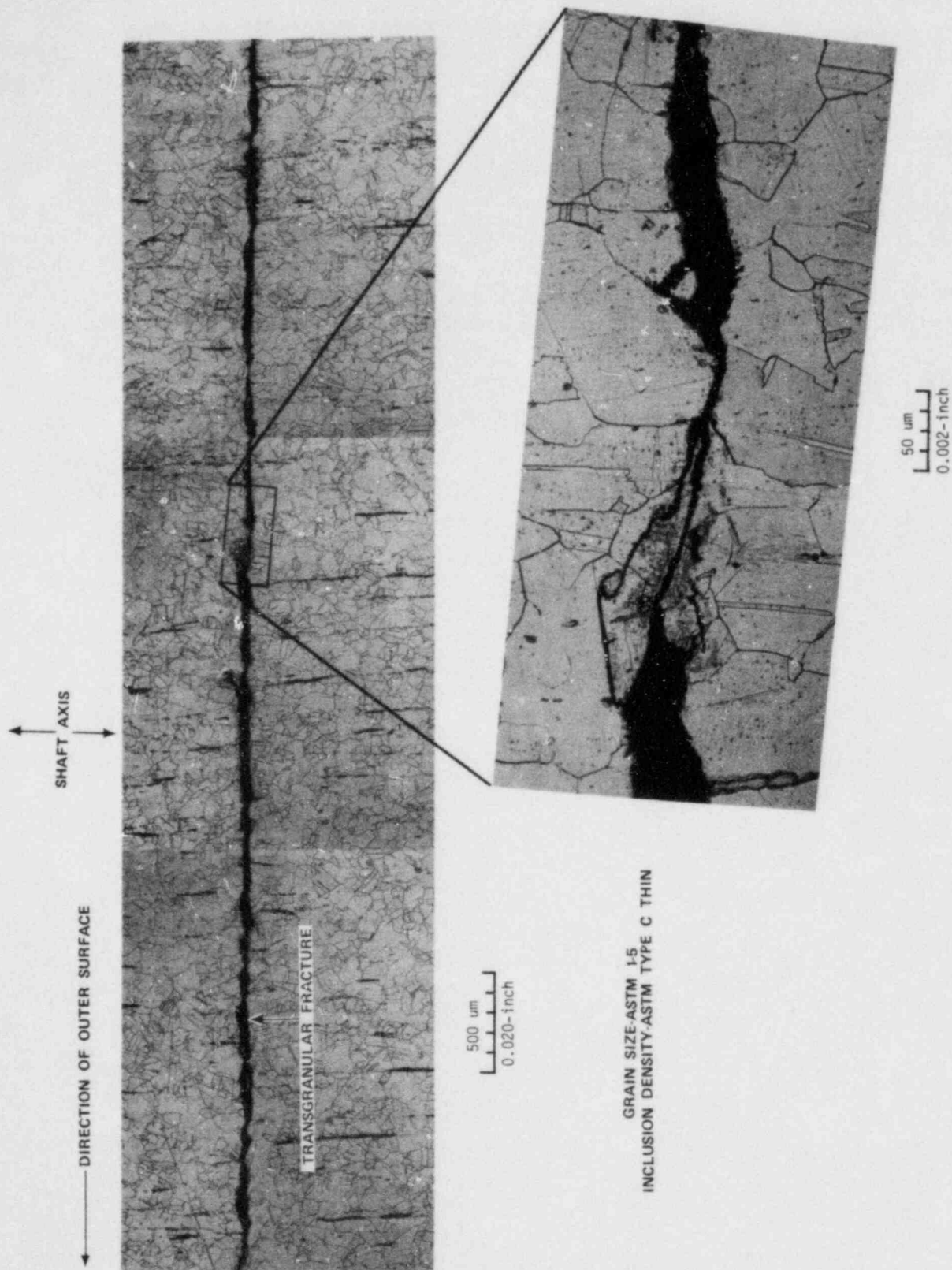o determine how deep in the surface film the sulphur existed. These analyses were performed at the B&W Alliance Research Center (ARC) using a Physical Electronics Model 545 Auger system. Appendix C contains a copy of the ARC report.

The examination was performed on section A1B. This section had been cut from the shaft with the crack unopened and only a thin ligament remaining at one end. Just prior to insertion into the vacuum chamber of the Auger unit, the specimen was pulled apart to expose the fracture surfaces.

Sputter depth profiling was done at four locations, two on the failure area and two on the forced fracture as shown in Figure 3.4-1. The concentration in atomic percent of the elements found along with the depths at which they were detected are recorded in Table 6.

The graph seen in Figure 3.4-2 represents the sputter depth profile of the major elements to a depth of 5000Å taken at Location A on the surface as viewed in Figure 3.4-1. The sulphur concentration reaches a maximum of 13 atomic percent at 400Å and then decreases to 3.6 atomic percent at 9500Å. This indicates a film that was significantly enriched in sulphur when compared to the sputter depth profile of the forced fracture Area C. The sulphur concentration was highest at the surface (5.9 atomic percent) in the forced fracture region and decreased slightly at the 100Å and 200Å levels to 4 atomic percent.

The sulphur was not expected to sputter completely away. The reasons for this were that the Auger system has a continuous background level of sulphur of approximately 1 atomic percent and that the sample was known to have sulphide inclusions which would be virtually impossible to sputter away. This explains the remaining 2 atomic percent sulphur at the 1700Å depth of the forced fracture (Area C) and the 3.6 atomic percent remaining at 9500Å on failure area A.

Another characteristic of the film was an enrichment of manganese at the surface and to a depth of 200Å. Below 200Å, manganese was not detected. The concentration of manganese was not calculated because of interference from an iron secondary peak; however, it's presence is noted by a checkmark in the table. Manganese concentrations are reported in the microprobe data in Table 7. The Auger findings also indicate a high level of oxygen in the failure area.

In summary, the contamination film appears to be predominantly an oxide(s) rich in sulphur throughout, with manganese enrichment near the surface. The metal oxide composition of the film was not determined by Auger analysis since it is an elemental technique and a multiplicity of metals were detected.

3.4.2 Microprobe Analyses

Microprobe analyses were performed on the A1B fracture surface opposite that used for Auger analyses, and on specimen A1C which had been metallographically polished but not etched.

Based on the results of the Auger analysis on specimen A1B, the following elements were included in the microprobe analysis: Cr, Mn, Fe, Ni, Nb, S, and O. The results of the quantitiative analysis on the A1B fracture surface are given in Table 7. Four randomly chosen locations were analyzed on the surface away from the forced fracture. The readings were compared to normal base metal on a piece taken adjacent to the Auger sample such that a plane perpendicular to the defect surface was analyzed. Fracture surface readings were taken, but the surface roughness proved to be too great to achieve good quantitiative results. A beam search for sulphur revealed high concentrations in rough surfaces adjacent to the forced fracture, but again surface roughness made quantification impossible.

Based on results listed in Table 7, it can be concluded that the entire defect surface contained sulphur at levels significantly higher than the base metal. The surface was also enriched in manganese, probably in the form of MnO because oxygen readings showed the surface to be oxidized. Niobium levels were found to be lower than the base metal levels in three locations and significantly higher in the fourth location. This higher level may have been caused by a niobium carbide inclusion present at the fracture location being excited.

Based on oxygen readings, it appears that the oxidized, sulphur-rich surface was less than $1-2\mu$ thick and the underlying base metal was simultaneously analyzed due to normal beam penetration. This is substantiated by the results of Auger sputter depth profiling which indicates base material beginning at approximately 0.5μ below the surface.

An SEM photomicrograph of the polished defect cross section can be seen in Figure 3.4-3. The crack was very tight and microanalysis along this plane only revealed occasional oxide patches. The white line in Figure 3.4-3a indicates the location of a beam traverse for oxygen while Figure 3.4-3b is the associated oxygen profile to illustrate the presence of oxides. No sulphur enrichment could be detected along the defect line in this sample orientation.

Several stringered inclusions were observed in the sample orientation analyzed. Elemental dot mapping was done on several inclusions for the following elements: C, N, Ta, S, O, Mn and Nb, and Al. It was observed that the majority of the inclusions were of the form Nb (C, N). Figure 3.4-4 displays an SEM photomicrograph and several associated element dot maps of a typical cluster of inclusions seen in the sample. The white appearing inclusions were niobium rich. The carbon and nitrogen maps were abnormally faint, most likely because material had smeared over during polishing. The surface was in the unetched condition. The grayish inclusion was identified by mapping as Al_2O_3. MnS had precipitated out around this and other observed oxide inclusions. MnS inclusions were also found separately in clusters with oxides and Nb (C, N) as well as isolated in the matrix. Sulphide inclusions were found much less frequently than Nb (C, N) inclusions throughout the sample.

3.4.3 Bulk Chemical Analyses

A slab of shaft material was removed from the shaft just adjacent to specimen 1-5. This slab was sent to National Spectrographic Laboratory for bulk

chemical analysis covering all elements in the material specification as well as a few other elements not specified. The results are listed in Table 8. The shaft material conforms to ASTM A182-71 Grade F347 chemical requirements.

3.4.4 Deposit Analyses

Scrape samples were supplied by GPU from the thermal sleeve and from the "flange area" of the pump. A subsequent sample was collected at the LRC from the inside surface of the thermal sleeve "B" section near the pin.

Emission spectroscopy was performed on the GPU supplied flange area and thermal sleeve scrape samples. The results shown in Table 9 indicate a difference in composition between the two samples. The flange area scrapings consisted mainly of Si, Fe, Al, Ca, and Cr. The external sleeve sample was principally Fe, Cr, Ni and Mn. The thermal sleeve sample was a dry, black powder. The flange area sample was rather inhomogeneous, consisting of large black sticky pieces of material, powder and lint-like particles.

The composite flange area sample was placed in an ultrasonic bath with freon during which the powdery material settled out from the larger pieces. The large pieces were discarded along with most of the lint-like substances. The remaining powder material was washed in freon again to remove any traces of oil or grease. It is expected that the low percentages of elements in this flange area sample was due to a high carbon content not detectable by emission spectroscopy.

X-ray powder diffraction was also performed on the scrape samples. The thermal sleeve sample consisted mainly of Fe_3O_4, with some Ni substitution, and Cr_5O_{12}. The flange area consisted mainly of alpha quartz with some minor amounts of Fe_2O_3, free carbon, and cristobalite.

Wet chemical techniques were used to analyze for total sulphur concentrations in the flange area sample supplied by GPU and the thermal sleeve sample obtained by B&W. An insufficient quantity of material prevented total sulphur analyses of the GPU supplied thermal sleeve sample. The flange sample was found to contain $0.156 \pm 0.016\%$ sulphur and the thermal sleeve scrapings < 0.13% sulphur.

3.4.5 Chemical Analyses Discussion

The key chemical analyses results are outlined below:

a. The abnormal presence of sulphur in the surface film on the fracture surface was confirmed down to a depth between 5000 and 9500A.

b. Sulphur was observed in the surface deposits removed from the thermal sleeve and from the flange area.

c. The flange area sample was rich in silicon and probably carbon and was probably contaminated by extraneous material. The thermal sleeve sample was composed of Fe, Cr, Ni and Mn. The compounds of Fe_3O_4 and Cr_5O_{12} were the predominant phases in the thermal sleeve deposits.

d. The inclusion population consisted of principally Nb (C, N) with Al_2O_3 and MnS. The MnS was observed to have existed as separate inclusions or precipitated out an Al_2O_3 or other oxides.

e.   The bulk chemistry of the shaft material was found to be
     within ASTM specification limits for type 347 forged
     materials.

The analyses for sulphur confirm the observations made using EDS. The frac-
ture surface contained an abnormal concentration of sulphur. The relatively
high concentration of Mn found in the surface film down to 200A is not well
understood. Higher than expected Mn contents were also observed in the emis-
sion spectroscopy results of the thermal sleeve samples and in the electron
microprobe results from the fracture surface. Two possible explanations are
the dissolution MnS inclusions and the selective oxidation of Mn from the al-
loy matrix.

The presence of MnS inclusions alone or precipitated on oxide inclusions lends
credence to the hypothesis that these inclusions were the sites of the local-
ized pitting at beachmark #15 as demonstrated in reference 22.

While the chemical structure of the sulphur observed in the film analyses is
not known, its source was most likely from a sulphur species in the reactor
coolant.

No reportable quantities of chloride were observed in any of the chemical analyses.

Table 6. Auger Electron Spectroscopy Results; Elemental Composition (Atomic %) of Fracture Surface As A Function of Sputter Depth (Angstroms)

Sputter Depth Å	Failure Area A (See Graph #1)									Failure Area B			Force Fracture Area C				Force Fracture Area D		
	0	100	200	400	600	1000	1400	5000	9500	0	100	200	0	100	200	1700	0	100	200
Element																			
C	43.7	22.0	15.2	16.2	12.7	10.5	9.4	10.4	12.3	34.1	16.2	11.4	17.1	13.0	12.0	10.2	40.6	25.4	22.0
N	---	---	---	---	---	---	---	---	---	0.9	---	---	---	---	---	---	1.1	1.8	1.7
O	43.3	49.7	51.2	46.4	46.8	44.4	44.1	28.2	18.7	43.5	55.6	58.2	41.2	33.0	25.0	3.2	31.0	30.3	24.1
S	3.9	9.9	11.0	13.0	11.5	11.0	9.9	5.5	3.6	6.8	8.2	8.2	5.9	4.0	4.0	2.0	3.8	3.3	3.0
Cl	---	---	---	---	---	---	---	---	---	1.1	---	---	0.8	---	---	---	0.3	0.1	0.05
Ti	---	---	---	---	---	---	---	---	---	---	---	---	---	---	---	---	---	---	0.1
Cr	---	---	1.3	2.1	3.3	4.6	5.3	9.8	12.0	---	---	✓	3.0	8.0	9.0	19.7	✓	5.0	7.8
Mn	✓	✓	✓	---	---	---	---	---	---	✓	✓	---	---	---	---	---	---	---	---
Fe	6.2	13.5	15.5	16.9	19.5	23.3	24.8	39.5	47.8	11.5	16.8	18.7	27.5	36.0	43.0	54.7	20.1	29.1	35.0
Ni	2.9	5.5	5.7	5.4	6.2	6.3	6.5	6.7	5.5	2.2	3.2	3.5	2.6	4.0	5.0	6.6	1.8	3.4	4.4
Nb	---	---	---	---	---	---	---	---	---	---	---	---	2.0	2.0	2.0	3.4	1.4	1.5	1.7

*Areas shown in Figure 3.4-1.

Table 7. Composition (Weight %) at Fracture
by Electron Microprobe

Elements	Random Locations Away From Forced Fracture				Base Material
Cr	18.05	17.50	18.39	17.57	18.30
Mn	2.32	2.09	1.95	1.88	1.32
Fe	62.90	57.15	58.08	61.06	68.02
Ni	9.68	8.88	7.56	9.09	10.39
Nb	0.40	0.66	0.42	6.73	1.17
S	0.10	0.35	0.10	0.10	<0.03
O	4.65	8.11	5.60	2.67	<0.50

Table 8. Bulk Chemical Analysis of TMI-1 RCP-1B Shaft

Element	Ni	Cr	Nb	Ta	Si	C	Mn	Co	P	S	N_2	Mo	Cu	Al	Ti	Fe
Weight %	10.11	18.29	0.83	<0.10	0.55	0.061	1.32	0.050	0.025	0.014	0.055	0.17	0.10	0.015	<0.01	Bal.

Table 9. Emission Spectroscopy Results
from GPU Furnished Scrapings

Compound*	Flange Area Scrapings (Weight %)	Thermal Sleeve Scrapings (Weight %)
ZnO	.50	<.10
Na_2O	.29	.25
CuO	.43	.29
MoO_3	.045	.080
V_2O_5	<.030	.069
CuO	1.9	.25
TiO_2	.74	.11
SnO_2	.042	.12
CoO	<.030	.054
ZrO_2	<.030	2.7
MnO_2	.13	3.0
Cr_2O_3	1.1	25
NiO	.80	8.1
Fe_2O_3	12	>25
PbO	.17	.18
MgO	.61	<.030
Al_2O_3	5.0	1.7
SiO_2	16	1.7

*The compounds listed are based on the standards used. The chemical
form of the element in the sample may be different.

Defect

Forced
Fracture

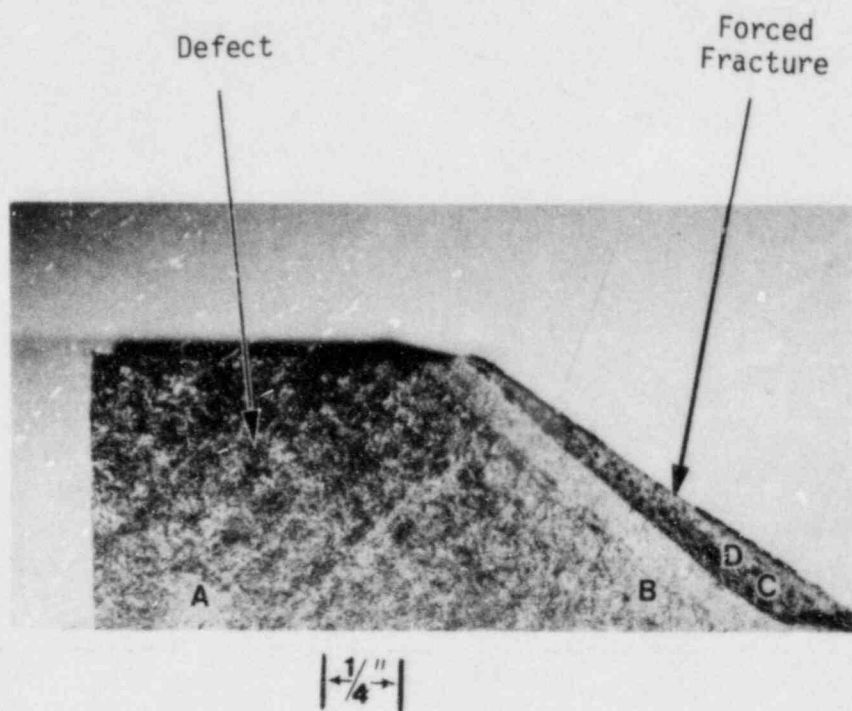$|\!\!\leftarrow\!\!\frac{1}{4}''\!\!\rightarrow\!\!|$

Figure 3.4-1.   View of Fracture Surface on Specimen
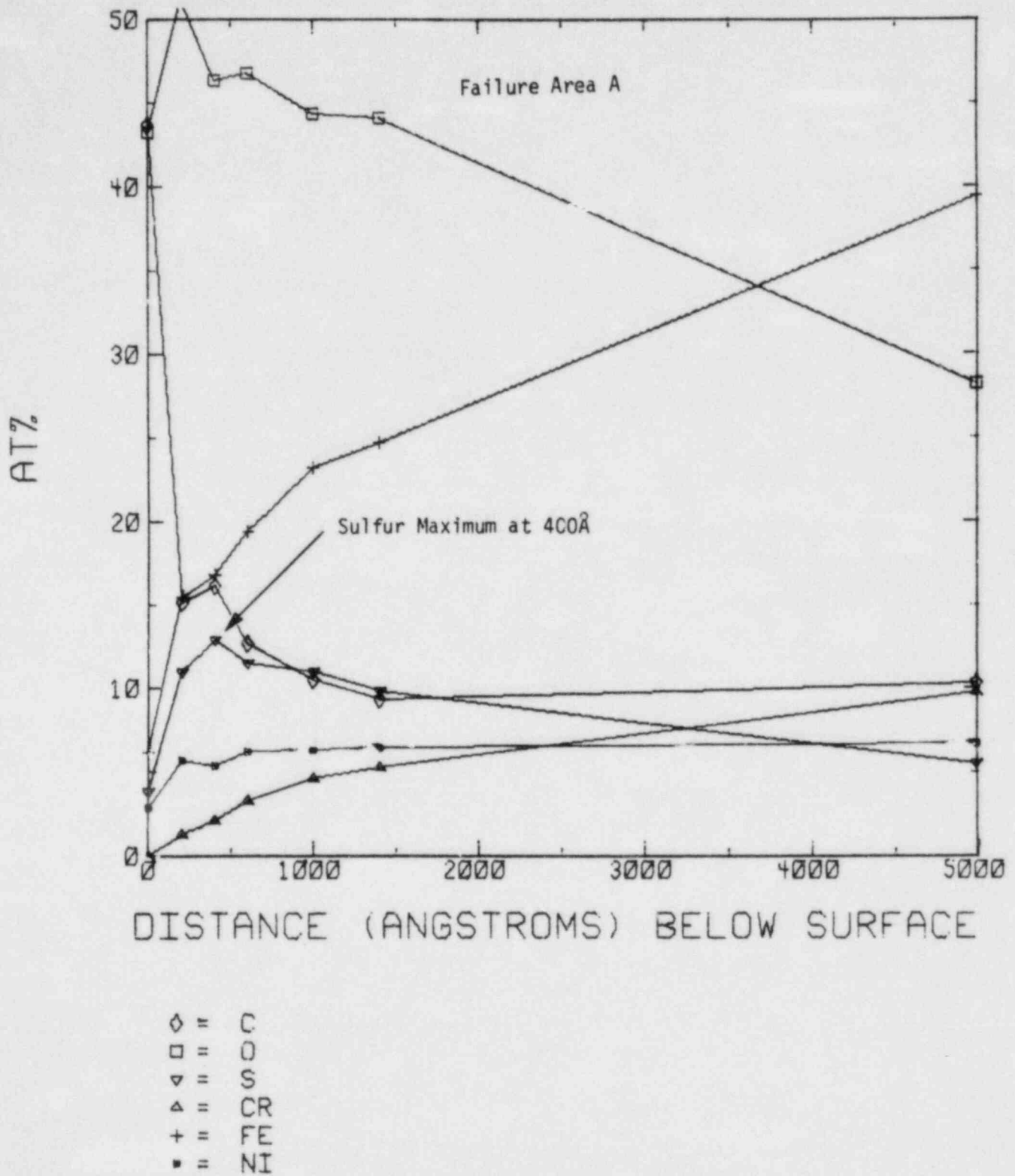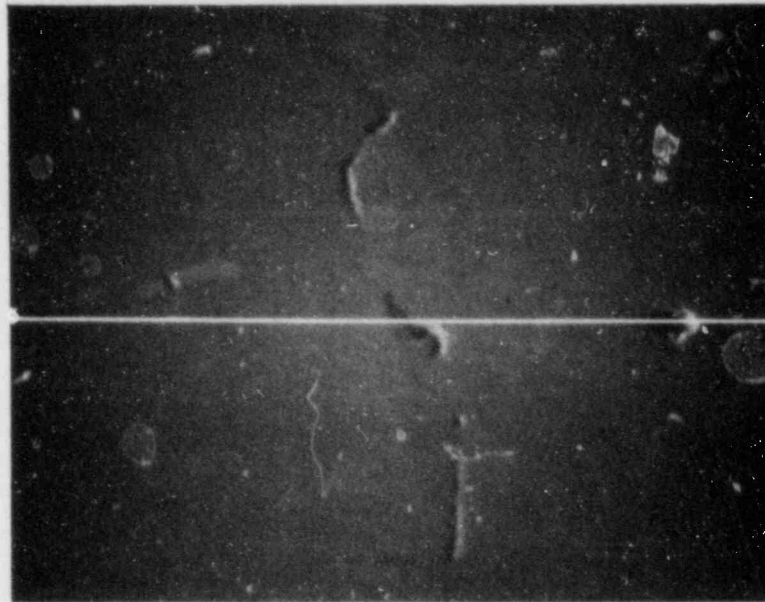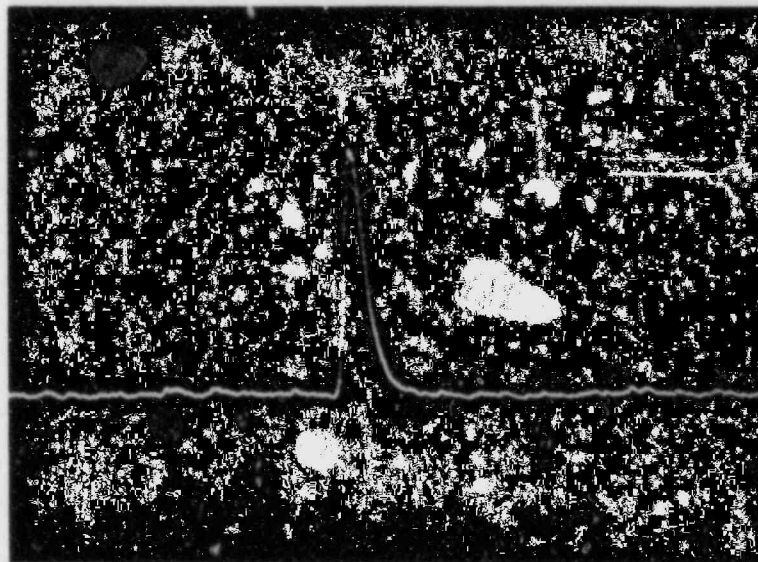A1B Which Was Used for Auger Analysis

Figure 3.4-2. Auger Analysis Sputter Depth Profiles
on the Fracture Surface in Figure 3.4-2

A

|←—¹⁄₁₀₀₀ IN.—→|

B
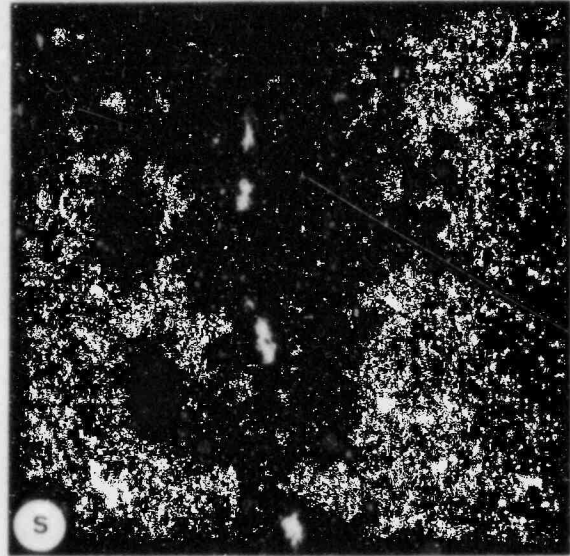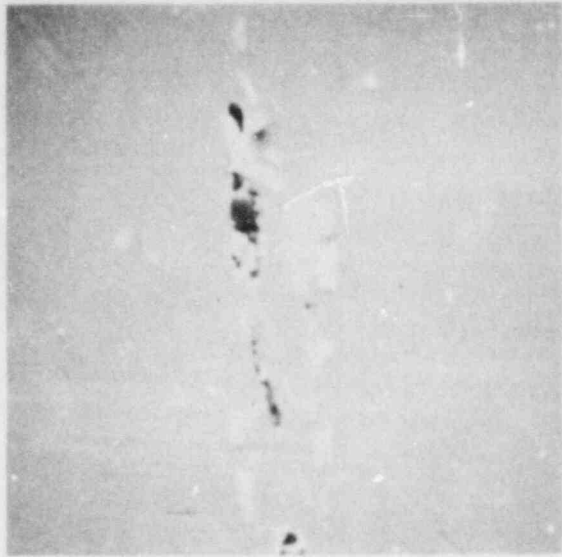
Figure 3.4-3.   Specimen A1C Used for Microprobe Analyses.
A. SEM View of Crack, B. Oxygen Profile
Corresponding to the Beam Traverse Location
Shown by White Line in View A

$\left|\leftarrow\frac{1}{1000}\text{ IN.}\rightarrow\right|$
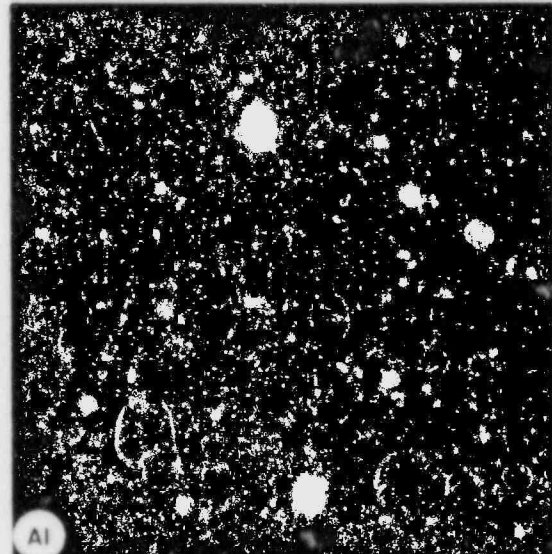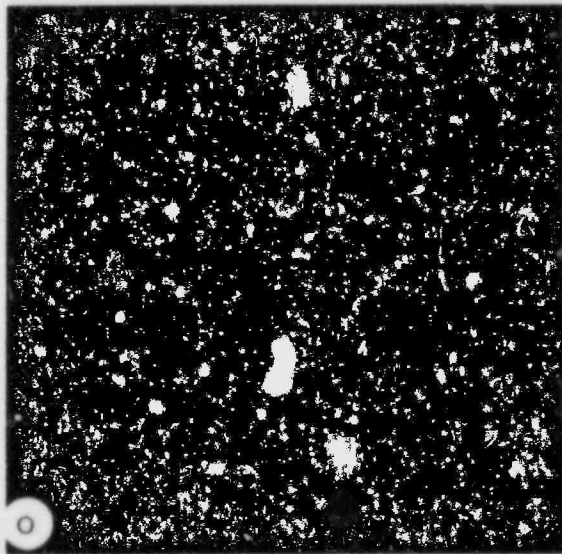
Figure 3.4-4. SEM Photomicrograph and Associated Element
Maps of a Typical Stringer Formation Found
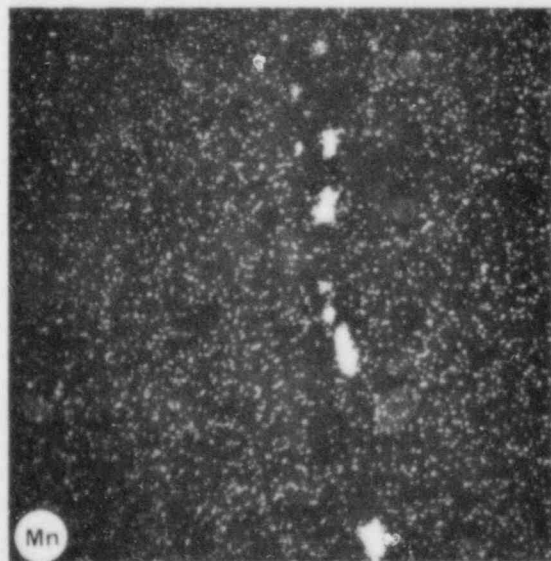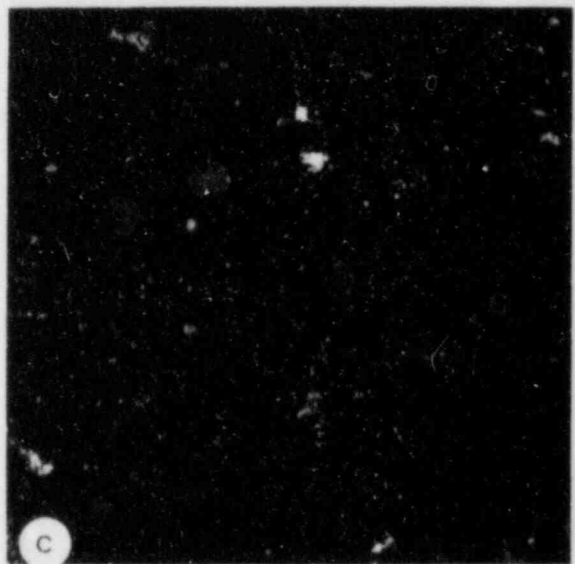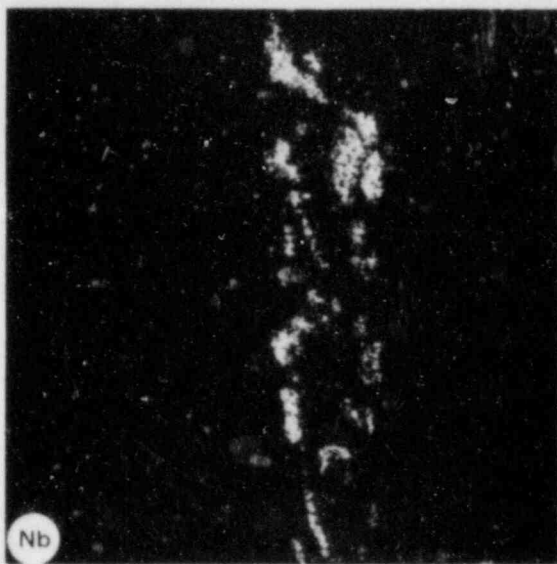in the 347SS Pump Shaft Material

Figure 3-4.4, continued

4. SHAFT FAILURE HYPOTHESIS

This failure hypothesis was assembled based upon the fractographic data, the implications of this data on crack initiation and growth, and, to be sure, some conjecture. It represents the most likely cause of failure.

o   At some point prior to Unit 1 shutdown, a fatigue crack initi-
     ated at the pin hole. The cause for the initiation at this
     location is certainly related to the stress concentration fac-
     tor of the hole; however, other fatigue resistance degrading
     conditions were found which could have been a factor. These
     include fretting, residual stress, and surface finish effects
     in and/or near the pin hole.

o   At the time of the Unit 1 shutdown in 1979, the crack level
     had advanced to the beachmark #15 (light microscopy). During
     the ensuing prolonged shutdown, the tight crack underwent cre-
     vice corrosion and pitting started at the crack tip, preferen-
     tially nucleating at MnS inclusions which had precipitated on
     other oxide inclusions.

o   When the pump was started again for wet layup conditions, it
     was the only pump running and the primary loop was cold. This
     raised the stress intensity range for rotational bending to
     its highest possible value. The stress intensity range which
     occurred produced nearly constant striation spacing of 0.2μ
     and eventually a mixed mode fracture. Crack propagation was
     relatively fast to the point of final shutdown.

o   The introduction of a sulphur species into the primary coolant
        is not considered to have accelerated the failure of the
        shaft. The crack growth rates and the fractography observed
        are well within the range of behavior for stainless steel in
        sulphur-free water or air environments. The sulphur may have
        contributed to increased acidity at the crack tip during peri-
        ods of extended shutdown, thereby enhancing the pitting ob-
        served at beachmark #15.

5. CONCLUSIONS

o   The pump shaft failed by fatigue from high cycle rotational bending.

o   The failure initiated at one of the thermal sleeve pin holes. Initiation may have been assisted by residual stress, surface finish effects and/or wear/fretting.

o   Well defined beachmarks were present on the fracture surface with the majority occurring within about 1 inch of the shaft outer surface.

o   The 1 inch region with the majority of the beach marks contained a dark red-brown film. No other region of this shaft fracture contained a similar film. This region was bounded by a beachmark which was pitted. This was the only pitted area on the fracture face.

o   The fracture was predominantly transgranular with only minor secondary branches penetrating for lengths of 1-2 grains. From initiation to about 1 inch deep, crystallographic transgranular fatigue fracture was present. From 1 to 2.5 inches, a fine transgranular structure existed with faint striations occasionally visible at approximately 0.2μ spacing. From 2.5 to 4.5 inches a mixed mode fracture occurred. The fine transgranular structure was interrupted with small colonies (5 to 10 grains) of coarse cleavage and intergranular separation. This mixed mode structure first gradually increased in frequency and then decreased and essentially disappeared at the final crack position.

o   No intergranular penetrations were observed extending from the pit surfaces. Pitting appeared to nucleate at inclusions.

o   Sulphur was found in the fracture surface film. At the crack tip, sul-
phur was present in levels as high as 13 atomic percent before reaching
background levels of 3 percent at 9500Å. No chlorine was detected on the
fracture. Bulk chemistry of the shaft was within specification limits.

o   While a sulphur species was found on the fracture surface, it is not
believed to have enhanced fatigue crack growth. The fractography
observed and crack growth rates projected from the fractography could be
achieved from fatigue under normal coolant chemistry conditions.

6. RECOMMENDATIONS

6.1 A correlation between pump operation history and the beachmark location and fractography should be performed.

6.2 The stress state, stress intensity range, and stress ratio (R) for the failure location should be calculated as a function of crack length. These should be evaluated against those values predicted from the fractographic observations in this report.

6.3 If judged necessary to experimentally verify the effect of sulphur (suspected lack of effect) on high cycle fatigue, tests should be run on actual shaft material with comparable surface finishes both with and without sulphur present. The influence of load ratio, R, should also be studied.

7. REFERENCES

1) GPUI memo, H. D. Hukill to Office of Nuclear Reactor Regulation.

2) Reactor Coolant Pump Shaft Failure, Docket No. 50-280, License No. DPR-32, Surry Power Station, Virginia Electric and Power Corp., Report No. USRE-SI-73-05, February 20, 1974.

3) Summary of Meeting on October 29, 1981 - Reactor Coolant Pump Shaft Crack, Prairie Island Unit 2, United States Nuclear Regulatory Commission Docket No. 50-306, November 12, 1981.

4) Westinghouse Report by J. A. Fickling, Review of Model 93A Reactor Coolant Pump Shafts in B&W Systems.

5) Standard Steel Test Report, Order No. 612-1419 Item 1, July 9, 1974.

6) S. C. Inman, Nuclear Materials, LRC to S. H. Campbell, Mechanical Design and Analysis - UPGD (OFR), Pump Shaft Failure Analysis Proposal, March 7, 1984.

7) S. C. Inman, Nuclear Materials, LRC, to L. J. Stanek, Engineering Services, UPGD (OFR), TMI-1 Pump Shaft Failure Analysis, dated March 30, 1984.

8) S. C. Inman and D. L. Baty, Nuclear Materials, LRC, to L. J. Stanek, Engineering Services - UPGD (OFR), Additional Work on TMI-1 RC Pump Shaft, dated May 1, 1984.

9) P. M. Yuzawich and C. W. Hughes, An Improved Technique for Removal of Oxide Scale from Fractured Surfaces of Ferrous Materials, Westinghouse R&D Center, Scientific Paper 77-1D9-FRTOG-P1, March 28, 1977.

10) Metals Handbook Vol. 9, Fractography and Atlas of Fractographs.

11) SEM/TEM Fractography Handbook, MCIC-HB-06, Metals and Ceramics Information Center, Battelle Columbus Laboratories, December 1975, 0499, 500, 527, 528, 531, 532, 639, 640, 643, 644.

12) Fracture Handbook, IIT Research Institute, January, 1979, p. 1-287, 288, 290, 305, 306.

13) E. K. Priddle and F. E. Walker, The Effect of Grain Size on the Occurrence of Cleavage Failure in 316 Stainless Steel, Journal of Materials Science, II (1976), p. 386.

14) A. C. Pickard, R. O. Richie, J. F. Knott, Fatigue Crack Propagation in a Type 316 Stainless Steel Weldment, Metals Technology, June 1975, p. 253.

15) R. J. Cooke, P. E. Irving, G. S. Booth and C. J. Beevers, The Slow Fatigue Crack Growth and Threshold Behavior of a Medium Carbon Alloy Steel in Air and Vacuum, Engineering Fracture Mechanics, Vol. 7, 1973, p. 69.

16) R. O. Richie, Influence of Impurity Segregation on Temper Embrittlement and on Slow Fatigue Crack Growth and Threshold Behavior in 300-M High Strength Steel, Metallurgical Transactions, Vol 8A, July, 1977, P. 1131.

17) P. E. Irving and C. J. Beevers, The Effect of Air and Vacuum Environments on Fatigue Crack Growth Rates in Ti-6Al-4V, Metallurgical Transactions, Vol, 5, February 1974, p. 391.

18) C. J. Beavers, Fatigue Crack Growth Characteristics at Low Stress Intensities of Metals and Alloys, Metal Science, August/September 1977, p. 362.

19) M. Akashi and T. Kawamoto, Stress Corrosion Cracking 9SCC) Susceptibility of Various Stainless Steels in Oxygenated High Temperature Water, IHI Engineering Review, Vol II, No. 1, January, 1978, p. 8.

20) G. J. Theus, J. V. Monter, H. A. Domain, Pipe Cracking in Pressurized Water Reactors with Low Pressure Borate-Water Systems, EPRI NP-3320, December, 1983.

21) W. H. Bamford, Fatigue Crack Growth of Stainless Steel Piping in a Pressurized Water Reactor Environment, presented at Energy Technology Conference and Exhibit, Houston, Texas, September 18-22, 1977, published by ASME.

22) Z. Szklarska - Smialowska, Influence of Sulfide Inclusions on the Pitting Corrosion of Steels, Corrosion, Vol. 28, No. 10, October, 1972.

23) R. W. Hertzberg and W. J. Mills, Character of Fatigue Fracture Surface Micromorphology in Ultra-Low Growth Rate regime, ASTM STP 600, June, 1976, p. 220.

APPENDIX A

Calculation of Axial Thrust and Bending Stress
at Location 1 on a Type B Pumpshaft.

JOURNAL SLEEVE

₵

②

9.262

9.1

①

43.35"

16.1

34.75"

18.65"

8.75

F
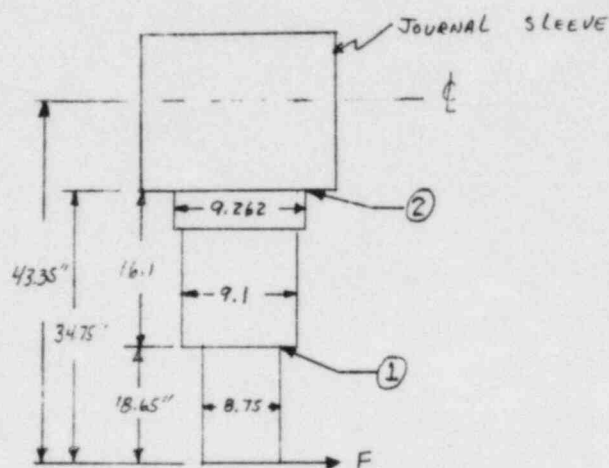
SHAFT CONFIGURATION

COLD OPERATION CALCULATIONS - ONE PUMP

Axial Thrust at 2 = 50,000 lbs, Find Thrust at 1
Mass of Bar Between Journal & Thermal Sleeve
Use 9.2" Dia. as   Uniform Dia.

$$A = \pi \frac{(9.2)^2}{4} = 66.48 \text{ in}^2$$

Vol. = (16.1)(66.48) = 1070.27 in^3

Density (using S.S. 0.29 lb/in^3)

Mass = (1070.29)(0.29) = 310.4 lbs.

Axial Load at 1 = 50,000-310 = <u>49690 lbs</u>

Cross section at Location 1

$$A = \pi \frac{(8.75)^2}{4} = 60.13 \text{ in}^2$$

Axial Stress at 1 = $\frac{49690}{60.13}$ = <u>826 PSI</u>

Bending Stress at 1 for F = 10,000 lbs (Reference 4)

$$\sigma = \frac{MY}{I} = \frac{(10,000)(18.65)\overset{r}{\frac{(8.75)}{2}}}{\frac{1}{4}\frac{(8.75)^4}{2}} = \underline{\underline{2835.66 \text{ PSI}}}$$

HOT OPERATION CALCULATIONS

Axial Load at 2 = 57,000 lb (Reference 4)

Axial Load at 1 = 57,000-310 = <u>56,690 lbs</u>

Axial Stress at 1 = $\frac{56690}{60.13}$ = <u>943 PSI</u>

Bending Stress at 1 for F = 4750 lbs (Reference 4)

$$\sigma = \frac{MY}{I} = \frac{4750(18.65)\frac{(8.75)}{2}}{\frac{1}{4}\frac{(8.75)^4}{2}} = \underline{\underline{1347 \text{ PSI}}}$$
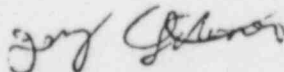
APPENDIX B

Laboratory Ultrasonic Inspection Details

To	
DISTRIBUTION	

From	
P. J. LATIMER/W. M. LATHAM, NDM&D	

Cust.	File No. or Ref.

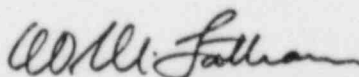| Subj.	Date
WORK REPORT ON THE UT OF THE TMI NO. 1 PUMP SHAFT	APRIL 13, 1984

Distribution: D. L. Baty
A. E. Holt
S. L. Inman
T. Powers

The fact that it was necessary to isolate the crack region from contamination prevented the use of an immersion technique, in particular it prevented the use of an ultrasonic C-scan. Therefore, a contact technique was used with a 10 MHz .25 inch transducer in conjunction with the USIP-11 field instrument. The transverse crack covered approximately 95% of the area of the sectioned shaft. Some false indications were initially observed due to crack closure which allowed complete transmission of sound through the crack. This gave an erroneous indication of "good" metal within the crack region.

Further inspections with a much higher signal amplitude allowed a reflected signal to be observed in the regions of crack closure. Therefore, the window of good metal was readily mapped out by simultaneously observing the signal from the crack and the end of the sample. This procedure was repeated for both ends of the pump shaft and the agreement was 100% concerning the location of the window. Also, the entire procedure was repeated several times in order to increase the confidence level of the measurement technique.

P. J. Latimer

W. M. Latham

PJL/WML/fch

APPENDIX C

Electron Microprobe Analysis and
Auger Electron Spectroscopy Results

To	D. L. BATY - NUCLEAR MATERIALS - LRC	
From	M. E. SCOTT T. R. MCCUE - METALLURGY SECTION - ARC	RC-1 (rev. 1-71)
Cust.		File No. or Ref. RDD:84:5639-01-01:01
Subj.	ANALYSIS OF TMI-347 SS PUMP SHAFT SAMPLE	Date MAY 9, 1984

This letter to cover one customer and one subject only

INTRODUCTION

Samples of 347 SS pump shaft material were sent to ARC for microanalysis of a failed surface for its chemical composition and bulk material inclusion analysis. The original failed surface section from which the samples were removed can be seen in Figure 1. The samples were taken in the area away from the notch beyond the fatigue striations just beyond the view in Figure 1.

SEM/EDX analysis was performed on similar samples at LRC which indicated high levels of sulfur on the surface. The result is potentially significant so that qualitative surface analysis and sputter depth profiling by Scanning Auger Microanalysis (SAM) was requested along with Quantitative Electron Microprobe Analysis for those elements detected by SAM.

Auger Results

The sample received at ARC was cut from the pump shaft in such a manner that the crack tip was intact. A narrow ligament held the two halves together. The failure surface was exposed for Auger analysis by breaking the sample into halves. Auger analyses were done on one half, and microprobe analyses were done on the other.

Sputter depth profiling was done at four locations, two on the failure area and two on the forced fracture. The concentration in atomic % of the elements found along with the depths at which they were detected are recorded in Table 1.

The graph seen in Figure 2 represents the sputter depth profile of the major elements to a depth of 5000Å taken at Location A on the surface as viewed in Figure 3. The sulfur concentration reaches a maximum at 400Å (13 atomic %) and then decreases to 3.6 atomic % at 9500Å. This indicates a film that is significantly rich in sulfur when compared to the sputter depth profile of the forced fracture Area C. The sulfur concentration is highest at the surface (5.9 atomic %) in the forced fracture region and has decreased slightly at the 100Å and 200Å levels to 4 atomic %.

The sulfur was not expected to sputter completely away. The reasons for this are that the Auger system has a continuous background level of sulfur of approximately 1 atomic % and that the sample is known to have sulfide inclusions which would be virtually impossible to sputter away. This explains the remaining 2 atomic % sulfur at the 1700Å depth of the forced fracture (Area C) and the 3.6 atomic % remaining at 9500Å on failure area A.

Another characteristic of the film is an enrichment of manganese at the surface and to a depth of 200Å. Below 200Å, manganese is not detected. The concentration of manganese was not calculated because of interference from an

iron secondary peak; however, it's presence is noted by a checkmark in the table. Manganese concentrations are reported in the microprobe data in Table 2. The Auger findings also indicate a high level of oxygen in the failure area.

In summary, the contamination film appears to be predominantly an oxide(s) rich in sulfur throughout and with manganese enrichment near the surface.

The metal oxide composition of the film cannot be determined by Auger analysis because it is an elemental technique and a multiplicity of metals were detected.

Microprobe Analysis of the Failed Surface

Based on the results of the Auger analysis, the following elements were included in the microprobe analysis: Cr, Mn, Fe, Ni, Nb, S, and O. The piece which was analyzed is the mating surface to the Auger sample (see Figure 3). The results of the quantitative analysis are given in Table 2. Four randomly chosen locations were analyzed on the surface away from the forced fracture. The readings were compared to normal base metal on a piece taken adjacent to the Auger sample such that a plane perpendicular to the defect surface was analyzed. Fracture surface readings were taken, but the surface roughness proved to be too great to achieve good quantitative results. A beam search for sulfur revealed high sulfur in rough surfaces adjacent to the forced fracture but again surface roughness made quantification impossible.

Based on Table 2, it can be concluded that the entire defect surface contains sulfur at levels significantly higher than the base metal. The surface is also enriched in manganese, probably in the form of MnO because oxygen readings show the surface to be oxidized. Niobium levels were found to be lower than the base metal levels in three locations and significantly higher in the fourth location.

Based on oxygen readings, it appears that the oxidized, sulfur-rich surface is less than 1-2μm thick and the underlying base metal was simultaneously analyzed due to normal beam penetration. This is substantiated by the results of Auger sputter depth profiling which indicates base material beginning at approximately 0.5μm below the surface.

An SEM micrograph of the defect surface prior to opening can be seen in Figure 4a. The crack is very tight and microanalysis along this plane only revealed occasional oxide patches. The white line on Figure 4a indicates the location of a beam traverse for oxygen while Figure 4b is the associated oxygen profile to illustrate the presence of oxides. No sulfur enrichment could be detected along the defect line in this sample orientation.

Inclusion Analysis

Several inclusions were seen to be in stringer formations in the sample orientation analyzed. Because sulfide inclusions may play a part in a proposed failure mechanism, the inclusions were analyzed to determine if the inclusions were sulfides.

Elemental dot mapping was done on several inclusions for the following elements: C, N, Ta, S, O, Mn and Nb, and Al. It was observed that the majority of the inclusions are of the form Ti (C, N). Figures 5a through 5g display an SEM micrograph and several associated element maps of a typical cluster of inclusions seen in the sample. The white inclusions are niobium rich. The carbon and nitrogen maps were abnormally faint, most likely because material had smeared over during polishing. The surface is in the unetched condition. The grayish inclusion can be identified by mapping as Al_2O_3. MnS has precipitated out around this and other observed oxide inclusions and MnS inclusions can also be found separately in clusters with oxides and Nb (C, N) as well as isolated in the matrix. Sulfide inclusions were found much less frequently than Nb (C, N) inclusions throughout the sample.

DISCUSSION

Identification of sulfide inclusions was desirable because of the possibility that the band of pits located in Figure 1 has been caused by corrosive attack of sulfide inclusions. There is evidence in the literature* to suggest that sulfides are sites for pitting attack. MnS inclusions were identified in the pump material. It has been found* that in the case of pitting at MnS sites, both the inclusion and metal are attacked while for FeS sites, the metal is attacked but the inclusion is not. Work done at LRC indicates no remaining material in the pits seen in Figure 1 which is consistent with the attack of MnS inclusions specifically. It has also been observed* that the most susceptible sites for pit formation are complex $MnS-Al_2O_3$ inclusions. Such complex inclusions were observed quite frequently in the pump shaft material so that a mechanism of pitting attack at either MnS or $MnS-Al_2O_3$ sites is consistent with the inclusion types found in the 347 material.

M. E. Scott

M. E. Scott

T. R. McCue

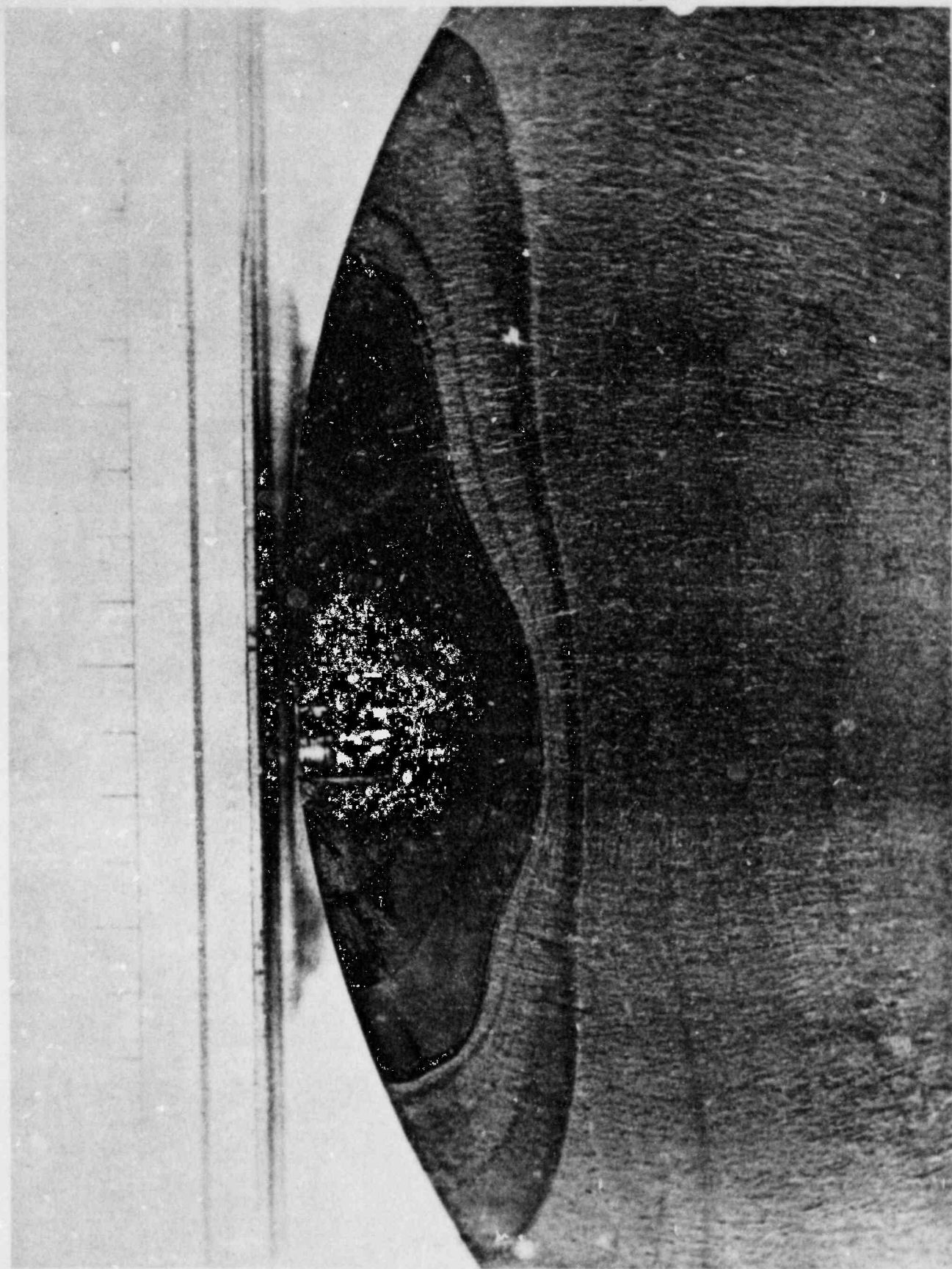T. R. McCue

db
Attachments

---

*Z. Szklarska-Smialowska, "Influence of Sulfide Inclusions on the Pitting Corrosion of Steels," Corrosion 1972, Volume 28, No. 10, pp. 388-96.

TABLE 1

TMI Pump Shaft A1B
Sputter Depth Profile
Atomic %

Sputter Depth Å	Failure Area A (See Graph #1)									Failure Area B			Force Fracture Area C				Force Fracture Area D		
	0	100	200	400	600	1000	1400	5000	9500	0	100	200	0	100	200	1700	0	100	200
Element																			
C	43.7	22.0	15.2	16.2	12.7	10.5	9.4	10.4	12.3	34.1	16.2	11.4	17.1	13.0	12.0	10.2	40.6	25.4	22.0
N	---	---	---	---	---	---	---	---	---	0.9	---	---	---	---	---	---	1.1	1.8	1.7
O	43.3	49.7	51.2	46.4	46.8	44.4	44.1	28.2	18.7	43.5	55.6	58.2	41.2	33.0	25.0	3.2	31.0	30.3	24.1
S	3.9	9.9	11.0	13.0	11.5	11.0	9.9	5.5	3.6	6.8	8.2	8.2	5.9	4.0	4.0	2.0	3.8	3.3	3.0
Cl	---	---	---	---	---	---	---	---	---	1.1	---	---	0.8	---	---	---	0.3	0.1	0.05
Ti	---	---	---	---	---	---	---	---	---	---	---	---	---	---	---	---	---	---	0.1
Cr	---	---	1.3	2.1	3.3	4.6	5.3	9.8	12.0	---	---	√	3.0	8.0	9.0	19.7	√	5.0	7.8
Mn	√	√	√	---	---	---	---	---	---	√	√	---	---	---	---	---	---	---	---
Fe	6.2	13.5	15.5	16.9	19.5	23.3	24.8	39.5	47.8	11.5	16.8	18.7	27.5	36.0	43.0	54.7	20.1	29.1	35.0
Ni	2.9	5.5	5.7	5.4	6.2	6.3	6.5	6.7	5.5	2.2	3.2	3.5	2.6	4.0	5.0	6.6	1.8	3.4	4.4
Nb	---	---	---	---	---	---	---	---	---	---	---	---	2.0	2.0	2.0	3.4	1.4	1.5	1.7

TABLE 2
337 Defect Surface Compositions

Elements	Random Locations Away From Forced Fracture				Base Material
Cr	18.05	17.50	18.39	17.57	18.30
Mn	2.32	2.09	1.95	1.88	1.32
Fe	62.90	57.15	58.08	61.06	68.02
Ni	9.68	8.88	7.56	9.09	10.39
Nb	0.40	0.66	0.42	6.73	1.17
S	0.10	0.35	0.10	0.10	<0.03
O	4.65	8.11	5.60	2.67	<0.50

2X

Figure 1. Original Failed Section from Which SAM and EPMA Samples
Were Removed.
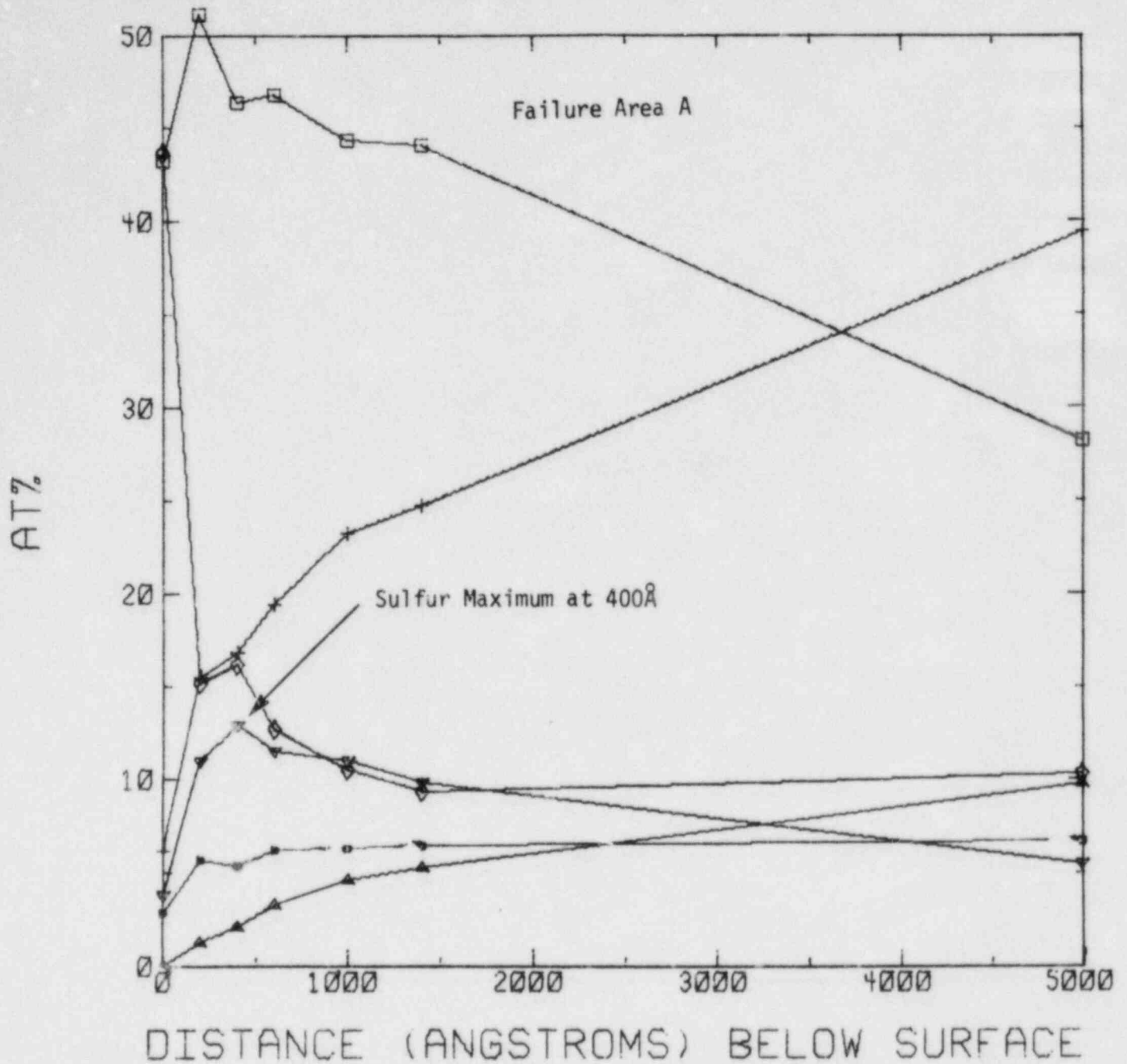
Figure 2. Auger' Analysis Sputter Depth Profiles on the Surface seen in Figure 3.
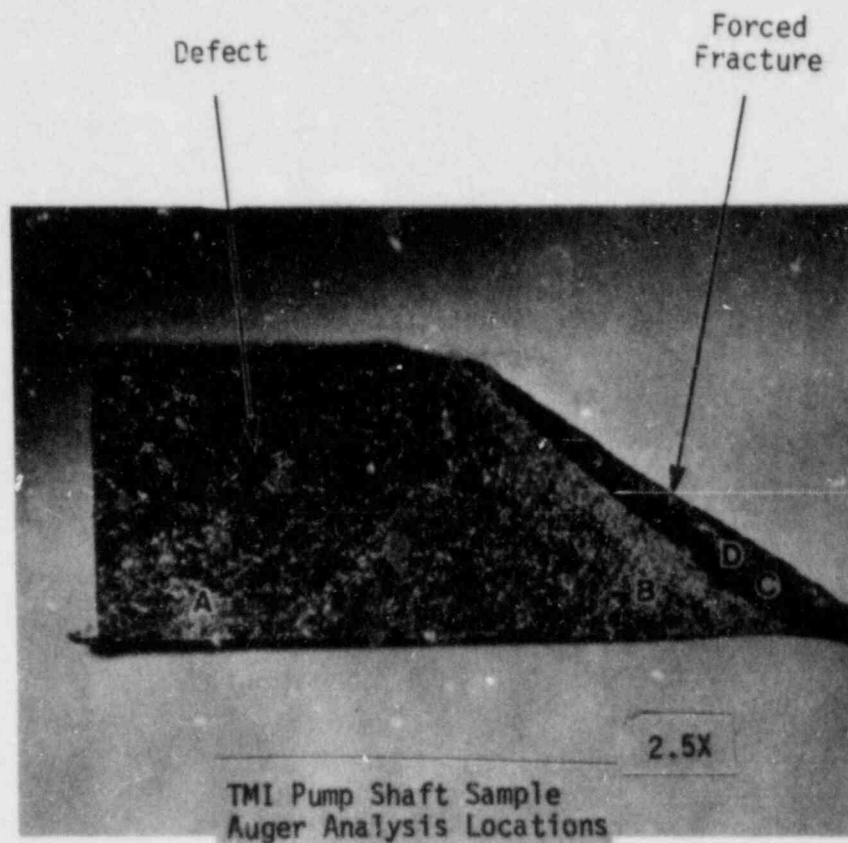
Figure 3. Defect Surface Examined by Auger Analysis. The Mating Face was Used for the Microprobe Analysis.
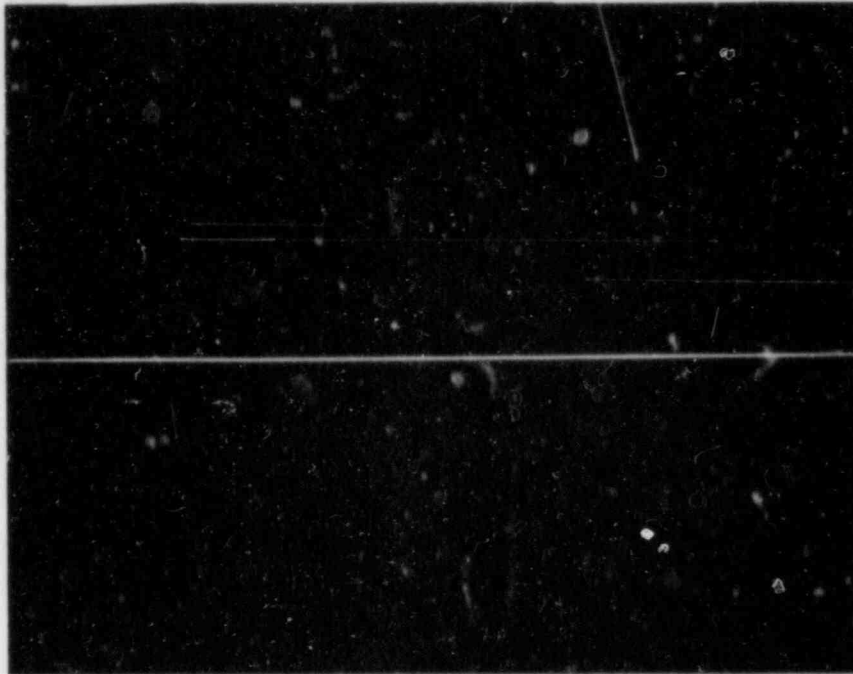
1000X

Figure 4a. SEM Micrograph of the Crack Prior to Opening to Reveal the Surface Seen in Figure 3.
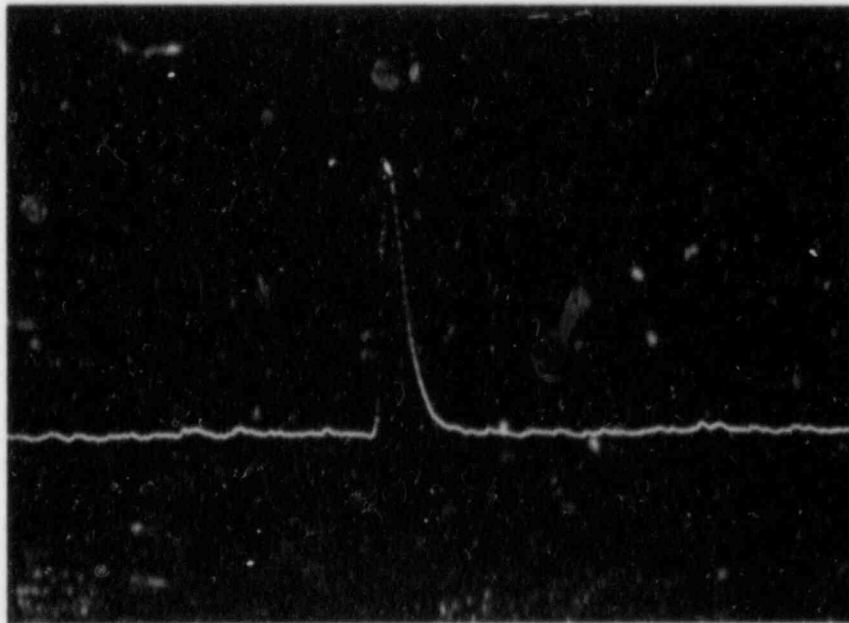
Figure 4b. Oxygen Profile Corresponding to the Beam Traverse Location (White Line) seen in Figure 4a.
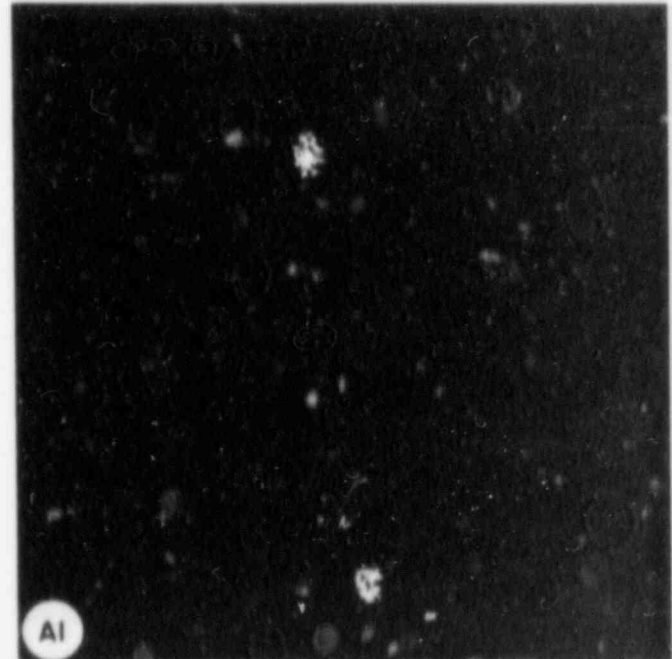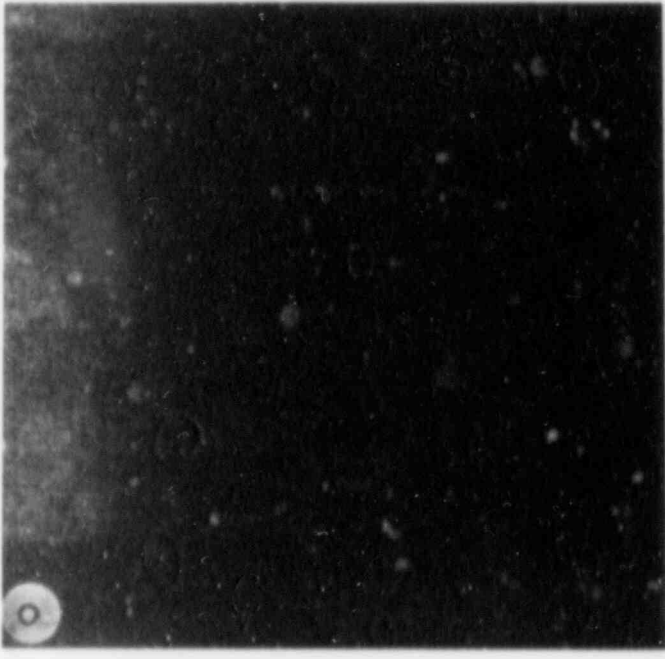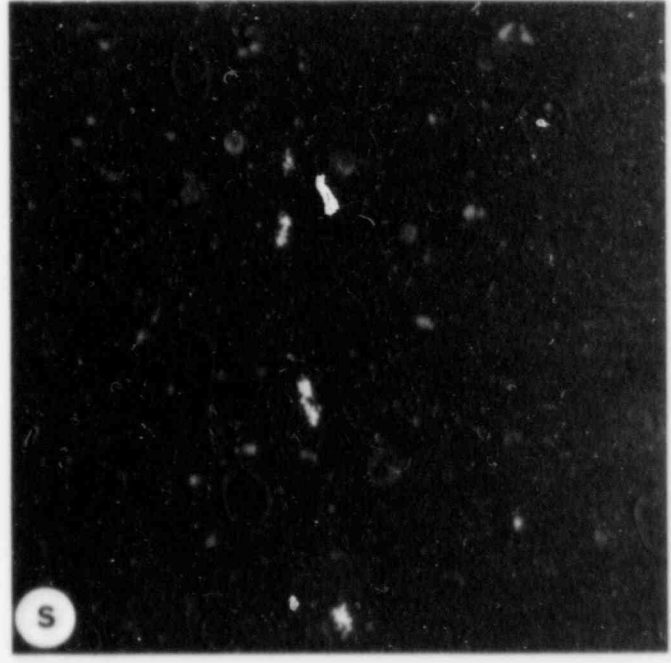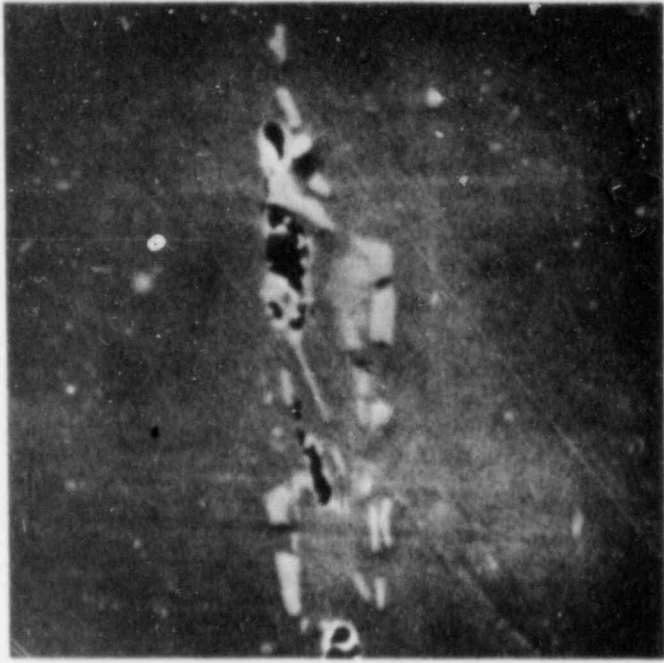
1000X

Figure 5. SEM Micrograph and Associated Element Maps of a Typical Stringer Formation Found in the 347SS Pump Shaft Material.
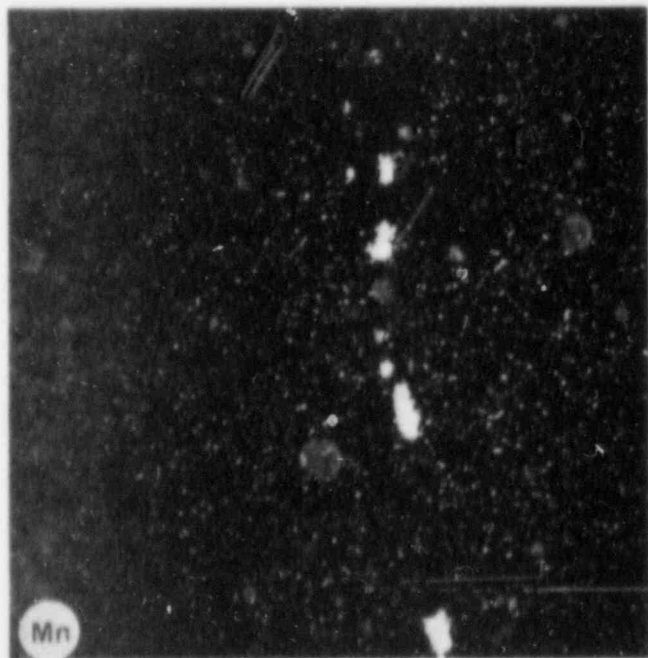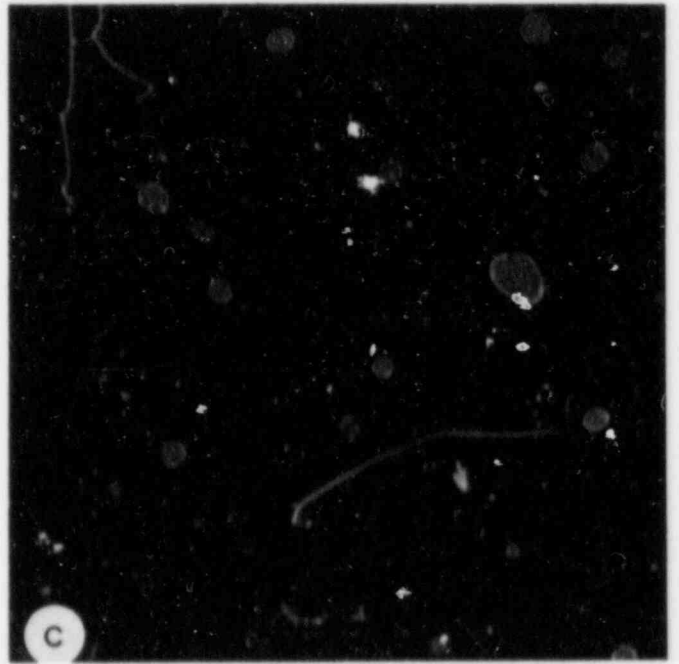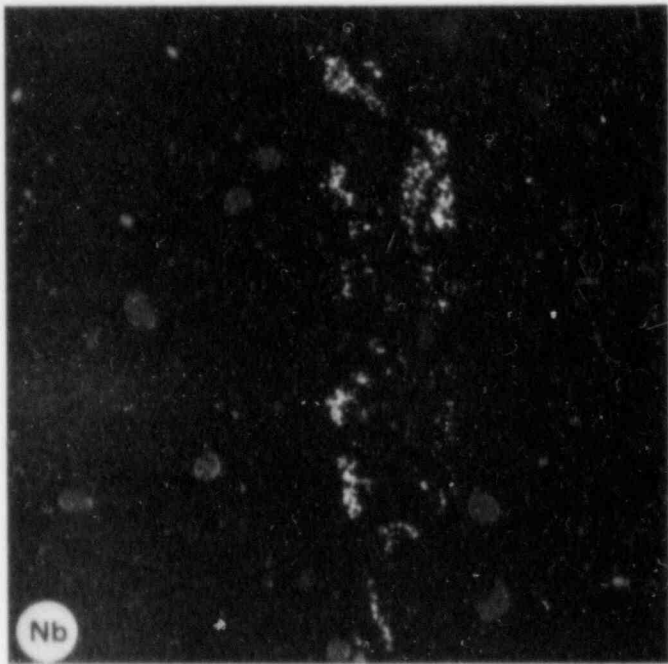
Figure 5 continued.

DISTRIBUTION

R&DD - LRC	ARC	UPGD
P. S. Ayres	H. A. Domian	L. J. Stanek
H. H. Davis	S. L. Harper	J. F. Cuvelier
G. O. Hayner	T. A. McNary	J. A. Castanes
T. J. Zeh	W. Markert	J. L. Smith
G. M. Bain	L. W. Sarver	J. D. Aadland
W. A. Pavinich	G. J. Theus	S. H. Campbell
J. F. Henderson	P. L. Daniel	R. E. Moore
W. A. McInteer	C. M. Weber	R. B. Camper
Library	W. A. Van Der Sluys	J. M. Becker
T. C. Engelder	M. E. Scott	W. L. Redd
C. W. Dalton	T. R. McCue	Library (2)
N. W. White	J. M. Bloom	W. T. Southards
W. A. Shield	CIS (Library) (3)	
B. J. Parham	R. K. Bhada	
B. C. Dudley		
W. T. Hamilton		
T. J. Marsh		
D. L. Baty		
S. C. Inman		

DISTRIBUTION